Charles University in Prague

Faculty of Mathematics and Physics

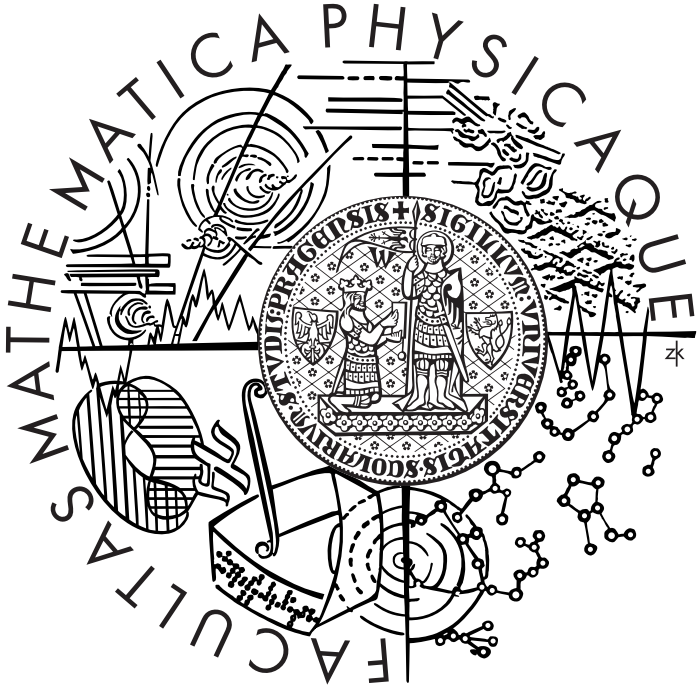

Global and regional scale modeling of dynamic processes in the Earth's mantle

Marie Běhounková

Ph.D. thesis

Supervisor: Hana Čížková

Prague 2007

Acknowledgements

Here I would like to thank everyone who supported me and helped me. First of all, I would like to thank my supervisor Dr. Hana Čížková for her guidance and support during my studies and for her help with writing my thesis. Many thanks also belong to Doc. Ctirad Matyska, Doc. Ondřej Čadek and Dr. Aleš Špičák for many inspiring discussions and valuable advice. I also thank Dr. Jakub Velímský for his advice concerning numerical and programming questions and for the corrections of this manuscript. Another thanks belong to Dr. Ladislav Hanyk for his help with solving numerical and technical problems. My gratitude belongs to Prof. David A. Yuen for his encouragement, continuous interest in my work and the invitation to University of Minnesota. I also thank the staff and students of the Department of Geophysics of the Faculty of Mathematics and Physics and the Department of Tectonics and Geodynamics of the Geophysical Institute of Academy of Sciences for friendly and stimulative atmosphere, especially to Prof. Jiří Zahradník, Prof. Zdeněk Martinec, Doc. Oldřich Novotný, Doc. Jiří Vaněk and Dr. Václav Hanuš.

I would like to thank Dr. Luděk Klimeš for providing the code for ray-tracing and for his valuable advice. Another thanks belong to Dr. Shuxia Zhang and Mark S. Wang for providing the three dimensional convection models used in the synthetic tomographic inversion. I would also like to express thanks to Prof. Renata M. Wentzcovitch for her program computing polycrystalline averages and for introducing me to the topic of elastic properties of the lower mantle minerals.

Most of the convection model runs were carried out at the ”Coupled Cluster” supercomputer of the School of Physics of the Faculty of Mathematics and Physics. This work was supported by the Research Program MSM0021620860 of the Ministry of Education, by Charles University Grant Agency grants No. 376/2004 and No. 2333/2007 and by the Grant Agency of the Academy of Sciences of the Czech Republic grant No. IAA3012303.

Missprints corrected 21.12.2007.

Contents

Preface

Both the forward and inverse modeling play an important role in learning about the processes in the Earth's interior. The tomographic inversion allows us to map its structure. Since the late nineties, the high resolution tomographic images have provided a detailed information about the Earth's mantle structure especially in the subduction zones (e.g. Masters et al. 1996, Grand et al. 1997, van der Hilst et al. 1997, Bijwaard et al. 1998, Fukao et al. 2003). From these images, we can estimate the shape and the dip angle of the plate or its behavior in the transition zone. The tomographic images suggest different scenarios of the subduction process. In some zones (e.g. Java, Central America, Kermadec) the slabs seem to penetrate into the lower mantle while in other zones the plates may be deflected (Tonga, Izu-Bonin). Further, in most regions (e.g. Central America, Java) the significant thickening of the subducted plate is observed in the lower mantle.

For years, geodynamicists have been attempting to reconcile these results of seismic tomography inversion and the images arising from numerical modeling of thermal and thermo-chemical convection. By varying the parameters of the geodynamic models, they aim at obtaining the convection patterns and their characteristics similar to those arising from the seismic tomography. To be able to make this comparison, it is essential to know the resolution and the characteristics of the tomographic inversion. Especially, the discrimination between the real anomalies and artificial features caused by the inversion is an important issue.

Problems of the resolution of the kinematic seismic tomography are subject of the first part of the thesis. Here we aim to assess the ability of tomography to resolve the different geodynamical models of the mantle evolution. In the second part of this thesis, we concentrate on the forward geodynamical modeling. We consider the lithospheric subduction process in models with strongly non-linear rheology. We try to find such parameters that yield the slab morphology similar to that from the tomographic images.

The structure of the thesis is as follows. Part I (chapters 1–4) deals with the resolution tests of the global geodynamic models by travel-time tomography. Chapter 1 gives a short introduction to the travel-time tomography, its resolution and the synthetic problem. In chapter 2, we describe our parametrization (both regular and irregular), the adopted damping method and the procedure we use to get our synthetic data. In chapter 3, we show the results of the inversion for the synthetic input based on both low and high Rayleigh numbers and for both regular and irregular parametrizations. Here we also discuss the dependence of the results on damping. Chapter 4 summarizes the advantages and disadvantages of both (regular vs. irregular) approaches and discusses the resolution of global geodynamic models by travel-time seismic tomography.

Part II of the thesis (chapters 5–8) deals with numerical modeling of mantle convec-

tion applied to the regional problem of the slab deformation in the transition zone and in the upper part of the lower mantle. In chapter 5, we give an overview of the governing equations, the boundary conditions, the equation of state, the rheology and the phase transition implementation. In chapter 6, we describe the method based on finite differences and marker advection which is used to solve the equations. We show here also several tests of our numerical code. In chapter 7, we discuss the results of the parametric study aimed at obtaining thick slabs in the lower mantle. In chapter 8, we summarize the results.

Part I

Resolution of global geodynamic models by seismic tomography

Chapter 1

Introduction

1.1 Motivation

Interpretation of the lateral heterogeneities of seismic wave velocities in the mantle is one of the most important issues in the geodynamical application of the results of seismic tomography. In particular, distinguishing between thermal and chemical origins of the heterogeneities is critical because the dynamical significance of the heterogeneity has different implications on the mode of the Earth's convective heat transfer. It has been well known from the early asymptotic analysis (Turcotte and Oxburgh 1967) that for high Rayleigh number, convection is characterized by thin thermal anomalies (horizontal boundary layers, upwellings and downwellings). Thus, it is very important for the inversion procedure to determine their thickness, how they are deflected by phase transitions, whether potential layering of mantle convection and/or the existence of small mantle plumes can be determined, what are characteristic wavelengths of temperature anomalies at different depths, etc. The kinematic seismic tomography is a suitable method to reveal the mode of the convection. However, it is very important to know what the resolution of particular tomographic techniques is to answer these questions.

In this part of thesis, we investigate the resolution of the global geodynamic models by kinematic seismic tomography. We employ both regular and irregular parametrization. We study the influence of the explicit regularization on the results. Since we know both input and output models, we can compute the correlation between them and compare their spectra.

1.2 Kinematic seismic tomography and resolution

Kinematic seismic tomography can provide us with the snapshot of the thermo-chemical evolution in the Earth. The use of the travel-time data for deducing the lateral variations of seismic velocities in the mantle has a long history going back to paper by Aki et al. (1977). This technique has been called travel-time tomography (Aki and Richards

Part of the results discussed in chapters 1–4 were published in Běhounková, M., Čížková, H., Matyska, C., Yuen, D., Wang, M., 2007, Resolution tests of 3-D convection models by travel-time tomography: Effects of Rayleigh number and regular vs. irregular parametrization, *Geophys. J. Int. 170*, 401–416.

1980) in contrast to tomography based on waveform analysis (Woodhouse and Dziewonski 1984, Li and Romanowicz 1995, Li and Romanowicz 1996). A comparison of these two approaches can be found e.g. in Dziewonski (2000).

To solve the tomographic inverse problem, the parametrization functions have to be chosen. In the global tomography, the parametrization functions with either global or local support are usually taken into account. The functions with the global support are typically spherical harmonic functions in horizontal direction combined with polynomial or spline function in the radial direction (e.g. Dziewonski 1984, Su et al. 1994, Li and Romanowicz 1996). The functions with local support are usually splines, wavelets or piecewise constant functions (e.g. Inoue et al. 1990, van der Hilst et al. 1997, Bijwaard et al. 1998, Kárason and van der Hilst 2001, Vasco et al. 2003, Chiao and Liang 2003, Montelli et al. 2004a). Due to the uneven distribution of the rays in the mantle, the functions with the irregular local support are also taken into account. These functions can reflect the uneven distribution of sources and receivers (e.g. Spakman and Bijwaard 2001, van der Hilst et al. 2004, Nolet and Montelli 2005). For comparison of the tomographic models see e.g. Becker and Boschi (2002).

To solve the tomographic inverse problem, the Cholesky factorization is usually used for the basis functions with the global support. For the basis functions with the local support, the iterative numerical solvers suitable for the spare matrix are used — e.g. Simultaneous Iterative Reconstruction Technique (SIRT), conjugate gradients or LSQR method (Paige and Saunders 1982a, Paige and Saunders 1982b). For comparison of these numerical methods see e.g. Boschi (2001).

Another important issue in seismic tomography is the choice of the regularization since the tomographic problems are usually ill-conditioned due to the uneven distribution of sources and receivers in the Earth's mantle. Additional conditions (model norm or model roughness minimization) are usually added with a weight. This weight is traditionally called damping coefficient or damping factor. These additional conditions are rather artificial stabilization of the inversion and the choice of the optimal damping can be tricky. If the value of the damping factor is underestimated, the inversion results are still damaged by oscillations. On the other hand, if the value of the damping factor is overestimated, not only the oscillation but even the amplitudes of the real structures are suppressed. Therefore, the optimal value of the damping coefficient has to be chosen to get reasonable solution. For determination of this optimal value, the trade-off analysis (Hansen 1992) is used (e.g. Montelli et al. 2004b, Boschi 2006).

As we mentioned above, it is very important to know the resolution of the tomographic technique to discuss the geodynamical questions such as the thickness of the boundary layers, deformation of slabs, plume evolution, etc. The resolution is best shown by the resolution matrix (e.g. Lévêque et al. 1993, Vasco et al. 2003, Soldati and Boschi 2005). However, the computation of the resolution matrix is computer demanding and time consuming (Boschi et al. 2007). This is one of the reasons why rather synthetic resolution tests like checker-board test (e.g. Inoue et al. 1990, Su et al. 1994, Vasco et al. 1995, Kárason and van der Hilst 2001, Fukao et al. 2003) or layer-cake test (e.g. Bijwaard et al. 1998) are used. In these tests, the artificial seismic velocity structures are used to obtain the synthetic travel-time data. These input synthetic structures are often constructed by means of particular parametrizations and then this same parametrization is employed in

the inversion of the synthetic data. It is clear that this approach can reveal only a part of the resolution problems, as it neglects mainly the projection error (see the next chapter for a detailed explanation).

Detailed resolution tests should thus start from models of seismic velocity structures containing a broader variety of wavelengths than those yielded by tomography parametrization and, simultaneously, these input models should be in agreement with the physics of mantle dynamics. Here we assume that the heterogeneities in the mantle are generated only by thermal convection. The ability of travel-time tomography to resolve thermal anomalies developed in mantle convection simulations has been investigated by "seismic tomographic" filtering (Johnson et al. 1993, Mégnin et al. 1997, Tackley 2002). However, it can be shown that the short-wavelength anomalies can leak into long-wavelength (Trampert and Snieder 1996), if the wavelength of the anomalies is underestimated. Thus, the tomographic inversion should be employed (Honda 1996, Bunge and Davies 2001, Běhounková et al. 2005).

Following the work by Bunge and Davies (2001), we use the thermal anomalies from 3-D spherical-shell convection to construct a synthetic input model of seismic velocity anomalies, and to compute the differential travel-times (delays) for a series of synthetic earthquake events and an array of stations positioned on the spherical model. We use the synthetic delays computed in the model for two Rayleigh numbers[1], $Ra = 3 \cdot 10^5$ and $Ra = 10^6$. We solve a travel-time tomography problem using P and pP waves. The addition of other phases would improve the resolution in some regions (see Lei and Zhao 2006). However, the total number of P waves used for the real tomographic inversion strongly exceeds the total number of other phases. Therefore, the characteristics of the travel-time inversion should not be changed essentially.

We employ the parametrization functions with the local support. We take into account both regular and irregular parametrizations to describe the model and we use the LSQR algorithm to solve the inversion. In case of regular parametrization, L-curve analysis is used to obtain an optimal value of the damping coefficient. As we take into account a linear tomographic problem, we do not assume the errors arising from the non-linearity of the tomographic problem (the path of the rays depending on the structure itself). Moreover, we neglect picking error, mislocation error and error of stations corrections. Hence, we analyse only errors arising from the projection of the real structure on the adopted parametrization. In the synthetic tomography, contrary to the real data tomography, both the input and output structures are known. Therefore, we can compare them and we can evaluate the efficiency of the inversion. We employ spectral and correlation analyses of the results to compare the synthetic input models with the results for both regular and irregular parametrizations.

[1]For definition of Rayleigh number, see paragraph 5.5.

Chapter 2

Theory and Method

2.1 Linearized delays

In the travel-time tomography, the image of the seismic velocity (slowness) structure in the Earth can be obtained by the analysis of the field of travel times $T_i,\ i = 1, \ldots, N$:

$$T_i = \int_V G_i(\boldsymbol{r}) s(\boldsymbol{r}) \mathrm{d}\boldsymbol{r} + \varepsilon_i, \tag{2.1}$$

where V denotes the integration domain, G_i is a ray characteristic function of the i^{th} ray, $s(\boldsymbol{r})$ is slowness and ε_i is the error of the i^{th} travel time. This error includes the picking error, the mislocation error, the error of origin time and the error of station correction. The ray characteristic function G_i (also known as the travel-time sensitivity function or the sampling function) is given by

$$G_i(\boldsymbol{r}) = \frac{\partial T_i}{\partial s(\boldsymbol{r})}. \tag{2.2}$$

It describe the sensitivity of the travel-times to the slowness distribution $s(\boldsymbol{r})$. In principle, the travel-times are sensitive to the slowness in the whole mantle, not only along the ray path. These rays are called "thick" (e.g. Coates and Chapman 1990, Woodward 1992, Marquering et al. 1998, Dahlen et al. 2000, Tromp et al. 2005, Chen et al. 2007, Peter et al. 2007). In this work, we use the high-frequency asymptotic ray theory, where the travel-time sensitivity function G_i is described by the two-dimensional Dirac distribution $\delta(q_1, q_2)$. Here (q_1, q_2, q_3) denotes ray-centered coordinates (q_1 and q_2 are local Cartesian coordinates in the plane perpendicular to the ray, $q_3 = l$ is the arc-length). Therefore the travel-time depends only on the slowness along the ray and this type of ray is called "thin". In this approximation the equation (2.1) takes form:

$$T_i = \int_V \delta(q_1, q_2) s(\boldsymbol{r}) \mathrm{d}\boldsymbol{r} + \varepsilon_i. \tag{2.3}$$

This equation can be then rewritten using the integral along the ray as follows:

$$T_i = \int_{\mathrm{L}_i} s(\boldsymbol{r}) \mathrm{d}l_i + \varepsilon_i, \qquad \mathrm{L}_i = \mathrm{L}_i(s). \tag{2.4}$$

L_i denotes the i^{th} ray, $\mathrm{d}l_i$ is the integrational step along the i^{th} ray. Similarly to the equation (2.4), we define the field of the reference travel-times $T_{0i},\ i = 1, \ldots, N$

$$T_{0i} = \int_{\mathrm{L}_{0i}} s_0(\boldsymbol{r})\mathrm{d}l_{0i}, \qquad \mathrm{L}_{0i} = \mathrm{L}_{0i}(s_0), \tag{2.5}$$

where the subscript 0 denotes the reference model quantities.

In the travel-time tomographic inversion, the field of delays d_i is usually defined as the difference between the travel-time T_i and the reference travel-time T_{0i}:

$$d_i = T_i - T_{0i} = \int_{\mathrm{L}_i} s(\boldsymbol{r})\mathrm{d}l_i - \int_{\mathrm{L}_{0i}} s_0(\boldsymbol{r})\mathrm{d}l_{0i} + \varepsilon_i. \tag{2.6}$$

We assume that the difference between slowness $s(\boldsymbol{r})$ and the reference slowness $s_0(\boldsymbol{r})$ is low compared to the reference velocity $s_0(\boldsymbol{r})$, i.e.

$$\left| \frac{s - s_0}{s_0} \right| \ll 1. \tag{2.7}$$

Then the equation (2.6) can be linearized as follows:

$$d_i = \int_{\mathrm{L}_{0i}} s(\boldsymbol{r})\mathrm{d}l_{0i} - \int_{\mathrm{L}_{0i}} s_0(\boldsymbol{r})\mathrm{d}l_{0i} + \varepsilon_i + \xi_i, \tag{2.8}$$

Here quantity ξ_i describes the error arising from approximating the ray-path L_i by the reference ray path L_{0i}. Thanks to the Fermat principle, ξ_i is a higher-order error. If we define the absolute slowness perturbance as $\Delta s(\boldsymbol{r}) = s(\boldsymbol{r}) - s_0(\boldsymbol{r})$, the relation (2.8) can be simplified into form

$$d_i = \int_{\mathrm{L}_{0i}} \Delta s(\boldsymbol{r})\mathrm{d}l_{0i} + \varepsilon_i + \xi_i. \tag{2.9}$$

2.2 Parametrization

To solve an inverse problem, a continuous seismic velocity structure has to be represented by discrete set of model parameters:

$$\Delta s(\boldsymbol{r}) = \sum_{j=1}^{M} \Delta s_j c_j(\boldsymbol{r}) + \zeta(\boldsymbol{r}). \tag{2.10}$$

Here Δs_j is j^{th} parameter, M is number of parameters, $c_j(\boldsymbol{r})$ is the j^{th} base function and $\zeta(\boldsymbol{r})$ is a parametrization error. In this thesis, we use piecewise constant functions c_j with non-overlapping cell support:

$$c_j(\boldsymbol{r}) = \begin{cases} C_j^{-\frac{1}{2}} & \text{if } \boldsymbol{r} \text{ is in the } j^{\mathrm{th}} \text{ cell,} \\ 0 & \text{elsewhere,} \end{cases} \tag{2.11}$$

where C_j denotes the volume of the j^{th} cell. If we define the scalar product of the real functions $f(\boldsymbol{r})$ and $g(\boldsymbol{r})$ on the area of interest V

$$(f,g) = \int_V f(\boldsymbol{r})g(\boldsymbol{r})\mathrm{d}V, \qquad \mathrm{d}V = r^2 \sin\vartheta \mathrm{d}r\mathrm{d}\vartheta\mathrm{d}\varphi \tag{2.12}$$

then the base $\{c_j\}_{j=1}^{M}$ is orthonormal ($(c_j, c_k) = \delta_{jk}$, where δ_{jk} is Kronecker delta). The supports of the base functions c_j in regular parametrization are usually represented by equi-angular (EA), equi-surface area (ESA) or equi-volume (EV) cells. On the other hand, the support of the base function can be also irregular and uneven distribution of the rays can be taken into account.

Here we use the irregular parametrization proposed by Abers and Roecker (1991) and Spakman and Bijwaard (2001). The irregular basis function c_j is constructed from basic base functions b_k ($k = 1, \ldots, M_{\mathrm{B}}$, M_{B} is number of basis function and $M < M_{\mathrm{B}}$) by joining. The supports of basic base functions b_k are non-overlapping and equi-angular cells with constant depth. The basic basis function b_k is defined as

$$b_k(\boldsymbol{r}) = \begin{cases} B_k^{-\frac{1}{2}} & \text{if } \boldsymbol{r} \text{ is in the } k^{\mathrm{th}} \text{ cell,} \\ 0 & \text{elsewhere,} \end{cases} \tag{2.13}$$

B_k is a volume of k^{th} basic cell and the base functions are orthonormal ($(b_j, b_k) = \delta_{jk}$). As we mentioned above, the irregular basis $\{c_j\}_{j=1}^{M}$ is constructed from basic (regular) basis $\{b_k\}_{k=1}^{M_{\mathrm{B}}}$:

$$\begin{aligned} c_j &= \sum_{k=1}^{M_{\mathrm{B}}} P_{jk} b_k, \\ P_{jk} &= (c_j, b_k) = \frac{B_k^{\frac{1}{2}}}{C_j^{\frac{1}{2}}} \Delta_{jk}, \\ C_j &= \sum_{k=1}^{M_{\mathrm{B}}} \Delta_{jk} B_k, \end{aligned} \tag{2.14}$$

where P_{jk} is a projection matrix and Δ_{jk} can be written as:

$$\Delta_{jk} = \begin{cases} 1 & \text{if } b_k \text{ is part of base function } c_j, \\ 0 & \text{otherwise.} \end{cases} \tag{2.15}$$

We assume that both resulting irregular base functions and basic base functions are non-overlapping. Therefore, a given support of the basic base function is part of only one irregular cell. The scheme of the matrix $\boldsymbol{\Delta}$ and construction of the projection vector $\mathbf{p}$ is illustrated in Fig. 2.1. The suitable (memory-saving) representation of the matrix $\boldsymbol{\Delta}$ is a projection vector $p(k) = j,\ k = 1, \ldots, M_{\mathrm{B}}$ (b_k is part of a c_j, i.e. $\Delta_{jk} = 1 \Leftrightarrow p(k) = j$). We construct the projection vector by the hit equalizing algorithm.

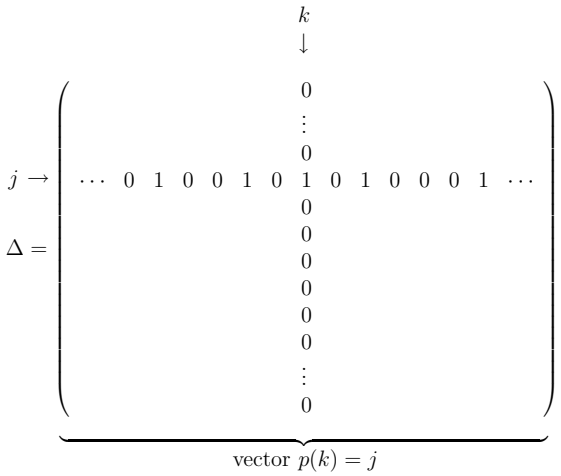

Figure 2.1 Scheme of the projection matrix $\boldsymbol{\Delta}$ and construction of projection vector $\mathbf{p}$.

2.3 Hit equalizing algorithm

To construct the irregular basis, we use the hit equalizing algorithm based on van der Hilst et al. (2004). The principle of this algorithm is demonstrated in a schematic 2-D case in Fig. 2.2. First, we divide the domain into regular, equi-angular basic (small) cells (see Fig. 2.2**a**; number in each cell gives corresponding hit count — number of rays crossing given cell). Then we have to choose two parameters that characterize our target irregular parametrization: a) minimum number of rays $n_{\min}$ demanded in each resulting parametrization cell and b) the size of largest admissible parametrization cell (in terms of small basic cells). In the example shown in Fig. 2.2, $n_{\min}$ is 500 and largest irregular parametrization cell can contain maximum 4×4 basic cells (see Fig. 2.2**b**). The number of basic cells in each direction (r, ϑ, φ) has to satisfy the condition: $K_\bullet = L_\bullet \cdot 2^{M_E}$, where $\bullet$ denotes directions r, ϑ or φ. $K_\bullet$ defines the number of basic cells and $L_\bullet$ is the number of the largest cells in each direction and 2^{M_E} defines number of basic cells in each largest cell in each direction. If the number of rays in the largest cell is higher than $n_{\min}$, this cell is a candidate for recursive splitting. That is: we try to divide each cell containing at least $n_{\min}$ rays into halves. If both halves still contain at least $n_{\min}$ rays and the ratio of the sides does not exceed 2:1, the cell is divided. If there is more than one option how to make division, the one with the lowest hit count difference between the halves is chosen. The loop ends, either when we reach the basic cell or when the cells cannot be divided anymore, because the new cells after the division would not contain enough ($n_{\min}$) rays. In Fig. 2.2**c**, resulting parametrization is shown. While in the regular basic cells, Fig. 2.2**a**, the hit count varies from zero in some parts of the domain to 800

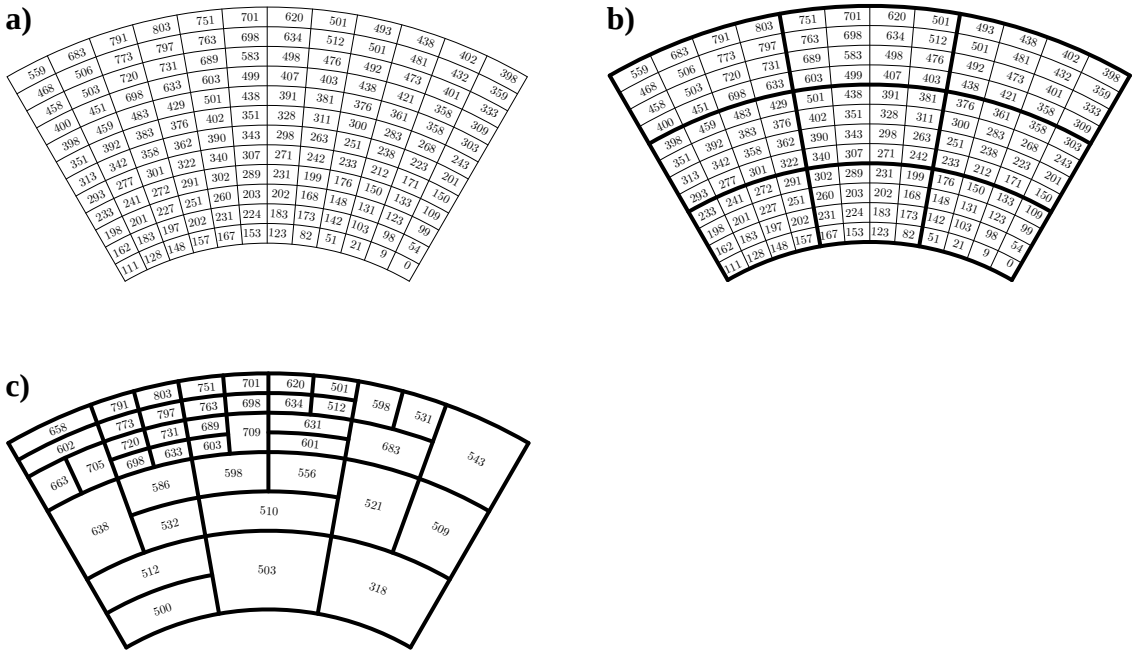

Figure 2.2 Two dimensional sketch of the hit equalizing algorithm, **a)** basic cells and hit counts, **b)** basic cells (thin line) and largest possible target cells (thick line), **c)** irregular cell parametrization and hit counts, $L_r = 3$, $L_\varphi = 3$, $M_E = 2$, a minimum hit count of 500 rays per cell.

rays per cell in other parts, after applying the hit equalizing algorithm the number of rays in cells ranges from about 300 rays to 800 rays. Therefore, each parametrization cell is constrained by approximately the same amount of data. It should be noted, that due to the a priori choice of the largest irregular cell, there may remain some cells, which contain less than the required 500 rays (see the cell in the lower right corner in Fig. 2.2**c**).

2.4 Definition of the inverse problem

By substituting (2.10) into (2.9), we get

$$d_i = \sum_{j=1}^{M} \Delta s_j \left(\int_{\mathrm{L}_{0i}} c_j(\boldsymbol{r}) \mathrm{d}l_{0i} \right) + \varepsilon_i + \xi_i + \zeta_i \tag{2.16}$$

where ζ_i denotes the integral of the parametrization error $\zeta(\boldsymbol{r})$ along the i^{th} ray ($\zeta_i = \int_{\mathrm{L}_i} \zeta(\boldsymbol{r}) \mathrm{d}l_i$). The integral of the basis function along the i^{th} reference ray is equal to the arc-length of the i^{th} ray in the j^{th} cell (l_{ij}, see schematic Fig. 2.3) except for the normalization constant $C_j^{-\frac{1}{2}}$. So the equation (2.16) can be rewritten into

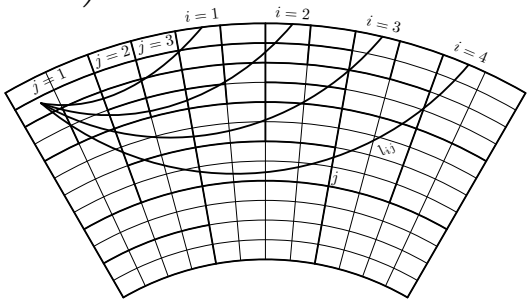

Figure 2.3 The arc-length of i^{th} ray in the j^{th} irregular cell.

$$d_i = \sum_{j=1}^{M} \Delta s_j C_j^{-\frac{1}{2}} l_{ij} + \varepsilon_i + \xi_i + \zeta_i. \tag{2.17}$$

If we define model parameter m_j

$$m_j = C_j^{-\frac{1}{2}} \Delta s_j \tag{2.18}$$

then the equation (2.17) reads:

$$d_i = \sum_{j=1}^{M} m_j l_{ij} + \varepsilon_i + \xi_i + \zeta_i. \tag{2.19}$$

and the model parameter m_j has a simple physical interpretation — it is the absolute slowness perturbation in the j^{th} cell. The equation (2.19) can be also rewritten into the matrix form

$$\mathbf{d} = \mathbf{G} \cdot \mathbf{m} + \mathbf{e}, \tag{2.20}$$

where $G_{ij} = l_{ij}$ and $e_i = \varepsilon_i + \xi_i + \zeta_i$.

The arc-lengths in the irregular cells (l_{ij}) are calculated as follows. First, we compute the arc-lengths in the basic base function (the elements of matrix $\mathbf{G}^{\mathrm{B}}$). From these

elements, we obtain the elements of the matrix $\mathbf{G}$: we substitute (2.14) into (2.16)

$$d_i = \sum_{j=1}^{M} \Delta s_j \left[\int_{\mathrm{L}_{0i}} \left(\sum_{k=1}^{M_\mathrm{B}} P_{jk} b_k \right) \mathrm{d}l_{0i} \right] + \varepsilon_i + \xi_i + \zeta_i, \tag{2.21}$$

$$d_i = \sum_{j=1}^{M} \Delta s_j C_j^{-\frac{1}{2}} \sum_{k=1}^{M_\mathrm{B}} B_k^{\frac{1}{2}} \Delta_{jk} \int_{\mathrm{L}_{0i}} b_k \mathrm{d}l_{0i} + \varepsilon_i + \xi_i + \zeta_i, \tag{2.22}$$

$$d_i = \sum_{j=1}^{M} \Delta s_j C_j^{-\frac{1}{2}} \sum_{k=1}^{M_\mathrm{B}} \Delta_{jk} l_{ik}^\mathrm{B} + \varepsilon_i + \xi_i + \zeta_i, \tag{2.23}$$

where l_{ik}^B is the arc-length of i^{th} ray in the k^{th} basic cell. By comparing equations (2.17) and (2.23), we get

$$l_{ij} = \sum_{k=1}^{M_\mathrm{B}} \Delta_{jk} l_{ik}^\mathrm{B} \tag{2.24}$$

$$\mathbf{G} = \mathbf{G}^\mathrm{B} \cdot \boldsymbol{\Delta}^\mathrm{T} \tag{2.25}$$

It is obvious from the equation (2.24) that we can compute elements of matrix l_{ij} by the summation of arc-lengths in the basic cells (the elements of matrix l_{ik}^B). The main advantage of this method is that the arc-length in the basic (equi-angular) cells can be easily computed and they can be used for different projection vectors.

2.5 Solution

Problem (2.20) is usually solved as an overdetermined one. We have more data ($d_i,\ i = 1, \ldots, N$) then the unknown parameters ($m_j,\ j = 1, \ldots, M$) $N > M$ (see Fig. 2.4). If the error vector $\mathbf{e}$ is non zero, i.e. $\mathbf{e} \neq \mathbf{0}$, the data cannot be exactly explained by the model vector $\mathbf{m}$. Therefore, we consider the solution of the inverse problem using L_2-norm — the solution $\mathbf{m}^\mathrm{pred}$ is the model vector $\mathbf{m}$ which describes the data vector $\mathbf{d}$ the best using the L_2-norm. We minimize the misfit function S:

$$\begin{pmatrix} \\ \mathrm{d} \\ \\ \end{pmatrix}_{\mathrm{N}\times 1} = \begin{pmatrix} \\ \mathrm{G} \\ \\ \end{pmatrix}_{\mathrm{N}\times\mathrm{M}} \begin{pmatrix} \\ \mathrm{m} \\ \\ \end{pmatrix}_{\mathrm{M}\times 1} + \begin{pmatrix} \\ \mathrm{e} \\ \\ \end{pmatrix}_{\mathrm{N}\times 1}$$

Figure 2.4 Scheme of the overdetermined problem.

$$S = ||\mathbf{d} - \mathbf{G} \cdot \mathbf{m}||_{\mathrm{L}_2}^2 = \min, \tag{2.26}$$

It can be shown (e.g. Tarantola 1987) that the solution $\mathbf{m}^\mathrm{pred}$ of the problem (2.26) is

$$\mathbf{m}^\mathrm{pred} = \left(\mathbf{G}^\mathrm{T} \cdot \mathbf{G}\right)^{-1} \cdot \mathbf{G}^\mathrm{T} \cdot \mathbf{d}, \tag{2.27}$$

where $\left(\mathbf{G}^\mathrm{T} \cdot \mathbf{G}\right)^{-1}$ is the generalised inversion of the matrix $\mathbf{G}$. However, the matrix $\left(\mathbf{G}^\mathrm{T} \cdot \mathbf{G}\right)$ can be singular or close to the singular (the matrix is ill-conditioned) due to the uneven distribution of the rays in the Earth. And the inversion of this matrix may not exist. This problem can be essential mainly for the regular parametrization.

2.6 Regularization

Some strategy has to be adopted if the problem (2.26) is ill-conditioned which is mostly the case, especially in the global inversions. For example: singular value decomposition (SVD) can be used to find the eigenvalues and cut-off low or zero eigenvalues (e.g. Press et al. 1992). However, this method is rather time-demanding. The problem can be also stabilized if we have some a priori information about the structure (e.g. from a previous inversion) of the model (e.g. Tarantola 1987). If there is no a priori information about the model, another a priori information can be chosen. This information should arise from the physics of the given problem. We assume that the additional requirements are described by a set of the linear equations $\mathbf{D} \cdot \mathbf{m} = \mathbf{c}$. Then the inverse problem with additional requirements is represented by

$$\begin{pmatrix} \mathbf{G} \\ \lambda\mathbf{D} \end{pmatrix} \cdot \mathbf{m} = \begin{pmatrix} \mathbf{d} \\ \lambda\mathbf{c} \end{pmatrix} + \begin{pmatrix} \mathbf{e} \\ \mathbf{0} \end{pmatrix}. \tag{2.28}$$

This method is often called ”damping” or ”regularization” (see e.g. Menke 1989). Analogically to (2.26), we define the solution $\mathbf{m}^{\mathrm{pred}}$ of the problem (2.28). This predicted model vector represents the best fit of the data vector $\mathbf{d}$ and the additional condition with weight λ using the L_2-norm

$$S = ||\mathbf{d} - \mathbf{G} \cdot \mathbf{m}||^2_{\mathrm{L}_2} + \lambda^2 ||\mathbf{c} - \mathbf{D} \cdot \mathbf{m}||^2_{\mathrm{L}_2} = \min. \tag{2.29}$$

Analogically to (2.27), we can write

$$\mathbf{m}^{\mathrm{pred}} = \left(\mathbf{G}^{\mathrm{T}} \cdot \mathbf{G} + \lambda^2 \mathbf{D}^{\mathrm{T}} \cdot \mathbf{D}\right)^{-1} \cdot \left(\mathbf{G}^{\mathrm{T}} \cdot \mathbf{d} + \lambda^2 \mathbf{D}^{\mathrm{T}} \cdot \mathbf{c}\right). \tag{2.30}$$

If the matrix $\mathbf{D}$ is chosen suitably and $\lambda \neq 0$, the inversion of the matrix $\left(\mathbf{G}^{\mathrm{T}} \cdot \mathbf{G} + \right.$ $\left. + \lambda^2 \mathbf{D}^{\mathrm{T}} \cdot \mathbf{D}\right)$ exists.

There are many possibilities, how to choose the damping. The norm of the gradient of vector $\mathbf{m}$ (roughness minimization — Inoue et al. 1990, Boschi and Dziewonski 1999) is typically used. Another possibility is the minimization of the norm of the model vector $\mathbf{m}$. For comparison of these two approaches see e.g. Boschi (2001). Klimeš (2002) proposes using minimization of Sobolev norm of model vector $\mathbf{m}$. Here we use the minimization of the model vector $\mathbf{m}$ ($\mathbf{D} = \mathbf{I}$ and $\mathbf{c} = \mathbf{0}$, where $\mathbf{I}$ is the identity matrix). Then the equations (2.28) and (2.29) take the forms

$$\begin{pmatrix} \mathbf{G} \\ \lambda\mathbf{I} \end{pmatrix} \cdot \mathbf{m} = \begin{pmatrix} \mathbf{d} \\ \mathbf{0} \end{pmatrix} + \begin{pmatrix} \mathbf{e} \\ \mathbf{0} \end{pmatrix} \tag{2.31}$$

and

$$S = ||\mathbf{d} - \mathbf{G} \cdot \mathbf{m}||^2_{\mathrm{L}_2} + \lambda^2 ||\mathbf{I} \cdot \mathbf{m}||^2_{\mathrm{L}_2} = \min. \tag{2.32}$$

For the ill-conditioned problems, the choice of the proper damping factor λ is another crucial issue. For this purpose, the L-curve criterion is used (e.g. Hansen 2000). L-curve shows the trade-off between the norm of the model vector $||\mathbf{m}||_{\mathrm{L}_2}$ and residual norm $||\mathbf{G} \cdot \mathbf{m} - \mathbf{d}||_{\mathrm{L}_2}$ in the log-log scale. Such curve is L-shaped (it has corner $\lambda = \lambda_{\mathrm{corner}}$

— see schematic Fig. 2.5). For $\lambda < \lambda_{\mathrm{corner}}$, the minimization of the residual norm dominates. For $\lambda > \lambda_{\mathrm{corner}}$, the minimization of the model norm outweighs the minimization of the residual norm; at $\lambda = \lambda_{\mathrm{corner}}$ these two trends intersect. This point can be computed using the maximum curvature κ of the L-curve (see Hansen 2000):

$$\begin{aligned} \alpha &= ||\mathbf{m}(\lambda)||^2_{\mathrm{L}_2} \quad , \quad \beta = ||\mathbf{G}\cdot\mathbf{m}(\lambda) - \mathbf{d}||^2_{\mathrm{L}_2} \\ \tilde{\alpha} &= \log(\alpha) \quad , \quad \tilde{\beta} = \log(\beta) \\ \kappa(\lambda) &= 2\frac{\tilde{\alpha}'\tilde{\beta}'' - \tilde{\alpha}''\tilde{\beta}'}{\left((\tilde{\alpha}')^2 + (\tilde{\beta}')^2\right)^{3/2}}, \end{aligned} \tag{2.33}$$

where $\bullet'$ and $\bullet''$ denotes the first and second derivatives with respect to λ.

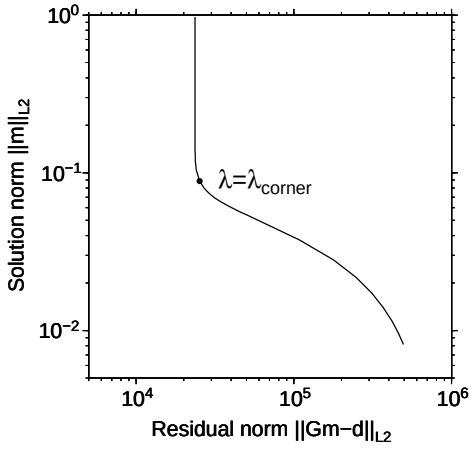

Figure 2.5 Schematic figure of the L-curve.

2.7 Synthetic inversion

In this thesis, we study the resolution of the travel-time tomography using the synthetic data. We take into account a linear problem: the i^{th} ray and the i^{th} reference rays are identical, i.e. ξ_i from the equation (2.31) is equal to zero ($\xi_i = 0,\ \forall i$). Moreover, we neglect all non-projection error, i.e. picking error, mislocation error and error of stations corrections ($\varepsilon_i = 0,\ \forall i$). We concentrate only on the role played by the projection error $\zeta(\boldsymbol{r})$ (the whole unpredictable part of the equation (2.31) is caused by projection error). Therefore, our obtained resolution should be considered as an upper limit. In reality, where non-projection errors are of course present, the resolution would be worse.

The scheme of our synthetic tomography inversion is following (cf. Fig. 2.6). First, we choose the sources and receivers and compute the rays (paragraph 2.7.1). Then the input

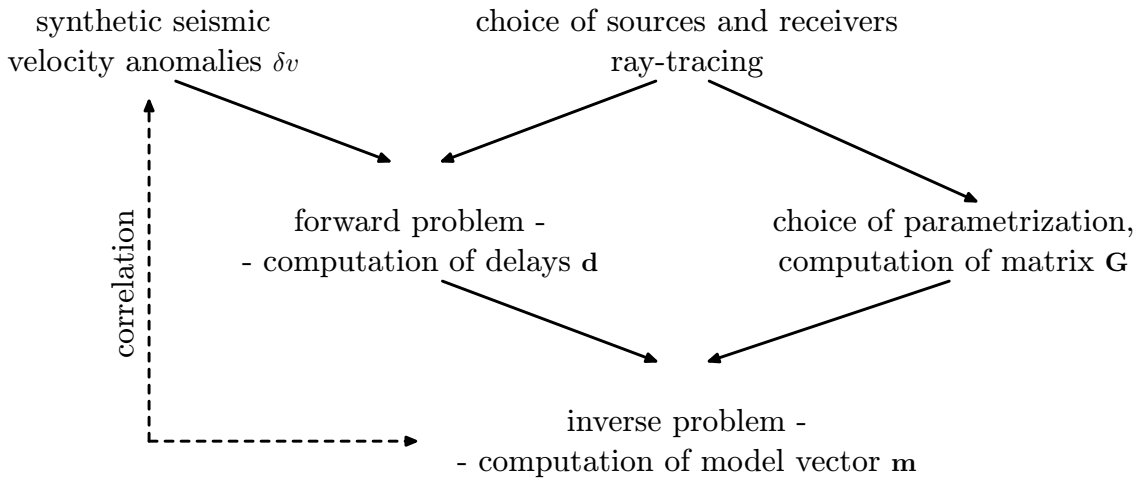

Figure 2.6 Scheme of the synthetic problem.

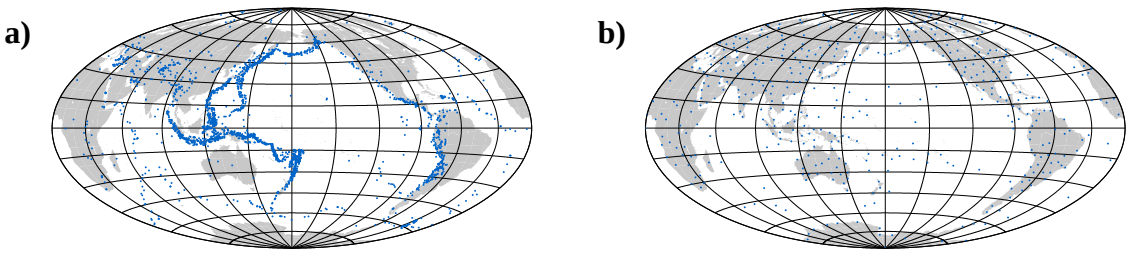

Figure 2.7 Distributions of **a)** sources and **b)** receivers.

model of seismic velocity structures is chosen based on thermal convection (paragraph 2.7.2). Then we solve the forward problem — we compute the vector of delays $\mathbf{d}$ — our synthetic data (paragraph 2.7.2). To solve the inverse problem, we parametrize our model (paragraph 2.7.3) and compute the matrix $\mathbf{G}$ (paragraph 2.7.3). Finally, we solve the inverse problem (paragraph 2.7.3). After obtaining the solution of the inverse problem, we visualize the results and further we compare the input synthetic model and the output tomographic model (paragraph 2.7.4).

2.7.1 Sources, receivers and ray tracing.

The distributions of sources and receivers is chosen from the ISC (1964-2001) database. From this database, we use 2500 randomly chosen locations of events with $m_b > 5.5$ and 462 stations. Chosen stations are not closer than 4° to avoid linearly dependent rows in the matrix $\mathbf{G}$. The distributions of sources and receivers are given in Fig. 2.7.

The program CRT (Červený et al. 1988) is employed for the ray-tracing. Since we assume a linear problem, the rays are calculated only once (the i^{th} ray is identical to the i^{th} reference ray). The rays are traced through the depth dependent model PREM (Dziewonski and Anderson 1981) where the ocean layer is omitted for simplicity (see Fig. 2.8). We take into account only teleseismic P (epicentral distance between the given source and receiver is greater than 25°) and for sources in the depth greater then $100\,\mathrm{km}$ also pP waves. The total number of rays is $925,054$.

2.7.2 Synthetic velocity model and delays

Synthetic seismic velocity anomalies are derived from the models of basally-heated thermal convection of Zhang and Yuen (1996) for the Rayleigh numbers $Ra = 3 \cdot 10^5$ and $Ra = 10^6$ with constant viscosity and thermal expansivity. The cut-off degree of the spherical harmonic expansion of the model is 256 and thus the horizontal resolution of the model is 0.7°. The vertical resolution has 128 points. We suppose that density linearly depends on temperature

$$\Delta\rho(\boldsymbol{r}) = -\rho_{\mathrm{M}}\alpha\Delta T(\boldsymbol{r}), \tag{2.34}$$

where $\rho_{\mathrm{M}} = 4500\,\mathrm{kg/m^3}$ is the reference density of the convection model and $\alpha = 1.4 \cdot 10^{-5}\,\mathrm{K}^{-1}$. Relative density and seismic velocity anomalies are related by

$$\frac{\Delta\rho(\boldsymbol{r})}{\rho_0(r)} = P_k(r)\frac{\Delta v(\boldsymbol{r})}{v_0(r)}, \tag{2.35}$$

where $\rho_0(r)$ and $v_0(r)$ are the reference density and velocity models (Dziewonski and Anderson 1981, see Fig. 2.8), P_k is the proportionality factor (Karato 1993, Fig. 2.9) which depends on radius r, Δv is seismic velocity anomaly and $\Delta\rho$ describes the density anomalies in the convection model.

The delays are computed by integrating of the seismic slowness anomalies Δs ($\Delta s = -\Delta v/v_0^2$) along the rays.

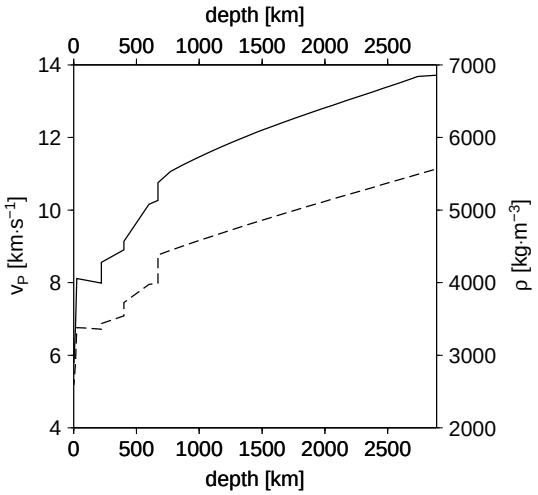

Figure 2.8 PREM (Dziewonski and Anderson 1981) P-velocity (solid line) and density (dashed line) in the mantle.

2.7.3 Parametrization, matrix G and inversion

We use both regular (equal surface area — ESA) and irregular parametrization. In the regular parametrization model, we employ $36,428$ cells ($207\,\mathrm{km} \times 4^\circ \times 4^\circ$ cell size on equator). The ESA basis is constructed from the regular basic cells ($n_r \times n_\vartheta \times n_\varphi = 14 \times 45 \times 720$, size $\sim 207\,\mathrm{km} \times 4^\circ \times 0.5^\circ$). The projection vector $\mathbf{p}$ is constructed by $i_r \times i_\vartheta \times i_\varphi = 1 \times 1 \times f(\vartheta)$ basic cells, i.e. the number of basic cells creating ESA cell is constant for direction r and ϑ and it is dependent on latitude for direction φ (longitudinal direction).

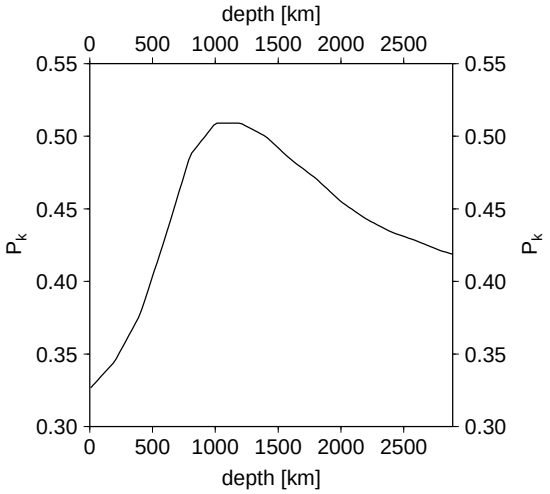

Figure 2.9 Proportionality factor P_k (Karato 1993).

In the irregular parametrization model, the size of cells are defined by $L_r = 3$, $L_\vartheta = 10$, $L_\varphi = 20$, $M_E = 4$ (see section 2.3), which yields $48 \times 160 \times 320$ basic cells with size $60\,\mathrm{km} \times 1.125^\circ \times 1.125^\circ$. After applying hit equalizing algorithm with a minimum of $1,000$ rays per cell, we get $35,886$ cells. The resolution of the regular parametrization model was chosen to produce approximately the same number of parameters as the irregular one. That allows us to compare these two methods with similar computer costs.

The matrix of the arc-lengths in the basic cells $\mathbf{G}_{\mathrm{B}}$ is computed by integration of basic base function along the rays equation (2.22). The arc-length in the ESA or irregular cells $\mathbf{G}$ is computed from equation (2.24). Both matrix $\mathbf{G}$ and $\mathbf{G}_{\mathrm{B}}$ are sparse due to base

functions with the local support. The non-zero elements of the matrix $\mathbf{G}$ are in order of 0.1 per cent for both regular and irregular parametrization. We use the CSR (compressed sparse row) format to store the matrix $\mathbf{G}$ and we use the package SPARSKIT to perform the operation with the matrix $\mathbf{G}$.

We suppose the inverse problem in the form (2.32) and we use LSQR algorithm by Paige and Saunders (1982a) and its numerical implementation (`http://www.stanford.edu/group/SOL/software/lsqr.html`) to find a solution.

2.7.4 Characteristics and visualizations of input and output model

Large parametrization cells demanded in some parts of the mantle by the poor ray coverage are unable to resolve relatively small-scale convection features. And in these regions, high projection error could be expected. In order to estimate its amplitude and spatial distribution, we calculate the projection of an input model described by function $\Delta s(\boldsymbol{r})$ onto the parametrization basis $\{c_j\}_{j=1}^{M}$ (see equation 2.10):

$$\Delta s_j = \int_V \Delta s(\boldsymbol{r}) c_j \mathrm{d}V = C_j^{-1/2} \int_{C_j} \Delta s(\boldsymbol{r}) \mathrm{d}V. \tag{2.36}$$

When comparing this equation with the definition of the average $\Delta\overline{s_j}$ of the input model Δs in the j^{th} cell

$$\Delta\overline{s_j} = \frac{\int_{C_j} \Delta s(\boldsymbol{r}) \mathrm{d}V}{C_j} \tag{2.37}$$

and using the equation (2.18), we get

$$\Delta\overline{s_j} = C_j^{-1/2} \Delta s_j = m_j \tag{2.38}$$

We define the projection (also called average) model of the input model

$$\Delta\overline{s}(\boldsymbol{r}) = \Delta\overline{s_j}, \tag{2.39}$$

if $\boldsymbol{r}$ is in the j^{th} cell. Using the projection of the input model onto the basis, we can write for the projection error $\zeta(\boldsymbol{r})$:

$$\zeta(\boldsymbol{r}) = \Delta s(\boldsymbol{r}) - \Delta\overline{s}(\boldsymbol{r}). \tag{2.40}$$

In the seismic tomography, the relative velocity anomalies in per cent $\delta v(\boldsymbol{r})$ are usually visualized. From now on, we also display the results and their characteristics using the percent of velocity anomalies $\delta v(\boldsymbol{r})$ instead of slowness anomalies:

$$\delta v(\boldsymbol{r}) = \frac{v(\boldsymbol{r}) - v_0(r)}{v_0(r)} \cdot 100\%, \tag{2.41}$$

where $v(\boldsymbol{r}) = 1/s(\boldsymbol{r})$ is velocity and $v_0(r)$ is the reference velocity. This quantity can be computed from the model parameter m_j by

$$\delta v(\boldsymbol{r}) = -m_j v_0(r) \cdot 100\%, \quad \text{if } \boldsymbol{r} \text{ is in the } j^{\mathrm{th}} \text{ cell.} \tag{2.42}$$

This equation can be derived by the Taylor expansion under the condition (2.7).

In the synthetic problem, we know both input and output seismic structures. Consequently, we can compare the input synthetic model and inversion results and thus assess the resolving power of the inversion. For this purpose, we use the spectral decomposition of the input, average and output model. We compute their spectra by integration

$$f_{lm}(r) = \int_0^{2\pi} \int_0^{\pi} \sin\vartheta f(r,\vartheta,\varphi) Y^*_{lm}(\vartheta,\varphi) \mathrm{d}\vartheta \mathrm{d}\varphi \tag{2.43}$$

with integrational step equal to size of the basic cell (i.e. $207\,\mathrm{km} \times 4^\circ \times 0.5^\circ$ for regular parametrization and $60\,\mathrm{km} \times 1.125^\circ \times 1.125^\circ$ for irregular parametrization). In equation (2.43), the Y_{lm} is a fully normalized spherical harmonic function (see Varshalovich et al. 1989), * denotes complex conjugate function and $f_{lm}(r)$ are expansion coefficients of a function $f(r,\vartheta,\varphi)$. Using the spherical harmonic expansion coefficient, we compute the power spectra of functions $f(r,\vartheta,\varphi) = \sum_l \sum_{m=-l}^{l} f_{lm}(r) Y_{lm}(\vartheta,\varphi)$ depending on degree and depth:

$$P_l(r) = \sum_{m=-l}^{l} f_{lm}(r) f^*_{lm}(r). \tag{2.44}$$

The correlation coefficient ρ is another way how to compare the input models with the inversion results. We define the global correlation coefficient ρ as follows:

$$\rho = \frac{(f,g)}{||f||_{\mathrm{L}_2} \cdot ||g||_{\mathrm{L}_2}}, \tag{2.45}$$

where f and g are slownesses of the input, average or output model. To compare the match between the input and output model depending on the wavelength and depth, we use the correlation coefficient $\rho_l(r)$ between functions $f(r,\vartheta,\varphi) = \sum_l \sum_{m=-l}^{l} f_{lm}(r) Y_{lm}(\vartheta,\varphi)$ and $g(r,\vartheta,\varphi) = \sum_l \sum_{m=-l}^{l} g_{lm}(r) Y_{lm}(\vartheta,\varphi)$:

$$\rho_l(r) = \frac{\sum_{m=-l}^{l} f_{lm} g^*_{lm}}{\sqrt{\sum_{m=-l}^{l} f_{lm} f^*_{lm}} \sqrt{\sum_{m=-l}^{l} g_{lm} g^*_{lm}}} \tag{2.46}$$

The correlation coefficient ρ reflects only the pattern fit of two function and not the amplitude. Hence, we use also comparison of root mean square (RMS) of the input, average and output models dependent on radius r

$$\mathrm{RMS}(r) = \left(\int_\Omega f(\boldsymbol{r}) f(\boldsymbol{r}) \sin(\vartheta) \mathrm{d}\vartheta \mathrm{d}\varphi \right)^{1/2}. \tag{2.47}$$

As another characteristic of the inversion resolution, we define the percentage fit r as:

$$r = \left(1 - \frac{||\mathbf{d} - \mathbf{d}^{\mathrm{pred}}||^2}{||\mathbf{d}||^2} \right) \cdot 100\%, \tag{2.48}$$

where $\mathbf{d}^{\mathrm{pred}} = \mathbf{G} \cdot \mathbf{m}^{\mathrm{pred}}$ are data predicted by output model and $\mathbf{d}$ is a synthetic vector of the input delays. The percentage fit describes per cent of the data vector $\mathbf{d}$ which can be explained by the model $\mathbf{m}^{\mathrm{pred}}$. It can be evaluated not only for our synthetic inversion but also in the real data inversion, where the input structure is not known.

Chapter 3

Results

In this chapter, we show hit count (number of rays in a cell), efficiency of the hit equalizing algorithm and the results of the synthetic tomographic inversion for two different Rayleigh numbers ($Ra = 3 \cdot 10^5$ and $Ra = 10^6$) and for both regular and irregular parametrizations.

3.1 Hit count

First let us have a look at the hit count (number of rays per cell) and efficiency of the hit equalizing algorithm. Fig. 3.1 shows resulting hit count at four depths ($200\,\mathrm{km}$ — first row, $600\,\mathrm{km}$ — second row, $1,000\,\mathrm{km}$ — third row and $2,500\,\mathrm{km}$ — fourth row).

In the first column, there is the hit count per the basic (small) cells (equi-angular cells with size $60\,\mathrm{km} \times 1.125^\circ \times 1.125^\circ$) which are used to construct the irregular parametrization. Here we demonstrate the non-uniformity of the rays distribution. In the regions close to sources and receivers, we may find well covered cells. On the other hand, the areas having very low ray coverage can be found especially below the Pacific. The hit count ranges between 0 and $\sim 7,000$, 86.2% cells has hit count between 0 and 100 and only 0.2% cells are covered by more than $1,000$ rays.

The hit count distribution is more uniform after applying hit equalizing algorithm with parameters $L_r = 3,\ L_\theta = 10,\ L_\varphi = 20,\ M_E = 4$ and the condition of $1,000$ rays per cell (see paragraph 2.7.3). Small parametrization cells can be found in the well-covered parts of the mantle. In poorly-covered regions, rather large cells can be found. In the second column of Fig. 3.1, the hit count for irregular cells is plotted. The histogram of hit count in cells is shown in Fig. 3.2**a**. The hit count ranges between 63 and 9992. Hence the cells (16 cells which is 0.04% of the total amount of cells) with coverage lower than $1,000$ rays still exist due to a priori choice of the largest possible cell. Approximately 20% cells have hit count between $1,000$ and $1,100$, 19.9% of cells range between $1,100$ and $1,200$ hit count. Then the relative number of cells descends rapidly with increasing hit count. Only 4% of cells reach hit count higher than $2,000$. Clearly, the hit equalizing algorithm is effective but it is limited by the a priori choice of the parameters. We may expect a relatively well-conditioned matrix $\mathbf{G}^\mathrm{T} \cdot \mathbf{G}$ from equation (2.27) and the inversion of the matrix $\mathbf{G}^\mathrm{T} \cdot \mathbf{G}$ should exist.

Hit count for the regular cells (ESA cells with size $207\,\mathrm{km} \times 4^\circ \times 4^\circ$ cell size on

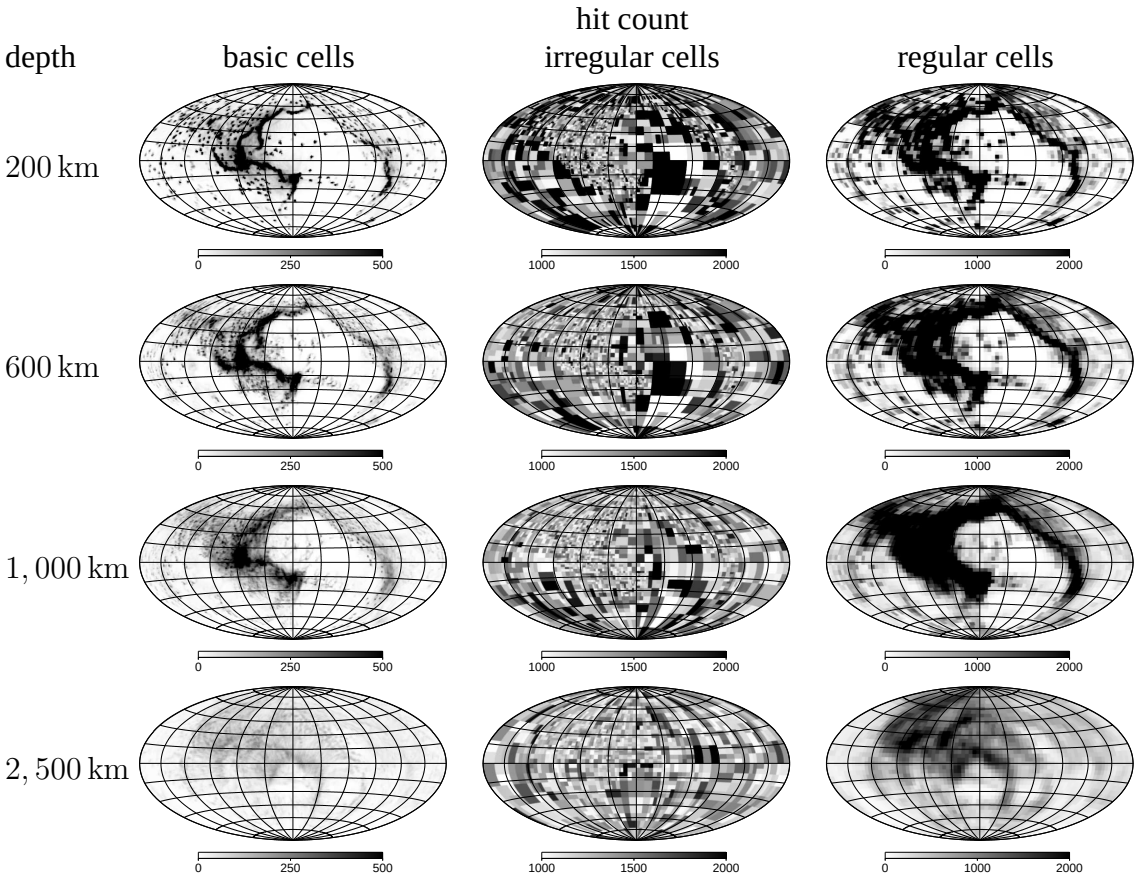

Figure 3.1 Hit count for basic cells (first column), irregular (second column) and regular (equal surface area cells, third column) cell parametrization for depth $200\,\mathrm{km}$ (first row), $600\,\mathrm{km}$ (second row), $1,000\,\mathrm{km}$ (third row) and $2,500\,\mathrm{km}$ (fourth row).

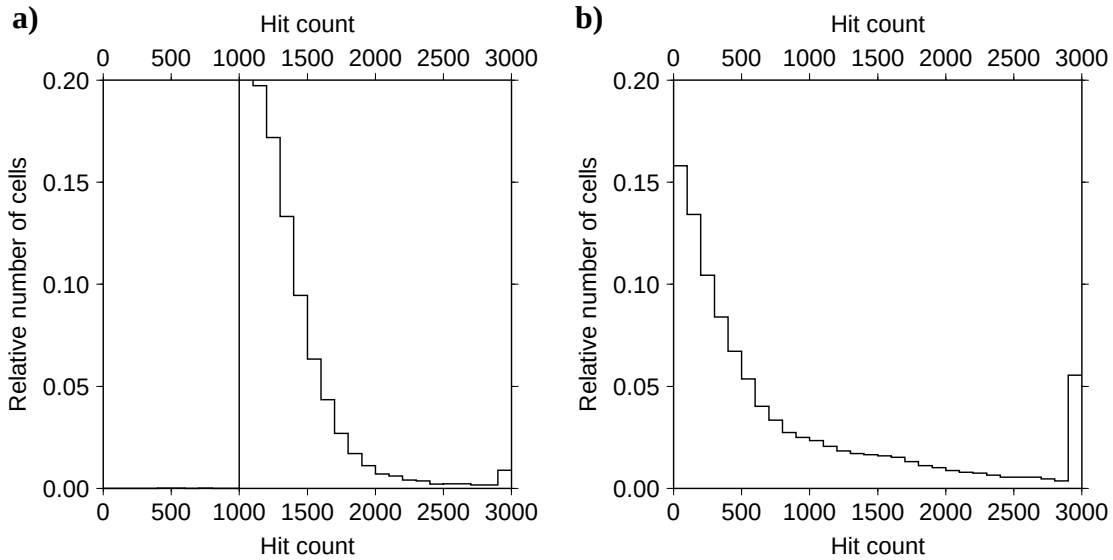

Figure 3.2 Histogram of hit count for **a)** irregular and **b)** regular parametrization.

equator) is plotted in the third column of Fig. 3.1. As expected, the hit count is uneven because the cell distribution does not reflect the uneven ray coverage. The histogram of the hit count is plotted in Fig. 3.2**b**. The hit count ranges between 0 and 32,200 rays, 15% of cells have the hit count between 0 and 100 rays. Then the relative number of cells decreases with increasing hit count. 70% cells have the ray coverage lower than $1,000$ rays. However, the number of cells with coverage higher than $2,000$ rays is also relatively high (11% cells). Therefore we can expect an ill-conditioned problem and the damping would be necessary to obtain the acceptable solution.

3.2 Irregular parametrization

3.2.1 Results for $Ra = 3 \cdot 10^5$

In this paragraph, we discuss the results for irregular parametrization and for the Rayleigh number $Ra = 3 \cdot 10^5$. In Fig. 3.3, the results of tomographic inversion for several values of the damping coefficients are plotted. We show here the horizontal cross-section at the depth $h = 450\,\mathrm{km}$. The cross-section through the input model is in Fig. 3.3**a**, the average model (cf. Eq. 2.37) is in Fig. 3.3**b**. The inversion results for damping coefficients $\lambda = 0$, 100, $1,000$ and 10^4 are shown in Fig. 3.3**c–f**. The wavelengths of the input anomalies (Fig. 3.3**a**) are relatively long in comparison with the size of the parametrization cells even in the poorly-covered regions. Therefore, the average model (Fig. 3.3**b**) shows that the input model can be resolved quite successfully by this parametrization even in the poorly-covered regions. The correlation between the input and the average model is relatively high, $\rho_{\mathrm{input}\times\mathrm{average}} = 0.82$ and the projection error is rather low. Results do not differ signicantly between the model without damping (Fig. 3.3**c**) and models with damping factors 100 (Fig. 3.3**d**) and $1,000$ (Fig. 3.3**e**). These results have small-scale oscillations which are suppressed with increasing damping coefficient. Higher damping ($\lambda = 10^4$, Fig. 3.3**f**) already reduces the amplitude of resulting velocity anomalies considerably.

Another way how to discuss the inversion results is to compare the spectra of the input and output models. Fig. 3.4 shows the spectra of the input model, average model and results for four values of the damping coefficient λ. The decadic logarithm of the power spectra as a function of the spherical harmonic degree and the depth is plotted there for the input model (Fig. 3.4**a**), the average model (Fig. 3.4**b**) and the output models for damping coefficients $\lambda = 0$, 100, $1,000$ and 10^4 (Figs. 3.4**c–f**). The input model (Fig. 3.4**a**) has relatively long-wavelength spectrum. It has two maxima corresponding to the convection boundary layers ($h < 700\,\mathrm{km}$ and $h > 2,100\,\mathrm{km}$). The spectrum of the average model (Fig. 3.4**b**) reflects the input quite well. However, the width of the spectral maxima corresponding to the boundary layers in the vertical direction is wider than in the input model. This leakage is caused by averaging over the large cells in the badly-covered regions. Hence the boundary layers seem to be wider than for the input model. The spectrum of the output model without damping (Fig. 3.4**c**) has slightly higher power on the short-wavelengths than the average model (Fig. 3.4**b**) because of the small-scale oscillations of the result. The power of the oscillations decreases with increasing damping coefficient (Fig. 3.4**d–f**).

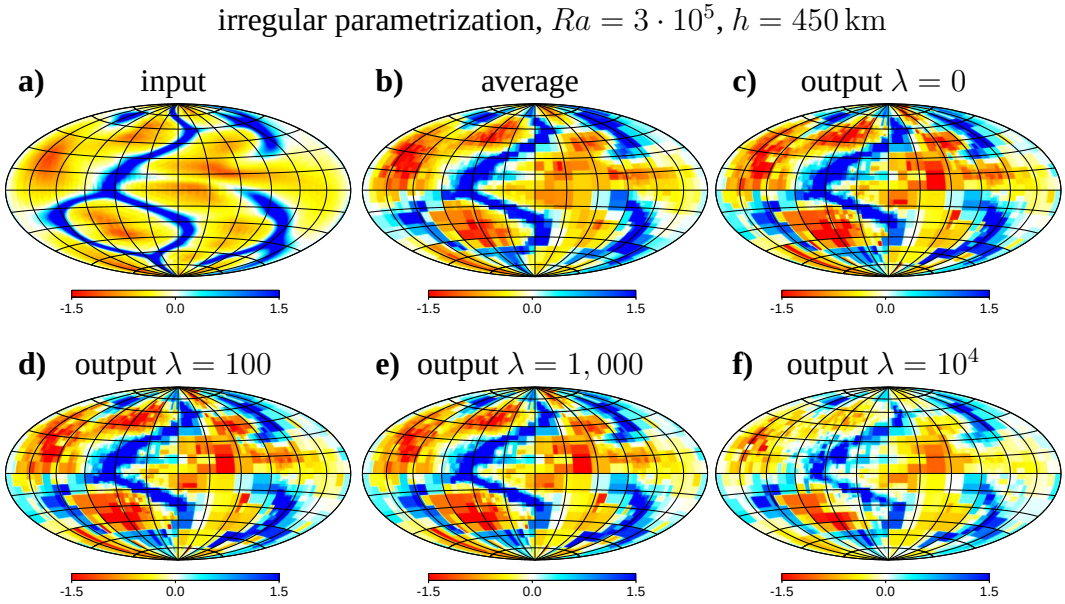

Figure 3.3 Results of the inversion for the irregular parametrization and for Rayleigh number $Ra = 3 \cdot 10^5$. Relative seismic velocity anomalies (in percents of reference velocity) are shown. Figures are plotted at a depth of $450\,\mathrm{km}$, **a)** input model, **b)** average over irregular cell parametrization, **c–f)** results for the damping coefficient $\lambda = 0$, 100, $1,000$ and 10^4.

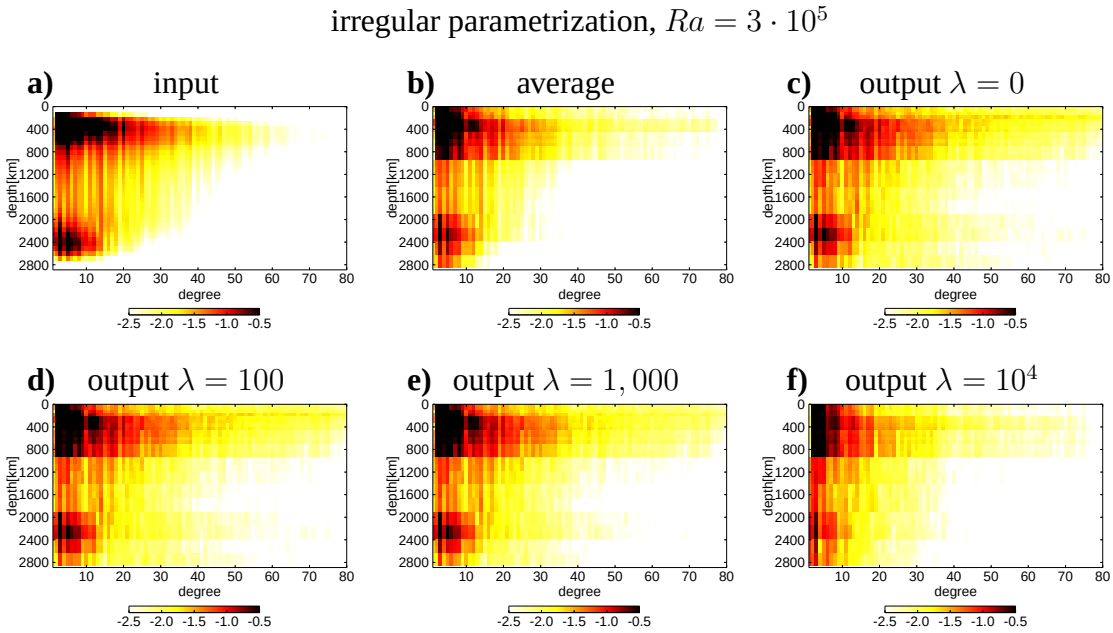

Figure 3.4 Results of the inversion for the irregular parametrization and for Rayleigh number $Ra = 3 \cdot 10^5$. Decadic logarithm of the power spectra (shown as a function of the spherical harmonic degree and the depth, see Eq. 2.44) for **a)** input model, **b)** average over irregular cell parametrization, **c–f)** results for the damping coefficient $\lambda = 0$, 100, $1,000$ and 10^4.

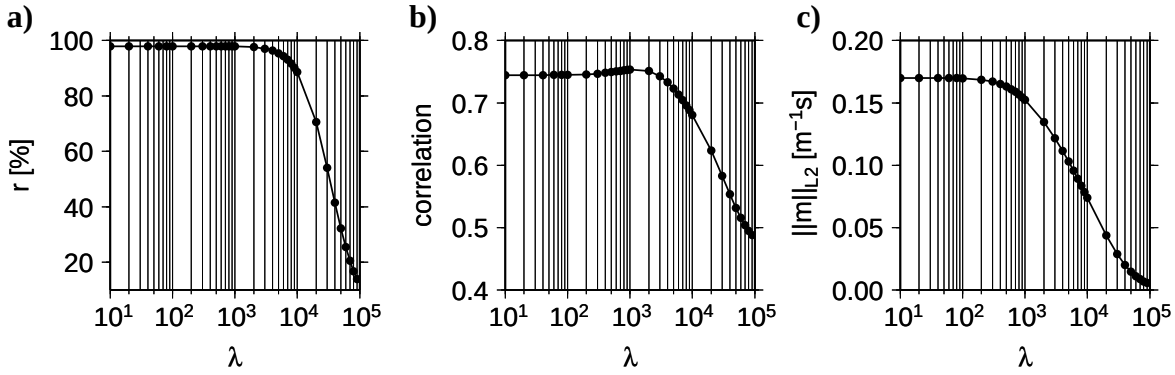

Figure 3.5 Characteristics of results for irregular parametrization and for Rayleigh number $Ra = 3 \cdot 10^5$, **a)** percentage fit r, **b)** correlation ρ and **c)** L_2-norm of the model vector $\mathbf{m}$ as a function of a damping coefficient λ.

In Fig. 3.5, we summarize the characteristics of the results depending on the damping coefficient λ. Fig. 3.5**a** shows the percentage fit r as a function of damping coefficient λ in log-scale. Without damping or with damping $\lambda \lesssim 3,000$ the percentage fit is high ($r \simeq 97.9\%$) and it is almost constant. For higher lambda ($\lambda \gtrsim 3,000$), the minimization of the model norm $\mathbf{m}$, see equation (2.32), dominates over the minimization of the data misfit $\mathbf{d} - \mathbf{G} \cdot \mathbf{m}$ and the percentage fit decreases. The correlation coefficient ρ between the input and output model is shown in Fig. 3.5**b**. Only a weak trend is observed for the damping coefficient λ in the range between $\lambda = 0$ and $\lambda \sim 3,000$. The correlation without damping is $\rho_{\mathrm{input}\times\mathrm{output}(\lambda=0)} = 0.745$. Then the value of the correlation coefficient slightly increases with increasing λ, it reaches its maximum for $\lambda = 1,000$ ($\rho_{\mathrm{input}\times\mathrm{output}(\lambda=1,000)} = 0.753$). Then the correlation coefficient decreases rather steeply. The relation between the L_2-norm of the model vector $\mathbf{m}$ and the damping coefficient is monotonous (Fig. 3.5**c**). For $\lambda \leq 500$, L_2-norm of the model vector is almost constant. Only weak decrease could be observed if we look closely. For higher lambda, the minimization of the norm of the model vector $||\mathbf{m}||_{\mathrm{L}_2}$ (equation (2.32) overweighs the minimization of data misfit norm ($||\mathbf{d} - \mathbf{G} \cdot \mathbf{m}||_{\mathrm{L}_2}$). Therefore, the norm of model vector $||\mathbf{m}||_{\mathrm{L}_2}$ falls.

The damping improves the inversion results only slightly (see weak maximum in Fig. 3.5**b**). Therefore, from now on, we restrict ourselves to the inversion without the damping ($\lambda = 0$). The improvement caused by regularization is hardly visible and we avoid artificial damping procedure.

In Fig. 3.6, there are the details of solution without damping for the depth $200\,\mathrm{km}$ (first column), $600\,\mathrm{km}$ (second column), $1,000\,\mathrm{km}$ (third column) and $2,500\,\mathrm{km}$ (fourth column). In the first row of Fig. 3.6, there are the horizontal cross-sections of the input model. The wavelengths of the anomalies are long due to the low Rayleigh number. The projection of the input model is shown in the second row of Fig. 3.6. The shape of the anomalies is resolved quite successfully. However, the amplitude of anomalies is underestimated in both the upper part (cross-section at $h = 200\,\mathrm{km}$) and the lower part (cross-section at $h = 2,500\,\mathrm{km}$) of the mantle. This effect is caused by averaging over the cells in the parts of the mantle where the amplitude is changing rapidly with the depth. Further, we introduce the projection error — the percentage of the absolute value of the difference between the input and average normalized by 4πRMS at the given depth.

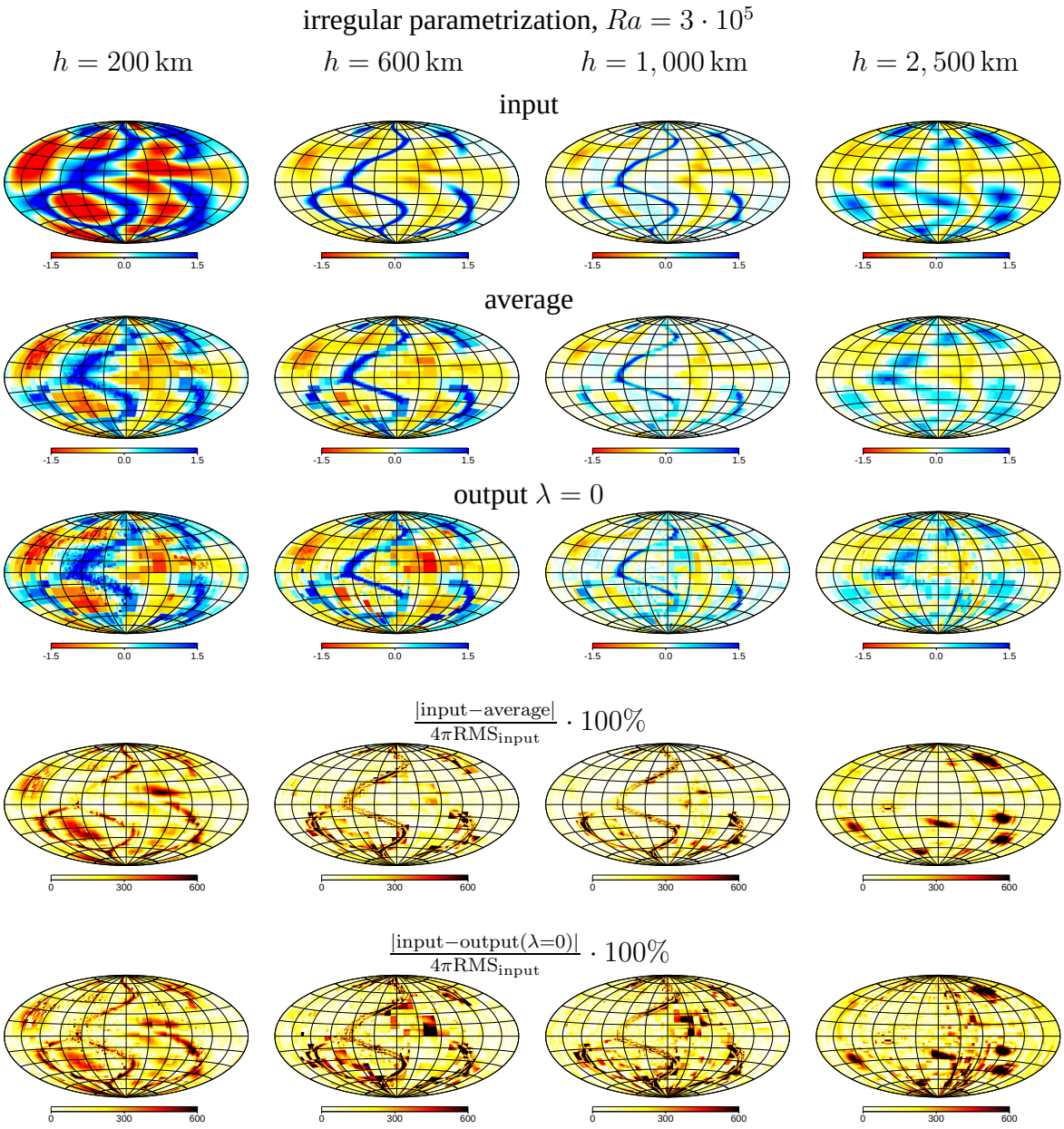

Figure 3.6 Results for the irregular parametrization for Rayleigh number $Ra = 3 \cdot 10^5$. Relative seismic velocity anomalies (in percents of reference velocity) are shown. Horizontal cross-section at the depth of $200\,\mathrm{km}$ (first column), $600\,\mathrm{km}$ (second column), $1,000\,\mathrm{km}$ (third column) and $2,500\,\mathrm{km}$ (fourth column). The first row — cross-section of input model, the second row — average over irregular cells, the third row — results of the inversion for $\lambda = 0$, the fourth row — absolute value of difference between input model and average normalized by 4πRMS of the input model at given depth, the fifth row — the normalized difference between input and output ($\lambda = 0$) model.

This error is shown in the fourth row of Fig. 3.6. This clearly illustrates that the error is relatively large for the depth $h = 200\,\mathrm{km}$ and $h = 2,500\,\mathrm{km}$ due to averaging over the cells. At all depths, the error is mostly concentrated around the major anomalies in the part of the mantle with the large parametrization cells.

For the inversion without damping (the third row of Fig. 3.6), the major features of the output are similar to the average model. The correlation between the result without damping and average model is $\rho_{\mathrm{average}\times\mathrm{output}(\lambda=0)} = 0.91$. However, the small-scale oscillations occur mainly in the regions with the high resolution (small parametrization cells). Further, the anomalies are overestimated in the large cells (cf. red "square" in the center of the output velocity distribution at $600\,\mathrm{km}$ — Fig. 3.6, third row). In the fifth row of Fig. 3.6, the error of the resulting model without damping is plotted there. The error is represented by the percentage of the absolute value of the difference between the input model and result normalized by 4πRMS at the given depth. The amplitude of this error (the fifth row of Fig. 3.6) is higher than for the projection error (the fourth row of Fig. 3.6) due to the oscillations of the output model. Moreover, this error clearly illustrates the over-estimation of the amplitudes in the large cells.

The resolving power of the tomographic inversion is also demonstrated in two vertical cross-sections in Fig. 3.7. We choose the vertical cross-sections through the upwelling in the poorly covered region Fig. 3.7**a–e**. We show here the cross-section location (Fig. 3.7**a**), the hit count (Fig. 3.7**b**), the input model (Fig. 3.7**c**), the average model (Fig. 3.7**d**) and the inversion output without damping (Fig. 3.7**e**). Due to poor ray coverage, this region is discretized by large cells (Fig. 3.7**b**). The input model (Fig. 3.7**c**) cannot be resolved in details by the irregular parametrization (cf. average model Fig. 3.7**d**). Hence the inversion output (Fig. 3.7**e**) is only able to resolve the main features of the upwelling and rather strong oscillations occur.

The other cross-section is chosen through the downwelling in the well covered region Fig. 3.7**f–j**. We show here the cross-section location (Fig. 3.7**f**), the hit count (Fig. 3.7**g**), the input model (Fig. 3.7**h**), the average model (Fig. 3.7**i**) and the result without damping (Fig. 3.7**j**). This region is well covered (see the hit count in Fig. 3.7**g**). Therefore, the input model (Fig. 3.7**h**) is described quite successfully by the average model (Fig. 3.7**i**). Even the weak upwelling in the left part of the cross-section can be resolved. The inversion output without damping (Fig. 3.7**j**) resolves the strong downwelling easily. The weak upwelling is detectable but its shape is disturbed by the oscillations.

The ability of the inversion to reveal the amplitude of the tomographic inversion is demonstrated in Fig. 3.8. Fig. 3.8**a** shows the root mean square of the input model (black line), the average model (green line) and the output model without damping (blue line). Fig. 3.8**b** shows the RMS of the differences between the input and average model (black line), between the input and output model without damping (green line) and between the average and output model (blue line). Both RMS in Fig. 3.8**a** and Fig. 3.8**b** are computed in per cent of the velocity anomalies.

The RMS of the input model (Fig. 3.8**a**, black line) has two maxima corresponding to the boundary layers of the convection. Due to the low Rayleigh number, the boundary layers are relatively wide. The RMS of the average model (Fig. 3.8**a**, green line) is underestimated in most parts of the mantle as could be expected. On the other hand, the RMS of the average model is overestimated at the upper and lower edges of the bound-

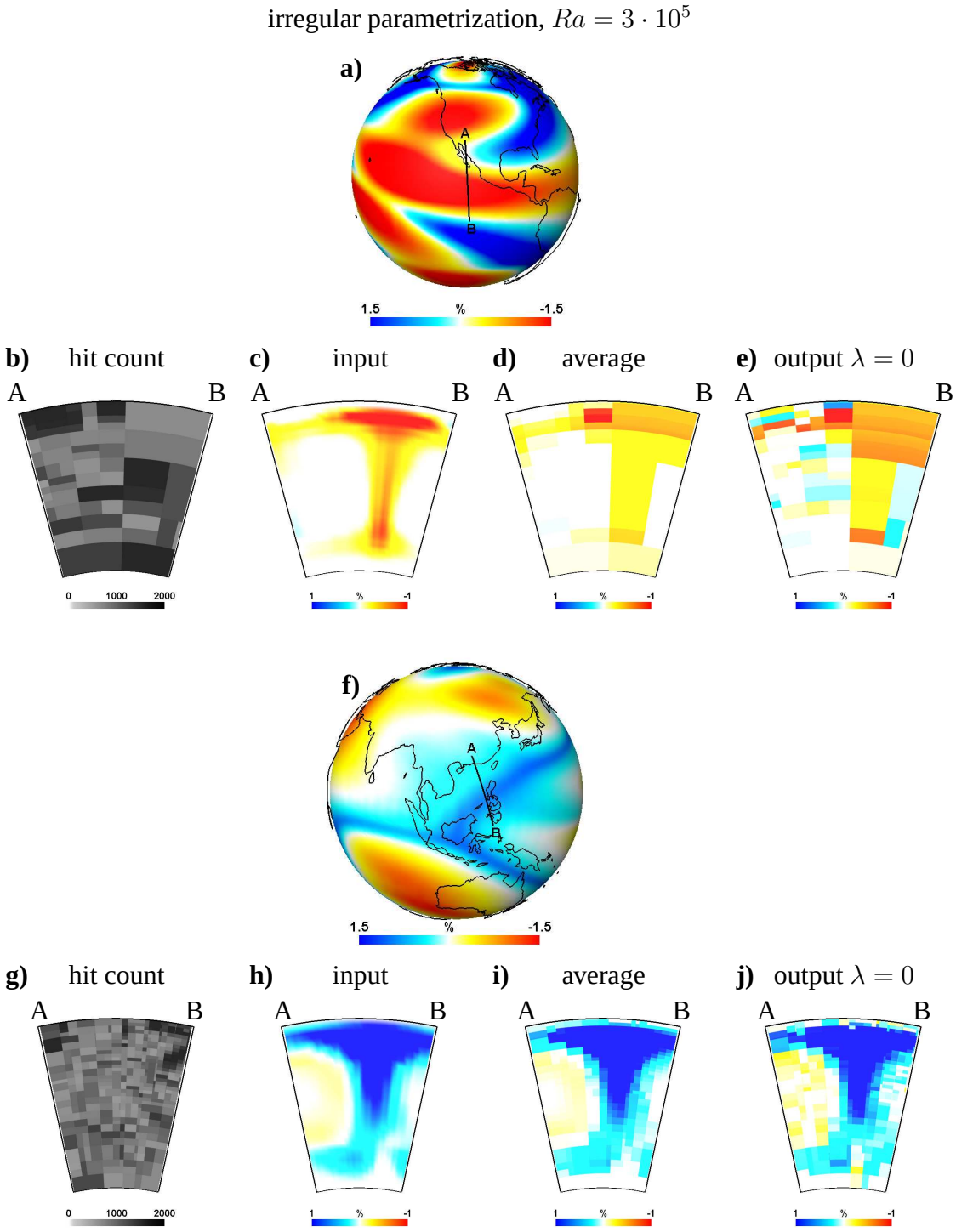

Figure 3.7 Two vertical cross-sections in the model with $Ra = 3 \cdot 10^5$ and irregular parametrization. Vertical cross-section (**a–e**) through upwelling, **a)** location of the cross-section, **b)** hit count, **c)** input, **d)** average, **e)** result of the inversion for $\lambda = 0$. Vertical cross-section (**f–j**) through downwelling, **f)** location of the cross-section, **g)** hit count, **h)** input, **i)** average, **j)** result of the inversion for $\lambda = 0$. Relative seismic velocity anomalies (in percents of reference velocity) are shown.

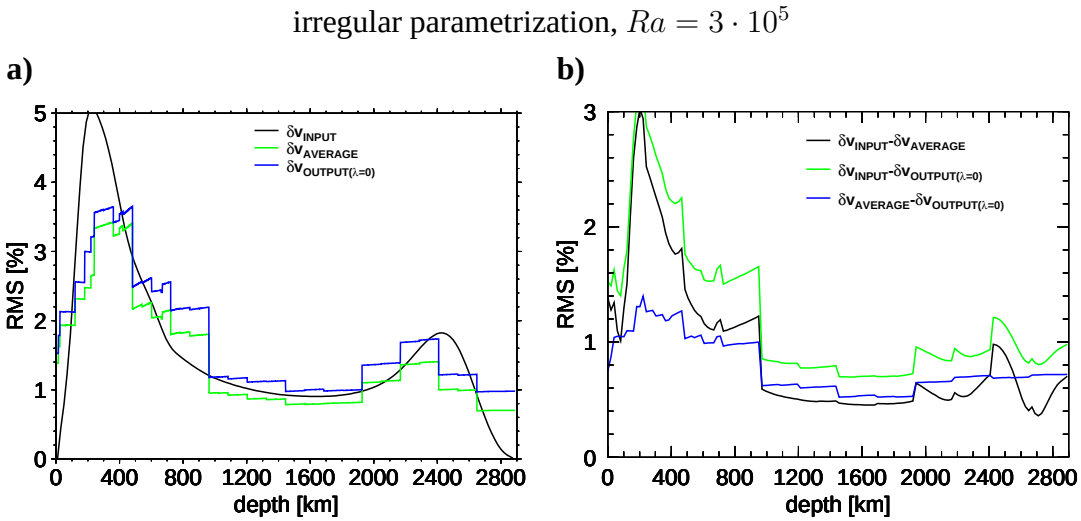

Figure 3.8 Root mean square (RMS) for irregular parametrization and for **a)** the input model ($Ra = 3 \cdot 10^5$), average and inversion result ($\lambda = 0$) and **b)** their differences.

ary layers (depth range between 0 and $120\,\mathrm{km}$, between 720 and $960\,\mathrm{km}$, between $1,920$ and $2,160\,\mathrm{km}$ and for depths greater than $2,640\,\mathrm{km}$). This smearing of the amplitudes is caused by averaging of the input model over the large cells. The RMS of the difference between the input and the average model (Fig. 3.8**b**, black line) can be interpreted as RMS of the projection error. The error has rather large amplitudes and also sharp jumps at the depths corresponding to the boundaries of the large cells.

The RMS output model (Fig. 3.8**a**, blue line) has similar characteristics as RMS of the average model (cf. Fig. 3.8**a**, green line). The RMS of the difference between the input and output models (Fig. 3.8**b**, green line) can be interpreted as the RMS of the error of the inversion. It has similar shape as the difference between the input and average models (Fig. 3.8**a**, green line), however, it has higher amplitudes. The RMS of the difference between the average and output models is plotted in Fig. 3.8**b** (blue line). This curve is more-or-less constant except for the depths up to $1,000\,\mathrm{km}$, where higher amplitudes are observed.

3.2.2 Results for $Ra = 10^6$

In Fig. 3.9, the result for $Ra = 10^6$ and four damping coefficients λ are shown. The wavelengths of the input anomalies (Fig. 3.9**a**) are shorter in comparison with the anomalies based on $Ra = 3 \cdot 10^5$. Hence, the average model fits the input model (Fig. 3.9**b**) only with difficulties in most of the mantle. The input anomalies are resolvable only in the well-covered regions. Elsewhere, the anomalies are smeared. The correlation between the input and average model is $\rho_{\mathrm{input}\times\mathrm{average}} = 0.60$. The results of the inverse problem are again rather insensitive on damping coefficient up to $\lambda = 1,000$ (Fig. 3.9**c–e**). For the damping coefficient 10^4, the amplitudes are already significantly underestimated (Fig. 3.9**f**).

The spectrum of the input model (Fig. 3.10**a**) shows the maxima of the power corresponding to the boundary layers. Compared to the case with $Ra = 3 \cdot 10^5$, the spectrum decays slower (it has higher power on higher degrees) and the boundary layers are nar-

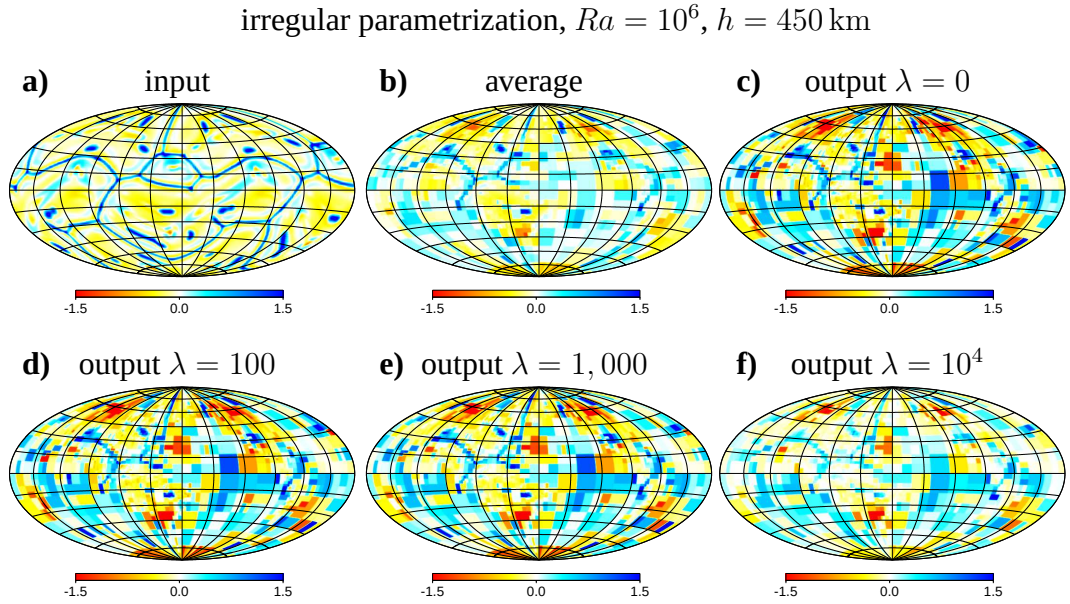

Figure 3.9 Results of the inversion for the irregular parametrization and for Rayleigh number $Ra = 10^6$. Relative seismic velocity anomalies (in percents of reference velocity) are shown. Figures are plotted at a depth of $450\,\mathrm{km}$, **a)** input model, **b)** average over irregular cell parametrization, **c–f)** results for the damping coefficient $\lambda = 0$, 100, $1,000$ and 10^4.

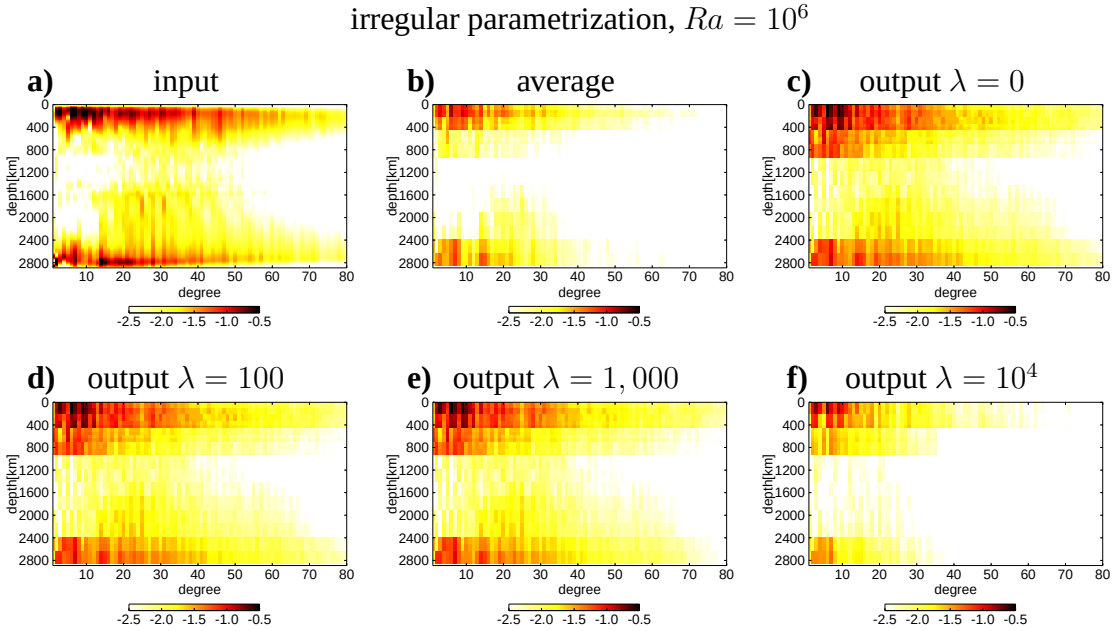

Figure 3.10 Results of the inversion for the irregular parametrization and for Rayleigh number $Ra = 10^6$. Decadic logarithm of the power spectra (shown as a function of the spherical harmonic degree and the depth, see Eq. 2.44) for **a)** input model, **b)** average over irregular cell parametrization, **c–f)** results for the damping coefficient $\lambda = 0$, 100, $1,000$ and 10^4.

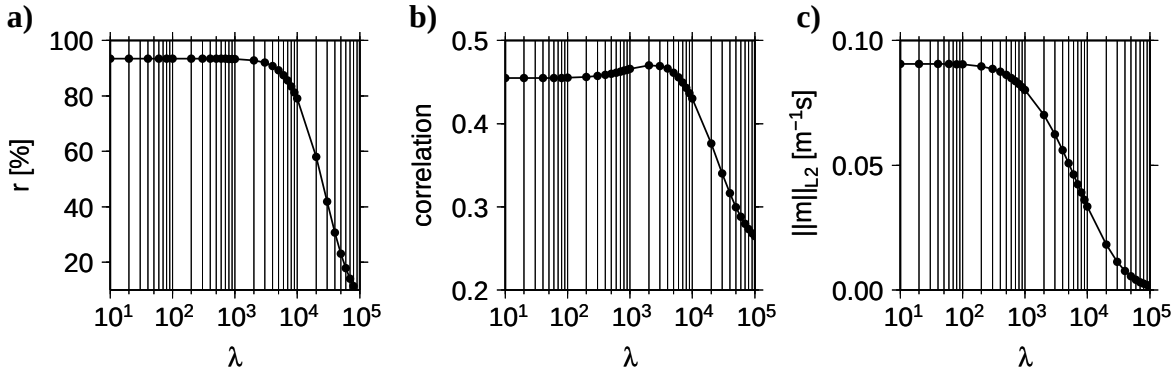

Figure 3.11 Characteristics of results for irregular parametrization and for Rayleigh number $Ra = 10^6$, **a)** percentage fit r, **b)** correlation ρ and **c)** L_2-norm of the model vector $\mathbf{m}$ as a function of a damping coefficient λ.

rower (c.f. Fig. 3.4**a**). The spectrum of the average model (Fig. 3.10**b**) has faster decay in comparison with the input model (Fig. 3.10**a**). The maxima of power observed at the boundary layers are smeared due to the averaging over the large cells even stronger than for the average model with $Ra = 3 \cdot 10^5$ (cf. Fig. 3.4**b**). The spectra of the output models with no damping or with low damping (Fig. 3.10**c–e**) have higher power on the high degree than the average model due to the oscillations. The behavior of the power spectra of the output model for $\lambda \leq 1,000$ (Fig. 3.10**c-e**) is similar to the output models for the low Rayleigh number $Ra = 3 \cdot 10^5$ (cf. Fig. 3.4**c-e**) — the spectra do not change essentially for different damping coefficients. For higher damping coefficient (Fig. 3.10**f**), the power is significantly lower on high degrees.

In Fig. 3.11, we show the characteristics of the results as a function of the damping coefficient λ. The shapes of these characteristics are similar to the inversion results for the Rayleigh number $Ra = 3 \cdot 10^5$ (c.f. Fig. 3.5). Fig. 3.11**a** shows the percentage fit r of the results as a function of a damping coefficient λ. For the damping coefficient lower than $\lambda = 3,000$, the percentage fit is high $r \sim 93.4\%$. This value is lower than the value of the percentage fit for the Rayleigh number $Ra = 3 \cdot 10^5$ ($r \sim 98\%$). As expected, the results for the long-wavelength model ($Ra = 3 \cdot 10^5$) are explained better than for the model with short-wavelength ($Ra = 10^6$) if the same parametrization is used. The correlation coefficient ρ (Fig. 3.11**b**) does not change dramatically for the damping factor lower than $3,000$. The correlation without damping is equal to $\rho_{\mathrm{input}\times\mathrm{output}(\lambda=0)} = 0.45$. Then the correlation slightly increases and reaches its maximum for the damping coefficient $\lambda = 2,000$ ($\rho_{\mathrm{input}\times\mathrm{output}(\lambda=2,000)} = 0.47$). For the damping coefficient higher than $2,000$, the value of correlation coefficient decreases. These values of the correlation coefficient are considerably lower than for the model with $Ra = 3 \cdot 10^5$. The relation between the L_2-norm of the model vector $\mathbf{m}$ and the damping coefficient is plotted in Fig. 3.11**c**. Only low decrease is observed for $\lambda \lesssim 500$. For higher λ, the norm of the model vector fall steeply again (cf. Fig. 3.5**c**).

In the figure Fig. 3.12, we demonstrate the results for $Ra = 10^6$ without damping on four horizontal cross-sections taken at the depths $h = 200\,\mathrm{km},\ 650\,\mathrm{km},\ 1,000\,\mathrm{km}$ and $2,500\,\mathrm{km}$. In the first row of Fig. 3.12, there are the cross-sections of the input model. The wavelengths of the anomalies are rather short due to the relatively high Rayleigh number. The downwelling anomalies in the top part of the mantle and upwelling anomalies at the

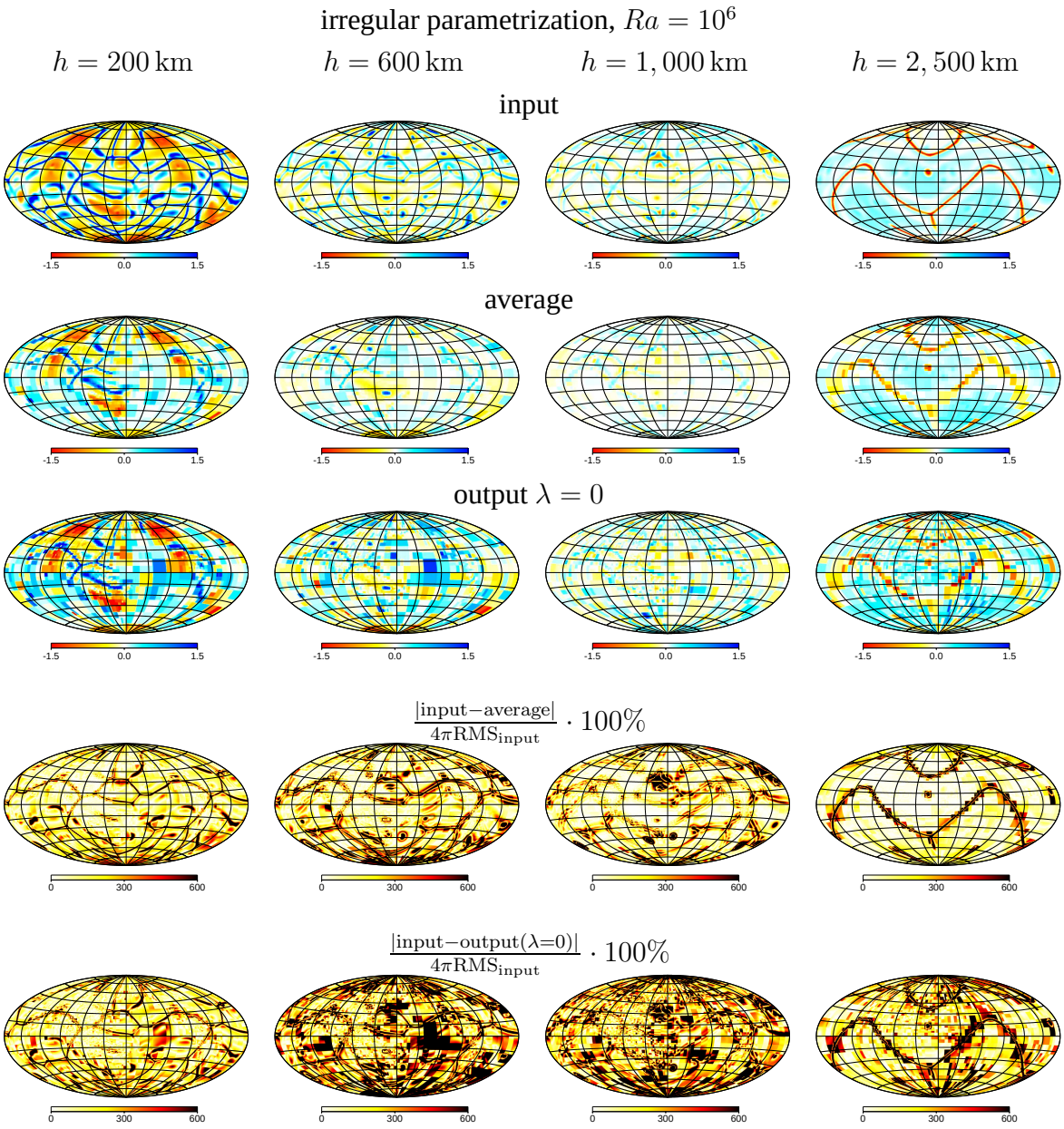

Figure 3.12 Results for the irregular parametrization for Rayleigh number $Ra = 10^6$. Relative seismic velocity anomalies (in percents of reference velocity) are shown. Horizontal cross-section at the depth of $200\,\mathrm{km}$ (first column), $600\,\mathrm{km}$ (second column), $1,000\,\mathrm{km}$ (third column) and $2,500\,\mathrm{km}$ (fourth column). The first row — cross-section of input model, the second row — average over irregular cells, the third row — results of the inversion for $\lambda = 0$, the fourth row — absolute value of difference between input model and average normalized by 4πRMS of the input model at given depth, the fifth row — the normalized difference between input and output ($\lambda = 0$) model.

bottom part of the mantle are of linear character. The average of the input model is plotted in the second row of Fig. 3.12. In the upper mantle, the linear-shaped anomalies can be fitted by the parametrization cells only in the well-covered regions. On the other hand, the resolution in the well-covered parts is relatively high. In the lowermost parts of the mantle ($h = 2,500\,\mathrm{km}$), the linear features are relatively well detected. At this depth, the distribution of rays is more even than in the upper mantle. However, the maximum resolution is lower than in the upper part of the mantle. The error of the average model is plotted in the fourth row of Fig. 3.12. At the depth $h = 200\,\mathrm{km}$, the normalized projection error is rather high near the anomalies with large amplitudes in badly covered regions, whereas the lowest amplitudes of the error are observed in well resolved (well-covered) region. At the depths $h = 650\,\mathrm{km}$ and $h = 1,000\,\mathrm{km}$, the amplitudes of the error seem to be rather large. This effect is caused by the normalizing of the error by the low amplitude of input anomalies at a given depth. For the depth $h = 2,500\,\mathrm{km}$, the maximum error is found in the vicinity of the major features.

The output of the tomographic inversion without damping for all depths is similar to the average model. The correlation between output and average models is $\rho_{\mathrm{average}\times\mathrm{output}(\lambda=0)} = 0.76$. However, the oscillations appear in the whole mantle. These oscillations influence the output pattern negatively even in the well-covered regions mainly at the depths where the input anomalies have low amplitudes. The error of the inverse problem without damping is in the fifth row of Fig. 3.12. In the well-covered regions, the characteristic features of this error are similar to the normalized projection error (cf. Fig. 3.12, the fourth row). However, the amplitudes of the error are larger than for the normalized parametrization error. This effect is caused by oscillations and it dominates mainly in the mid-mantle (cross-sections at the depth $650\,\mathrm{km}$ and $1,000\,\mathrm{km}$).

Two vertical cross-sections illustrating the resolution of the inversion are plotted in Fig. 3.13, one through an upwelling and one through downwelling. The position of the cross-section is in the same place (for an upwelling) or at least close to the region (for a downwelling) where we selected the cross-sections for the Rayleigh number $Ra = 3 \cdot 10^5$ (cf. Fig. 3.7).

The first vertical cross-section is taken through the upwelling in the poorly-covered region Fig. 3.13**a–e**. The hit count (Fig. 3.13**b**) shows that this region is parametrized by large parametrization cells. Hence, the input upwelling (see Fig. 3.13**c**) cannot be resolved (Fig. 3.13**e**). The second vertical cross-section is taken through the downwelling structure in the relatively well-covered region Fig. 3.13**f–j**. The hit count (Fig. 3.13**g**) demonstrates fine resolution in the area of the cross-section. The input model (Fig. 3.13**h**) shows the narrow vertical anomaly with the high amplitudes near the surface and core-mantle boundary and with significantly lower amplitudes in the mid-mantle. The figure of the average model (Fig. 3.13**i**) illustrates that the chosen parametrization is able to describe this particular upwelling as a continuous narrow feature. Nevertheless, the output of the inversion without damping (Fig. 3.13**j**) shows a structure damaged by the oscillation in the mid-mantle.

The amplitudes fit of the inversion problem is illustrated in Fig. 3.14. The RMS of the input model (Fig. 3.14**a**, black line) has two maxima corresponding to the boundary layers. The boundary layers are more narrow than for the model with Rayleigh number $Ra = 3 \cdot 10^5$ (c.f. Fig. 3.8**a**, black line). The RMS of the average model (Fig. 3.14**a**, green

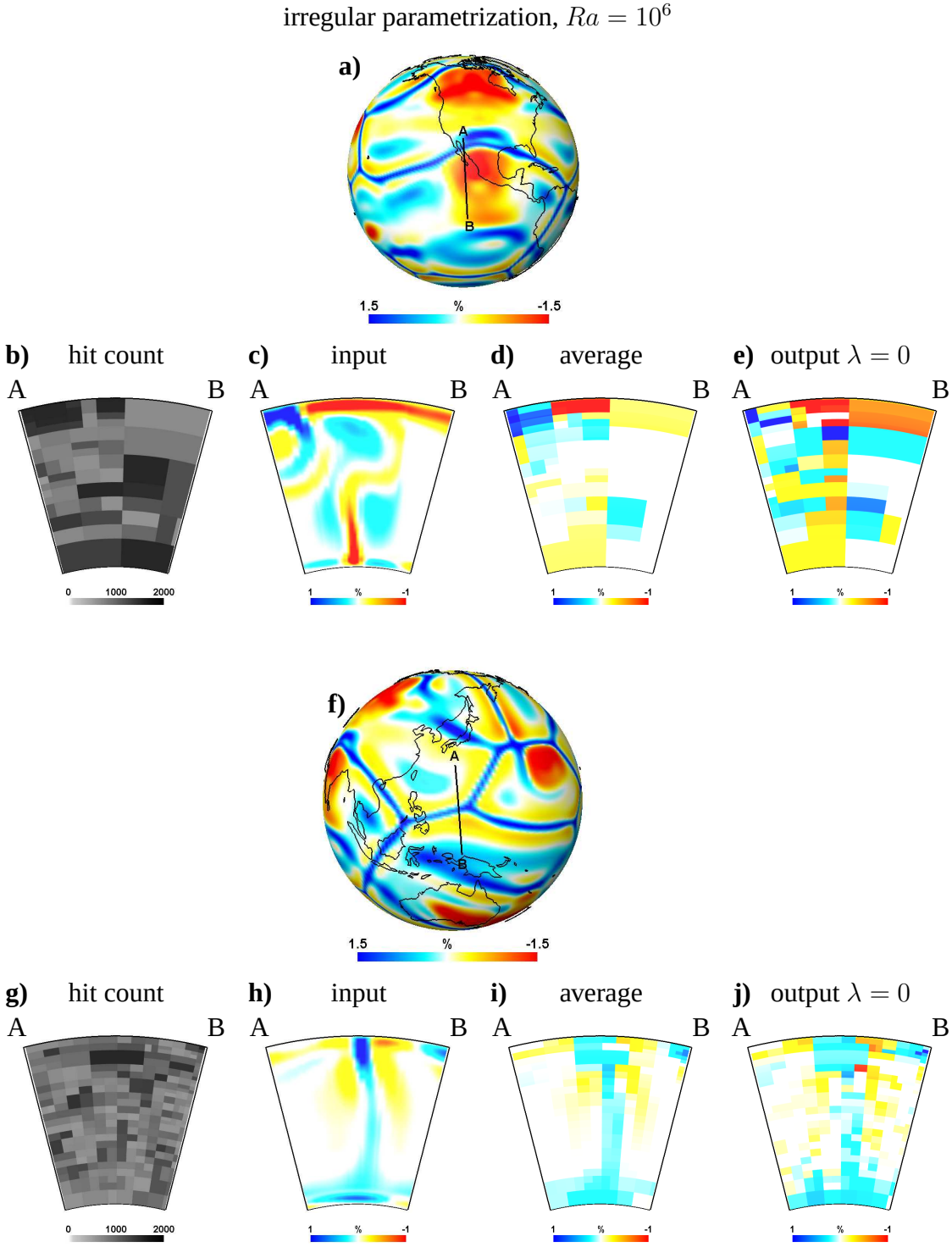

Figure 3.13 Two vertical cross-sections in the model with $Ra = 10^6$ and irregular parametrization. Vertical cross-section (**a–e**) through upwelling, **a)** location of the cross-section, **b)** hit count, **c)** input, **d)** average, **e)** result of the inversion for $\lambda = 0$. Vertical cross-section (**f–j**) through downwelling, **f)** location of the cross-section, **g)** hit count, **h)** input, **i)** average, **j)** result of the inversion for $\lambda = 0$. Relative seismic velocity anomalies (in percents of reference velocity) are shown.

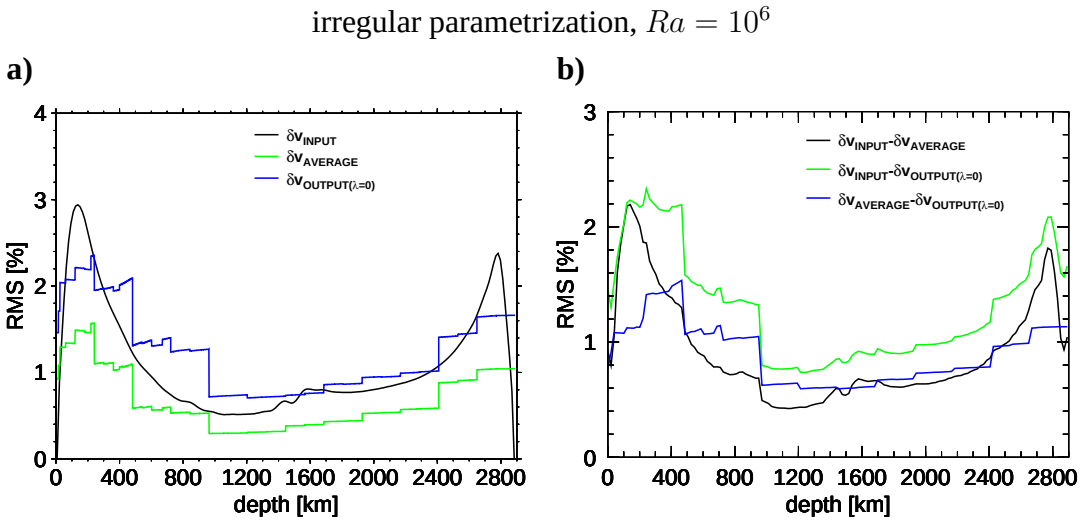

Figure 3.14 Root mean square (RMS) for irregular parametrization and for **a)** the input model ($Ra = 10^6$), average and inversion result ($\lambda = 0$) and **b)** their differences.

line) has also two maxima, however, the amplitudes are underestimated for all depths. Due to averaging over the cells, the sharp changes of the RMS are observed. Therefore, the width of the boundary layers seem to be close to the width of the boundary layer of the output model for low Rayleigh number. (cf. Fig. 3.8**a**, green line). The RMS of the output model without damping (Fig. 3.14**a**, blue line) has similar character as the RMS of the average model (Fig. 3.14**a**, green line), nevertheless, the value of RMS is higher than the RMS of the average model. The RMS of the output model (Fig. 3.14**a**, blue line) is comparable to the RMS of the input model (Fig. 3.14**a**, black line) except for the boundary layers. At depth $h < 300\,\mathrm{km}$ and $h > 2,600\,\mathrm{km}$, the output anomalies are underestimated. Further, at the depth range between $400\,\mathrm{km}$ and $960\,\mathrm{km}$, the RMS is higher than the RMS of the input model. Hence, the boundary layer seems to be wider than the boundary layer of the input model. The RMS of the differences between the input, average and output models are in Fig. 3.14**b**. The characteristics of the RMS of these differences has similar character as the RMS of differences for the low Rayleigh number (cf. Fig. 3.8**b**).

3.3 Regular parametrization

In this section, we discuss the results of the inverse problem using the regular parametrization which does not reflect the uneven distribution of the sources and receivers in the model. We represent the regular parametrization by equal surface area cells (ESA). The construction of these cells is described in the paragraph 2.7.3. The regularization is essential for this parametrization as we mentioned before and appropriate value of the damping coefficient λ has to be found.

3.3.1 Results for $Ra = 3 \cdot 10^5$

Fig. 3.15 shows the inversion results for four damping coefficients λ. Fig. 3.15**a** shows the horizontal cross-section of the input model at the depth of $450\,\mathrm{km}$. The anomalies

are long-wavelengths and their size is larger than the size of the parametrization cells. Therefore, the average model (Fig. 3.15**b**) can explain the input model successfully — the correlation between the input and the average models is high ($\rho_{\mathrm{input}\times\mathrm{average}} = 0.92$). The results of the inversion for damping coefficient $\lambda = 0$, 100, $1,000$ and 10^4 are plotted in Figs. 3.15**c–f**. Black color marks the cells with no information, i.e. no ray passing through the cell. We set the seismic slowness anomaly equal to zero in these cells when we calculate the correlation, root mean square and power spectra. The inversion output without damping (Fig. 3.15**c**) indicates that the regularization will be necessary to obtain reasonable solution. The output model oscillates strongly in the badly covered regions. The iterative solution (using LSQR, paragraph 2.7.3) of this model converges very slowly and the stopping-criterion of the maximum number of iterations (we set $20,000$ iterations) is reached. For the output model with damping coefficient $\lambda = 100$ (Fig. 3.15**d**) the oscillation are still observed. However, the solution converges more rapidly than for the inversion without damping. For comparison, it is necessary to compute $2,300$ iterations for the same convergence criterion as for the solution without damping. The damping factor $\lambda = 1,000$ (Fig. 3.15**e**) seems to be optimal, the oscillations almost disappear. If we increase the value of the damping coefficient even more ($\lambda = 10^4$, Fig. 3.15**f**), the minimization of the model vector $\mathbf{m}$ overweighs the minimization of vector $\mathbf{d} - \mathbf{G} \cdot \mathbf{m}$ and the amplitudes of the anomalies are suppressed.

Fig. 3.16 shows the spectra of the inversion results. The spectrum of the input model is shown in Fig. 3.16**a**. The spectrum of the average model (Fig. 3.16**b**) has faster decay compared to the spectrum of the input model. However, generally their character is quite similar. The spectrum of the output model without damping (Fig. 3.16**c**) is flat and it has high power on high degrees above $\sim 1,000\,\mathrm{km}$ due to the oscillations. Under the $\sim 1,000\,\mathrm{km}$ the spectrum is rather similar to the average one though it decays significantly slower. Clearly the inversion is more successful there — most probably due to the relatively uniform ray coverage in the lower mantle (cf. Fig. 3.1, third column, depth $h = 2,500\,\mathrm{km}$). With increasing the damping coefficient ($\lambda = 100$ and $1,000$, Fig. 3.16**d–e**) the strong oscillations are more and more suppressed. From the spectral point of view, the optimal value of the damping coefficient is $\sim 1,000$ — the strong oscillations disappear and only low small-scale oscillations (yellow color for the high degree) occur. For higher increase of the damping coefficient ($\lambda = 10^4$), not only high degree oscillations are suppressed — even a part of the "real" structure is filtered out and the spectrum is significantly shorter than the average one.

The characteristics of the inversion output as a function of the damping coefficient λ are summarized in Fig. 3.17. The explained data r depending on the damping coefficient λ in the log-scale are displayed in Fig. 3.17**a**. The shape of the curve is similar to the shape of the curve for the irregular parametrization (cf. Fig. 3.5**a**). The value of the explained data r is more-or-less constant ($r = 96.8\%$) up to $\lambda \lesssim 3,000$. For $\lambda > 3,000$, the value of explained data r decreases. The character of the correlation and the norm of the model vector differs between the irregular (Fig. 3.5**b** and Fig. 3.5**c**) and regular (Fig. 3.17**b** and Fig. 3.17**c**) parametrizations. The correlation coefficient as a function of the damping coefficient in the log-scale is shown in Fig. 3.17**b**. The correlation between input and output model is very low if no damping is applied ($\rho_{\mathrm{input}\times\mathrm{output}(\lambda=0)} = 0.11$). Then the correlation coefficient steeply increases with the increasing damping factor λ

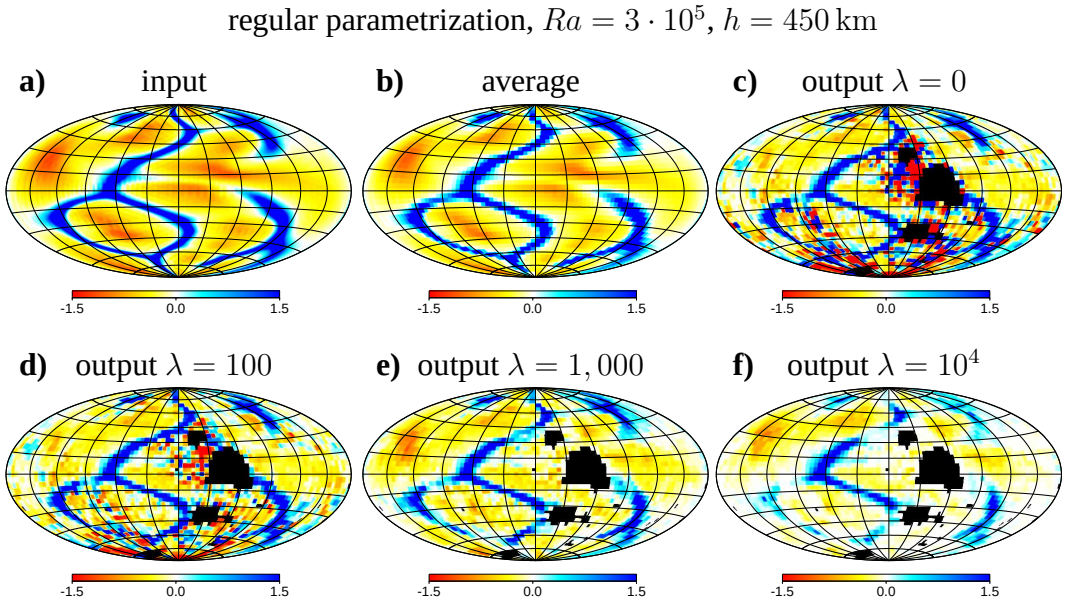

Figure 3.15 Results of the inversion for the regular parametrization and for Rayleigh number $Ra = 3 \cdot 10^5$. Relative seismic velocity anomalies (in percents of reference velocity) are shown. Figures are plotted at a depth of $450\,\mathrm{km}$, **a)** input model, **b)** average through regular cell parametrization, **c–f)** results for the damping coefficient $\lambda = 0$, 100, $1,000$ and 10^4, black color means no information (no rays) in the cell.

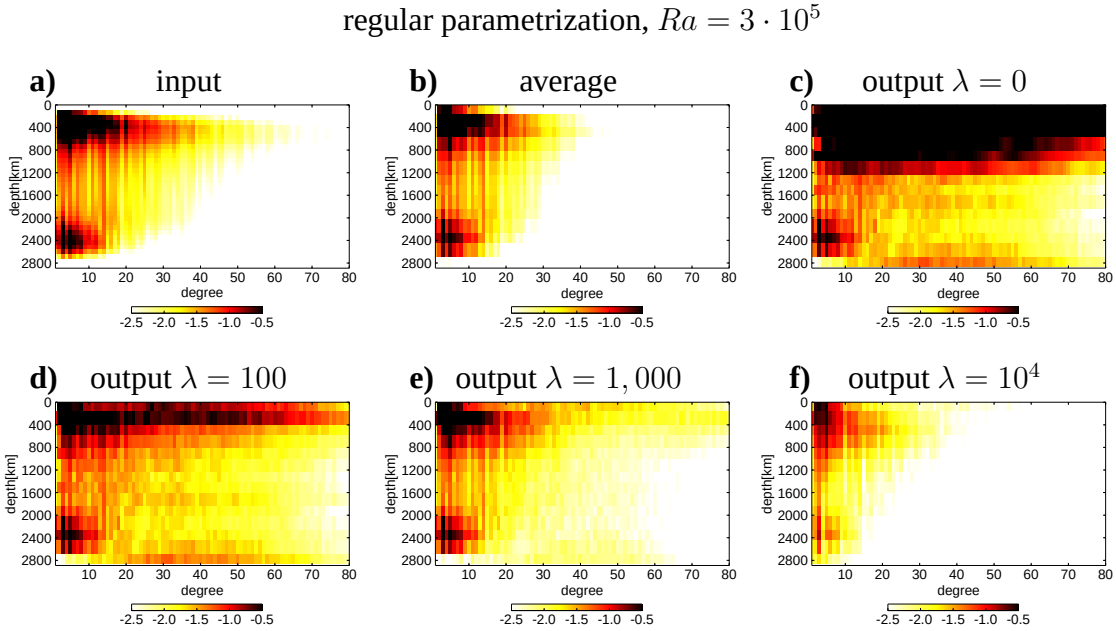

Figure 3.16 Results of the inversion for the regular parametrization and for Rayleigh number $Ra = 3 \cdot 10^5$. Decadic logarithm of the power spectra (shown as a function of the spherical harmonic degree and the depth, see Eq. 2.44) for **a)** input model, **b)** average through regular cell parametrization, **c–f)** results for the damping coefficient $\lambda = 0$, 100, $1,000$ and 10^4.

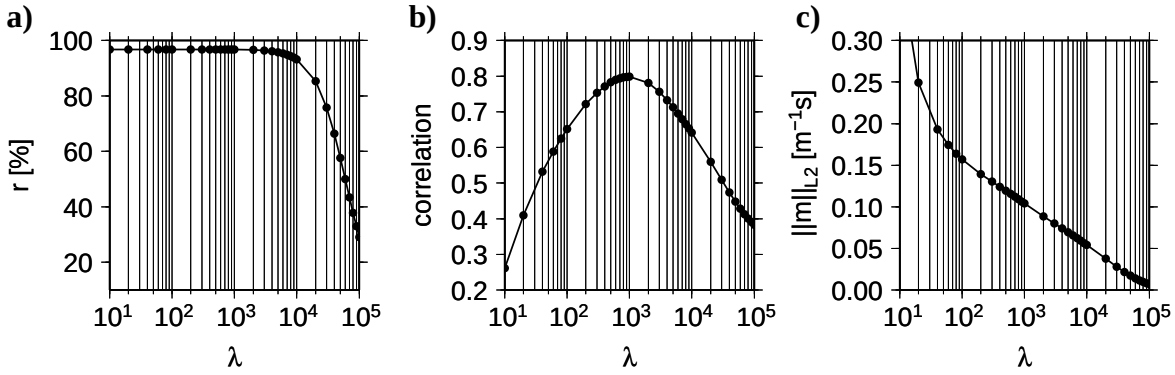

Figure 3.17 Characteristics of results for regular parametrization and for Rayleigh number $Ra = 3 \cdot 10^5$, **a)** percentage fit r, **b)** correlation ρ and **c)** L_2-norm of the model vector $\mathbf{m}$ as a function of a damping coefficient λ.

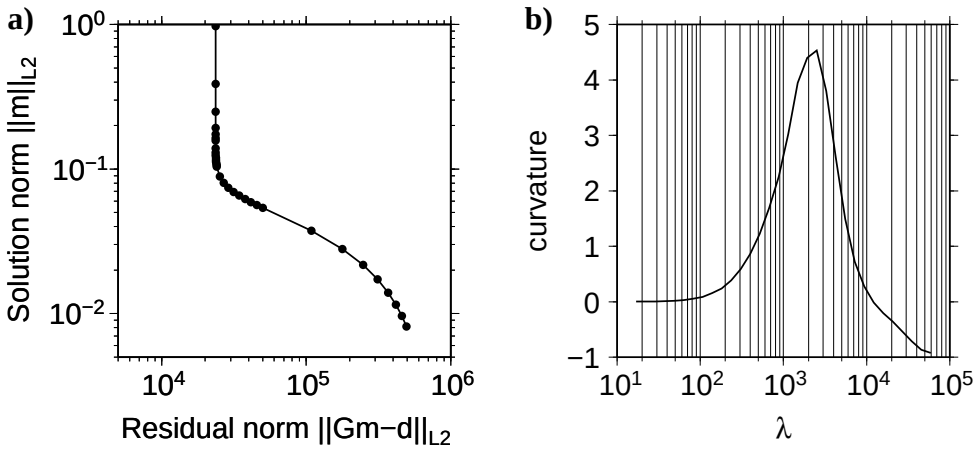

Figure 3.18 Characteristics of results for regular parametrization and for Rayleigh number $Ra = 3 \cdot 10^5$, **a)** L-curve, **b)** curvature of the L-curve.

as the oscillations are being filtered out. The correlation reaches maximum for $\lambda = 1,000$ $\rho_{\text{input}\times\text{output}(\lambda=1,000)} = 0.80$. If we increase the damping factor even more, the correlation coefficient decreases again. The norm of the model vector $\mathbf{m}$ depending on the damping factor in the log-scale is in Fig. 3.17**c**. The curve is monotonous, it decreases with increasing damping coefficient in the whole studied range of λ.

In the case of the regular parametrization the results of the inversion are strongly affected by the adopted damping, therefore the choice of proper damping is an important issue. To determine the most suitable value of damping, we use the L-curve analysis (section 2.6). We plot the L-curve in Fig. 3.18**a**. We compute the inversion for 34 different values of the damping coefficient (Fig. 3.18**a**, dots). Then we interpolate these points by the natural cubic splines (Press et al. 1992) (Fig. 3.18**a**, solid line). We determine the corner damping factor λ_{corner} from the position of the maximum curvature of the interpolated curve, see equation (2.33). The curvature as a function of the damping coefficient in the log-scale is plotted in Fig. 3.18**b**. It reaches maximum for the damping coefficient between $2,000$ and $3,000$. This value corresponds quite well to the maximum correlation between the input and output models reached in synthetic inversion (which cannot be computed in the real inversion). For the corner value determined by L-curve analysis,

the correlation is still very high ($\rho_{\mathrm{input}\times\mathrm{output}(2{,}000)} = 0.78$ and $\rho_{\mathrm{input}\times\mathrm{output}(3{,}000)} = 0.76$) though it is not the absolute maximum of the correlation coefficient (which was obtained for $\lambda = 1,000$).

From now on, we restrict ourselves to the inversion output with value of the damping coefficient $\lambda = 2,000$ which was determined by L-curve criterion. Several horizontal cross-sections for the results with the damping coefficient $\lambda = 2,000$ are displayed in Fig. 3.19. The projection (cf. average model in Fig. 3.19, second row) of the input model (Fig. 3.19, first row) on the regular basis is quite successful (it fits the input quite well). The amplitude of the projection error (Fig. 3.19, fourth row) is highest at the depth of $200\,\mathrm{km}$. The amplitude of input velocity anomalies grows rapidly in the vertical direction at this depth. The size of parametrization cells in the vertical direction is not able to describe such steep changes. Therefore, the input model is vertically smeared. At the depths $h = 600\,\mathrm{km}$ and $h = 1,000\,\mathrm{km}$, the highest error is located in the vicinity of the high-amplitude anomalies. Above the core-mantle boundary ($h = 2,500\,\mathrm{km}$), the anomalies are stronger in long-wavelengths, so the projection error is very low there.

The input model is predicted successfully by the output model with $\lambda = 2,000$ (Fig. 3.19, third row). However, the weak oscillations are observed for all depths. The cells with no information ("unpredictable cells") can be found at the depths $200\,\mathrm{km}$, $600\,\mathrm{km}$ and $1,000\,\mathrm{km}$. At the shallow depth ($200\,\mathrm{km}$), the cells with no information are scattered — they reflect the areas with no sources/receivers. At the depth of 600 km, four large regions with no information occur due to the sources-receivers geometry. The ray distribution becomes more uniform with increasing depth. At the depth of $1,000\,\mathrm{km}$, there is a rather small region with no information. The cells with no information do not occur anymore at the depth of $2,500\,\mathrm{km}$. The long-wavelength features of the inversion error (Fig. 3.19, fifth row) copying the projection error in most of the mantle. As we mentioned above, we assume that the slowness anomaly is zero in the regions with no information (no rays). Hence, the inversion errors arising from regions with no-information appear at the depth of $200\,\mathrm{km}$, $600\,\mathrm{km}$ and $1,000\,\mathrm{km}$. The short-wavelength inversion error correspond to the oscillations. In the cross-section at the depth $2,500\,\mathrm{km}$, we observe that the inversion error is higher than the projection error (Fig. 3.19, fourth row). The inversion output slightly underestimates the amplitudes of long-wavelength anomalies at this depth.

Further, we again display two vertical cross-sections in Fig. 3.20. The cross-sections are the same as in the case of irregular parametrization and low Rayleigh number (cf. Fig. 3.7). The vertical cross-section through the upwelling in the poorly covered region is in Fig. 3.20**a–e**. This region is covered unevenly by the rays (Fig. 3.20**b**, scale ranges between 0 and $2,000$). Since we use the regular parametrization, the projection of the input model is able to describe the upwelling (Fig. 3.20**d**) better than in the corresponding case with irregular parametrization (Fig. 3.7**d**). The inversion output (Fig. 3.20**e**) detects the upwelling, however, the feature is strongly deteriorated by the oscillations. The other cross-section passes through the downwelling in the well covered region (Fig. 3.20**f–j**). The input feature (Fig. 3.20**h**) can be easily described by the average model (Fig. 3.20**i**). The downwelling is successfully resolved also in the inversion output (Fig. 3.20**j**). Both the strong downwelling and weak upwelling can be resolved. However, the resolution is lower than for model with irregular parametrization (Fig. 3.7**j**)

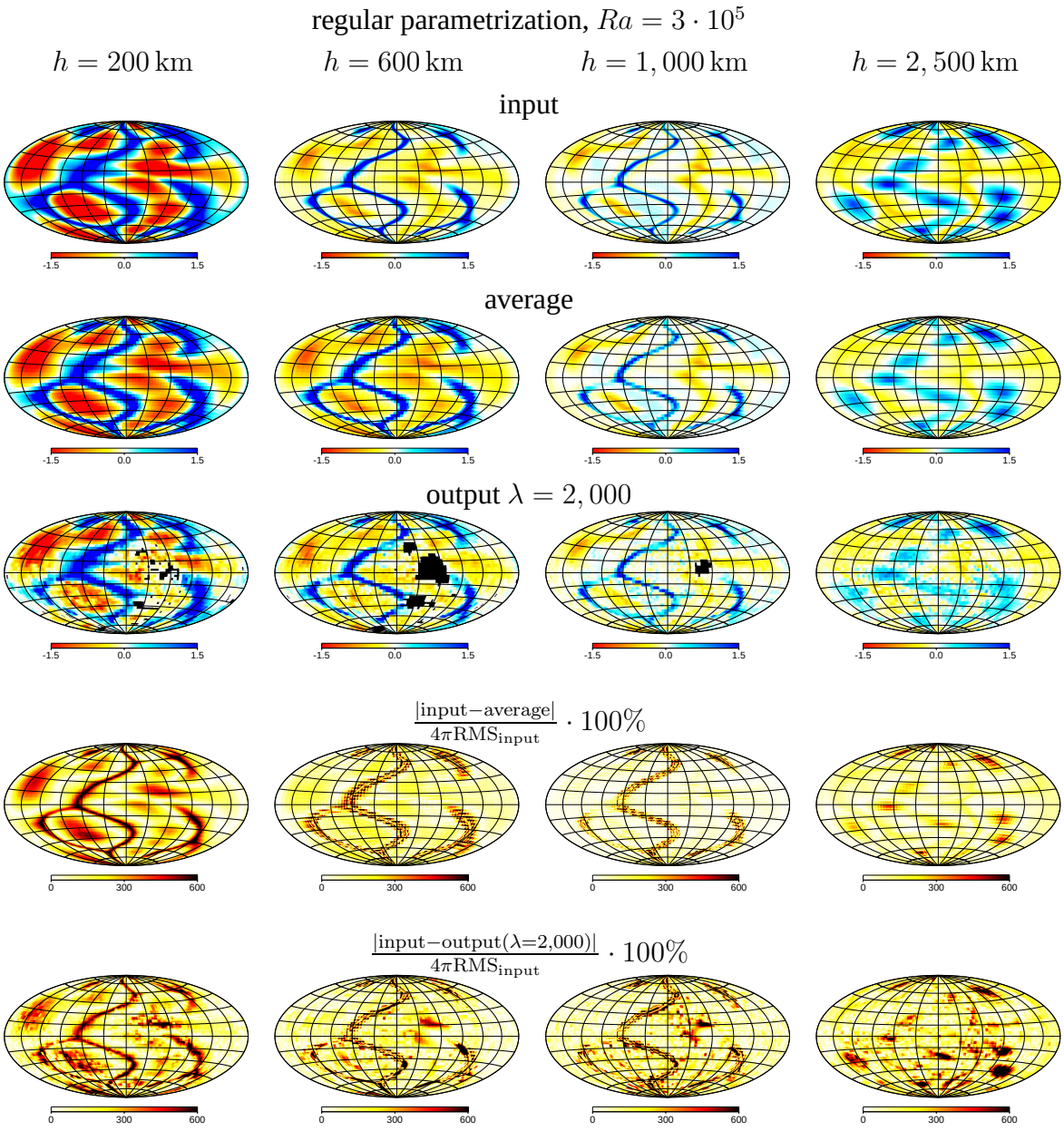

Figure 3.19 Results for the regular parametrization for Rayleigh number $Ra = 3 \cdot 10^5$. Relative seismic velocity anomalies (in percents of reference velocity) are shown. Horizontal cross-section at the depth of $200\,\mathrm{km}$ (first column), $600\,\mathrm{km}$ (second column), $1,000\,\mathrm{km}$ (third column) and $2,500\,\mathrm{km}$ (fourth column). The first row — cross-section of input model, the second row — average through regular cells, the third row — results of the inversion for $\lambda = 2,000$, the fourth row — absolute value of difference between input model and average normalized by 4πRMS of the input model at given depth, the fifth row — the normalized difference between input and output ($\lambda = 2,000$) model.

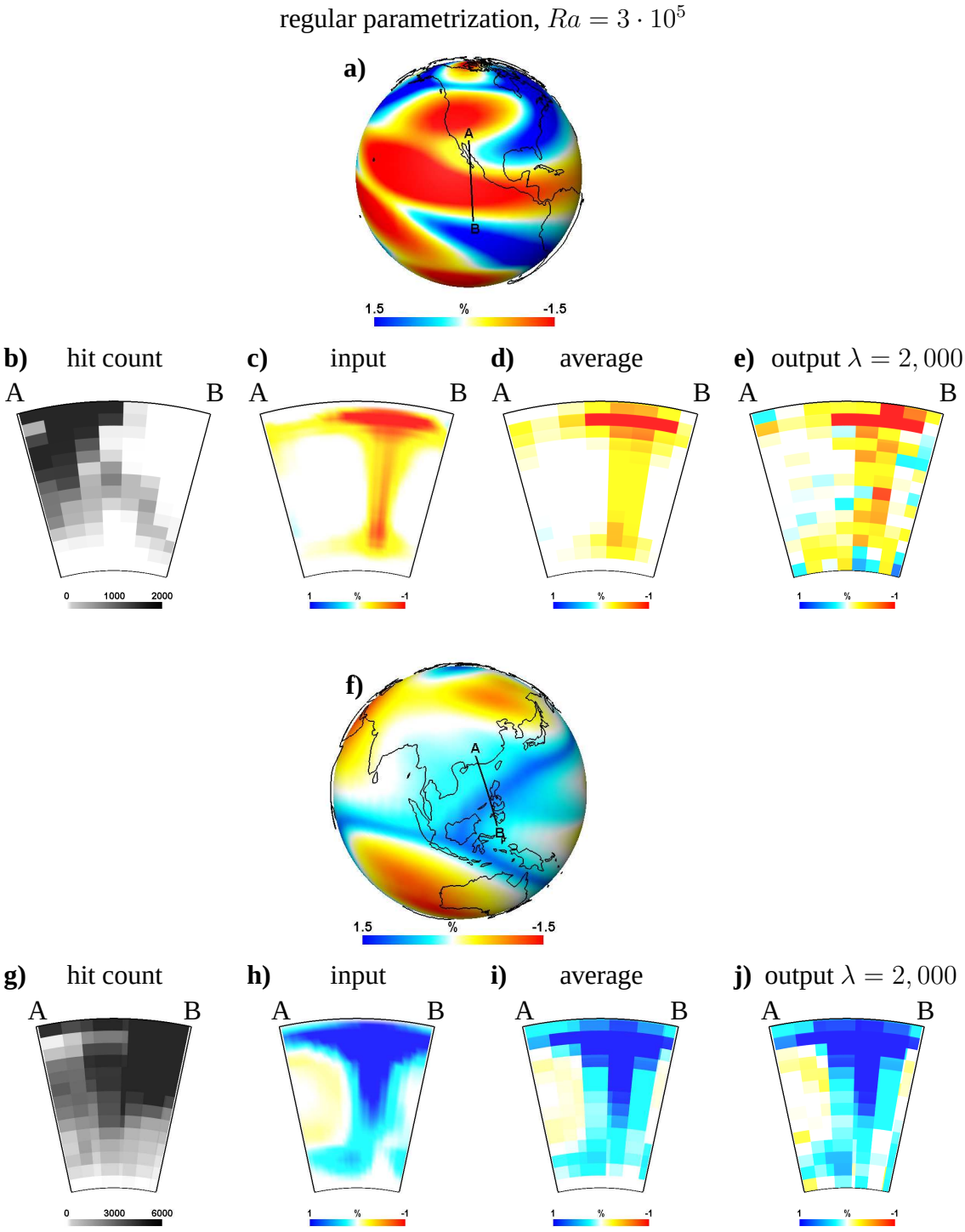

Figure 3.20 Two vertical cross-sections in the model with $Ra = 3{\cdot}10^5$ and regular parametrization. Vertical cross-section (**a–e**) through upwelling, **a)** location of the cross-section, **b)** hit count, **c)** input, **d)** average, **e)** result of the inversion for $\lambda = 2,000$. Vertical cross-section (**f–j**) through downwelling, **f)** location of the cross-section, **g)** hit count, **h)** input, **i)** average, **j)** result of the inversion for $\lambda = 2,000$. Relative seismic velocity anomalies (in percents of reference velocity) are shown.

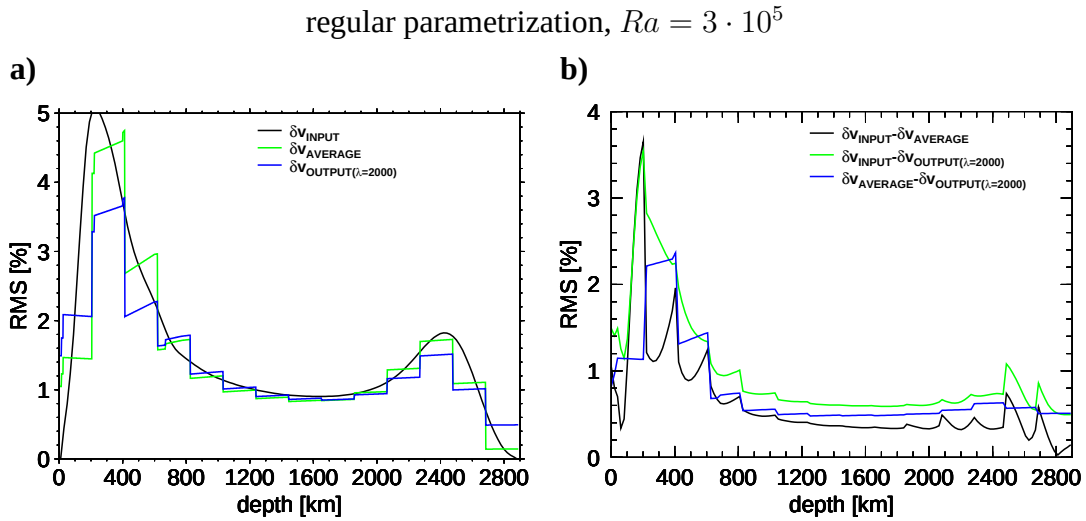

Figure 3.21 Root mean square (RMS) for regular parametrization and for **a)** the input model ($Ra = 3 \cdot 10^5$), average and inversion result ($\lambda = 2,000$) and **b)** their differences.

The amplitude resolution of the inversion for the damping coefficient $\lambda = 2,000$ is illustrated in Fig. 3.21 where the RMS of the anomalies is plotted as a function of depth. The RMS of the input (Fig. 3.21**a**, black line) is reproduced successfully by the average model (Fig. 3.21**a**, green line). In the RMS of both average (Fig. 3.21**a**, green line) and output models (Fig. 3.21**a**, blue line), the jumps caused by the boundaries of the cells are observed. The RMS of the output model (Fig. 3.21**a**, blue line) is underestimated in the regions of the boundary layers. In the upper mantle, the underestimation of the RMS of the output model is also affected by the cells with no rays (where we set the anomaly equal to zero). On the other hand, the width of the boundary layers is predicted quite successfully. Fig. 3.21**b** shows the RMS of differences between the input and average models (Fig. 3.21**b**, black line), input and output models (Fig. 3.21**b**, green line), average and output models (Fig. 3.21**b**, blue line). All curves have similar character, they have two maxima corresponding to the boundary layers.

3.3.2 Results for $Ra = 10^6$

In this paragraph, we describe the results for the Rayleigh number $Ra = 10^6$ and regular parametrization. The inversion output for four values of damping coefficient is illustrated in Fig. 3.22. The input anomalies have linear shape and they are relatively short-wavelengths (Fig. 3.22**a**). The average model (Fig. 3.22**b**) is able to describe the main features, though they are slightly smeared. The correlation between the input and the average model is $\rho_{\mathrm{input}\times\mathrm{average}} = 0.77$. Similarly to the previously discussed case with $Ra = 3 \cdot 10^5$ and regular parametrization, the inversion output is strongly affected by damping factor, with "optimal" result obtained for $\lambda = 1,000$ (cf. Fig. 3.15**c–f**).

The spectra are plotted in Fig. 3.23. The spectrum of the input model (Fig. 3.23**a**) has two maxima, one in the upper and the other in the lower mantle and relatively high power on the high degrees. The spectrum of the average model (Fig. 3.23**b**) describes the input quite successfully. However, it has slightly lower power at the high degrees in comparison with the spectra of the input model (Fig. 3.23**a**). The spectra of the output are flat for

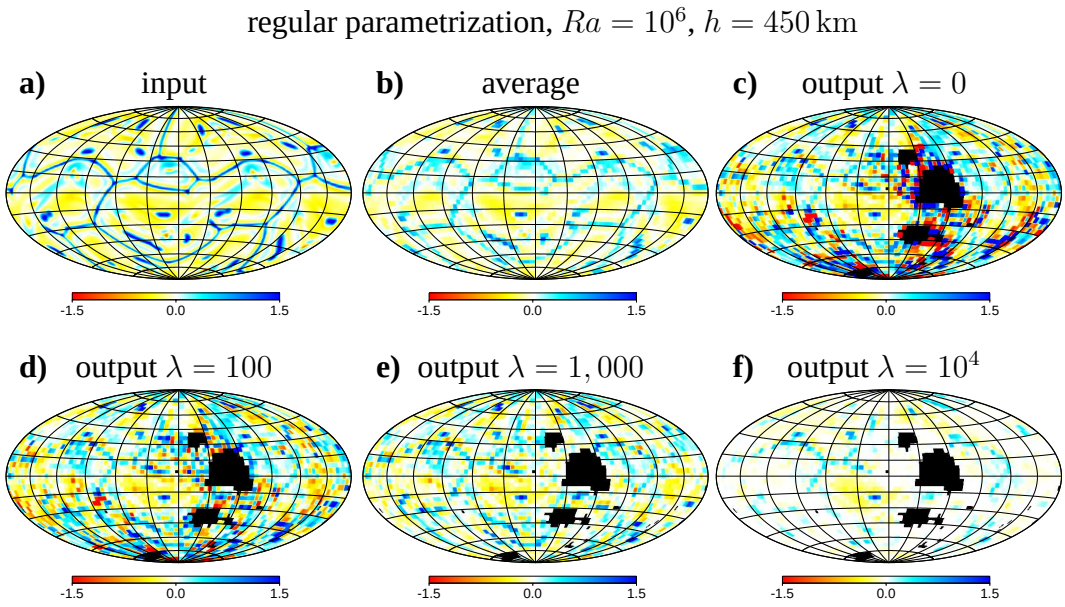

Figure 3.22 Results of the inversion for the regular parametrization and for Rayleigh number $Ra = 10^6$. Relative seismic velocity anomalies (in percents of reference velocity) are shown. Figures are plotted at a depth of $450\,\mathrm{km}$, **a)** input model, **b)** average through regular cell parametrization, **c–f)** results for the damping coefficient $\lambda = 0$, 100, $1,000$ and 10^4, black color means no information (no rays) in the cell.

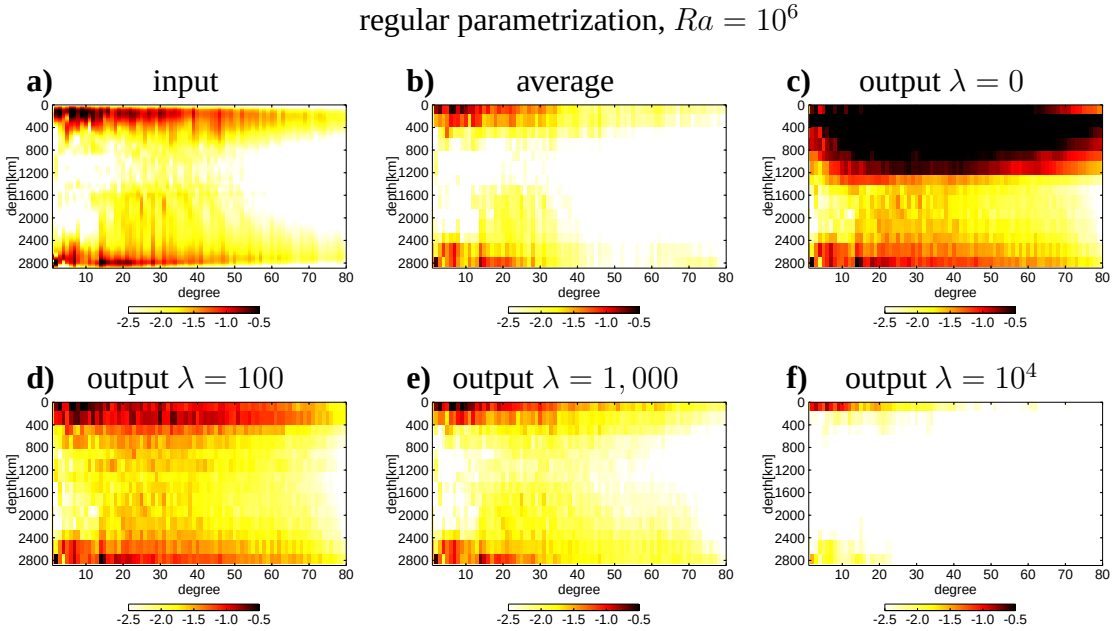

Figure 3.23 Results of the inversion for the regular parametrization and for Rayleigh number $Ra = 10^6$. Decadic logarithm of the power spectra (shown as a function of the spherical harmonic degree and the depth, see Eq. 2.44) for **a)** input model, **b)** average through regular cell parametrization, **c–f)** results for the damping coefficient $\lambda = 0$, 100, $1,000$ and 10^4.

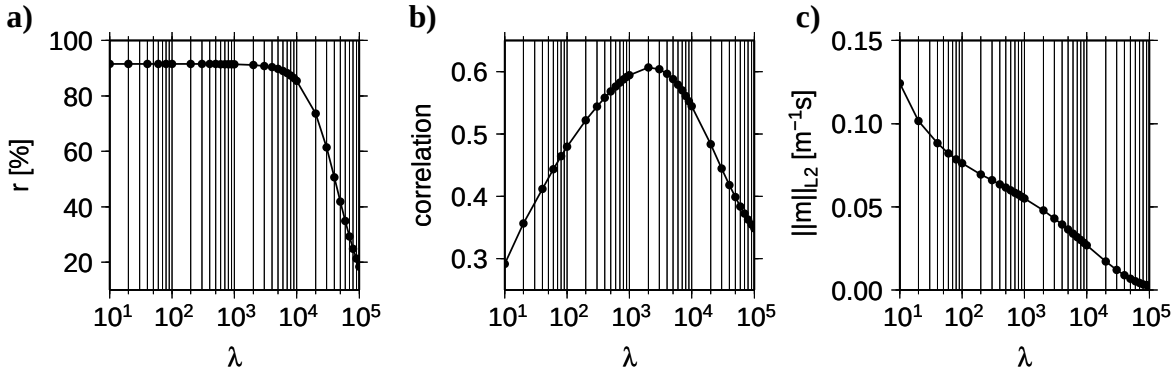

Figure 3.24 Characteristics of results for regular parametrization and for Rayleigh number $Ra = 10^6$, **a)** percentage fit r, **b)** correlation ρ and **c)** L_2-norm of the model vector $\mathbf{m}$ as a function of a damping coefficient λ.

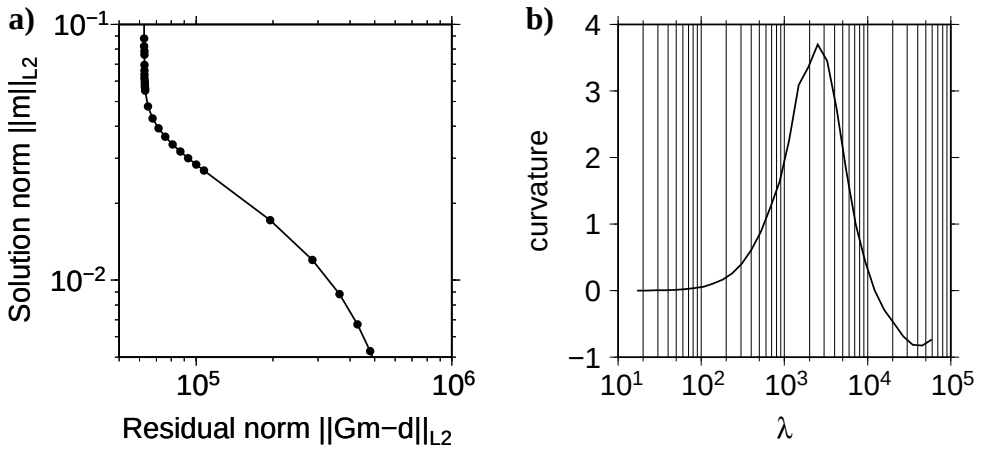

Figure 3.25 Characteristics of results for regular parametrization and for Rayleigh number $Ra = 10^6$, **a)** L-curve, **b)** curvature of the L-curve.

$\lambda = 0$ and $\lambda = 100$ (Figs. 3.23**c-d**). For the output model with the damping coefficient $\lambda = 1,000$ (Fig. 3.23**e**), the oscillations are mostly suppressed and the spectrum describes the input and the average successfully. If we use too high value of the damping coefficient $\lambda = 10^4$ (Fig. 3.23**f**), the spectrum is short. Not only the oscillations but also the input structures are suppressed.

The characteristics of the output models as a function of the damping coefficient in the log-scale are resumed in Fig. 3.24. The shapes of the curves do not differ significantly from the curves for the regular parametrization and low Rayleigh number. The percentage of the explained data (Fig. 3.24**a**) is rather constant $r = 93.6\%$ for $\lambda \lesssim 3,000$. For higher λ, it decrases rapidly. The correlation coefficient ρ between the input and output model has low value $\rho_{\mathrm{input}\times\mathrm{output}(\lambda=0)} = 0.11$ for the inversion without damping. The value of the correlation increases with increasing damping coefficient. And it reaches the maximum for the damping coefficient $\lambda = 2,000$ $\rho_{\mathrm{input}\times\mathrm{output}(\lambda=2,000)} = 0.63$. Hence, slightly higher value of damping is necessary to obtain the maximum correlation than for the inversion with the low Rayleigh number (cf. Fig. 3.17**b**). For higher value of the damping coefficient $\lambda > 2,000$, the value of the correlation coefficient decreases again. The norm of the model vector (Fig. 3.24**c**) is monotonous, it decreases with increasing the

damping coefficient. We use the L-curve analysis to obtain the proper damping. The L-curve is plotted in Fig. 3.25**a**. We again compute the curvature of this curve (Fig. 3.25**b**) to get the proper damping. The highest value of the curvature is again obtained for damping between $\lambda = 2,000$ and $\lambda = 3,000$ (cf. Fig. 3.18**b**). This value of the damping coefficient corresponds well to the inversion output with the maximum correlation.

From now on, we again restrict ourselves to the most successful model (using the L-curve criterion). We display four horizontal cross-section through the model in Fig. 3.26. The input anomalies (Fig. 3.26, first row) have a linear shape and they are short-wavelengths, and in the mid-mantle at the depth $1,000\,\mathrm{km}$, they have rather low amplitudes. The average model (Fig. 3.26, second row) describes the model successfully even though the anomalies are slightly smeared. This is reflected in the normalized projection error (Fig. 3.26, fourth row) — the biggest error is concentrated in the vicinity of the features. The amplitude of the projection error seems to be relatively high at the depth $1,000\,\mathrm{km}$. This effect is caused by the low amplitude at this depth and hence by the low normalizing factor.

The output anomalies are shown in Fig. 3.26, third row. The inversion with the damping coefficient $\lambda = 2,000$ is able to detect the main features in the well-covered regions in most parts of the mantle, however, the oscillations still occur. The characteristic features of the output anomalies are the most deteriorated in the mid-mantle ($h = 1,000\,\mathrm{km}$) by the oscillation — the amplitudes of the input anomalies are comparable to the amplitudes of oscillations at this depth. The normalized inversion errors (Fig. 3.26, fifth row) arise from three main contributions — the projection error, the error caused by oscillations and disability to describe the input anomalies in the badly-covered regions.

Further, we show two vertical cross-sections through the upwelling in the badly covered region (Figs. 3.27**a–e**) and through the downwelling (Figs. 3.27**f–j**) in relatively well covered region. For Rayleigh number $Ra = 10^6$, the cross-sections locations are the same for both regular (Fig. 3.27) and irregular parametrization (Fig. 3.13).

The uneven distribution of the rays is demonstrated by the hit count (Fig. 3.27**b**, scale ranges between 0 and $2,000$). The input anomalies (Fig. 3.27**c**) can be described by the average model (Fig. 3.27**d**) only partly. The regular parametrization does not recover the continuity of the upwelling through the whole mantle. The inversion output (Fig. 3.27**e**) roughly detects the position of the upwelling. However, the upwelling image is strongly deteriorated by the oscillations. The location of the vertical cross-section through well covered region is in Fig. 3.27**f**. The density of rays in this region is demonstrated in Fig. 3.27**g** (the scale ranges between 0 and $6,000$ rays per cell). The input feature (Fig. 3.27**h**) is passing through the whole mantle and can be resolved by the chosen parametrization quite well (average model, Fig. 3.27**i**). Even though the oscillations disturb the output, the inversion output for the damping coefficient $\lambda = 2,000$ predicts the input anomaly quite successfully. However, the output anomaly seems to be broken around the depth $h = 1,700\,\mathrm{km}$.

The amplitude resolving power is illustrated in Fig. 3.28. We show the RMS of the input model (Fig. 3.28**a**, black line), average model (Fig. 3.28**a**, green line) and of the inversion output for $\lambda = 2,000$ (Fig. 3.28**a**, blue line). The RMS of the input model (Fig. 3.28**a**, black line) has two maxima corresponding to the boundary layers. These two maxima can be observed also for the RMS of the average model (Fig. 3.28**a**, green line)

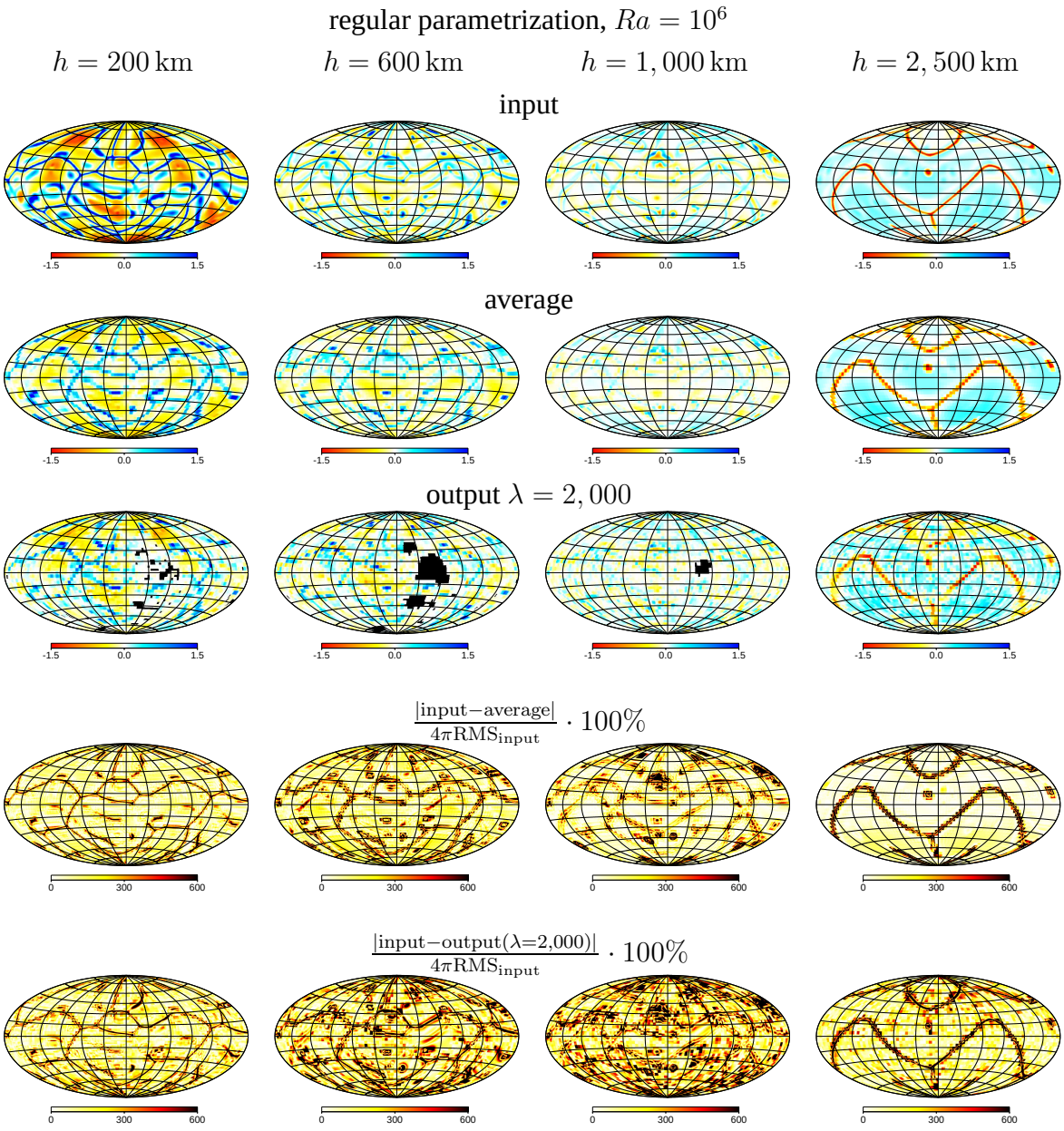

Figure 3.26 Results for the regular parametrization for Rayleigh number $Ra = 10^6$. Relative seismic velocity anomalies (in percents of reference velocity) are shown. Horizontal cross-section at the depth of $200\,\mathrm{km}$ (first column), $600\,\mathrm{km}$ (second column), $1,000\,\mathrm{km}$ (third column) and $2,500\,\mathrm{km}$ (fourth column). The first row — cross-section of input model, the second row — average through irregular cells, the third row — results of the inversion for $\lambda = 2,000$, the fourth row — absolute value of difference between input model and average normalized by 4πRMS of the input model at given depth, the fifth row — the normalized difference between input and output ($\lambda = 2,000$) model.

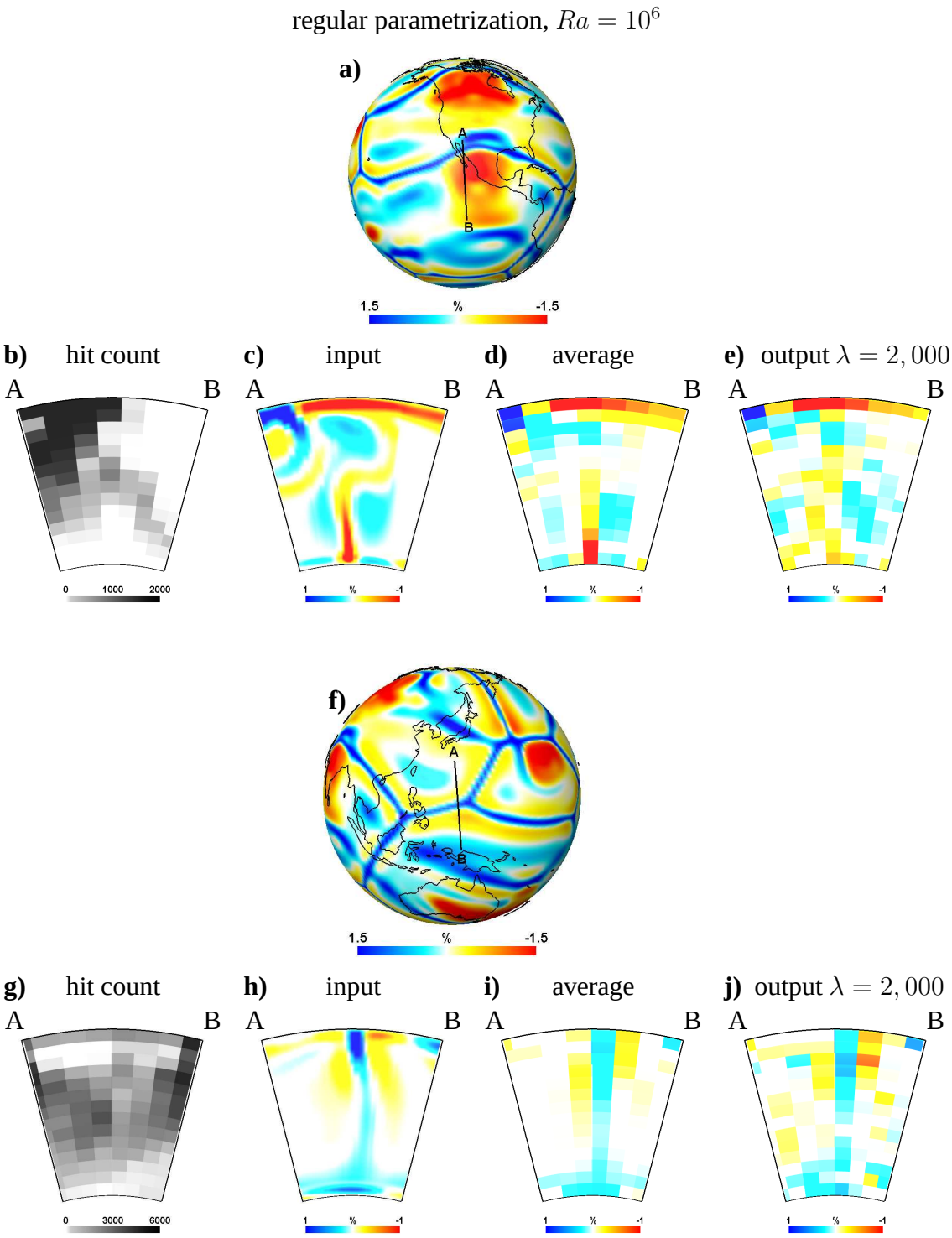

Figure 3.27 Two vertical cross-sections in the model with $Ra = 10^6$ and regular parametrization. Vertical cross-section (**a–e**) through upwelling, **a)** location of the cross-section, **b)** hit count, **c)** input, **d)** average, **e)** result of the inversion for $\lambda = 2,000$. Vertical cross-section (**f–j**) through downwelling, **f)** location of the cross-section, **g)** hit count, **h)** input, **i)** average, **j)** result of the inversion for $\lambda = 2,000$. Relative seismic velocity anomalies (in percents of reference velocity) are shown.

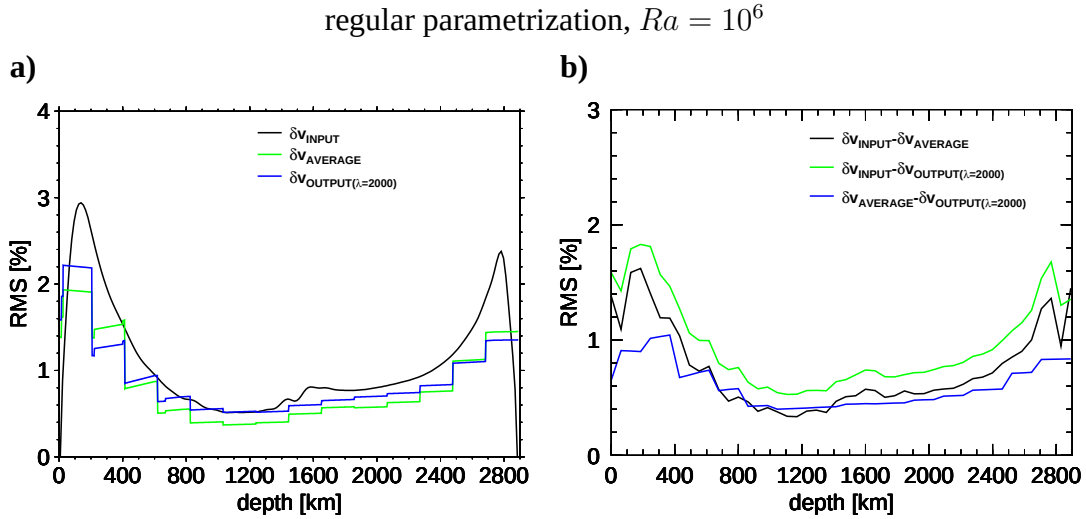

Figure 3.28 Root mean square (RMS) for regular parametrization and for **a)** the input model ($Ra = 10^6$), average and inversion result ($\lambda = 2,000$) and **b)** their differences.

and for the RMS of the output model (Fig. 3.28**a**, blue line). The width of the boundary layers of the inversion output describes quite well the width of the boundary layers of the input model. But they have considerably lower amplitude. The curves of the RMS of the average model (Fig. 3.28**a**, green line) and RMS of the output model (Fig. 3.28**a**, blue line) have similar shape. However, the RMS of the output model is higher than the RMS of the average model in most of the mantle. The RMSs of differences are plotted in Fig. 3.28**b**. For all curves, the RMS of differences have maxima of the amplitudes at depths corresponding to the both boundary layers.

3.4 Discussion

The upper limit of the resolution of the irregular parametrization model is given by the size of basic cells which is 1.125° in horizontal and $\sim 60\,\mathrm{km}$ in vertical direction. On the other hand, the lowest resolution is very rough — the size of the largest possible cell is $18°$ in horizontal and $\sim 960\,\mathrm{km}$ in vertical direction. In order to have approximately the same number of parameters (and comparable computer demands), the used regular parametrization grid is coarser — its best possible resolution is 4° in horizontal and $\sim 207\,\mathrm{km}$ in vertical direction. Therefore, we cannot reach the best resolution of the irregular parametrization model in well covered regions under the same computational cost. On the other hand, in the poorly covered regions, where the low hit count demands large irregular parametrization cells, the regular model has better resolution (provided we use proper damping). By using finer regular grid, we could reach the resolution comparable to the resolution in well covered regions of irregular model, but at the cost of considerably higher number of model parameters and, therefore, more memory-demanding and time-consuming requirements.

The results for irregular parametrization without damping are in Fig. 3.6 and Fig. 3.12 (horizontal cross-sections), in Fig. 3.7 and Fig. 3.13 (vertical cross-sections) and in Fig. 3.4 and Fig. 3.10 (power spectra). The results for regular parametrization for optimal damp-

	irregular parametrization					
	$Ra = 3 \cdot 10^5$ $\rho_{\mathrm{INPUT\times AVERAGE}} = 0.82$			$Ra = 10^6$ $\rho_{\mathrm{INPUT\times AVERAGE}} = 0.60$		
λ	$r\ [\%]$	$\rho_{\mathrm{IN\times OUT}}$	$\rho_{\mathrm{OUT\times AV}}$	$r\ [\%]$	$\rho_{\mathrm{IN\times OUT}}$	$\rho_{\mathrm{OUT\times AV}}$
0	97.92	0.74	0.91	93.41	0.45	0.76
100	97.92	0.74	0.91	93.41	0.46	0.76
10^3	97.86	0.75	0.92	93.32	0.46	0.78
10^4	88.58	0.68	0.83	79.07	0.43	0.72
10^5	11.66	0.48	0.59	7.75	0.26	0.44
	regular parametrization					
	$Ra = 3 \cdot 10^5$ $\rho_{\mathrm{INPUT\times AVERAGE}} = 0.92$			$Ra = 10^6$ $\rho_{\mathrm{INPUT\times AVERAGE}} = 0.77$		
λ	$r\ [\%]$	$\rho_{\mathrm{IN\times OUT}}$	$\rho_{\mathrm{OUT\times AV}}$	$r\ [\%]$	$\rho_{\mathrm{IN\times OUT}}$	$\rho_{\mathrm{OUT\times AV}}$
0	96.80	0.11	0.12	93.60	0.11	0.15
100	96.80	0.65	0.71	93.59	0.47	0.61
10^3	96.74	0.80	0.87	93.46	0.63	0.82
10^4	93.20	0.64	0.70	85.33	0.54	0.71
10^5	29.00	0.38	0.42	14.88	0.43	0.44

Table 3.1 Comparison of the irregular and regular parametrizations — correlations ρ and percentage fit r.

ing are in Fig. 3.19 and Fig. 3.26 (horizontal cross-sections), in Fig. 3.20 and Fig. 3.27 (vertical cross-sections) and in Fig. 3.16 and Fig. 3.23 (power spectra).

If we compare the spectra for the inversion results for low Rayleigh number ($Ra = 3 \cdot 10^5$) for the irregular parametrization without damping (Fig. 3.4**c**) and results for the regular parametrization with damping $\lambda = 1,000$ (Fig. 3.16**e**) with the spectrum of the input model (Fig. 3.4**a**), we get that both parametrization can predict the input spectrum quite successfully. However, the boundaries corresponding to the edges of the biggest cells occur for the spectrum of the output model parametrized by irregular cells (Fig. 3.4**c**). For higher Rayleigh number $Ra = 10^6$, the spectra of the inversion results with the optimal damping are in Fig. 3.10**c** (irregular parametrization, without damping) and in Fig. 3.23**e** (regular parametrization, $\lambda = 1,000$). Both spectra corresponds to the input one (Fig. 3.10**a**) again quite well. However, the influence of the large cells for the irregular parametrizations is even more obvious than for the inversion with Rayleigh number $Ra = 3 \cdot 10^5$. The width of boundary layers in model using the irregular parametrization seems to be wider than the width of the boundary layers in the input model.

The negative influence of the large parametrization cells in a case of the irregular parametrization also explains values of the correlation coefficient. The correlation ρ and the explained data r are summarized in the Tab. 3.1. The regular parametrization seems to reflect the input model better than the irregular parametrization — the correlation between the input and average model is higher for the regular one than for the irregular one. Even the correlation between the input and the inversion output for optimal damping ($\lambda = 2,000$ for regular and $\lambda = 0$ for irregular parametrization) reaches higher values for the regular parametrization.

However, we should keep in mind that the correlation and power spectra are global

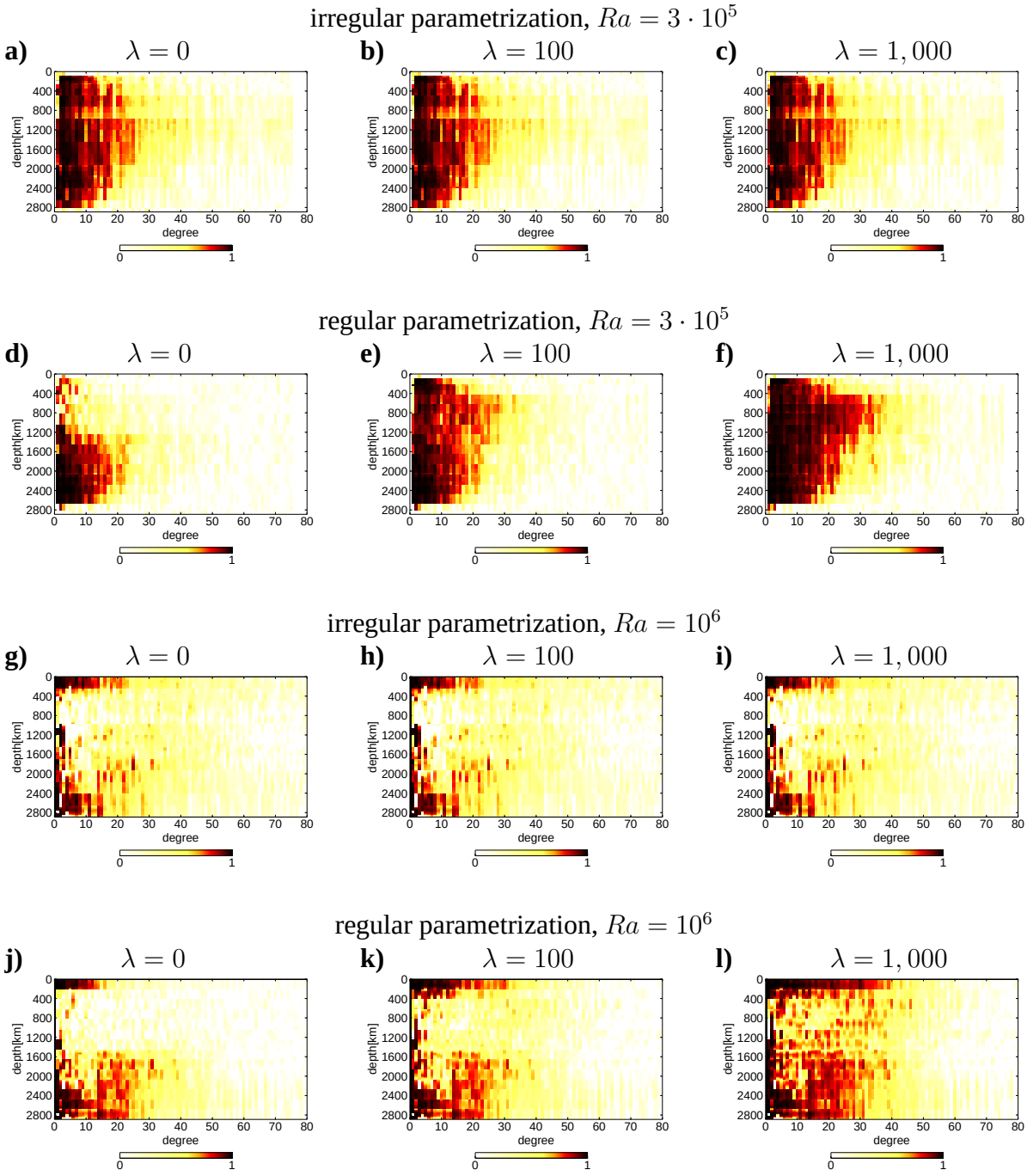

Figure 3.29 Correlation between the input and the output model ($\lambda = 0$ first column, $\lambda = 100$ second column, $\lambda = 1,000$ third column) depending on the depth and degree of spherical harmonics coefficient; results for **a–c)** irregular parametrization and $Ra = 3 \cdot 10^5$, **d–f)** regular parametrization and $Ra = 3 \cdot 10^5$, **g–i)** irregular parametrization and $Ra = 10^6$, **j–l)** regular parametrization and $Ra = 10^6$.

characteristics. Apparently, globally the regular parametrization gives better results than the irregular one. But as we already mentioned above, the main advantage of the irregular parametrization is that we can obtain higher resolution in the well-covered regions at the same computational costs. Moreover, the inversion is better conditioned and the explicit regularization is not necessary. If we compare the inversion results for the irregular and regular parametrization in the well-covered regions (Fig. 3.7**f–j** vs. Fig. 3.20**f–j** and Fig. 3.13**f–j** vs. Fig. 3.27**f–j**), we see that the irregular parametrization has better resolution there.

Another important question is, how tomography can reveal geodynamic models (Mégnin and Romanowicz 2000; Becker and Boschi 2002). The ability of our kinematic tomographic inversion to retrieve geodynamic (convection) models is illustrated in Fig. 3.29. Here the correlation between the inversion input and output of seismic velocity distributions is shown as a function of depth and spherical harmonic degree, see equation (2.46). We display here the correlation for three different values of the damping coefficient $\lambda = 0$, 100 and $1,000$. For Rayleigh number $Ra = 3 \cdot 10^5$, the correlation of the input and output models is in Fig. 3.29**a–c** for irregular parametrization and in Fig. 3.29**d–f** for regular parametrization. For irregular parametrizations, the correlation is relatively high up to degree ~ 20 for irregular parametrization. It has, however, a minimum at the depth $h \sim 900\,\mathrm{km}$ where is the lower edge of the large cells. Moreover, as expected, the correlation is independent on the damping coefficient in the range $0 - 1,000$. For the regular parametrization, the correlation is rather low especially above $1,000\,\mathrm{km}$ if the damping is not used (Fig. 3.29**d**). For higher value of lambda $\lambda = 100$ (Fig. 3.29**e**) and $\lambda = 1,000$ (Fig. 3.29**f**), the correlation increases above $1,000\,\mathrm{km}$. For the damping coefficient $\lambda = 1,000$, the correlation is relatively high up to the degree ~ 25 for depths $h = 0 - 400\,\mathrm{km}$ and $h > 1,200\,\mathrm{km}$. At the depth of $400 - 1,200\,\mathrm{km}$, the high correlation can be found up to the degree ~ 35.

The correlation between the input and output models for Rayleigh number $Ra = 10^6$ is in Fig. 3.29**g–i** for irregular and in Fig. 3.29**j–l** for regular parametrizations. As expected, the value of the correlation is considerably lower for both parametrization than for the lower Rayleigh number due to the shorter-wavelength character of the input anomalies. The correlation for the irregular parametrization, does not depend on the value of the damping coefficient. However, the amplitude of correlation is rather low in most parts of the mantle. Only above $h \sim 200\,\mathrm{km}$ and under $h \sim 2,400\,\mathrm{km}$, the correlation coefficient is relatively high up to the degree 15. The correlation between the input model for Rayleigh number $Ra = 10^6$ and the output model using the regular parametrization depends on the value of the damping factor. For the output model without damping (Fig. 3.29**j**), the correlation is low especially between $400\,\mathrm{km}$ and $1,600\,\mathrm{km}$. If we increase the value of damping coefficient $\lambda = 100$ (Fig. 3.29**k**), the correlation increases. For the optimal damping $\lambda = 1,000$ (Fig. 3.29**l**), correlation is relatively high up to degree ~ 30 at depths $h < 400\,\mathrm{km}$ and $h > 1,600\,\mathrm{km}$. However, it is rather insignificant at depth range $400 - 1,600\,\mathrm{km}$.

This means that on global scale the regular parametrization is more successful if an optimal damping is applied. In irregular parametrization model, the global correlation is lower because of the large parametrization cells in poorly covered areas, however, it gives more detailed results in well covered areas.

Chapter 4

Conclusions

We have found differences between the inversion output for regular and irregular parametrization due to the uneven distribution of rays. For the irregular parametrization, the input structures are resolved successfully in the well-covered regions. In the poorly-covered areas, where the distribution of rays is very sparse, rather large parametrization cells can occur and the projection error can be significant there. However, the explicit regularization is not needed in our inversion unless the data error is included (Montelli et al. 2004a). The inversion results are rather independent on the damping up to $\lambda \sim 1,000$. The power spectra of the inversion output decays reasonably even if no damping is applied. The widths of the boundary layers seem to be wider in the vertical direction especially for the high Rayleigh number $Ra = 10^6$ in the upper part of the upper mantle and in the lowermost mantle. At the surface and CMB boundary layer and in the upper part of the lower mantle, the inversion results are negatively influenced by the large parametrization cells in the poorly covered regions.

The regular parametrization produces much lower parametrization error in the badly covered regions than the irregular one. However, the inverse problem is unstable and oscillations occur unless explicit regularization is applied. Without damping, the spectra of inversion output are flat due to high degree oscillations, especially in the upper mantle. On the other hand, if a proper damping is used, the output spectrum is much closer to the input one than in any irregular parametrization model. The best fit of the input and output spectra is obtained for the damping parameter $\lambda \sim 1,000$ for both considered Rayleigh numbers ($Ra = 3 \cdot 10^5$ and $Ra = 10^6$). This value of damping coefficient corresponds well to the maximum of correlation. In the real data inversion, however, we do not know the input structure and, therefore, some strategy how to choose a proper damping factor is needed. We use the L-curve and the curvature of the L-curve to determine optimal damping. We find that the optimal value of the damping coefficient is $\lambda \sim 2,000$ by L-curve criterion. This value also corresponds quite well to the values for the maximum correlation between the input and the output model.

In this study, we have restricted ourselves purely on the effect of parametrization error. Therefore, we get the best possible resolution for adopted parametrization. If the picking error and error arising from mis-determination of sources would be included, the resolution would be even worse. Hence, some extra damping would be necessary for both types of parametrization to eliminate the effect of these errors.

Synthetic tests discussed in this thesis are carried out for Rayleigh numbers $Ra = 3 \cdot 10^5$ and $Ra = 10^6$. Although the Rayleigh number estimates based on the uppermost mantle values of viscosity, thermal expansivity and thermal conductivity are higher than Ra = 10^6 (e.g. Turcotte and Schubert 2002) for whole mantle convection and may reach even Ra = 10^8 (Yanagisawa and Yamagishi 2005), an effective Rayleigh number is much lower due to the material variability throughout the mantle. An increase of viscosity in the lower mantle can be more than one order of magnitude (e.g. Čadek and Fleitout 2003, Mitrovica and Forte 2004), decrease of thermal expansivity may reach one order of magnitude (Katsura et al. 2005) and thermal conductivity can be substantially increased by its component corresponding to the radiative transfer (e.g. Badro et al. 2004, Hofmeister 2005). Thus the convection simulations with Rayleigh number ranging from $3 \cdot 10^5$ to 10^6 should provide a reasonable approximation of the mantle structure wavelengths except for the shallow upper mantle, where the plate-like behavior is hard to simulate unless complex rheological description is used.

The main advantage of the inversion using irregular parametrization is that we are able to resolve relatively fine structures in well covered areas. Moreover, the explicit damping is not necessary if only the projection error is included. However, in the poorly covered regions the large projection error causes extremely bad resolution. Large parametrization cells negatively influence the overall resolution and power spectra of the output model. Therefore, on a global scale, the inversion with regular parametrization is generally more successful in resolving the input seismic velocity structure, provided that a proper damping is chosen to suppress the oscillations caused by the ill-conditioned inverse problem. On the other hand, the irregular parametrization is more suitable to obtain better resolution in well-covered regions at the same computational costs.

Part II

Regional scale convection models

Chapter 5

Mantle convection

The thermal/thermo-chemical convection in the Earth's mantle is described by the equations based on conservation laws, rheology description, the equation of state and material advective transport equation. These equations together with the initial and boundary conditions describe the motion of the fluid driven by thermal/thermo-chemical buoyancy.

Further, the flow within the mantle is influenced by the major solid-solid phase transitions. At the depth of $400\,\mathrm{km}$, the exothermic phase transition in mantle material is observed (Bina and Helffrich 1994), which tends to increase the vertical flow. At the depth of $670\,\mathrm{km}$, there is an endothermic phase transition which reduces the vertical flow and may even prevent the subducting plates to penetrate into the lower mantle. Recently, a new phase transition has been discovered in the deepest part of the lower mantle (Murakami et al. 2004, Tsuchiya et al. 2004, Oganov and Ono 2004, Iitaka et al. 2004). This exothermic change of perovskite to post-perovskite may strongly influence the dynamics of the core-mantle boundary region and the deformation of the subducted material in the lowermost mantle. However, the deformation of the slabs in the transition zone and in the upper part of the lower mantle are the main focus of this thesis, therefore we do not include the post-perovskite phase transition in our calculations.

Rheological properties represent another important issue in the mantle convection. Viscous rheology is expected for the long period processes in the mantle. Three main deformation mechanisms (diffusional creep, dislocation creep and Peierl's mechanism) are supposed (Ashby and Verrall 1977, Frost and Ashby 1982, Karato and Wu 1993, Yamazaki and Karato 2001) in the Earth's mantle. The diffusion creep (Newtonian flow) describes the material behavior at high temperatures and low stresses. The strain rate in this case depends linearly on the stress. Further, the strain rate depends on temperature, pressure and the grain size. The dislocation (non-Newtonian, power-law) creep describes the material behavior at intermediate stresses $10^{-1} - 10^{2}\,\mathrm{MPa}$. Strain rate depends on temperature, pressure and approximately 3.5^{th} power of the stress. The Peierl's mechanism (low temperature plasticity) describes material behavior at low temperatures and high stresses. For numerical simulations, this mechanism is usually approximated by a power-law stress limiting mechanism (e.g. Čížková et al. 2002, van Hunen et al. 2004). Further, it is generally accepted that the viscosity increases by a factor of $10 - 1000$ in the lower mantle (e.g. Hager and Richards 1989, Peltier 1996, Kido and Čadek 1997, Čížková et al. 1997, Lambeck and Johnston 1998, Mitrovica and Forte 2004). This vis-

cosity increases together with the phase transition at $670\,\mathrm{km}$ can provide a significant barrier to the vertical fluxes and significantly influence the convection pattern within the Earth's mantle.

In this part of the thesis, we concentrate on the convection modeling. We use the method introduced by Gerya and Yuen (2003) to solve the governing equation of the mantle convection. Further, we take into account phase transitions and strongly non-linear viscosity. We employ our code to perform the simulation of the subduction processes. We focus on the problem of the slabs thickening in the lower mantle.

5.1 Governing equations

We use the incompressible extended Boussinesq approximation with infinite Prandtl number (Ita and King 1994). Therefore, the density is assumed to be constant except for the buoyancy term and the inertia is neglected. Moreover, the velocity field is divergence-free (incompressible flow). Further, we neglect the self-gravitation.

Inside the model domain excluding boundaries, the laws of conservation have Eulerian form (used symbols are explained in Tab. 5.1):

$$\begin{aligned} \nabla \cdot \mathbf{v} &= 0, && (5.1)\\ -\nabla\pi + \nabla\cdot\boldsymbol{\sigma} + \Delta\rho\mathbf{g} &= 0, && (5.2)\\ \rho_0 c_p \frac{\partial T}{\partial t} &= \nabla\cdot(k\nabla T) - \rho_0 c_p(\mathbf{v}\cdot\nabla)T + \rho_0\alpha T\mathbf{v}\cdot\mathbf{g} + \\ &\quad +\boldsymbol{\sigma} : \nabla\mathbf{v} + Q_\mathrm{L} + H_\mathrm{R}, && (5.3)\\ \frac{\partial C}{\partial t} + (\mathbf{v}\cdot\nabla)C &= 0. && (5.4) \end{aligned}$$

Eq. (5.1) is continuity equation for incompressible fluid. The momentum equations is given in (5.2). Eq. (5.3) is the conservation of the energy (heat equation). It describes the temperature changes with time at given point (left-hand side (lhs) term) caused by heat diffusion (right-hand side (rhs), first term), heat advection (rhs, second term), adiabatic heating/cooling (rhs, third term), viscous dissipation (rhs, fourth term), latent heat (rhs, fifth term) and radioactive heating (rhs, last term). For multicomponent (thermochemical) convection, another additional equation describing the composition advection has to be solved, Eq. (5.4).

5.2 Rheology

Beside the conservation laws, it is necessary to specify the rheological description of the mantle material. Here we define the strain rate tensor $\dot{\boldsymbol{\varepsilon}}$ as follows (see e.g. Ashby and Verrall 1977)

$$\dot{\boldsymbol{\varepsilon}} = \frac{1}{2}\left(\nabla\mathbf{v} + (\nabla\mathbf{v})^\mathrm{T}\right), \quad \dot{\varepsilon}_{ij} = \frac{1}{2}\left(\frac{\partial v_i}{\partial x_j} + \frac{\partial v_j}{\partial x_i}\right) \qquad (5.5)$$

and its second invariant $\dot{\varepsilon}_{\mathrm{II}}$

$$\dot{\varepsilon}_{\mathrm{II}} = \left(2\dot{\boldsymbol{\varepsilon}} : \dot{\boldsymbol{\varepsilon}}\right)^{1/2} = \left(2\sum_{ij} \dot{\varepsilon}_{ij}\dot{\varepsilon}_{ij}\right)^{1/2}. \tag{5.6}$$

We use viscous rheology in the form

$$\boldsymbol{\sigma} = 2\eta(\dot{\varepsilon}_{\mathrm{II}})\dot{\boldsymbol{\varepsilon}} = \eta(\dot{\varepsilon}_{\mathrm{II}})\left(\nabla\mathbf{v} + (\nabla\mathbf{v})^{\mathrm{T}}\right),\ \sigma_{ij} = 2\eta(\dot{\varepsilon}_{\mathrm{II}})\dot{\varepsilon}_{ij} = \eta(\dot{\varepsilon}_{\mathrm{II}})\left(\frac{\partial v_i}{\partial x_j} + \frac{\partial v_j}{\partial x_i}\right). \tag{5.7}$$

We assume that the relationship between the deviatoric parts of the stress tensor $\boldsymbol{\sigma}$ and the strain rate tensor $\dot{\boldsymbol{\varepsilon}}$ could be non-linear: the viscosity can depend on the strain rate $\eta = \eta(\dot{\varepsilon}_{\mathrm{II}})$. The second invariant of the deviatoric part of the stress tensor σ_{II} is defined as follows:

$$\sigma_{\mathrm{II}} = \left(\frac{1}{2}\boldsymbol{\sigma} : \boldsymbol{\sigma}\right)^{1/2} = \left(\frac{1}{2}\sum_{ij} \sigma_{ij}\sigma_{ij}\right)^{1/2}. \tag{5.8}$$

5.3 Equation of state

The buoyancy forces in the thermo-chemical convective system are caused by the thermally induced density variations, chemical density variations and density variations due to the phase changes:

$$\Delta\rho(T, p, C) = -\rho_0\alpha\left(T - T_{\mathrm{ref}}\right) + \Delta\rho_c + \sum_k \delta\rho_k\Gamma_k. \tag{5.9}$$

We assume simple linear relation between the density and temperature variations (rhs, first term). The second term describes the compositional density anomalies in the multicomponent convection system. The last term on right-hand side expresses the density changes associated with the phase transitions, k denotes the k^{th} phase transition and Γ_k is phase function (see next paragraph).

5.4 Phase transitions

The k^{th} phase transition is characterized by the Clapeyron slope $\gamma_k = \frac{\mathrm{d}p}{\mathrm{d}T}$ and by the density jump $\delta\rho_k$ in the passing material. The uplift/depression of the transition depth together with the phase-transition density jump define the phase-change related density anomalies. To describe the effect of phase transitions, the phase function Γ_k is often used (Christensen and Yuen 1985). Here we use following parametrization (van Hunen 2001):

$$\Gamma_k = \frac{1}{2}\left(1 + \sin\left(\pi\frac{z - z^k_{\mathrm{ph}}(T)}{d^k_{\mathrm{ph}}}\right)\right). \tag{5.10}$$

The phase function Γ_k varies between 0 and 1, $d^k_{\rm ph}$ is a parameter defining the width of the phase transition, z is the depth. The transition depth dependence on the temperature T is described by $z^k_{\rm ph}(T)$ using following formula:

$$z^k_{\rm ph} = z^k_0 + \frac{1}{\rho_0 g_0}\gamma_k (T(z^k_0) - T^{{\rm ph},k}_0). \tag{5.11}$$

Here z^k_0 is a reference transition depth of at a reference temperature $T^{{\rm ph},k}_0$.

Phase transitions influence also the heat equation (5.3) through the latent heat. The latent heat per unit volume for the $k^{\rm th}$ phase $q^k_{\rm L}$ (see e.g. Christensen 1998) can be expressed as

$$q^k_{\rm L} = \frac{\gamma_k \delta\rho_k T}{\rho_0}. \tag{5.12}$$

Then the total latent heat $Q_{\rm L}$ release from Eq. (5.3) can be rewritten into (see e.g. van Hunen 2001)

$$Q_{\rm L} = \sum_k \frac{\gamma_k \delta\rho_k T}{\rho_0}\frac{{\rm D}\Gamma_k}{{\rm D}t}. \tag{5.13}$$

5.5 Dimensionless variables

In this thesis, we use dimensionless formulation of the governing equations. The scaling parameters are following:

$$\boldsymbol{x} = d\boldsymbol{x}', \quad t = \frac{d^2}{\kappa_0}t', \quad \mathbf{v} = \frac{\kappa_0}{d}\mathbf{v}', \quad \pi = \frac{\eta_0\kappa_0}{d^2}\pi', \quad T = T_{\rm S} + (T_{\rm B} - T_{\rm S})T' \tag{5.14}$$

The used symbols are explained in Tab. 5.1. Hence, the conservation laws (5.1)–(5.4) together with the equation of state (5.9) and rheology equation (5.7) yield following set of equations:

$$\nabla\cdot\mathbf{v} = 0, \tag{5.15}$$

$$-\nabla\pi + \nabla\cdot\frac{\eta}{\eta_0}\left(\nabla\mathbf{v} + (\nabla\mathbf{v})^{\rm T}\right) = \left(\frac{\alpha}{\alpha_0}Ra(T - T_{\rm ref}) - \sum_k Rb_k\Gamma_k - RcC\right)\frac{\mathbf{g}}{g_0}, \tag{5.16}$$

$$\frac{\partial C}{\partial t} + (\mathbf{v}\cdot\nabla)C = 0. \tag{5.17}$$

$$\frac{\partial T}{\partial t} = \nabla\cdot(k\nabla T) - (\mathbf{v}\cdot\nabla)\,T + Di\frac{\alpha}{\alpha_0}\left(T + \frac{T_{\rm S}}{T_{\rm B} - T_{\rm S}}\right)\mathbf{v}\cdot\frac{\mathbf{g}}{g_0} + \frac{Raq}{Ra} + \\ + \frac{Di}{Ra}\frac{\eta}{\eta_0}\left(\nabla\mathbf{v} + (\nabla\mathbf{v})^{\rm T}\right) : \nabla\mathbf{v} + \sum_k \frac{Rb_k}{Ra}Di\left(T + \frac{T_{\rm S}}{T_{\rm B} - T_{\rm S}}\right)\gamma_k\frac{{\rm D}\Gamma_k}{{\rm D}t}. \tag{5.18}$$

In these equations, all variables and operators are dimensionless. However, we omit $\bullet'$ for simplicity. Ra, Rb_k, Rc, Raq and Di are dimensionless numbers:

$$\begin{aligned}
\text{thermal Rayleigh number} &: Ra = \frac{\rho_0(T_\mathrm{B}-T_\mathrm{S})\alpha_0 d^3 g_0}{\eta_0\kappa_0},\\
\text{phase Rayleigh number} &: Rb_k = \frac{\delta\rho_k d^3 g_0}{\eta_0\kappa_0},\\
\text{compositional Rayleigh number} &: Rc = \frac{\Delta\rho_c d^3 g_0}{\eta_0\kappa_0},\\
\text{Rayleigh number for heat sources} &: Raq = \frac{\alpha_0 g_0 H_\mathrm{R} d^5 \rho_0}{\eta_0\kappa_0 k_0},\\
\text{dissipation number} &: Di = \frac{\alpha_0 g_0 d}{c_p}.
\end{aligned}$$

5.6 Boundary and initial conditions

To be able to solve the system (5.15–5.18), we have to prescribe the boundary and initial conditions. For the equations (5.15–5.16), we use a combination of the following boundary conditions:

$$\begin{aligned}
\text{prescribed velocity} \quad & \mathbf{v} = \mathbf{v}^\mathrm{BC}, && (5.19)\\
\text{free-slip} \quad & \mathbf{v}\cdot\mathbf{n} = 0, \quad \boldsymbol{\tau}\cdot\mathbf{n} - ((\boldsymbol{\tau}\cdot\mathbf{n})\cdot\mathbf{n})\mathbf{n} = \mathbf{0} && (5.20)\\
\text{normal-free-flux} \quad & (\boldsymbol{\tau}\cdot\mathbf{n})\cdot\mathbf{n} = 0, \quad \mathbf{v} - (\mathbf{v}\cdot\mathbf{n})\mathbf{n} = \mathbf{0} && (5.21)\\
\text{free-flux} \quad & (\boldsymbol{\tau}\cdot\mathbf{n})\cdot\mathbf{n} = 0, \quad \boldsymbol{\tau}\cdot\mathbf{n} - ((\boldsymbol{\tau}\cdot\mathbf{n})\cdot\mathbf{n})\mathbf{n} = \mathbf{0} && (5.22)
\end{aligned}$$

The first boundary condition (5.19) means that we describe the velocity in both normal and tangential directions on the boundaries. For the second (free-slip) condition (5.20), the normal component of the velocity is prescribed to be zero (the in/out flux is not possible) and there are no stresses in the tangential directions. For the normal-free-flux condition (5.21), the in/out flux is permitted only in the normal direction (tangential components of velocity are zero) and no stress is prescribed in the normal direction. For the free-flux condition (5.22), the in/out flux is permitted in all directions and no stress condition is prescribed in normal and tangential direction.

For the heat equation (5.18), we use the following boundary conditions

$$\begin{aligned}
\text{prescribed temperature} \quad & T = T^\mathrm{BC}, && (5.23)\\
\text{or prescribed heat flux} \quad & q_n = -k\nabla T\cdot\mathbf{n} = q_n^\mathrm{BC}. && (5.24)
\end{aligned}$$

Hence, we prescribe either the temperature (5.23) or the normal heat flux (5.24) on the boundaries.

The initial conditions differ for various problems and will be specified for each model separately.

$\frac{\mathrm{D}\bullet}{\mathrm{D}t} = \frac{\partial \bullet}{\partial t} + (\mathbf{v} \cdot \nabla)\bullet$	material time derivative operator
t	time
ρ	density
ρ_0	reference density
$\Delta\rho$	density variation
$\Delta\rho_\mathrm{C}$	density variation arising from the multicomponent convection
$\mathbf{v}$	vector of velocity
T	temperature
T_S	surface temperature
T_B	bottom temperature
T_ref	reference temperature (geotherm)
$\dot{\boldsymbol{\varepsilon}} = \frac{1}{2}\left(\nabla\mathbf{v} + (\mathbf{v})^\mathrm{T}\right)$	strain rate tensor
$\dot{\varepsilon}_\mathrm{II} = (2\dot{\boldsymbol{\varepsilon}} : \dot{\boldsymbol{\varepsilon}})^{1/2}$	second invariant of the strain rate tensor
π	dynamic pressure
$\boldsymbol{\tau} = -\pi\mathbf{I} + \boldsymbol{\sigma}$	stress tensor
$\tau_\mathrm{II} = \left(\frac{1}{2}\boldsymbol{\tau} : \boldsymbol{\tau}\right)^{1/2}$	second invariant of the stress tensor
$\boldsymbol{\sigma}$	deviatoric part of stress tensor
$\sigma_\mathrm{II} = \left(\frac{1}{2}\boldsymbol{\sigma} : \boldsymbol{\sigma}\right)^{1/2}$	second invariant of the deviatoric part of the stress tensor
C	composition parameter
$\mathbf{g}$	vector of the gravity acceleration
g_0	the gravity acceleration
g_x	the x-component of the gravity acceleration
g_z	the z-component of the gravity acceleration
η	viscosity
η_0	reference viscosity
d	characteristic dimension of the system
k	thermal conductivity
k_0	reference thermal conductivity
$\kappa = \frac{k}{\rho c_p}$	thermal diffusivity
$\kappa_0 = \frac{k_0}{\rho_0 c_p}$	reference thermal diffusivity
α	thermal expansion coefficient
α_0	reference thermal expansion coefficient
c_p	heat capacity
H_R	radiogenic heat production

Table 5.1 Used symbols

Q_{L}	total latent heat release
q_{L}^k	latent heat per unit volume for the k^{th} phase transition
$\delta\rho_k$	density change for the k^{th} phase transition
γ_k	Clapeyron slope for the k^{th} phase transition
Γ_k	phase function for the k^{th} phase transition
z_{ph}^k	depth of the k^{th} phase transition
z_0^k	reference depth of the k^{th} phase transition
d_{ph}^k	width of the k^{th} phase transition
T_0^k	reference temperature of the k^{th} phase transition
Ra	thermal Rayleigh number
Rb_k	k^{th} phase Rayleigh number
Rc	compositional Rayleigh number
Raq	Rayleigh number for heat sources
Di	dissipation number
$\mathbf{n}$	normal vector to the boundary

Table 5.1 Continuation.

Chapter 6

Method

We use the method of Gerya and Yuen (2003) to solve equations governing the thermal/ thermo-chemical convection in a two-dimensional Cartesian domain. This method combines the Eulerian and Lagrangian approaches. The system (5.15–5.16) is solved by the finite difference method on a staggered (Eulerian) grid. The heat equation (5.18) without advection and latent heat is also solved by the finite differences on the Eulerian grid. The heat advection term plus latent heat part of the equation (5.18) and compositional advection Eq. (5.17) are solved using the marker technique (e.g. Shepard 1968, Christensen and Yuen 1984, Hockney and Eastwood 1988, Birdsall and Langdon 1991, Weinberg and Schmeling 1992, Gerya et al. 2000). The markers are particles containing the information about properties of the fluid. We use two kinds of markers — markers carrying the temperature and markers containing the compositional information.

The scheme of the method is following:

0. We take the temperature field T^{i-1}, distribution of the chemical markers, density variation ($\Delta\rho$) and scalar properties (e.g. η, k, α) of the fluid from the previous time-step $i-1$ (or the initial conditions).
1. We solve two-dimensional equations (5.15) and (5.16) together with the boundary conditions using the finite differences scheme on the staggered grid, we get $\mathbf{v}^i$ and π^i (see section 6.3).
2. We compute the adiabatic heating H_{A} and shear heating H_{S} (see section 6.4).
3. We compute the time step Δt (see section 6.5).
4. We solve implicitly the heat equation (5.18) without the heat advection and latent heat terms, we get $T^{0,i}$ (see section 6.6).
5. We advect markers using velocity field $\mathbf{v}^i$ and compute the latent heat (see section 6.8).
6. We interpolate the temperature from the markers on the Eulerian grid, we get T^i (see section 6.9).
7. We calculate the chemical concentrations and scalar properties on the Eulerian grid (section 6.10).
0. We repeat the procedure in time step $i+1$.

6.1 Staggered grid

For solving the continuity (5.15) and momentum (5.16) equations, we use the finite difference scheme on the staggered grid (Fornberg 1995) with $nx \times nz$ nodal points. The scheme of the used grid is in Fig. 6.1. The primary (non-staggered) grid is marked by solid lines and their cross-sections are denoted by the solid squares. In these nodes, the temperature $T_{(ix,iz)}$, xz-component of the strain rate tensor $(\dot{\varepsilon}_{xz})_{(ix,iz)}$ and xz-component of deviatoric part of the stress-tensor $(\sigma_{xz})_{(ix,iz)}$ and scalar properties of the fluid (e.g. $\eta_{(ix,iz)}$, $\alpha_{(ix,iz)}$, $k_{(ix,iz)}$ etc.) are prescribed. The staggered grid is marked by dashed lines. In nodal points of half-staggered grid marked by open triangles, the x-component of the velocity $v_{x\,(ix,iz+1/2)}$ and z-component of the heat flux $q_{z\,(ix,iz+1/2)}$ are prescribed. In the nodal points denoted by open circles, the the z-component of the velocity $v_{z\,(ix+1/2,iz)}$ and x-component of the heat flux $q_{x\,(ix+1/2,iz)}$ are computed. In the nodal points of staggered grid marked by open squares, the dynamic pressure and xx- and zz-components of the strain rate and deviatoric part of the stress tensor ($\dot{\varepsilon}_{xx\,(ix+1/2,iz+1/2)}$, $\dot{\varepsilon}_{zz\,(ix+1/2,iz+1/2)}$, $\sigma_{xx\,(ix+1/2,iz+1/2)}$, $\sigma_{zz\,(ix+1/2,iz+1/2)}$) are prescribed. To express the derivatives in nodal points, we use following formulas:

- derivatives in points x_{ix}, z_{iz} (solid squares)

$$\frac{\partial A}{\partial x}(x_{ix}, z_{iz}) = \frac{A(x_{ix+1/2}, z_{iz}) - A(x_{ix-1/2}, z_{iz})}{0.5(\Delta x_{ix+1/2} + \Delta x_{ix-1/2})} \tag{6.1}$$

$$\frac{\partial A}{\partial z}(x_{ix}, z_{iz}) = \frac{A(x_{ix}, z_{iz+1/2}) - A(x_{ix}, z_{iz-1/2})}{0.5(\Delta z_{iz+1/2} + \Delta z_{iz-1/2})} \tag{6.2}$$

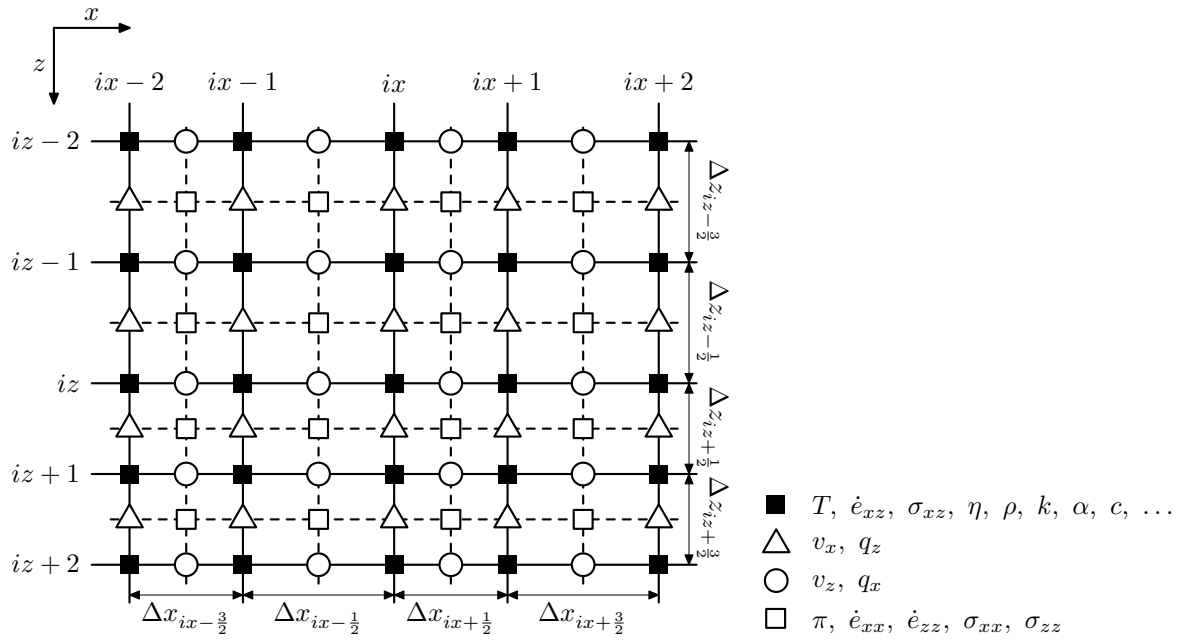

Figure 6.1 Scheme of the staggered grid.

- derivatives in point $x_{ix+1/2}, z_{iz}$ (open circles)

$$\frac{\partial A}{\partial x}(x_{ix+1/2}, z_{iz}) = \frac{A(x_{ix+1}, z_{iz}) - A(x_{ix}, z_{iz})}{\Delta x_{ix+1/2}} \tag{6.3}$$

$$\frac{\partial A}{\partial z}(x_{ix+1/2}, z_{iz}) = \frac{A(x_{ix+1/2}, z_{iz+1/2}) - A(x_{ix+1/2}, z_{iz-1/2})}{0.5(\Delta z_{iz+1/2} + \Delta z_{iz-1/2})} \tag{6.4}$$

- derivatives in points $x_{ix}, z_{iz+1/2}$ (open triangles)

$$\frac{\partial A}{\partial x}(x_{ix}, z_{iz+1/2}) = \frac{A(x_{ix+1/2}, z_{iz+1/2}) - A(x_{ix-1/2}, z_{iz+1/2})}{0.5(\Delta x_{ix+1/2} + \Delta x_{ix-1/2})} \tag{6.5}$$

$$\frac{\partial A}{\partial z}(x_{ix}, z_{iz+1/2}) = \frac{A(x_{ix}, z_{iz+1}) - A(x_{ix}, z_{iz})}{\Delta z_{iz+1/2}} \tag{6.6}$$

- derivatives in points $x_{ix+1/2}, z_{iz+1/2}$ (open squares)

$$\frac{\partial A}{\partial x}(x_{ix+1/2}, z_{iz+1/2}) = \frac{A(x_{ix+1}, z_{iz+1/2}) - A(x_{ix}, z_{iz+1/2})}{\Delta x_{ix+1/2}} \tag{6.7}$$

$$\frac{\partial A}{\partial z}(x_{ix+1/2}, z_{iz+1/2}) = \frac{A(x_{ix+1/2}, z_{iz+1}) - A(x_{ix+1/2}, z_{iz})}{\Delta z_{iz+1/2}} \tag{6.8}$$

If the Eulerian staggered grid is regular (i.e. $\Delta x_{ix+1/2} = \Delta x = \text{const}_x$, $\Delta z_{iz+1/2} = \Delta z = \text{const}_z$), all these formulas are second order of accuracy. However, if we use the irregularly-spaced staggered grid (i.e. $\Delta x_{ix+1/2} \neq \text{const}_x$, $\Delta z_{iz+1/2} \neq \text{const}_z$), only formulas (6.3), (6.6), (6.7) and (6.8) are second order of accuracy. The error of formulas (6.1), (6.2), (6.4) and (6.5) is kept under control by the condition

$$\frac{1}{c} \leq \frac{\Delta x_{ix-1/2}}{\Delta x_{ix+1/2}} \leq c \quad \forall ix, \qquad \frac{1}{c} \leq \frac{\Delta z_{iz-1/2}}{\Delta z_{iz+1/2}} \leq c \quad \forall iz, \qquad 1 \leq c \leq 1.05. \tag{6.9}$$

This condition means, that we allow only limited shrinking/expanding of the grid. For the details concerning the Eulerian grid see Gerya and Yuen (2003).

6.2 Interpolation between the Eulerian grid and markers

Another important issue, if the Eulerian grid and markers are used, is interpolation from the staggered grid to the markers. We use the bilinear interpolation

$$\begin{aligned} A_{im} = & \left(1 - \frac{\Delta x_{im}}{\Delta x_{ix+1/2}}\right)\left(1 - \frac{\Delta z_{im}}{\Delta z_{ix+1/2}}\right) A_{(ix,iz)} + \\ & + \left(\frac{\Delta x_{im}}{\Delta x_{ix+1/2}}\right)\left(1 - \frac{\Delta z_{im}}{\Delta z_{ix+1/2}}\right) A_{(ix+1,iz)} + \\ & + \left(1 - \frac{\Delta x_{im}}{\Delta x_{ix+1/2}}\right)\left(\frac{\Delta z_{im}}{\Delta z_{ix+1/2}}\right) A_{(ix,iz+1)} + \\ & + \left(\frac{\Delta x_{im}}{\Delta x_{ix+1/2}}\right)\left(\frac{\Delta z_{im}}{\Delta z_{ix+1/2}}\right) A_{(ix+,iz+1)}, \end{aligned} \tag{6.10}$$

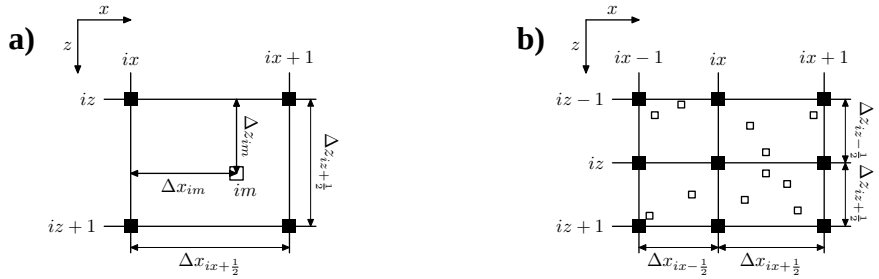

Figure 6.2 Scheme of the interpolation **a)** to the markers and **b)** from the markers.

where Δx_{im} and Δz_{im} are distances of the im^{th} marker to the grid (see Fig. 6.2). Analogically to this interpolation from non-staggered grid, we use also the interpolation from half-staggered grids and staggered grid.

For interpolation from the markers to the Eulerian grid, we use formula

$$A_{(ix,iz)} = \frac{\sum_{im} A_{im} w_{im\ (ix,iz)}}{\sum_{im} w_{im\ (ix,iz)}}, \tag{6.11}$$

$$w_{im\ (ix,iz)} = \frac{1}{\Delta x_{ix+1/2} \Delta z_{iz+1/2}} \left(1 - \frac{\Delta x_{im}}{\Delta x_{ix+1/2}}\right) \left(1 - \frac{\Delta z_{im}}{\Delta z_{iz+1/2}}\right), \tag{6.12}$$

where we sum up variables A_{im} over all markers in the cells surrounding the nodal point x_{ix}, z_{iz} (see Fig. 6.2**b**).

6.3 Solving continuity and momentum equations

The continuity and momentum equations (5.15 and 5.16) are solved on the Eulerian staggered grid. The unknown quantities in these equations are dynamic pressure $\pi_{(ix+1/2,iz+1/2)}$ for $ix = 1, \ldots, nx-1$ and $iz = 1, \ldots, nz-1$, x-components of the velocity $v_{x\ (ix,iz+1/2)}$ for $ix = 1, \ldots, nx$ and $iz = 0, \ldots, nz$, z-components of the velocity $v_{z\ (ix+1/2,iz)}$ for $ix = 0, \ldots, nx$ and $iz = 1, \ldots, nz$. The quantities $v_{x\ (ix,1/2)}$, $v_{x\ (ix,nz+1/2)}$, $v_{z\ (1/2,iz)}$ and $v_{z\ (nx+1/2,iz)}$ are calculated in the virtual points (they lie outside of the studied area) and they are used to prescribe the boundary conditions (see paragraph 6.3.4). Hence, we have $3 \cdot nx \cdot nz + 1$ unknowns (π: $(nx-1)(nz-1)$ unknowns, v_x: $nx(nz+1)$ unknowns, v_z: $(nx+1)nz$ unknowns).

6.3.1 Derivatives, strain rate and stress tensor on the staggered grid

To formulate the continuity and momentum equations, the xx-, zz- and xz- components of the deviatoric part of the stress tensor and their derivatives and the derivatives of the velocity components and dynamic pressure have to be expressed. The x- and z- derivatives of the velocity x-components v_x are computed in nodal points $x_{ix+1/2}, z_{iz+1/2}$ (open

squares) and x_{ix}, z_{iz} (solid squares) using (6.7) and (6.2)

$$\left(\frac{\partial v_x}{\partial x}\right)_{(ix+1/2,iz+1/2)} = \frac{v_{x\ (ix+1,iz+1/2)} - v_{x\ (ix,iz+1/2)}}{\Delta x_{ix+1/2}}, \tag{6.13}$$

$$\left(\frac{\partial v_x}{\partial z}\right)_{(ix,iz)} = \frac{v_{x\ (ix,iz+1/2)} - v_{x\ (ix,iz-1/2)}}{0.5\left(\Delta z_{iz+1/2} + \Delta z_{iz-1/2}\right)}. \tag{6.14}$$

The x- and z-derivatives of v_z are expressed in nodal points x_{ix}, z_{iz} (solid squares) and $x_{ix+1/2}$, $z_{iz+1/2}$ (open squares). Using (6.1) and (6.8), we can write

$$\left(\frac{\partial v_z}{\partial x}\right)_{(ix,iz)} = \frac{v_{z\ (ix+1/2,iz)} - v_{z\ (ix-1/2,iz)}}{0.5\left(\Delta x_{ix+1/2} + \Delta x_{ix-1/2}\right)}, \tag{6.15}$$

$$\left(\frac{\partial v_z}{\partial z}\right)_{(ix+1/2,iz+1/2)} = \frac{v_{z\ (ix+1/2,iz+1)} - v_{z\ (ix+1/2,iz)}}{\Delta z_{iz+1/2}}. \tag{6.16}$$

The x- and z-derivatives of the dynamic pressure π are computed in the nodal points x_{ix}, $z_{iz+1/2}$ (open triangles) and in $x_{ix+1/2}$, z_{iz} (open circles) using (6.5) and (6.4)

$$\left(\frac{\partial \pi}{\partial x}\right)_{(ix,iz+1/2)} = \frac{\pi_{(ix+1/2,iz+1/2)} - \pi_{(ix-1/2,iz+1/2)}}{0.5\left(\Delta x_{ix+1/2} + \Delta x_{ix-1/2}\right)}, \tag{6.17}$$

$$\left(\frac{\partial \pi}{\partial z}\right)_{(ix+1/2,iz)} = \frac{\pi_{(ix+1/2,iz+1/2)} - \pi_{(ix+1/2,iz-1/2)}}{0.5\left(\Delta z_{iz+1/2} + \Delta z_{iz-1/2}\right)}. \tag{6.18}$$

The components of the deviatoric part of the stress tensor are expressed in nodal points $x_{ix+1/2}$, $z_{iz+1/2}$ (open squares) for xx- and zz-components. The xz-component is computed in the nodal points x_{ix}, z_{iz} (solid squares). The rheological relation (5.7) for dimensionless variables can be written on staggered grid as follows:

$$(\sigma_{xx})_{(ix+1/2,iz+1/2)} = \frac{2}{\eta_0}\eta^{\mathrm{S}}_{(ix+1/2,iz+1/2)}\left(\frac{\partial v_x}{\partial x}\right)_{(ix+1/2,iz+1/2)}, \tag{6.19}$$

$$(\sigma_{zz})_{(ix+1/2,iz+1/2)} = \frac{2}{\eta_0}\eta^{\mathrm{S}}_{(ix+1/2,iz+1/2)}\left(\frac{\partial v_z}{\partial z}\right)_{(ix+1/2,iz+1/2)}, \tag{6.20}$$

$$(\sigma_{xz})_{(ix,iz)} = \frac{1}{\eta_0}\eta_{(ix,iz)}\left[\left(\frac{\partial v_x}{\partial z}\right) + \left(\frac{\partial v_z}{\partial x}\right)\right]_{(ix,iz)}, \tag{6.21}$$

where $\eta^{\mathrm{S}}_{(ix+1/2,iz+1/2)} = {}^1\!/_4(\eta_{(ix,iz)} + \eta_{(ix,iz+1)} + \eta_{(ix+1,iz)} + \eta_{(ix+1,iz+1)})$ is viscosity in the points $x_{ix+1/2}$, $z_{iz+1/2}$ (open squares).

The x- derivatives of σ_{xx} and z-derivatives of σ_{zz} are expressed in the nodal points x_{ix}, $z_{iz+1/2}$ (open triangles) and $x_{ix+1/2}$, z_{iz} (open circles). Using formulas (6.5) and (6.4), we can write

$$\left(\frac{\partial \sigma_{xx}}{\partial x}\right)_{(ix,iz+1/2)} = \frac{(\sigma_{xx})_{(ix+1/2,iz+1/2)} - (\sigma_{xx})_{(ix-1/2,iz+1/2)}}{0.5\left(\Delta x_{ix+1/2} + \Delta x_{ix-1/2}\right)}, \tag{6.22}$$

$$\left(\frac{\partial \sigma_{zz}}{\partial z}\right)_{(ix+1/2,iz)} = \frac{(\sigma_{zz})_{(ix+1/2,iz+1/2)} - (\sigma_{zz})_{(ix+1/2,iz-1/2)}}{0.5\left(\Delta z_{iz+1/2} + \Delta z_{iz-1/2}\right)}. \tag{6.23}$$

The x- and z-derivatives of the σ_{xz} are computed in the nodal points $x_{ix+1/2}, z_{iz}$ (open circles) and $x_{ix}, z_{iz+1/2}$ (open triangles). Using formulas (6.3) and (6.6), we get

$$\left(\frac{\partial \sigma_{xz}}{\partial x}\right)_{(ix+1/2,iz)} = \frac{(\sigma_{xz})_{(ix+1,iz)} - (\sigma_{xz})_{(ix,iz)}}{\Delta x_{ix+1/2}}, \tag{6.24}$$

$$\left(\frac{\partial \sigma_{xz}}{\partial z}\right)_{(ix,iz+1/2)} = \frac{(\sigma_{xz})_{(ix,iz+1)} - (\sigma_{xz})_{(ix,iz)}}{\Delta z_{iz+1/2}}. \tag{6.25}$$

The components of the strain rate tensor $\dot{\boldsymbol{\varepsilon}}$ are expressed analogically to $\boldsymbol{\sigma}$ components. Then for the equation (5.5), we get

$$(\dot{\varepsilon}_{xx})_{(ix+1/2,iz+1/2)} = \left(\frac{\partial v_x}{\partial x}\right)_{(ix+1/2,iz+1/2)}, \tag{6.26}$$

$$(\dot{\varepsilon}_{zz})_{(ix+1/2,iz+1/2)} = \left(\frac{\partial v_z}{\partial z}\right)_{(ix+1/2,iz+1/2)}, \tag{6.27}$$

$$(\dot{\varepsilon}_{xz})_{(ix,iz)} = 1/2\left[\left(\frac{\partial v_x}{\partial z}\right) + \left(\frac{\partial v_z}{\partial x}\right)\right]_{(ix,iz)}. \tag{6.28}$$

However, it is necessary to express $\dot{\varepsilon}_{xx}$ and $\dot{\varepsilon}_{zz}$ a posteriori on the non-staggered grid (solid squares) to compute the shear heating H_{S} and second invariant of the strain rate tensor $\dot{\varepsilon}_{\mathrm{II}}$.

$$(\dot{\varepsilon}_{xx})_{(ix,iz)} = \frac{v^{\mathrm{I}}_{x\ (ix+1/2,iz)} - v^{\mathrm{I}}_{x\ (ix-1/2,iz)}}{0.5\left(\Delta x_{ix-1/2} + \Delta x_{ix+1/2}\right)}, \tag{6.29}$$

$$(\dot{\varepsilon}_{zz})_{(ix,iz)} = \frac{v^{\mathrm{I}}_{z\ (ix,iz+1/2)} - v^{\mathrm{I}}_{z\ (ix,iz-1/2)}}{0.5\left(\Delta z_{iz-1/2} + \Delta z_{iz+1/2}\right)}, \tag{6.30}$$

The variables $v^{\mathrm{I}}_{x\ (ix,iz)}$ and $v^{\mathrm{I}}_{z\ (ix,iz)}$ are x- and z- component of the velocity vector interpolated from the half-staggered grid using Eq. (6.10). For computing $\frac{\partial v_x}{\partial x}$ on the vertical boundaries and $\frac{\partial v_z}{\partial z}$ on the horizontal boundaries in the points x_{ix}, z_{iz}, we use the forward/backward formulas to express the derivatives. For example, we get for the left and upper boundaries

$$(\dot{\varepsilon}_{xx})_{(1,iz)} = \frac{v^{\mathrm{I}}_{x\ (3/2,iz)} - v^{\mathrm{I}}_{x\ (1,iz)}}{0.5\Delta x_{3/2}}, \tag{6.31}$$

$$(\dot{\varepsilon}_{zz})_{(ix,1)} = \frac{v^{\mathrm{I}}_{z\ (ix,3/2)} - v^{\mathrm{I}}_{z\ (ix,1)}}{0.5\Delta z_{3/2}}. \tag{6.32}$$

6.3.2 Continuity equation on the staggered grid

The continuity equation (5.15)

$$\frac{\partial v_x}{\partial x} + \frac{\partial v_z}{\partial z} = 0$$

is prescribed in the points $x_{ix+1/2}, z_{iz+1/2}$ (open squares), for $ix = 1, \ldots, nx-1$ and $iz = 1, \ldots, nz-1$. From equation (5.15) using formulas (6.13) and (6.16), we get

$$\begin{aligned} \alpha^1_{ix+1/2}\left(v_{x\ (ix+1,iz+1/2)} - v_{x\ (ix,iz+1/2)}\right) &+ \\ +\alpha^2_{iz+1/2}\left(v_{z\ (ix+1/2,iz+1)} - v_{z\ (ix+1/2,iz)}\right) &= 0, \end{aligned} \tag{6.33}$$

where the coefficients $\alpha^1_{ix+1/2}$ and $\alpha^2_{iz+1/2}$ denote

$$\alpha^1_{ix+1/2} = \frac{1}{\Delta x_{ix+1/2}} \qquad \text{and} \qquad \alpha^2_{iz+1/2} = \frac{1}{\Delta z_{iz+1/2}}.$$

The discretization scheme of the continuity equation is in Fig. 6.3**a**.

6.3.3 Momentum equation on the staggered grid

The x-component of the momentum equation (5.16)

$$-\frac{\partial \pi}{\partial x} + \frac{\partial \sigma_{xx}}{\partial x} + \frac{\partial \sigma_{xz}}{\partial z} = -\Delta\rho \frac{g_x}{g_0}$$

is prescribed in the points $x_{ix}, z_{iz+1/2}$ (open triangles). Using the rheological properties (6.19) and (6.21), derivatives of the stress-tensor (6.22) and (6.25), derivative of the dynamic pressure (6.17), derivatives of the velocity (6.13), (6.14), (6.15) and linear interpo-

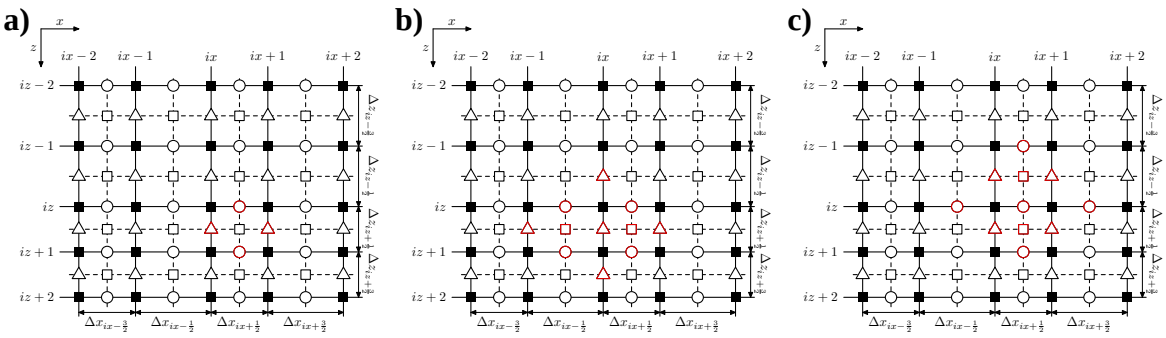

Figure 6.3 The discretization scheme of **a)** continuity equation (6.33) in point $x_{ix+1/2}, z_{iz+1/2}$, **b)** x-component of the momentum equation (6.34) in point $x_{ix}, z_{iz+1/2}$, **c)** z-component of the momentum equation (6.35) in point $x_{ix+1/2}, z_{iz}$. Red color marks the points used for the discretization of the equations in the central point.

lation of the density variation $\Delta\rho$, this equation can be rewritten into:

$$\begin{aligned}
&\beta^1_{(ix,iz+1/2)}\left(v_x\right)_{(ix,iz+3/2)} + \beta^2_{(ix,iz+1/2)}\left(v_x\right)_{(ix,iz-1/2)} + \\
&+\beta^3_{(ix,iz+1/2)}\left(v_x\right)_{(ix+1,iz+1/2)} + \beta^4_{(ix,iz+1/2)}\left(v_x\right)_{(ix-1,iz+1/2)} - \\
&-\left(\beta^1+\beta^2+\beta^3+\beta^4\right)_{(ix,iz+1/2)}\left(v_x\right)_{(ix,iz+1/2)} + \\
&+\beta^5_{(ix,iz+1/2)}\left(\left(v_z\right)_{(ix+1/2,iz+1)} - \left(v_z\right)_{(ix-1/2,iz+1)}\right) + \\
&+\beta^6_{(ix,iz+1/2)}\left(\left(v_z\right)_{(ix-1/2,iz)} - \left(v_z\right)_{(ix+1/2,iz)}\right) + \\
&+\beta^7_{(ix,iz+1/2)}\left(\pi_{(ix-1/2,iz+1/2)} - \pi_{(ix+1/2,iz+1/2)}\right) = \\
&\qquad\qquad = -0.5\frac{g_x}{g_0}(\Delta\rho_{(ix,iz)} + \Delta\rho_{(ix,iz+1)}). \qquad (6.34)
\end{aligned}$$

The discretization scheme of the x-component of momentum equation is in Fig. 6.3**b**. The coefficients $\beta^{\bullet}_{(ix,iz+1/2)}$ denote

$$\begin{aligned}
\beta^1_{(ix,iz+1/2)} &= \eta_{(ix,iz+1)}\frac{1}{\Delta z_{iz+1/2}}\frac{1}{0.5\left(\Delta z_{iz+1/2}+\Delta z_{iz+3/2}\right)},\\
\beta^2_{(ix,iz+1/2)} &= \eta_{(ix,iz)}\frac{1}{\Delta z_{iz+1/2}}\frac{1}{0.5\left(\Delta z_{iz-1/2}+\Delta z_{iz+1/2}\right)},\\
\beta^3_{(ix,iz+1/2)} &= 2\eta^{\mathrm{S}}_{(ix+1/2,iz+1/2)}\frac{1}{\Delta x_{ix+1/2}}\frac{1}{0.5\left(\Delta x_{ix-1/2}+\Delta x_{ix+1/2}\right)},\\
\beta^4_{(ix,iz+1/2)} &= 2\eta^{\mathrm{S}}_{(ix-1/2,iz+1/2)}\frac{1}{\Delta x_{ix-1/2}}\frac{1}{0.5\left(\Delta x_{ix-1/2}+\Delta x_{ix+1/2}\right)},\\
\beta^5_{(ix,iz+1/2)} &= \eta_{(ix,iz+1)}\frac{1}{\Delta z_{iz+1/2}}\frac{1}{0.5\left(\Delta x_{ix-1/2}+\Delta x_{ix+1/2}\right)},\\
\beta^6_{(ix,iz+1/2)} &= \eta_{(ix,iz)}\frac{1}{\Delta z_{iz+1/2}}\frac{1}{0.5\left(\Delta x_{ix-1/2}+\Delta x_{ix+1/2}\right)},\\
\beta^7_{(ix,iz+1/2)} &= \frac{1}{0.5\left(\Delta x_{ix-1/2}+\Delta x_{ix+1/2}\right)}.
\end{aligned}$$

The z-component of the momentum equation (5.16)

$$-\frac{\partial\pi}{\partial z}+\frac{\partial\sigma_{zz}}{\partial z}+\frac{\partial\sigma_{xz}}{\partial x} = -\Delta\rho\frac{g_z}{g_0}$$

is computed in the points $x_{ix+1/2}, z_{iz}$ (open circles). Using the rheological properties (6.20) and (6.21), derivatives of the stress-tensor (6.23) and (6.24), derivative of the dynamic pressure (6.18), derivatives of the velocity (6.16), (6.14), (6.15) and linear interpo-

lation of the density variation $\Delta\rho$, this equation can be rewritten into:

$$\begin{aligned}
&\gamma^1_{(ix+1/2,iz)}\,(v_z)_{(ix+1/2,iz+1)} + \gamma^2_{(ix+1/2,iz)}\,(v_z)_{(ix+1/2,iz-1)} + \\
&+\gamma^3_{(ix+1/2,iz)}\,(v_z)_{(ix+3/2,iz)} + \gamma^4_{(ix+1/2,iz)}\,(v_z)_{(ix-1/2,iz)} - \\
&-\left(\gamma^1+\gamma^2+\gamma^3+\gamma^4\right)_{(ix+1/2,iz)}\,(v_z)_{(ix+1/2,iz)} + \\
&+\gamma^5_{(ix+1/2,iz)}\left((v_x)_{(ix+1,iz+1/2)} - (v_x)_{(ix+1,iz-1/2)}\right) + \\
&+\gamma^6_{(ix+1/2,iz)}\left((v_x)_{(ix,iz-1/2)} - (v_x)_{(ix,iz+1/2)}\right) + \\
&+\gamma^7_{(ix+1/2,iz)}\left(\pi_{(ix+1/2,iz-1/2)} - \pi_{(ix+1/2,iz+1/2)}\right) = \\
&\qquad\qquad = -0.5\frac{g_z}{g_0}(\Delta\rho_{(ix,iz)} + \Delta\rho_{(ix+1,iz)}). \qquad (6.35)
\end{aligned}$$

The discretization scheme of the z-component of momentum equation is in Fig. 6.3**c**. The coefficients $\gamma^{\bullet}_{(ix+1/2,iz)}$ represent

$$\begin{aligned}
\gamma^1_{(ix+1/2,iz)} &= 2\eta^{\mathrm{S}}_{(ix+1/2,iz+1/2)}\frac{1}{\Delta z_{iz+1/2}}\frac{1}{0.5\left(\Delta z_{iz-1/2}+\Delta z_{iz+1/2}\right)},\\
\gamma^2_{(ix+1/2,iz)} &= 2\eta^{\mathrm{S}}_{(ix+1/2,iz-1/2)}\frac{1}{\Delta z_{iz-1/2}}\frac{1}{0.5\left(\Delta z_{iz-1/2}+\Delta z_{iz+1/2}\right)},\\
\gamma^3_{(ix+1/2,iz)} &= \eta_{(ix+1,iz)}\frac{1}{\Delta x_{ix+1/2}}\frac{1}{0.5\left(\Delta x_{ix+1/2}+\Delta x_{ix+3/2}\right)},\\
\gamma^4_{(ix+1/2,iz)} &= \eta_{(ix,iz)}\frac{1}{\Delta x_{ix+1/2}}\frac{1}{0.5\left(\Delta x_{ix-1/2}+\Delta x_{ix+1/2}\right)},\\
\gamma^5_{(ix+1/2,iz)} &= \eta_{(ix+1,iz)}\frac{1}{\Delta x_{ix+1/2}}\frac{1}{0.5\left(\Delta z_{iz-1/2}+\Delta z_{iz+1/2}\right)},\\
\gamma^6_{(ix+1/2,iz)} &= \eta_{(ix,iz)}\frac{1}{\Delta x_{ix+1/2}}\frac{1}{0.5\left(\Delta z_{iz-1/2}+\Delta z_{iz+1/2}\right)},\\
\gamma^7_{(ix+1/2,iz)} &= \frac{1}{0.5\left(\Delta z_{iz-1/2}+\Delta z_{iz+1/2}\right)}.
\end{aligned}$$

6.3.4 Boundary conditions on the staggered grid

To be able to solve the system (5.15–5.16), the boundary conditions have to be prescribed. This is implemented by using the virtual points outside the studied area. These virtual points corresponding to staggered-grid points are symmetrically mirrored around horizontal/vertical boundaries. For example, for the left hand side (lhs) boundary $\Delta x_{1/2} = \Delta x_{3/2}$, (see Fig. 6.4). As we mentioned above, we use four types of the boundary conditions Eqs. (5.19–5.22). All these conditions can be expressed using the prescribed normal/tangential velocity or force. Here, we will re-

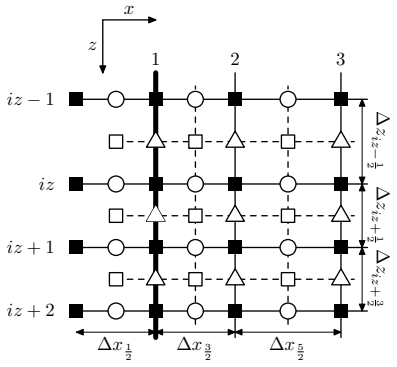

Figure 6.4 Staggered grid and the virtual points on the boundary.

strict ourselves to describe the boundary condition only on one boundary (lhs vertical boundary). On the other boundaries, the conditions are prescribed analogically.

The normal component of velocity $\mathbf{v} \cdot \mathbf{n}$ is given by

$$v_n = v_x = -v_x^{\mathrm{BC}},$$

where v_x^{BC} is a prescribed value on the horizontal velocity on the boundary and it is positive in the sense of the outer normal to the boundary. This condition is computed in the point $x_1, z_{iz+1/2}$

$$v_{x\ (1,iz+1/2)} = -\left(v_x^{\mathrm{BC}}\right)_{(1,iz+1/2)}. \tag{6.36}$$

The discretization scheme of this condition is in Fig. 6.5**a**.

The tangential component of the velocity $\mathbf{v} - (\mathbf{v} \cdot \mathbf{n})\,\mathbf{n}$ on the lhs boundary is

$$v_t = v_z = v_z^{\mathrm{BC}},$$

where v_z^{BC} is prescribed boundary value and it is positive in the sense of the z-axis. This condition is computed in the point x_1, z_{iz}

$$0.5\left[(v_z)_{(1/2,iz)} + (v_z)_{(3/2,iz)}\right] = \left(v_z^{\mathrm{BC}}\right)_{(1,iz,.)} \tag{6.37}$$

The discretization scheme of this condition is in Fig. 6.5**b**.

The normal component of the force $(\boldsymbol{\tau} \cdot \mathbf{n}) \cdot \mathbf{n}$ can be expressed as follows

$$f_n = \tau_{xx} = -f_x^{\mathrm{BC}},$$

where f_x^{BC} is prescribed boundary value and it is positive in the sense of the outer normal to the boundary. This condition is evaluated in the point $x_1, z_{iz+1/2}$

$$0.5\left[(\tau_{xx})_{(1/2,iz+1/2)} + (\tau_{xx})_{(3/2,iz+1/2)}\right] = -f_{x\ (1,z+1/2)}^{\mathrm{BC}}. \tag{6.38}$$

This condition is, however, not prescribed directly. The equation (6.38) is substituted into

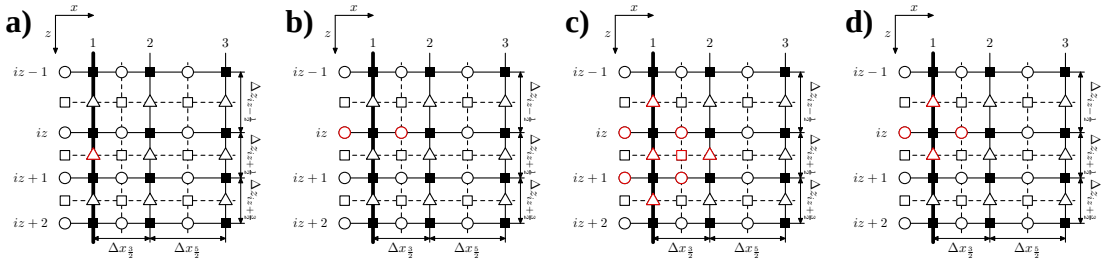

Figure 6.5 Scheme of the condition **a)** for normal velocity in point $x_1, z_{iz+1/2}$ (6.36), **b)** for tangential velocity in point x_1, z_{iz} (6.37), **c)** for normal force in point $x_1, z_{iz+1/2}$ (6.39) and **d)** for tangential velocity in point x_1, z_{iz} (6.40). Red color marks the points used for the discretization of the boundary conditions.

the x-component of the momentum equation (6.34). Then we get

$$\begin{aligned}
&\beta^1_{(1,iz+1/2)}\left(v_x\right)_{(1,iz+3/2)} + \beta^2_{(1,iz+1/2)}\left(v_x\right)_{(1,iz-1/2)} + 2\beta^3_{(1,iz+1/2)}\left(v_x\right)_{(2,iz+1/2)} - \\
&- \left(\beta^1+\beta^2+2\beta^3\right)_{(1,iz+1/2)}\left(v_x\right)_{(1,iz+1/2)} + \beta^5_{(1,iz+1/2)}\left(\left(v_z\right)_{(3/2,iz+1)} - \left(v_z\right)_{(1/2,iz+1)}\right) + \\
&+\beta^6_{(1,iz+1/2)}\left(\left(v_z\right)_{(1/2,iz)} - \left(v_z\right)_{(3/2,iz)}\right) - 2\beta^7_{(1,iz+1/2)}\left(\pi_{(1/2,iz+1/2)}\right) = \\
&= -0.5\frac{g_x}{g_0}(\Delta\rho_{(1,iz)} + \Delta\rho_{(1,iz+1)}) - 2\beta^7_{(1,iz+1/2)}\left(f_x^{\mathrm{BC}}\right)_{(1,iz)} \qquad (6.39)
\end{aligned}$$

The x-component of the momentum equation in the form (6.39) is computed, if the normal component of the force is prescribed. The discretization scheme of this equation is demonstrated in Fig. 6.5**c**.

Tangential component of force $\boldsymbol{\tau}\cdot\mathbf{n} - ((\boldsymbol{\tau}\cdot\mathbf{n})\cdot\mathbf{n})\cdot\mathbf{n}$ is given by

$$f_t = \sigma_{xz} = f_z^{\mathrm{BC}},$$

where f_z^{BC} is prescribed boundary value and it is positive in the sense of the z-axis. This condition is evaluated in the point x_{ix}, z_{iz}. Using Eqs. (6.21), (6.14) and (6.15), we get

$$\begin{aligned}
&\eta_{(1,iz)}\frac{1}{0.5\left(\Delta z_{iz-1/2}+\Delta z_{iz+1/2}\right)}\left[\left(v_x\right)_{(1,iz+1/2)} - \left(v_x\right)_{(1,iz-1/2)}\right] + \\
&+\eta_{(1,iz)}\frac{1}{0.5\left(\Delta x_{1/2}+\Delta x_{3/2}\right)}\left[\left(v_z\right)_{(3/2,iz)} - \left(v_z\right)_{(1/2,iz)}\right] = \left(f_z^{\mathrm{BC}}\right)_{(1,ix)} \qquad (6.40)
\end{aligned}$$

the discretization scheme of this equation is shown in Fig. 6.5**d**.

In the corners, the normal boundary conditions are computed on the half-staggered nodal points (open triangles and open circles) and they do not collide with each other. On the other hand, the tangential boundary conditions are prescribed on non-staggered grid and hence in the same nodal point (solid square). If the velocity is prescribed from both directions, the tangential component from both direction should be equal, i.e for upper left corner

$$\left(v_x^{\mathrm{BC}}\right)_{(1,1)}^{\text{upper boundary}} = -\left(v_z^{\mathrm{BC}}\right)_{(1,1)}^{\text{left boundary}},$$

$\left(v_x^{\mathrm{BC}}\right)_{(1,1)}^{\text{upper boundary}}$ is positive in the sense of x-axis and $\left(v_z^{\mathrm{BC}}\right)_{(1,1)}^{\text{left boundary}}$ is positive in the sense of z-axis. If the free-slip or free-flux is prescribed (tangential forces from both direction are zero), we split the condition (6.40) into two parts. We use the boundary conditions in the form

$$\left[\left(v_x\right)_{(1,3/2)} - \left(v_x\right)_{(1,1/2)}\right] = 0 \qquad \text{and} \qquad \left[\left(v_z\right)_{(3/2,1)} - \left(v_z\right)_{(1/2,1)}\right] = 0$$

If the normal force condition is not prescribed on any part of the boundaries, the dynamic pressure is determined except for the additional constant. In this case, we prescribe in one of the corners the condition on the dynamic pressure $\pi = 0$ instead of the continuity equation. Then we calculate the additive constant a posteriori from the condition $\int_{x_1}^{x_{nx}} \pi(x, z=0)\mathrm{d}x = 0$ (integral of the dynamic pressure on the surface is equal to zero). Analogically, if the x-/z-component of the velocity is not prescribed on any part of the boundaries, the x-/z-component of the velocity is also computed except for the additional constant. However, we do not use this type of boundary conditions.

6.3.5 Inversion

As we mentioned above, we have $3 \cdot nx \cdot nz + 1$ unknowns. For these unknowns, we prescribe $(nx-1)(nz-1)$ the continuity equation (6.33) in the nodal points $x_{ix+1/2}, z_{iz+1/2}$ for $ix = 1, \ldots, nx-1$ and $iz = 1, \ldots, nz-1$ (open squares). The x-component of the momentum equation (6.34) is computed in the points $x_{ix}, z_{iz+1/2}$ for $ix = 2, \ldots, nx-1$ and $iz = 1, \ldots, nz-1$, hence we have $(nx-2)(nz-1)$ conditions. The z-component of the momentum equation (6.35) is described in the points $x_{ix+1/2}, z_{iz}$ for $ix = 1, \ldots, nx-1$ and $iz = 2, \ldots, nz-1$, we have $(nx-1)(nz-2)$ equations. Moreover, we prescribe $2(2nx-1)$ condition on the horizontal and $2(2nz-1)$ condition on the vertical boundaries. Hence, we have $3 \cdot nx \cdot nz + 1$ equations for the $3 \cdot nx \cdot nz + 1$ unknowns.

The system of Eqs. (5.15–5.16) leads to the matrix problem $\mathbf{A} \cdot \mathbf{x} = \mathbf{b}$, where $\mathbf{x}$ is vector of unknowns and $\mathbf{b}$ is right-hand side vector. If we use appropriate order of unknowns ($v_{z\ (ix+1/2,iz)}$, $p_{(ix+1/2,iz+1/2)}$, $v_{x\ (ix,iz+1/2)}$) and equations (z-component of the momentum equation, continuity equation, x-component of the momentum equation), matrix $\mathbf{A}$ is a band matrix. We use the width of the band $6nx+11$. For the inversion, we use LU decomposition from LAPACK subroutines. The use of direct (non-iterative) method is necessary since we use the viscosity varying within the range of the several orders of magnitude.

6.3.6 Non-linear viscosity

In general, the viscosity η depends on the strain rate $\eta(\dot{\varepsilon}_{\mathrm{II}})$, hence the problem is non-linear. In this case, we solve the system (5.15–5.16) iteratively. First ($j = 0$ iteration), we get the viscosity η from the previous time step (or take a guess of the viscosity for the 1^{st} time step). Then the iterative process is as follows: for the $(j+1)^{\mathrm{th}}$ iteration, we solve the system (5.15–5.16) using the viscosity from the previous j^{th} step. We repeat this procedure until the following condition is satisfied:

$$\max \left| \frac{\dot{\varepsilon}_{\mathrm{II}}^{j+1} - \dot{\varepsilon}_{\mathrm{II}}^{j}}{\max\left(\dot{\varepsilon}_{\mathrm{II}}^{j}\right)} \right| < c, \qquad c = 0.01. \tag{6.41}$$

6.4 Adiabatic and shear heating

Dimensionless adiabatic heating H_{A}

$$H_{\mathrm{A}} = Di \frac{\alpha}{\alpha_0} \left(T + \frac{T_{\mathrm{S}}}{T_{\mathrm{B}} - T_{\mathrm{S}}} \right) \mathbf{v} \cdot \frac{\mathbf{g}}{g_0}$$

is computed in the nodal points x_{ix}, z_{iz} (solid squares)

$$H_{\mathrm{A}\ (ix,iz)} = Di \frac{\alpha_{(ix,iz)}}{\alpha_0} \left(T_{(ix,iz)}^{i-1} + \frac{T_{\mathrm{S}}}{T_{\mathrm{B}} - T_{\mathrm{S}}} \right) \left(v_{x\ (ix,iz)}^{\mathrm{I}} {}^{g_x}\!/_{g_0} + v_{z\ (ix,iz)}^{\mathrm{I}} {}^{g_z}\!/_{g_0} \right). \tag{6.42}$$

The variables $v_{x\ (ix,iz)}^{\mathrm{I}}$ and $v_{z\ (ix,iz)}^{\mathrm{I}}$ are x- and z- components of the velocity vector interpolated from the half-staggered grid using Eq. (6.10).

Dimensionless shear heating H_{S} is

$$H_{\mathrm{S}} = \frac{Di}{Ra}\frac{\eta}{\eta_0}\left(\nabla\mathbf{v} + (\nabla\mathbf{v})^{\mathrm{T}}\right) : \nabla\mathbf{v}.$$

In the points x_{ix}, z_{iz} (solid squares), we get

$$(H_{\mathrm{S}})_{(ix,iz)} = \frac{Di}{Ra}\left(\sigma_{xx}\dot{\varepsilon}_{xx} + \sigma_{zz}\dot{\varepsilon}_{zz} + 2\sigma_{xz}\dot{\varepsilon}_{xz}\right)_{(ix,iz)}. \tag{6.43}$$

To compute the $(H_{\mathrm{S}})_{(ix,iz)}$ on the grid, we use rheology relationship (5.7) and Eqs. (6.28–6.32).

6.5 Time step

For determining the time step, we use following two conditions.

The first condition describes the maximum allowed temperature changes $\Delta T_{\max}$ (typically $0.002 \leq \Delta T_{\max} \leq 0.005$) per time step:

$$\Delta t_{\mathrm{T}} = \min_{(ix,iz)}\left[\Delta T_{\max}\left(\left(\frac{\mathrm{D}T}{\mathrm{D}t}\right)^{\mathrm{E}}_{(ix,iz)}\right)^{-1}\right],$$

where $\left(\frac{\mathrm{D}T}{\mathrm{D}t}\right)^{\mathrm{E}}_{(ix,iz)}$ the time change computed using the explicit scheme in time

$$\left(\frac{\mathrm{D}T}{\mathrm{D}t}\right)^{\mathrm{E},i}_{(ix,iz)} = -\left(\frac{q_x}{\partial x}\right)^{i-1}_{(ix,iz)} - \left(\frac{q_z}{\partial z}\right)^{i-1}_{(ix,iz)} + \frac{Raq}{Ra} + (H_{\mathrm{A}})_{(ix,iz)} + (H_{\mathrm{S}})_{(ix,iz)}.$$

For computing the $q_{x\ (ix,iz)}$ and $q_{z\ (ix,iz)}$, see paragraph 6.6.

The second condition describes the maximum allowed displacement.

$$\Delta t_{\mathrm{D}} = \min_{(ix,iz)}\left[cd_{(ix,iz)}\,(v)^{-1}_{(ix,iz)}\right],$$

where $v_{(ix,iz)} = \sqrt{\left(v^{\mathrm{I}}_{x\ (ix,iz)}\right)^2 + \left(v^{\mathrm{I}}_{z\ (ix,iz)}\right)^2}$ is the velocity in the point x_{ix}, z_{iz}, $d_{(ix,iz)}$ denotes the minimum grid distance in the vicinity of the point x_{ix}, z_{iz}, i.e. $d_{(ix,iz)} = \min\left(\Delta x_{ix-1/2}, \Delta x_{ix+1/2}, \Delta z_{iz-1/2}, \Delta z_{iz+1/2}\right)$. The constant c is maximum allowed displacement in the sense of the minimum grid distance and it is typically $0.2 \leq c \leq 0.5$.

The time-step Δt is defined as a minimum of these two conditions:

$$\Delta t = \min\left(\Delta t_{\mathrm{T}}, \Delta t_{\mathrm{D}}\right).$$

6.6 Solving the heat equation

The heat equation (5.18) without advection and latent heat is solved on the Eulerian staggered grid. The unknowns are temperatures in the non-staggered grid (solid squares) $T_{(ix,iz)}$ for $ix = 1, \ldots, nx$ and $iz = 1, \ldots, nz$.

6.6.1 Derivatives and heat flux on the staggered grid

To formulate the heat equation on the staggered grid, we have to express the x- and z-derivatives. The x- and z-derivatives are computed in the points $x_{ix+1/2}, z_{iz}$ (open circles) and $x_{ix}, z_{iz+1/2}$ (open triangles). Using (6.3) and (6.6), we get

$$\left(\frac{\partial T}{\partial x}\right)_{(ix+1/2,iz)} = \frac{T_{(ix+1,iz)} - T_{(ix,iz)}}{\Delta x_{ix+1/2}}, \tag{6.44}$$

$$\left(\frac{\partial T}{\partial z}\right)_{(ix,iz+1/2)} = \frac{T_{(ix,iz+1)} - T_{(ix,iz)}}{\Delta z_{iz+1/2}}. \tag{6.45}$$

The x- and z-components of the heat flux are computed in the points $x_{ix+1/2}, z_{iz}$ (open circles) and $x_{ix}, z_{iz+1/2}$ (open triangles). Using formulas (6.44), (6.45) and linear interpolation, the heat flux can be rewritten into

$$(q_x)_{(ix+1/2,iz)} = -0.5\left(k_{(ix+1,iz)} + k_{(ix,iz)}\right)\frac{T_{(ix+1,iz)} - T_{(ix,iz)}}{\Delta x_{ix+1/2}}, \tag{6.46}$$

$$(q_z)_{(ix,iz+1/2)} = -0.5\left(k_{(ix,iz+1)} + k_{(ix,iz)}\right)\frac{T_{(ix,iz+1)} - T_{(ix,iz)}}{\Delta z_{iz+1/2}}. \tag{6.47}$$

Using (6.1) and (6.2), the x- and z-derivatives of the x- and z-component of the heat flux are computed in the points x_{ix}, z_{iz} (solid squares) as follows

$$\left(\frac{\partial q_x}{\partial x}\right)_{(ix,iz)} = \frac{(q_x)_{(ix+1/2,iz)} - (q_x)_{(ix-1/2,iz)}}{0.5\left(\Delta x_{ix-1/2} + \Delta x_{ix+1/2}\right)}, \tag{6.48}$$

$$\left(\frac{\partial q_z}{\partial z}\right)_{(ix,iz)} = \frac{(q_z)_{(ix,iz+1/2)} - (q_x)_{(ix,iz-1/2)}}{0.5\left(\Delta z_{iz-1/2} + \Delta z_{iz+1/2}\right)}. \tag{6.49}$$

6.6.2 Heat equation on the staggered grid

The heat equation (5.18) without advection and latent heat reads

$$\frac{\partial T}{\partial t} = -\nabla \cdot \mathbf{q} + \frac{Raq}{Ra} + H_{\mathrm{A}} + H_{\mathrm{S}}.$$

If we apply the time-implicit scheme (i is the current time step, $i-1$ is the previous time step), we can write

$$\frac{T^{0,i}_{(ix,iz)} - T^{i-1}_{(ix,iz)}}{\Delta t} = -\left(\frac{q_x}{\partial x}\right)^{0,i}_{(ix,iz)} - \left(\frac{q_z}{\partial z}\right)^{0,i}_{(ix,iz)} + \frac{Raq}{Ra} + (H_{\mathrm{A}})^{i-1}_{(ix,iz)} + (H_{\mathrm{S}})_{(ix,iz)}\,. \tag{6.50}$$

Using formulas for heat flux (6.46–6.47) and their derivatives (6.48–6.49), adiabatic and shear heating (6.42) and (6.43), the heat equation can be reformulated into

$$\begin{aligned} -\delta^1_{(ix,iz)}T^{0,i}_{(ix,iz+1)} - \delta^2_{(ix,iz)}T^{0,i}_{(ix,iz-1)} - \delta^3_{(ix,iz)}T^{0,i}_{(ix+1,iz)} - \delta^4_{(ix,iz)}T^{0,i}_{(ix-1,iz)} + \\ \left(1 + \delta^1 + \delta^2 + \delta^3 + \delta^4\right)_{(ix,iz)} T^{0,i}_{(ix,iz)} = \\ = T^{i-1}_{(ix,iz)} + \Delta t\left(\frac{Raq}{Ra} + (H_{\mathrm{A}})^{i-1}_{(ix,iz)} + (H_{\mathrm{S}})_{(ix,iz)}\right) \end{aligned} \tag{6.51}$$

The discretization scheme of the heat equation is on Fig. 6.6**a**. The coefficients $\delta^{\bullet}_{(ix,iz)}$ denote

$$\begin{aligned}
\delta^1_{(ix,iz)} &= 0.5\Delta t\left(k_{(ix,iz+1)}+k_{(ix,iz)}\right)\frac{1}{\Delta z_{iz+1/2}}\frac{1}{0.5\left(\Delta z_{iz-1/2}+\Delta z_{iz+1/2}\right)},\\
\delta^2_{(ix,iz)} &= 0.5\Delta t\left(k_{(ix,iz-1)}+k_{(ix,iz)}\right)\frac{1}{\Delta z_{iz-1/2}}\frac{1}{0.5\left(\Delta z_{iz-1/2}+\Delta z_{iz+1/2}\right)},\\
\delta^3_{(ix,iz)} &= 0.5\Delta t\left(k_{(ix+1,iz)}+k_{(ix,iz)}\right)\frac{1}{\Delta x_{ix+1/2}}\frac{1}{0.5\left(\Delta x_{ix-1/2}+\Delta x_{ix+1/2}\right)},\\
\delta^4_{(ix,iz)} &= 0.5\Delta t\left(k_{(ix-1,iz)}+k_{(ix,iz)}\right)\frac{1}{\Delta x_{ix-1/2}}\frac{1}{0.5\left(\Delta x_{ix-1/2}+\Delta x_{ix+1/2}\right)}.
\end{aligned}$$

6.6.3 Boundary conditions on the staggered grid

For the heat equation (6.51), we prescribe either the temperature or the heat flux. For the left-hand side boundary, the prescribed temperature condition takes form

$$T = T^{\mathrm{BC}} \qquad T^{0,i}_{(1,iz)} = \left(T^{\mathrm{BC}}\right)^i_{(1,iz)}, \tag{6.52}$$

where T^{BC} is prescribed boundary temperature. The discretization scheme of this condition is in Fig. 6.6**b**. The normal-flux condition on the lhs boundary can be expressed using the virtual point as follows:

$$q_x = -q_x^{\mathrm{BC}} \qquad 0.5\left((q_x)^i_{(1/2,iz)}+(q_x)^i_{(3/2,iz)}\right) = -\left(q_x^{\mathrm{BC}}\right)^i_{(1,iz)}, \tag{6.53}$$

where q_x^{BC} is prescribed boundary value and it is positive in the sense of the outer normal. Similarly to the condition for the normal force (6.38), we do not prescribe this condition directly, however, we substitute it into the heat equation (6.51)

$$\begin{aligned}
&- \delta^1_{(ix,iz)}T^{0,i}_{(ix,iz+1)} - \delta^2_{(ix,iz)}T^{0,i}_{(ix,iz-1)} - 2\delta^3_{(ix,iz)}T^{0,i}_{(ix+1,iz)} +\\
&+ \left(1+\delta^1+\delta^2+2\delta^3\right)_{(ix,iz)}T^{0,i}_{(ix,iz)} = T^{i-1}_{(ix,iz)} +\\
&+ \Delta t\left(\frac{Raq}{Ra}+(H_{\mathrm{A}})^{i-1}_{(ix,iz)}+(H_{\mathrm{S}})_{(ix,iz)}+\frac{q^{\mathrm{BC}}_{x\ (1,iz)}}{\left(\Delta x_{1/2}+\Delta x_{3/2}\right)}\right).
\end{aligned} \tag{6.54}$$

The scheme of this equation is in Fig. 6.6**c**.

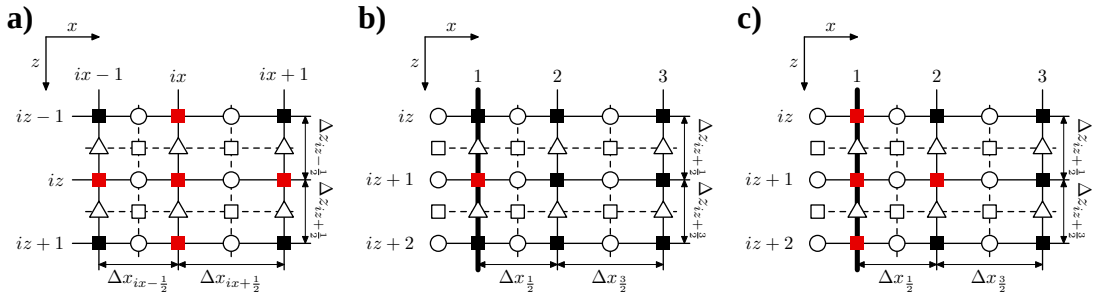

Figure 6.6 Scheme of **a)** the heat equation (6.51) in the point x_{ix}, z_{iz}; scheme of the boundary condition for **b)** prescribed temperature (6.52) and **c)** prescribed normal heat flux (6.54) in point x_1, z_{iz}. Red color marks the points used for the discretization of the heat equations and boundary conditions.

6.6.4 Inversion

As we mentioned above, we have $nx \cdot nz$ unknowns. For these unknowns, we prescribe $(nx-2)(nz-2)$ heat equations (6.51). Moreover, we prescribe $2nx+2nz-4$ boundary condition. Hence, $nx \cdot nz$ equations are solved for $nx \cdot nz$ unknowns. We can reformulate this problem into the matrix problem $\mathbf{C} \cdot \mathbf{y} = \mathbf{d}$, where $\mathbf{y}$ is a vector of unknowns, $\mathbf{d}$ is right-hand side vector and $\mathbf{C}$ is band matrix. The band-width of the matrix $\mathbf{C}$ is $2nx+1$. For the inversion, we again use LU decomposition and LAPACK subroutines.

6.7 Marker technique

Advection part of the heat equation is solved using the marker technique. The temperature markers are distributed evenly in each cell of the primary non-staggered grid. The starting positions of these markers are the same for each time step (after each time step they are put back into their original positions). After finding the solution of the heat equation without heat advection (6.51), the temperature $T^{0,i}$ is interpolated into markers using Eq. (6.10). Hence, we gain the temperature distribution T^i_{im} $im = 1, \ldots, M$ in markers, M is number of markers. Then the markers are moved using the velocity distribution $\mathbf{v}^i$ (section 6.8). Finally, the temperature is interpolated back from the updated position of the markers on the Eulerian grid and new temperature T^i is computed (see section 6.9).

The advective transport equation (5.17) is solved using the chemical markers (each marker carrying the information about chemical component). In each time step, the markers are shifted using the velocity field $\mathbf{v}^i$. From these markers, the chemical concentration can be computed on the Eulerian grid (see section 6.10). Moreover, the chemical markers are used to compute the latent heat (see section 6.8). Contrary to the temperature markers, chemical ones do not return to their original positions in each time step, but they move with the material. Therefore, the distribution of the chemical markers can be insufficient in some cells of the non-staggered grid (Fig. 6.7) after some time. In this case, we have to add some extra chemical markers. Firstly, the position of the new marker is computed randomly in the insufficiently covered cells. (Fig. 6.7, small solid circle). Then all markers in the distance less than l (Fig. 6.7, open circle) are counted. Finally, the resulting chemical component of the new marker is set randomly with probability corresponding to the concentration of the markers in the chosen circle (see Fig. 6.7, splitted circle).

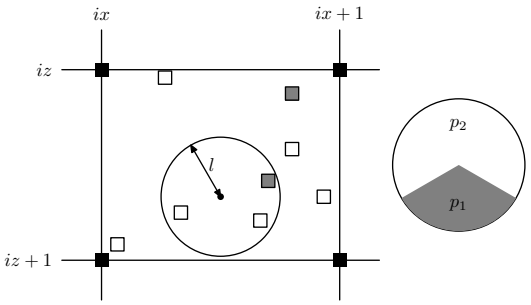

Figure 6.7 Scheme of the addition of the chemical markers.

6.8 Advection of the markers and latent heat

The advection of both temperature and chemical markers is the first order method in time and the fourth order method in space. We use fourth order Runge-Kutta scheme to

compute the displacement and the new position of the marker. For the position of the im^{th} marker, we use following scheme

$$\begin{aligned}
\mathbf{v}_1 &= \mathbf{v}^i(\mathbf{x}^i_{im}),\\
\mathbf{v}_2 &= \mathbf{v}^i(\mathbf{x}^i_{im} + 0.5\Delta t\mathbf{v}_1),\\
\mathbf{v}_3 &= \mathbf{v}^i(\mathbf{x}^i_{im} + 0.5\Delta t\mathbf{v}_2),\\
\mathbf{v}_4 &= \mathbf{v}^i(\mathbf{x}^i_{im} + \Delta t\mathbf{v}_3),\\
\mathbf{x}^{\mathrm{A}}_{im} &= \mathbf{x}^i_{im} + 1/6\Delta t\left(\mathbf{v}_1 + 2\mathbf{v}_2 + 2\mathbf{v}_3 + \mathbf{v}_4\right),
\end{aligned}$$

where $\mathbf{x}^i_{im} = (x^i_{im}, z^i_{im})$ is an original position of the $(im)^{\text{th}}$ marker at the beginning of the i^{th} time step, $\mathbf{x^A}_{im} = (x^{\mathrm{A}}_{im}, z^{\mathrm{A}}_{iz})$ is a position of the marker after advection. Moreover, the relation $\mathbf{x}^{\mathrm{A}} = \mathbf{x}^{i+1}$ holds for the chemical markers. Vector $\mathbf{v}^i$ denotes field of velocity interpolated to the marker using Eq. (6.10).

Since the latent heat can be different for various chemical components, it is computed together with the advection of the chemical markers. Using the relationship (5.13) generalized for $l = 1, \ldots, M_C$ components in dimensionless variables:

$$Q^l_{\mathrm{L}} = \sum_k \frac{Rb_{l,k}}{Ra} Di \left(T + \frac{T_{\mathrm{S}}}{T_{\mathrm{B}} - T_{\mathrm{S}}}\right) \gamma_{l,k} \frac{\mathrm{D}\Gamma_{l,k}}{\mathrm{D}t},$$

where $\bullet_{l,k}$ denotes parameters for the l^{th} material and the k^{th} phase transition in this material. Hence, for the im^{th} marker containing l^{th} material, it can be written

$$(\Delta T)^{Q_{\mathrm{L}}}_{im} = \sum_k \frac{Rb_{l,k}}{Ra} Di \left(T^{0,i}_{im} + \frac{T_{\mathrm{S}}}{T_{\mathrm{B}} - T_{\mathrm{S}}}\right) \gamma_{l,k} \left(\Gamma_{l,k}\left(\mathbf{x}^i_{im}, T^{0,i}\right) - \Gamma_{l,k}\left(\mathbf{x}^{i-1}_{im}, T^{0,i-1}\right)\right), \tag{6.55}$$

where $(\Delta T)^{Q_{\mathrm{L}}}_{im}$ denotes the temperature change caused by all phase transition in the im^{th} marker containing material l. $\Gamma_{l,k}\left(\mathbf{x}^i_{im}, T^{0,i}\right)$ and $\Gamma_{l,k}\left(\mathbf{x}^{i-1}_{im}, T^{0,i-1}\right)$ are phase functions computed for temperatures distributions $T^{0,i}$ and $T^{0,i-1}$ in the points $\mathbf{x}^i_{im}$ and $\mathbf{x}^{i-1}_{im}$, respectively. The phase functions $\Gamma_{l,k}$ are calculated using equations (5.10) and (5.11). The temperature changes caused by latent heat $(\Delta T)^{Q_{\mathrm{L}}}_{im}$ is interpolated from markers on Eulerian grid using Eq. (6.11), hence we get the temperature changes on the Eulerian grid $(\Delta T)^{Q_{\mathrm{L}}}_{(ix,iz)}$.

6.9 Interpolation of temperatures to the Eulerian grid

After advection of the temperature markers, the temperature field has to be interpolated back from the temperature markers to the Eulerian grid. For this interpolation, the formula (6.11) could be used as is done by Gerya and Yuen (2003). However, this relation does not describe the inversion process to the bilinear interpolation from the grid to the markers (6.10). Moreover using this relation (6.11) can cause oscillations of the resulting temperature field $T^i_{(ix,iz)}$ which have to be filtered out. Hence, the method which uses the inverse relationship to the formula (6.10) should be used. The inverse problem in the form $\mathbf{T}^{\mathrm{M}}_{\mathrm{all}} = \mathbf{W}_{\mathrm{all}} \cdot \mathbf{T}_{\mathrm{all}}$ should be solved. Vector $\mathbf{T}^{\mathrm{M}}_{\mathrm{all}}$ denotes temperature in the

markers $\left(T^{\mathrm{M}}_{\mathrm{all}}\right)_{im} = T_{im}$, matrix $\mathbf{W}^{\mathrm{all}}$ contains weights corresponding to Eq. (6.10) and vector $\mathbf{T}_{\mathrm{all}}$ is composed of temperature in the nodal points $T_{in} = T_{if(ix,iz)}$, in is in^{th} component of the vector, if is unique identifier of the nodal point (ix, iz). Therefore, the overdetermined inverse problem (we assume more markers than the nodal points) should be solved. However, this inversion is rather time-demanding. Therefore, we adopt the following scheme, where the inversion is splitted up into series of the inversions. In each cell of the non-staggered grid, we formulate the relation between markers in this cell and the surrounding nodal points as follows

$$\begin{pmatrix} T_1 \\ T_2 \\ \vdots \\ T_{m-1} \\ T_m \end{pmatrix} = \begin{pmatrix} w_{11} & w_{12} & w_{13} & w_{14} \\ w_{21} & w_{22} & w_{23} & w_{24} \\ \vdots & \vdots & \vdots & \vdots \\ w_{(m-1)1} & w_{(m-1)2} & w_{(m-1)3} & w_{(m-1)4} \\ w_{m1} & w_{m2} & w_{m3} & w_{m4} \end{pmatrix} \begin{pmatrix} T_{(ix,iz)} \\ T_{(ix+1,iz)} \\ T_{(ix,iz+1)} \\ T_{(ix+1,iz+1)} \end{pmatrix}, \quad (6.56)$$

$$\begin{aligned} \mathbf{T}^{\mathrm{M}} &= \mathbf{W} \cdot \mathbf{T}, \\ \mathbf{T} &= \left(\mathbf{W}^{\mathrm{T}} \cdot \mathbf{W}\right)^{-1} \cdot \mathbf{W}^{\mathrm{T}} \cdot \mathbf{T}^{\mathrm{M}}. \end{aligned} \quad (6.57)$$

where m is the number of markers in the $(ix, iz)^{\mathrm{th}}$ cell (i.e. all markers satisfying condition $x_{ix} \leq x_{im} \leq x_{ix+1}$ and $z_{iz} \leq z_{im} \leq z_{iz+1}$). For the im^{th} marker, weights $w_{im,(1,\ldots,4)}$ are computed using (6.10). We assume an overdetermined problem ($m > 4$ — more than four markers have to be in the each cell). The vector on the right-hand side contains unknown temperatures in the nodal points. For computing the temperature in the nodal points on the boundaries, we use the virtual markers mirrored around the boundary and temperature in these markers $\left(T^{\mathrm{virt}}_{im}\right)^i$ is prescribed for the lhs boundary as follows

$$\begin{aligned} \text{for prescribed temperature} \quad & 0.5\left(T_{im} + T^{\mathrm{virt}}_{im}\right)^i = T^{\mathrm{BC}} \\ \text{for prescribed normal heat flux} \quad & \frac{0.5}{2\Delta x_{im}}\left(T_{im} - T^{\mathrm{virt}}_{im}\right)^i = -q^{\mathrm{BC}}_x. \end{aligned}$$

For this markers, the inversion (6.57) is also solved. Hence, we solve $(nx+1)(nz+1)$ inverse problems (6.57) and for each nodal point, we get four solutions. The resulting temperature in the nodal points $T^i_{(ix,iz)}$ is calculated by averaging these four solutions and by adding the temperature changes caused by the latent heat $\left(\Delta T^{\mathrm{Q_L}}\right)^i_{(ix,iz)}$.

6.10 Computing concentration and scalar properties

The scalar properties of the fluid are computed in the nodal points of the non-staggered grid (solid squares). In general, we assume that thermal expansion coefficient α, thermal diffusivity k and density variation $\Delta\rho$ depend on the temperature T, depth z, concentration of the l^{th} material c_l and on the phase functions $\Gamma_{l,k}$, i.e. $\Delta\rho = \Delta\rho(T, c_l, \Gamma_{l,k}, z)$. Besides, viscosity η depends also on the second invariant of the strain rate tensor, i.e. $\eta = \eta(T, c_l, \Gamma_{l,k}, z, \dot{\varepsilon}_{\mathrm{II}})$.

The concentration $(c_l)_{(ix,iz)}$ for the l^{th} material is calculated using Eq. (6.11)

$$(c_l)_{(ix,iz)} = \frac{(w_l)_{(ix,iz)}}{w^{\text{all}}_{(ix,iz)}}, \tag{6.58}$$

where $(w_l)_{(ix,iz)}$ is a sum of weights (6.12) over all markers containing the l^{th} chemical component in adjacent cells to the nodal point (ix, iz) and $\left(w^{\text{all}}\right)_{(ix,iz)}$ is a sum of weights (6.12) over all markers in adjacent cells to the nodal point (ix, iz).

The density variation is computed using the equation of state (5.9) and for $l = 1, \ldots, M_C$ components. The density anomaly $(\Delta\rho_{\text{C}})_{(ix,iz)}$ caused by multichemical components can be computed as

$$(\Delta\rho_{\text{C}})_{(ix,iz)} = \left(\sum_l (c_l)_{(ix,iz)} \, Rc_l\right) - \Delta\rho_{\text{C, ref}}(z_{iz}), \tag{6.59}$$

where Rc_l is chemical Rayleigh number for the l^{th} material, z denotes depth and $\Delta\rho_{\text{C, ref}}(z_{iz})$ is chemical reference density at a given depth z_{iz}. For $\mathbf{g} = (0, g_z)$, it is given by

$$\Delta\rho_{\text{C, ref}}(z_{iz}) = \frac{1}{x_{n_x} - x_1} \int_{x_1}^{x_{nx}} \left(\sum_l (c_l)_{(ix,iz)} \, Rc_l\right) \mathrm{d}x.$$

The density variation in the nodal point (ix, iz) caused by the phase transitions can be expressed as follows

$$(\Delta\rho_{\text{ph}})_{(ix,iz)} = \left(\sum_l \sum_k (c_l)_{(ix,iz)} \, Rb_{l,k}\Gamma_{l,k}(x_{ix}, z_{iz})\right) - \Delta\rho_{\text{ph, ref}}(z_{iz}), \tag{6.60}$$

where l denotes the l^{th} material and k denotes the k^{th} phase transition, $Rb_{l,k}$ and $\Gamma_{l,k}$ are phase Rayleigh number and phase function for the k^{th} phase transition in the l^{th} material. $\Delta\rho_{\text{ph, ref}}(z_{iz})$ is phase transitions reference density at a given depth z_{iz}. For $\mathbf{g} = (0, g_z)$, it is given by

$$\Delta\rho_{\text{ph, ref}}(z_{iz}) = \frac{1}{x_{n_x} - x_1} \int_{x_1}^{x_{nx}} \left(\sum_l \sum_k (c_l)_{(ix,iz)} \, Rb_{l,k}\Gamma_{l,k}(x_{ix}, z_{iz})\right) \mathrm{d}x.$$

The temperature density variations $\Delta\rho_T$ are

$$(\Delta\rho_T)_{(ix,iz)} = -\frac{\alpha}{\alpha_0} RaT_{(ix,iz)} - \Delta\rho_{T\ \text{ref}}(z_{iz}), \tag{6.61}$$

where $\Delta\rho_T$ is temperature reference density. For $\mathbf{g} = (0, g_z)$, is given by

$$\Delta\rho_{\text{T, ref}}(z_{iz}) = \frac{1}{x_{n_x} - x_1} \int_{x_1}^{x_{nx}} -\frac{\alpha}{\alpha_0} RaT_{(ix,iz)}) \mathrm{d}x.$$

If we consider constant thermal expansivity, these equations can be rewritten into

$$\begin{aligned} (\Delta\rho_T)_{(ix,iz)} &= -Ra\left(T_{(ix,iz)} - T_{\mathrm{ref}}(z_{iz})\right) \\ T_{\mathrm{ref}}(z_{iz}) &= \frac{1}{x_{n_x} - x_1}\int_{x_1}^{x_{nx}} T_{(ix,iz)})\mathrm{d}x, \end{aligned} \tag{6.62}$$

where T_{ref} is reference temperature (geotherm).

The resulting density variation is given by the sum of contributions (6.59–6.61)

$$\Delta\rho_{(ix,iz)} = (\Delta\rho_{\mathrm{C}})_{(ix,iz)} + (\Delta\rho_{\mathrm{ph}})_{(ix,iz)} + (\Delta\rho_T)_{(ix,iz)}\,. \tag{6.63}$$

Viscosity $\eta_{(ix,iz)}$ is calculated as follows

$$\begin{aligned} \eta_{(ix,iz)}(T, c_l, z) &= \left(\sum_l \left(\frac{c_l}{\eta_l}\right)_{(ix,iz)}\right)^{-1} \\ (\eta_l)_{(ix,iz)} &= f_l(T_{(ix,iz)}, z_{iz}, (\dot{\varepsilon}_{\mathrm{II}})_{(ix,iz)}\,, \Gamma_{l,k}). \end{aligned} \tag{6.64}$$

The resulting viscosity is an inverse value of the sum of reciprocal values of the viscosities η_l with weights c_l. Viscosity of the l^{th} material can be a function (f_l) of temperature, depth, second invariant of the strain rate tensor and phase functions.

6.11 Tests

Before employing the code in mantle slabs modeling, we perform several numerical tests. First three tests (6.11.2–6.11.3) are based on Gerya and Yuen (2003). Moreover, we compare our results with benchmark of the thermal convection codes (Blankenbach et al. 1989) to test our code.

6.11.1 Sinking of rectangular block

The first example demonstrates the ability of our numeric implementation to handle sharp and large viscosity changes. In this test, equations (5.15–5.17) are solved for the heavy

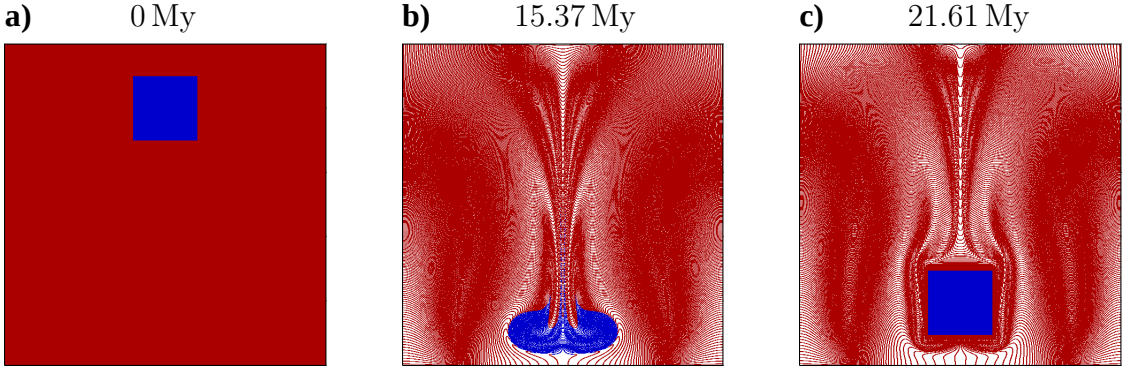

Figure 6.8 Markers distribution (blue — rectangular block, red — surrounding material), **a)** initial distribution of markers, **b)** markers distribution after 15.37 My and viscosity contrast $\eta_{\mathrm{block}}/\eta_0 = 1$, **c)** markers distribution after 21.61 My and viscosity contrast $\eta_{\mathrm{block}}/\eta_0 = 10^6$.

rectangular block falling due to the gravity acceleration $g = 10\,\mathrm{m/s^2}$. On the boundaries, the free-slip conditions are prescribed. The resolution of the staggered grid is 50×50 nodes and we have 25 markers in each cell. The initial conditions are shown in Fig. 6.8**a**. The size of studied area is $500\,\mathrm{km} \times 500\,\mathrm{km}$, the rectangular block measures $100\,\mathrm{km} \times 100\,\mathrm{km}$ and is placed $50\,\mathrm{km}$ below top boundary. The densities of the surrounding material and the rectangular block are $3,200\,\mathrm{kg/m^3}$ and $3,300\,\mathrm{kg/m^3}$, respectively. Viscosity is equal to $\eta_0 = 10^{21}\,\mathrm{Pa \cdot s}$ for surrounding material. The falling block has either the same or higher viscosity. For viscosity contrast between the rectangular block and surrounding material $\eta_{\mathrm{block}}/\eta_0 = 1$, the result is shown in Fig. 6.8**b** after $15.37\,\mathrm{My}$. For the viscosity contrast $\eta_{\mathrm{block}}/\eta_0 = 10^6$, the result after $21.61\,\mathrm{My}$ is plotted in Fig. 6.8**c**. The numerical method is able to successfully solve the problems with sharp viscosity contrast of at least 6 orders of magnitude.

6.11.2 Flow with non-Newtonian rheology

This test demonstrates the behavior of solution with strain-rate dependent rheology. We solve Eqs. (5.15–5.16) in the vertical channel with non-Newtonian rheology and with no gravity. No-slip is prescribed on vertical boundaries and the flow is driven by the vertical pressure gradient $\partial p/\partial z$. The rheology is described by the relation

$$\sigma_{xz} = M \frac{\partial v_z}{\partial x}.$$

The analytical solution (Gerya and Yuen 2003) of this problem is

$$v_z = v_z^0 \left(1 - \left(\frac{2x}{L}\right)^4\right), \quad -\frac{L^4}{64}\left(\frac{\partial p/\partial z}{M}\right)^3$$

$$\eta = \frac{\eta_0}{\left(2x/L - 1\right)^2}, \quad \eta_0 = \frac{4M^3}{\left(\partial p/\partial z L\right)^2}$$

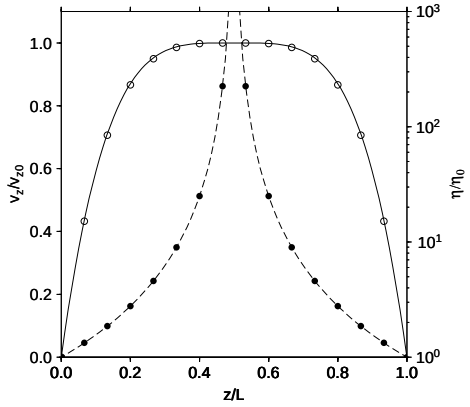

Figure 6.9 Solution for flow with non-Newtonian rheology. Solid circles and dashed lines are numerical and analytical solutions for viscosity. Open circles and solid line show the numerical and analytical solution of the velocity profile across the channel.

Both the analytical solution and the numerical solution for 16-nodes resolution agree very well (Fig. 6.9).

6.11.3 Couette flow with viscous heating

In this test, Eqs. (5.15–5.16) are solved together with the heat equation (5.18) with viscous heating. The equations are solved for the vertical channel without gravity. The vertical pressure gradient $\frac{\partial p}{\partial z}$ is equal to zero. On one vertical boundary, we prescribe velocity $v_z = v_{z0}$ and temperature $T = T_0$. On the other boundary, no-slip $v_z = 0$ and normal heat flux $\frac{\partial T}{\partial x} = 0$ is prescribed. The initial distribution of the temperature is constant. Viscosity

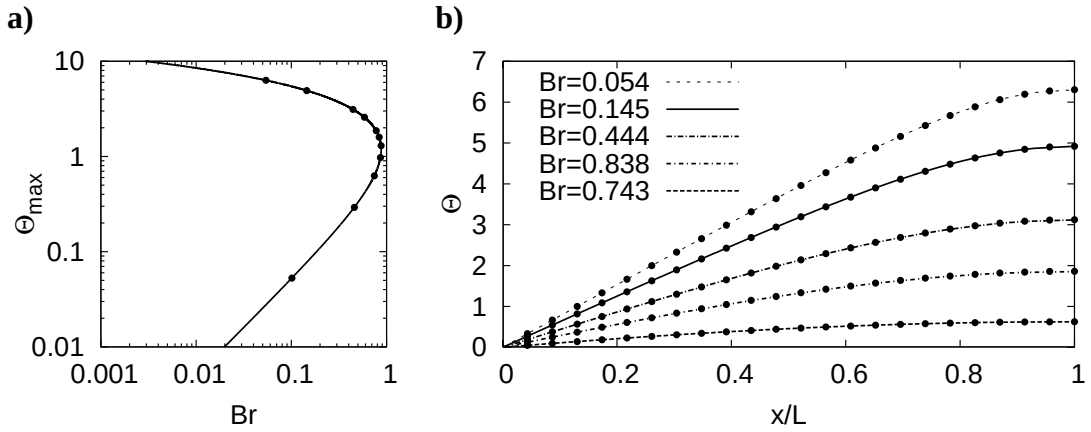

Figure 6.10 Solutions for Couette flow with viscous heating, numerical solutions are marked by solid points, the analytical one with the lines; **a)** dependence of the Brinkman number (for definition see Turcotte and Schubert 2002, p. 317) on the maximum of the dimensionless temperature change $\Theta = {}^{(T-T_0)}/_{T_0}$; **b)** the profile of the dimensionless change of the temperature in the channel for different Brinkman number.

is temperature-dependent

$$\eta = \eta_0 \exp\left[\frac{E}{RT_0}\left(\frac{T_0}{T} - 1\right)\right],$$

where E is activation energy, R denotes gas constant and η_0 is pre-exponential rheological constant. We solve the time evolution problem as long as the temperature profile changes for wide range of flow parameters. We use 24 nodal points and 115 temperature markers. The numerical solution agree with analytical steady-state one see Turcotte and Schubert (2002) (Fig. 6.10).

6.11.4 Thermal convection benchmark

In this test, we compare our results with the benchmark results of Blankenbach et al. (1989), i.e. we solve equations (5.15–5.16) and heat equation (5.18) without adiabatic heating, viscous dissipation and internal heat sources. On the boundaries, free-slip condition is prescribed for system (5.15–5.16). For heat equation (5.18), temperature is prescribed on the horizontal boundaries and zero heat-flux on the vertical boundaries. In the benchmark by Blankenbach et al. (1989), the steady-state problem is solved using various codes and numerical approaches. Here we use our time dependent code and we solve the time evolution of the thermal convection until we get steady solution.

Our tests 1a and 1b are performed for constant viscosity and Rayleigh numbers $Ra = 10^4$ and $Ra = 10^6$, respectively. The results are summarized in Tab. 6.1. For the low Rayleigh number $Ra = 10^4$, the solution converges to the benchmark results when we increase the resolution. The test with the same grid resolution and different numbers of markers per cell (last four rows of Tab. 6.1) shows that the solution is not influenced considerably even if rather low number of markers is used (test for only 9 markers in cell). For high Rayleigh number $Ra = 10^6$, the steady state is reached, however root mean square of velocity is slightly underestimated and Nusselt number (dimensionless mean surface temperature gradient over mean bottom temperature) and temperature gradient in one corner is overestimated. This effect should be eliminated by increasing the resolution.

Test 1a — constant viscosity, $Ra = 10^4$					
resolution	markers	v_{RMS}	Nu	q_1	q_2
Blankenbach et al. (1989)		42–44 (42.80)	5.2–4.5 (4.9)	5-11 (8.1)	0.5–0.8 (0.59)
24×24	64	42.67	5.42	9.15	0.59
36×36	64	42.78	5.13	8.57	0.59
48×48	64	42.81	5.02	8.35	0.59
64×64	64	42.83	4.96	8.22	0.59
48×48	9	42.64	5.02	8.36	0.59
48×48	25	42.82	5.03	8.38	0.59
48×48	144	42.82	5.02	8.34	0.59
48×48	225	42.82	5.02	8.34	0.59
Test 1b — constant viscosity, $Ra = 10^6$					
resolution	markers	v_{RMS}	Nu	q_1	q_2
Blankenbach et al. (1989)		777–979 (833)	18–23 (21.9)	35–55 (46)	0.7–1.1 (0.9)
64×64	64	821.02	27.60	61.68	0.81

Table 6.1 Benchmark for constant viscosity, test 1a is computed for Rayleigh number $Ra = 10^4$, test 1b is for $Ra = 10^6$; v_{RMS} denotes root mean square of the velocity, Nu is Nusselt number, q_1 and q_2 are temperature gradients in the corners near surface; the most frequently values obtained by Blankenbach et al. (1989) are in parentheses.

Test 2a — temperature dependent viscosity, $b = \ln(1,000)$, $c = 0$, $Ra = 10^4$							
resolution	markers	v_{RMS}	Nu	q_1	q_2	q_3	q_4
Blankenbach et al. (1989)		450–520 (480)	9-10.5 (10.0)	14–20 (17.5)	1–1.3 (1.0)	20–31 (32.7)	0.4–0.6 (0.43)
64×64	64	470.1	10.0	17.00	1.05	32.69	0.431
Test 2b — temperature dependent viscosity, $b = \ln(16,384)$, $c = 64$, $Ra = 10^4$							
resolution	markers	v_{RMS}	Nu	q_1	q_2	q_3	q_4
Blankenbach et al. (1989)		170–200 (171)	6–8 (6.93)	12–22 (18.5)	0.15–0.30 (0.17)	13–17 (14.1)	0.2–0.7 (0.61)
48×120	64	170.8	7.26	17.07	0.207	15.40	0.567
64×160	64	171.7	7.15	17.46	0.197	15.18	0.593
120×300	64	175.5	7.12	18.19	0.189	14.70	0.605

Table 6.2 Benchmark for temperature and depth dependent viscosity, test 2a is computed for Rayleigh number at surface $Ra = 10^4$, $b = \ln(1,000)$, $c = 0$, test 2b is computed for Rayleigh number at surface $Ra = 10^4$, $b = \ln(16,384)$, $c = \ln(64)$; v_{RMS} denotes root mean square of the velocity, Nu is Nusselt number, q_1, q_2, q_3 and q_4 are temperature gradients in all corners; the most frequently values obtained by Blankenbach et al. (1989) are in parentheses.

For tests 2a and 2b, the viscosity depends on depth z and temperature T:

$$\eta = \eta_0 \exp\left(-\frac{bT}{\Delta T} + \frac{cz}{h}\right).$$

The surface Rayleigh number is 10^4. Viscosity parameters are $b = \ln(1,000)$, $c = 0$ for test 2a and $b = \ln(16,384)$, $c = \ln(64)$ for test 2a. The results are shown in Tab. 6.2. For both tests 2a and 2b, the solution is in the bounds of results obtained by Blankenbach et al. (1989).

Chapter 7

Long-wavelength slabs in the lower mantle

Recent seismic tomographic models mapping the subduction areas in details provide unique information about the structure of the subducted plates. Interpretation of these heterogeneities is an important issue. From high resolution tomographic models (e.g. Bijwaard et al. 1998, Kárason and van der Hilst 2001), fast seismic anomalies traditionally connected to the subducting plates seem to be significantly thickened after they penetrate into the lower mantle. Further, the plate-like character of the downwelling anomalies vanishes and blob-like features are observed in the lower mantle. This thickening might be an artifact of the tomographic inversion — the relatively thin slabs could be interpreted as thick anomalies due to smearing. However, the authors of the tomographic models pay special attention to this problem. They claim to have a sufficient resolution in the slabs in the lower mantle (see e.g. Ribe et al. 2007). Ribe et al. (2007) found that the width of the slabs may thicken from $50 - 100\,\mathrm{km}$ above the $670\,\mathrm{km}$ boundary up to more than $400\,\mathrm{km}$ below it in Central America and Java zones. Further, they also suggest thickening by factors up to five in the Marianas, Kuril-Kamchatka and Tonga. Such an increase of the wavelengths of the cold downwellings may indeed be required in some geodynamical interpretations of e.g. long-wavelength geoid (Ricard et al. 1993) or long-term variations of the Earth's moment of inertia (Richards et al. 1997).

To be able to explain the slab long-wavelength character (thickening or blobbing of the slabs) in the lower mantle, the subducting plate has to pass through some mechanical barrier. At the depth of $670\,\mathrm{km}$, the significant increase of the viscosity is expected. The increase by factor $10 - 1,000$ is usually accepted (e.g. Hager and Richards 1989, Peltier 1996, Kido and Čadek 1997, Lambeck and Johnston 1998). At this depth, the subducting plate is also passing through the endothermic phase transition which forms another barrier against the slab penetration into the lower mantle (Tackley and Stevenson 1993). Possible mechanisms of the slabs thickening are compression due to the increasing viscous resistance with depth (e.g. Bunge et al. 1996, Čížková and Čadek 1997) or the fluid buckling (Ribe 2003). The compression is, however, supposed to thicken the slab approximately twice (Gurnis and Hager 1988, Gaherty and Hager 1994), therefore it may not be able to explain the tomographic results. The buckling, on the other hand, is supposed to explain even larger thickening (Ribe et al. 2007).

We employ the forward modeling method described in chapter 6 to study the circumstances under which the thickening of the subducting slabs occurs in the lower mantle. The deformation and potential thickening of the subducting plate in the lower mantle depends on several parameters, especially on the rheological properties. Rheology of the mantle material is known to be non-linear but its parameters are rather uncertain especially in the lower mantle. That is why we first concentrate on a simple mechanical model, where the subduction process is only governed by compositional buoyancy (slab is compositionally heavier than the ambient mantle) and the heat equation is not taken into account. Both plate and ambient mantle have constant viscosities, which can vary between the upper and the lower mantle. In this simplified model, we study characteristic behavior of slab deformation depending on the viscosity contrasts. Then we employ the model driven by the thermal anomalies, where the plates are defined purely thermally. The rheology of the mantle material is based on experimental studies of the mantle minerals. Further, the major phase transitions and complex driving mechanism (slab pull, ridge push and mantle drag) are included. In this second model, we study the influence of the plate strength, viscosity jump at $670\,\mathrm{km}$ boundary and boundary conditions.

7.1 Compositional model

7.1.1 Model setup

In this model, equations (5.15–5.17) are solved, i.e. we use chemical convection and the flow is driven only by the chemical buoyancy. The initial setup is shown in Fig. 7.1**a** and detail of the studied area is in Fig. 7.1**b**. In our model slab pull is taken into account, other two driving mechanisms (mantle drag and ridge push) are omitted. The studied area is $2,000\,\mathrm{km}$ deep and $3,000\,\mathrm{km}$ wide. On the bottom and vertical boundaries, the free-flux condition is prescribed (5.22). On the top boundary, the free-slip condition (5.20) is used for $x \leq 1,000\,\mathrm{km}$ and no-slip condition (5.19) for $x > 1,000\,\mathrm{km}$ is used. In horizontal direction, the maximum resolution of the staggered grid is $3\,\mathrm{km}$ for $x \in (900, 1330)\mathrm{km}$, the minimum resolution is $12\,\mathrm{km}$. The expansion of the grid is limited by factor $c = 1.03$ (Eq. 6.9). In vertical direction, the resolution is $3\,\mathrm{km}$ from top down to the depth of $z = 90\,\mathrm{km}$. In the transition zone, the resolution is $10\,\mathrm{km}$ and near the bottom boundary

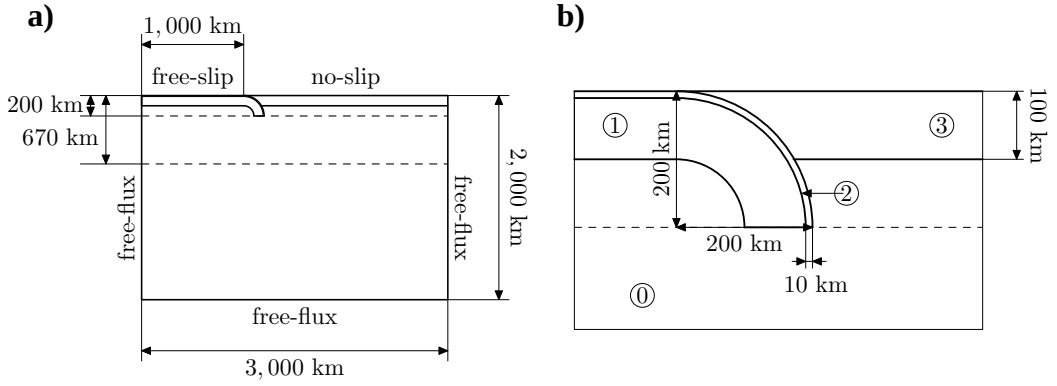

Figure 7.1 Initial setup of the compositional model for **a)** whole area and for **b)** detail, material 0 — surrounding mantle material, 1 — subducting plate, 2 — decoupling layer, 3 — over-riding plate.

ρ_0	reference density	$3,200$	$\mathrm{kg \cdot m^{-3}}$
$\Delta\rho$	density anomaly for material 1, 2 and 3	100	$\mathrm{kg \cdot m^{-3}}$
g_0	gravity acceleration	10	$\mathrm{m \cdot s^{-2}}$
η_0	reference viscosity	10^{21}	$\mathrm{Pa \cdot s}$
η_{UM}	viscosity of mantle (material 0) in the upper mantle	10^{21}	$\mathrm{Pa \cdot s}$
η_{LM}	viscosity of mantle (material 0) in the lower mantle	10^{22-24}	$\mathrm{Pa \cdot s}$
η_{USP}	viscosity of subducting plate (material 1) in the upper mantle	10^{21-23}	$\mathrm{Pa \cdot s}$
η_{LSP}	viscosity of subducting plate (material 1) in the lower mantle	10^{22-24}	$\mathrm{Pa \cdot s}$
η_{DL}	viscosity of decoupling layer (material 2) down to $200\,\mathrm{km}$	10^{21}	$\mathrm{Pa \cdot s}$
η_{OP}	viscosity of over-riding plate (material 3)	10^{25}	$\mathrm{Pa \cdot s}$

Table 7.1 Parameters used for the chemical simulation.

model	η_{UM} $[\mathrm{Pa \cdot s}]$	η_{LM} $[\mathrm{Pa \cdot s}]$	η_{USP} $[\mathrm{Pa \cdot s}]$	η_{LSP} $[\mathrm{Pa \cdot s}]$
C0b0b	10^{21}	10^{22}	10^{21}	10^{22}
C0b1b	10^{21}	10^{22}	10^{22}	10^{23}
C0b2b	10^{21}	10^{22}	10^{23}	10^{24}
C0b2a	10^{21}	10^{22}	10^{23}	10^{23}
C0c2a	10^{21}	10^{24}	10^{23}	10^{23}

Table 7.2 Parameters of the models for chemical convection, viscosity of the surrounding mantle is marked by η_{UM} in the upper and η_{LM} in the lower mantle, viscosity of the subducting plates is η_{USP} in the upper and η_{LSP} in the lower mantle.

the resolution is $60\,\mathrm{km}$. The expansion of the grid is limited by factor $c = 1.03$ and $c = 1.04$ for the upper and the lower mantle, respectively.

In our simulation, we use four different types of the material: material 0 (mantle material) is a reference material, material 1 denotes subducting plate, material 2 describes decoupling layer and material 3 is the over-riding plate. Materials 1 – 3 have negative buoyancy $100\,\mathrm{kg/m^3}$ with respect to the reference mantle material 0. The thickness of the subducting and over-riding plates is $100\,\mathrm{km}$. Decoupling layer thickness is $10\,\mathrm{km}$ and it creates the top part of the subducting plate. This layer insures separation of the subducting and over-riding plate during the subduction process (Fig. 7.1**b**).

The viscosity of both mantle and slab materials can vary between the upper and the lower mantle. The viscosity jump at the $670\,\mathrm{km}$ depth in the slab material can be different than the jump in the mantle material. The mantle material viscosity is equal to $10^{21}\,\mathrm{Pa \cdot s}$ in the upper mantle and it increases by factor $10 - 1,000$ in the lower mantle. The subducting plate material viscosity varies between $10^{21}\,\mathrm{Pa \cdot s}$ and $10^{23}\,\mathrm{Pa \cdot s}$ in the upper mantle and $10^{22} - 10^{24}\,\mathrm{Pa \cdot s}$ in the lower mantle. The decoupling layer viscosity is $10^{21}\,\mathrm{Pa \cdot s}$ down to the depth of $200\,\mathrm{km}$. For greater depths, the strength of the decoupling layer is equal to the strength of the subducting plate. The over-riding plate is rather rigid, its viscosity is $10^{25}\,\mathrm{Pa \cdot s}$. In our parametric study, we change only three parameters — viscosity contrast between the upper and lower mantle materials, contrast between the slab and the mantle materials in the upper mantle and contrast between slab and mantle materials in the lower mantle. All parameters used in the simulations and the model list

are shown in Tabs. 7.1 and 7.2. The models are closely described in paragraph 7.1.2.

7.1.2 Results

The results for all models are shown in Fig. 7.2. In model C0b0b, there is no viscosity contrast between the surrounding mantle material and the subducting plate in both the upper and the lower mantle. The viscosity increases with factor 10 in both the slab and ambient mantle material in the lower mantle. The result after $28\,\mathrm{My}$ of simulation is shown in Fig. 7.2, first row. As expected, the downwelling anomalies do not have plate character. Two downwelling plumes with large heads develop instead. No thickening of the plate occurs in the lower mantle.

In model C0b1b (Fig. 7.2, second row), the viscosity contrast between the plate and the ambient mantle is equal to 10 in both the upper and the lower mantle. At the $670\,\mathrm{km}$ boundary, both plate and mantle viscosities increase also with factor 10. The result after $48\,\mathrm{My}$ of simulation is plotted. The material of the subducting plate is somewhat thickened in the lower mantle. However, its wavelength is still considerably lower than in the tomographic models. During the slab penetration to the lower mantle, the compression regime is observed in the vertical direction under the $670\,\mathrm{km}$ boundary, which causes the thickening (see time evolution in Fig. 7.3). After $48\,\mathrm{My}$, the subduction is dilating in the vertical direction at depths lower than $500\,\mathrm{km}$ and then for $z \in (670, 1100)\mathrm{km}$ (blue areas, Fig. 7.3, second row). The compressional regime is observed under the $670\,\mathrm{km}$ boundary in approximately horizontal direction (red area, Fig. 7.3, third row). In the vicinity of the tip of the subducting plate, the compression occurs in the vertical direction as the plate penetrates into the viscous material.

For the model C0b2b (Fig. 7.2, third row), we again increase the viscosity of the plate in both the upper and the lower mantle to two orders of magnitude in comparison with the mantle material. In this case the plate penetrates to the lower mantle without any significant deformation. After $32\,\mathrm{My}$, when the subduction tip arrives at $670\,\mathrm{km}$ boundary, the material is again under mechanical compression, similarly to the previous model C0b1b. However, this compression is not sufficient to thicken the plate. The horizontal dilatation of the plate already occurs down to depth of $\sim 1,300\,\mathrm{km}$ (Fig. 7.2, third row). For even greater depth, the compression can be observed in the plate in vertical direction.

Model C0b2a (Fig. 7.2, fourth row) differs from model C0b2b by decreased viscosity of the plate by factor 10 in the lower mantle. The results are rather similar to the previous model. The stress regime is not very different, however, the transition between the vertical dilatation and compression in the plate is shifted to lower depths ($z \sim 1,200\,\mathrm{km}$).

In the last model C0c2a (Fig. 7.2, fifth row), the viscosity of the mantle material increases $1,000$ times in the lower mantle. The viscosity of the plate is constant in both the upper and the lower mantle. In this case, the plate is bending. However, no significant thickening is observed. The strong vertical compression occurs both above and under the boundary at $670\,\mathrm{km}$.

To summarize the characteristics in our models, we can observe some thickening of the subducting plate only in the model with relatively low contrast between the subducting plate and the mantle ($\eta_{\mathrm{USP}}/\eta_{\mathrm{UM}} = 10$) and with increase by factor 10 in the lower mantle

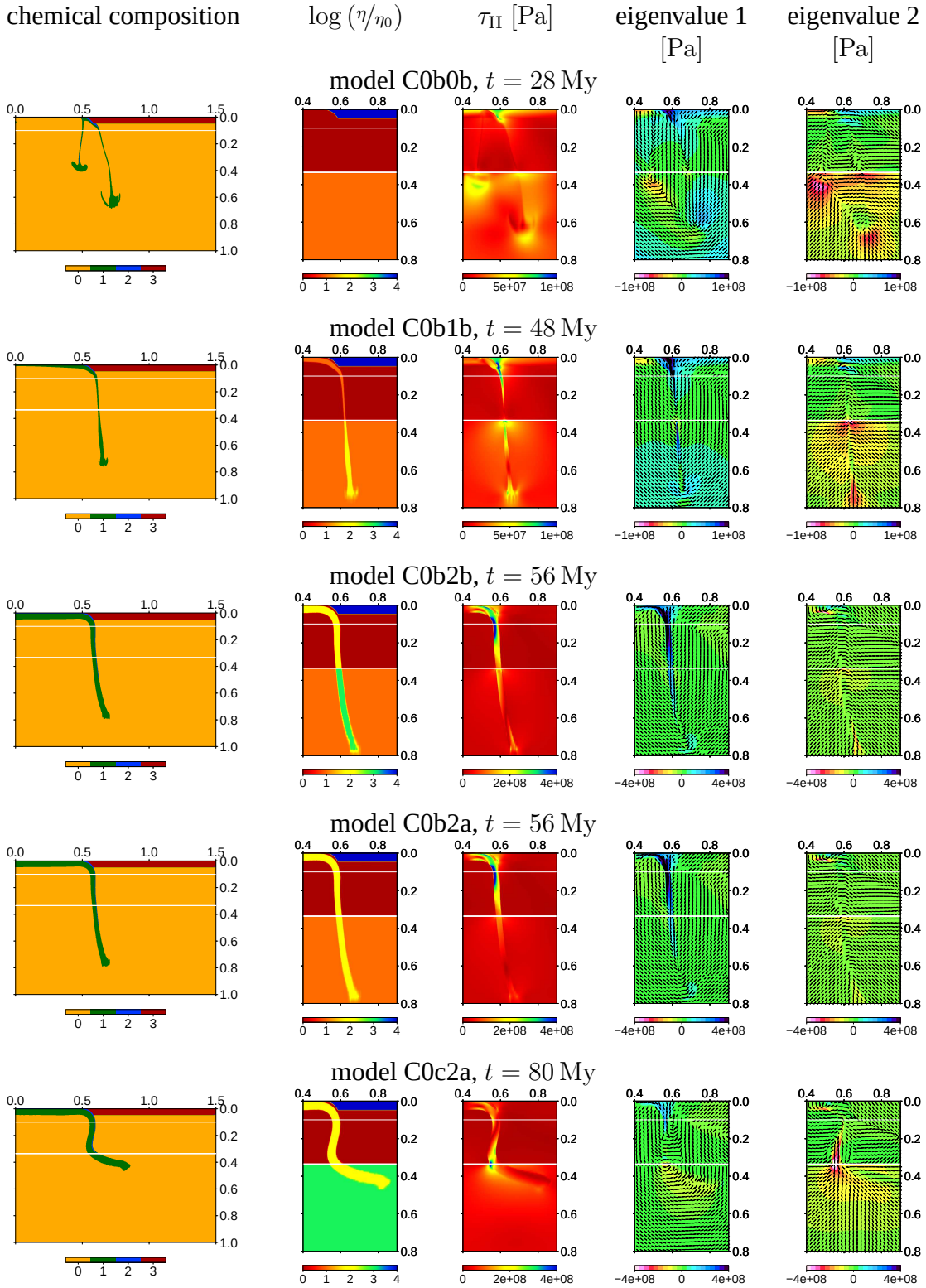

Figure 7.2 Results of chemical convection for model C0b0b (first row), C0b1b (second row), C0b2b (third row), C0b2a (fourth row) and C0c2a (fifth row). The chemical composition (first column) and $1,000\,\mathrm{km}$ wide and $1,600\,\mathrm{km}$ deep detail of relative viscosity in the log scale (second column), second invariant of stress tensor τ_{II} (third column) and eigenvalues and direction of eigenvectors of stress tensor (fourth and fifth columns, axis are marked by lines, amplitudes by color field, blue and red color denote dilatation and compression regimes, respectively) are shown. White lines denote depths of $200\,\mathrm{km}$ and $670\,\mathrm{km}$.

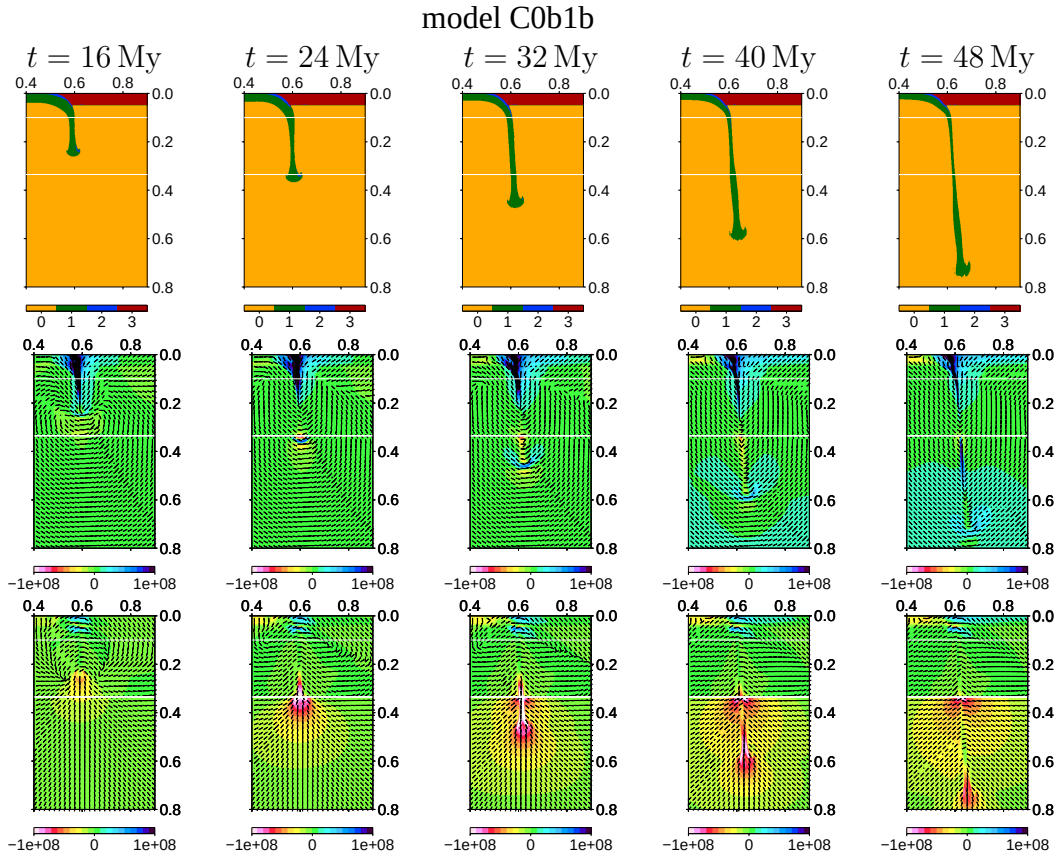

Figure 7.3 The time evolution of the model C0b1b for chemical composition (first row) and eigenvalues and eigenvectors (second and third row). $1,000\,\mathrm{km}$ wide and $1,600\,\mathrm{km}$ deep part of the model domain is shown.

(model C0b1b). The width of the plate increases approximately twice with respect to its upper mantle value. Such thickening is too low to explain the tomographic results. For even higher increase of viscosity in the lower mantle (model C0c2a), the subduction is bending after penetrating the lower mantle, however, no thickening is observed. Clearly some more complex model has to be considered to explain the tomographic observations.

7.2 Thermo-compositional model

7.2.1 Model setup and boundary condition

In this model, we solve Eqs. (5.15–5.18). The model setup is illustrated in Fig. 7.4**a**. The model is $7,000\,\mathrm{km}$ wide and $2,000\,\mathrm{km}$ deep. A ridge is positioned in the left-hand side upper corner. Plate width increases from the ridge to the trench following the half-space cooling model with maximal age $100\,\mathrm{My}$. Hence the ridge push, mantle drag and slab pull are all taken into account. The subducting plate is $5,000\,\mathrm{km}$ long. The over-riding plate is positioned for $x > 5,000\,\mathrm{km}$ and its width corresponds to the $100\,\mathrm{My}$ old plate. On the top of the subducting plate, there is a $10\,\mathrm{km}$ thick layer of relatively weak material. This crust-like layer enables the separation of the subducting and over-riding plates. Its characteristics are, however, quite simple (constant viscosity and no compositional density contrast) compared to complex properties of the real crust. The

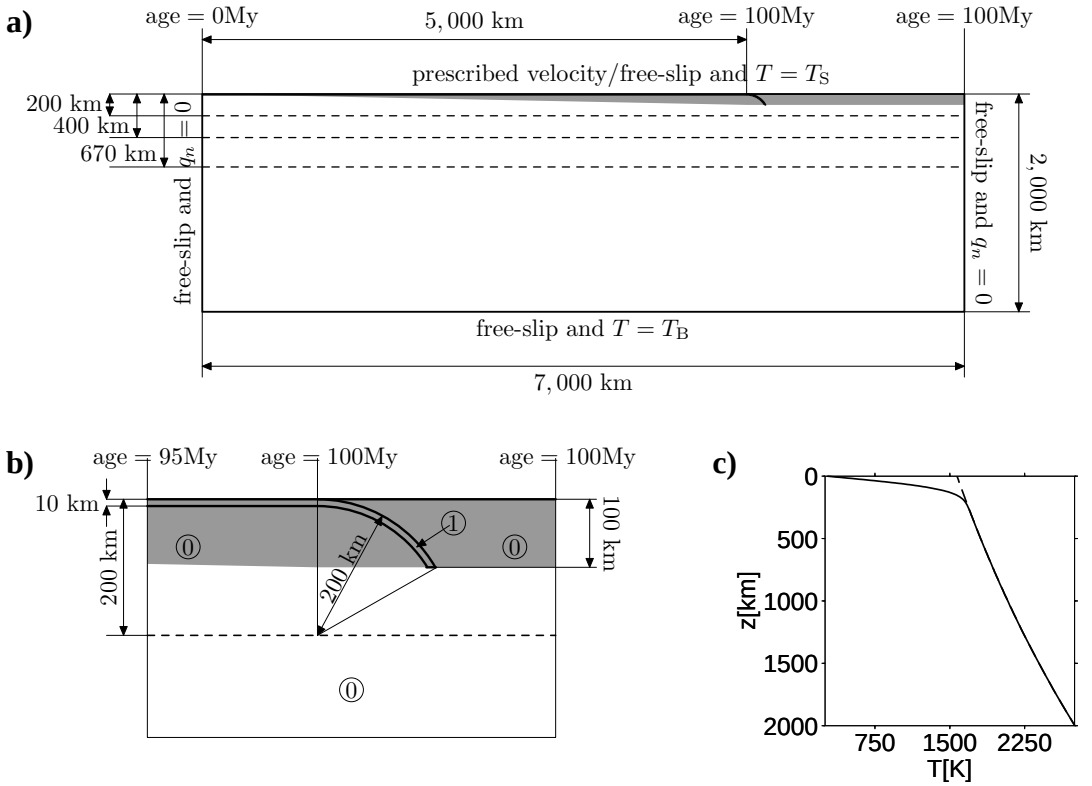

Figure 7.4 Initial setup of the model **a)** for whole area and **b)** for detail, material 0 — mantle material, 1 — decoupling layer; **c)** profile of initial temperature condition for age of the plate $100\,\mathrm{My}$ (solid line) and adiabatic profile for potential temperature $T_{\mathrm{pot}} = 1,573\,\mathrm{K}$ (dashed line).

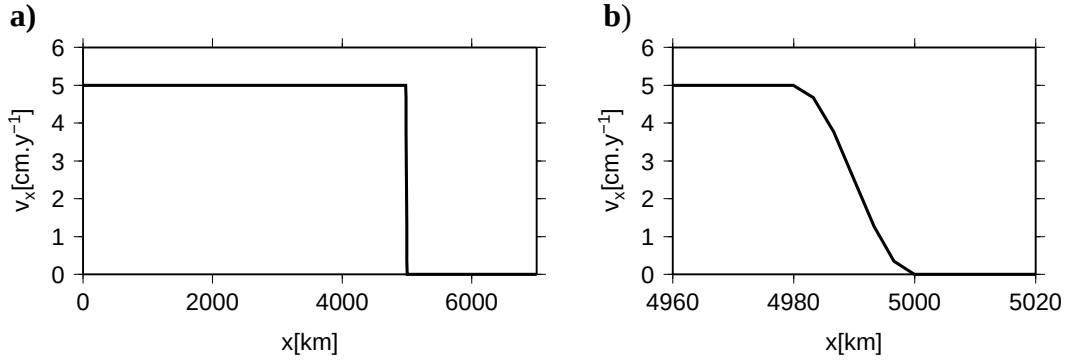

Figure 7.5 Profile of top boundary condition for prescribed velocity, **a)** whole profile, **b)** detail of transition between prescribed velocity and no-slip condition.

geometry of this decoupling layer on the contact between the subducting and the overriding plates is in Fig. 7.4**b**. The initial temperature condition is adiabatic

$$T_{\mathrm{adiab}}(z) = T_{\mathrm{pot}} \exp\left(\frac{\alpha_0 g_0 z}{c_p}\right)$$

with potential temperature $T_{\mathrm{pot}} = 1,573\,\mathrm{K}$ together with half-space cooling. The temperature profile for age $100\,\mathrm{My}$ is in Fig. 7.4**c**.

The resolution of Eulerian grid on the left-hand side is $\sim 40\,\mathrm{km}$, the grid is shrinking with the coefficient $c = 1.03$. Maximum resolution $3.33\,\mathrm{km}$ is reached for $x \in (4,800 - 5,300)\,\mathrm{km}$. Then the grid is expanding with coefficient $c = 1.035$ and the minimum

resolution on the right-hand side is $\sim 50\,\mathrm{km}$. In the vertical direction, the maximum resolution is $3\,\mathrm{km}$ for $z < 90\,\mathrm{km}$. The resolution down to $z = 700\,\mathrm{km}$ is $10\,\mathrm{km}$, the resolution near bottom of the model is $60\,\mathrm{km}$. The expansion of the grid is limited by factors 1.03 and 1.04. In each cell, we have 100 temperature markers and 150 chemical markers at the beginning.

We use the free-slip condition on the left, right and bottom boundaries. On the top boundary, we use either free-slip or prescribed velocity condition. The profile of the prescribed velocity is in Fig. 7.5**a**. The prescribed velocity is $v_x = 5\,\mathrm{cm}\cdot\mathrm{y}^{-1}$ and $v_z = 0\,\mathrm{cm}\cdot\mathrm{y}^{-1}$ for $x < 4,980\,\mathrm{km}$. For $x > 5,000\,\mathrm{km}$, no-slip is prescribed. The width of the transition between prescribed velocity and no-slip is $20\,\mathrm{km}$ (Fig. 7.5**b**). The boundary conditions for the heat equation (5.18) are as follows: on the top boundary the surface temperature T_S (Tab. 7.3) is prescribed except for the left-hand side upper corner, where the potential temperature T_pot is specified. On the bottom boundary, the temperature is T_B. On the left- and right-hand side boundaries, zero heat flux is prescribed. Further, the phase transitions at depth $400\,\mathrm{km}$ and $670\,\mathrm{km}$ are included in this model. All used parameters of the model are in Tab. 7.3.

For the rheological description of mantle material, we use a composite model (van den Berg et al. 1993) including diffusion creep, dislocation creep and power-law stress limiter approximating the strongly non-linear Peierl's creep. Effective viscosity is expressed as follows:

$$\eta_\mathrm{eff} = \left(\frac{1}{\eta_\mathrm{diff}} + \frac{1}{\eta_\mathrm{disl}} + \frac{1}{\eta_\mathrm{y}} + \frac{1}{\eta_\mathrm{max}}\right)^{-1}, \tag{7.1}$$

where η_diff and η_disl are viscosities of the diffusion creep and the dislocation creep, respectively. η_y is the viscosity of the stress-limiting mechanism and η_max is a maximum viscosity introduced to limit viscosity in the coldest shallow parts of the model. Pressure and temperature dependence of the viscosities of the diffusion creep and dislocation creep follow Arrhenius law

$$\eta_\mathrm{diff} = C A_\mathrm{diff}^{-1} \exp\left(\frac{E^*_\mathrm{diff} + pV^*_\mathrm{diff}}{RT}\right), \tag{7.2}$$

$$\eta_\mathrm{disl} = C A_\mathrm{disl}^{-1/n} \dot{\varepsilon}_\mathrm{II}^{(1-n)/n} \exp\left(\frac{E^*_\mathrm{disl} + pV^*_\mathrm{disl}}{nRT}\right). \tag{7.3}$$

Stress limiter viscosity η_y is calculated using

$$\eta_\mathrm{y} = C\sigma_\mathrm{y}\dot{\varepsilon}_\mathrm{y}^{-1/n_\mathrm{y}}\dot{\varepsilon}_\mathrm{II}^{1/n_\mathrm{y}-1}. \tag{7.4}$$

Stress-limiter replaces effectively Peierl's mechanism — low temperature plasticity (Kameyama et al. 1999). If power-law index n_y is 1, this mechanism describes the viscosity limit. For $n_\mathrm{y} \to \infty$, the maximum stress is limited to the σ_y regardless the yield strain rate $\dot{\varepsilon}_\mathrm{y}$. Here we use $n_\mathrm{y} = 5$, therefore, our stress-limiting functional description is in fact a strongly non-linear dislocation creep. Two values of the yield stress — $\sigma_\mathrm{y} = 0.1\,\mathrm{GPa}$ or $1\,\mathrm{GPa}$ are taken into account. Two values of the viscosity of the decoupling layer 10^{19} or $10^{21}\,\mathrm{Pa}\cdot\mathrm{s}$ are tested. At the depths higher than $200\,\mathrm{km}$, the decoupling layer material has the same rheological properties as the mantle material. The viscosity within the studied area varies between 10^{19} and $10^{28}\,\mathrm{Pa}\cdot\mathrm{s}$, hence the viscosity changes are approximately 9 orders of magnitude.

gravity acceleration	g_0	10	$\mathrm{m \cdot s^{-2}}$
height of the model domain	d	$2,000$	km
surface temperature	T_S	273	K
bottom temperature	T_B	$2,753$	K
potential temperature	T_pot	$1,573$	K
reference density	ρ_0	$3,400$	$\mathrm{kg \cdot m^{-3}}$
thermal conductivity	k	5	$\mathrm{W \cdot m^{-1} \cdot K^{-1}}$
heat capacity	$\mathrm{c_p}$	$1,250$	$\mathrm{J \cdot kg^{-1} \cdot K^{-1}}$
thermal expansivity	α	$3.5 \cdot 10^{-5}$	$\mathrm{K^{-1}}$
plate velocity	v_x	5	$\mathrm{cm \cdot y^{-1}}$
molar gas constant	R	8.3143	$\mathrm{J \cdot K^{-1} \cdot mol^{-1}}$
maximum viscosity	η_max	10^{28}	$\mathrm{Pa \cdot s}$
reference viscosity	η_0	10^{21}	$\mathrm{Pa \cdot s}$
upper mantle parameters:[1]			
pre-exponential parameter of diffusion creep	A_diff	$1.92 \cdot 10^{-10}$	$\mathrm{Pa^{-1} \cdot s^{-1}}$
activation energy for diffusion creep	E^*_diff	$300 \cdot 10^3$	$\mathrm{J \cdot mol^{-1}}$
activation volume for diffusion creep	V^*_diff	$6.0 \cdot 10^{-6}$	$\mathrm{m^3 \cdot mol^{-1}}$
pre-exponential parameter of dislocation creep	A_disl	$2.42 \cdot 10^{-16}$	$\mathrm{Pa^{-n} \cdot s^{-1}}$
activation energy for dislocation creep	E^*_disl	$540 \cdot 10^3$	$\mathrm{J \cdot mol^{-1}}$
activation volume for dislocation creep	V^*_disl	$15 \cdot 10^{-6}$	$\mathrm{m^3 \cdot mol^{-1}}$
power-law stress exponent	n	3.5	
lower mantle parameters:[2]			
pre-exponential parameter of diffusion creep	A_diff	$3.65 \cdot 10^{-15}$	$\mathrm{Pa^{-1} \cdot s^{-1}}$
activation energy for diffusion creep	E^*_diff	$208 \cdot 10^3$	$\mathrm{J \cdot mol^{-1}}$
activation volume for diffusion creep	V^*_diff	$2.5 \cdot 10^{-6}$	$\mathrm{m^3 \cdot mol^{-1}}$
pre-exponential parameter of dislocation creep	A_disl	$6.63 \cdot 10^{-32}$	$\mathrm{Pa^{-n} \cdot s^{-1}}$
activation energy for dislocation creep	E^*_disl	$285 \cdot 10^3$	$\mathrm{J \cdot mol^{-1}}$
activation volume for dislocation creep	V^*_disl	$1.37 \cdot 10^{-6}$	$\mathrm{m^3 \cdot mol^{-1}}$
power-law stress exponent	n	3.5	
yield stress	σ_y	10^8, 10^9	Pa
reference strain rate in yield strength determination	$\dot{\varepsilon}_y$	10^{-15}	$\mathrm{s^{-1}}$
yield stress exponent	n_y	5	
viscosity of decoupling layer	η_DL	10^{19}, 10^{21}	$\mathrm{Pa \cdot s}$
pre-factor coefficient in the upper mantle	C	1	
pre-factor coefficient in the lower mantle	C	1, 10, 30	
Clapeyron slope 400 km phase transition[3]	γ_{400}	3.0	$\mathrm{MPa \cdot K^{-1}}$
density difference across 400 km phase transition[4]	$\Delta\rho_{400}$	273	$\mathrm{kg \cdot m^{-3}}$
Clapeyron slope 670 km phase transition[3]	γ_{670}	-2.5	$\mathrm{MPa \cdot K^{-1}}$
density difference across 670 km phase transition[4]	$\Delta\rho_{670}$	342	$\mathrm{kg \cdot m^{-3}}$
width of all phase transitions	d_ph	5	km

[1] adapted from Karato and Wu (1993)
[2] Yamazaki and Karato (2001), Frost and Ashby (1982), see text for details
[3] Bina and Helffrich (1994)
[4] Steinbach and Yuen (1995)

Table 7.3 Parameters used for thermo-chemical convection.

The rheological parameters such as the activation energy E^*, activation volume V^*, pre-exponential parameters A and viscosity stress-exponent n are listed in Tab. 7.3. We use different parameters for the upper and the lower mantle. For the upper mantle (UM), the parameters adapted from Karato and Wu (1993) are used. The scaling pre-factor C in Eqs. (7.2)–(7.4) is equal to 1. In the lower mantle (LM), the parameters are less constrained. Here we use parameters based on Yamazaki and Karato (2001) and Frost and Ashby (1982). They both use viscosity parametrization based on homologous temperature. We estimate our activation parameters by fitting their viscosity curves. Pre-exponential parameters $A^{\mathrm{LM}}_{\mathrm{diff}}$ and $A^{\mathrm{LM}}_{\mathrm{disl}}$ are computed from conditions $\eta^{UM}_{\mathrm{diff}}(670\,\mathrm{km}) = \eta^{LM}_{\mathrm{diff}}(670\,\mathrm{km})$ and $\eta^{UM}_{\mathrm{disl}}(670\,\mathrm{km}) = \eta^{LM}_{\mathrm{disl}}(670\,\mathrm{km})$. Further, we use scaling factors $C = 1, 10, 30$ from Eqs. (7.2)–(7.4) in the lower mantle. Hence, this factor defines the viscosity jump at $670\,\mathrm{km}$ boundary.

The effective viscosity and its decomposition is demonstrated in Figs. 7.6 and 7.7. In Fig. 7.6, the vertical profiles of viscosity after first time step are shown. At shallow depths (approximately uppermost $100\,\mathrm{km}$), the stress limiter controls the deformation in the cold subducting plate (Fig. 7.6**a–b**). Below the subducting plate, the dislocation creep is prevailing (Fig. 7.6**a–b**) though its viscosity is only slightly lower than the viscosity of the diffusion creep. In the rest of the mantle, the diffusion creep viscosity prevails. In the lower mantle, the viscosity is almost constant. The viscosity is rather low $\sim 4 \cdot 10^{21}\,\mathrm{Pa \cdot s}$ (Fig. 7.6**a**) if no additional jump is assumed in the lower mantle ($C = 1$). If the viscosity jump is $C = 10$ (Fig. 7.6**b**), the diffusion creep viscosity increases with factor 10 in comparison with model without viscosity jump (cf. Fig. 7.6**a**). On the other hand, the dislocation creep and stress limiter viscosity can increase more than 10 times due to non-linearity — the second invariant of strain rate tensor decreases due to high viscosity.

The decomposition of the effective viscosity is demonstrated in a model with higher stress limit $\sigma_{\mathrm{y}} = 1\,\mathrm{GPa}$ and viscosity jump $C = 10$ (Fig. 7.7). The logarithm of relative effective viscosity and prevailing mechanism are in Fig. 7.7**a–b**. Two horizontal viscosity profiles in the upper mantle are given in Fig. 7.7**c–d**. In the subducting plate, the stress limiter controls the viscosity. In the over-riding plate, the viscosity limit dominates because of small deformation (the second invariant of strain rate tensor is low). In the material surrounding the subducting plate, the dislocation creep prevails. In the rest of the upper mantle, the diffusion creep mechanism controls the viscosity. Similar viscosity decomposition for one lower mantle horizontal profile is given in Fig. 7.7**e**. The dislocation creep prevails in the subducting plate and around it, elsewhere the diffusion creep mechanism controls viscosity.

Here we concentrate on the influence of the viscosity jump between the upper and the lower mantle ($C = 1, 10, 30$). Further, we study the effects of the boundary conditions, the viscosity of the decoupling layer $\eta_{\mathrm{DL}} = 10^{19}$ or $10^{21}\,\mathrm{Pa \cdot s}$ and stress limiter $\sigma_{\mathrm{y}} = 0.1$ or $1\,\mathrm{GPa}$. The list of the models is in Tab. 7.4.

7.2.2 Results

Here, we discuss the results obtained in the series of models. We sort the models by the value of stress limiter ($\sigma_{\mathrm{y}} = 0.1$ and $1\,\mathrm{GPa}$) and by the value of the viscosity of the decoupling layer ($\eta_{\mathrm{DL}} = 10^{19}$ and $10^{21}\,\mathrm{Pa \cdot s}$).

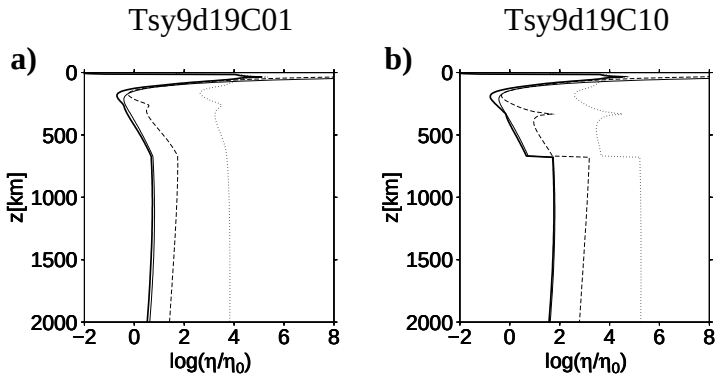

Figure 7.6 Vertical viscosity profiles for $x = 4,800\,\mathrm{km}$ after the first time step for models **b)** Tsy9d19C01 and **b)** Tsy9d19C10. The effective viscosity η_{eff} is marked by thick solid line, diffusion-creep viscosity η_{diff} by thin solid line, dislocation-creep viscosity η_{disl} by dashed line and stress limit viscosity η_y by dotted line.

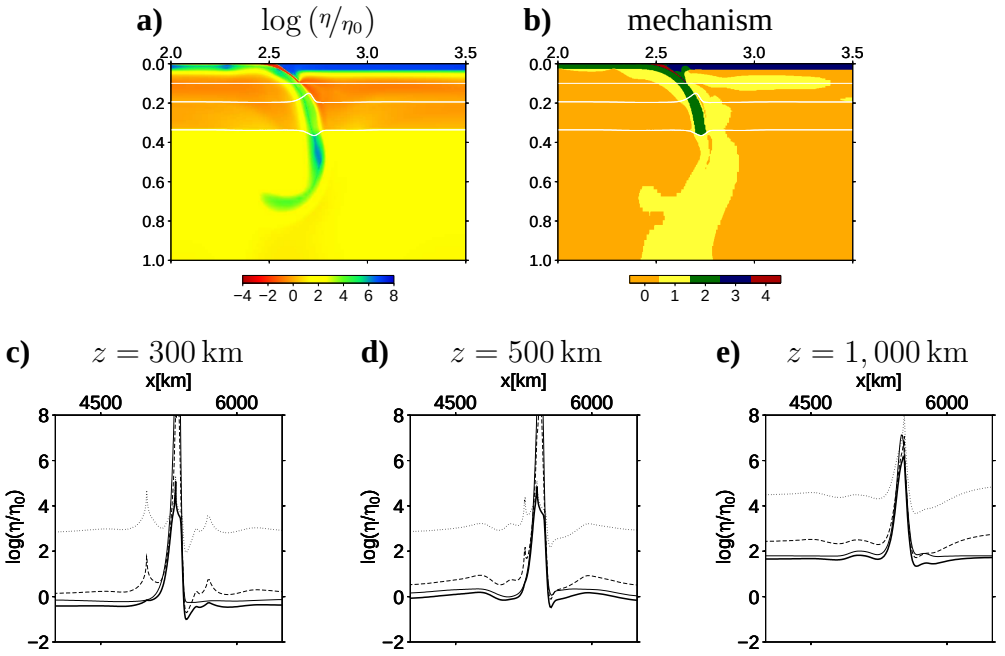

Figure 7.7 Example of viscosity decomposition and horizontal viscosity profiles for model Tsy9d19C10_v after $63\,\mathrm{My}$. For $2,000\,\mathrm{km}$ deep and $3,000\,\mathrm{km}$ wide part, **a)** logarithm of relative effective viscosity $\log(\eta/\eta_0)$, **b)** prevailing deformation mechanism (0 — diffusion creep, 1 — dislocation creep, 2 — stress-limiter, 3 — viscosity limit, 4 — decoupling layer for $z > 200\,\mathrm{km}$). White lines denote the depth of $200\,\mathrm{km}$ and phase transitions at $400\,\mathrm{km}$ and $670\,\mathrm{km}$. Horizontal profiles of viscosity at depth **c)** $300\,\mathrm{km}$, **d)** $500\,\mathrm{km}$ and **e)** $1,000\,\mathrm{km}$. The effective viscosity η_{eff} is marked by thick solid line, diffusion-creep viscosity η_{diff} by thin solid line, dislocation-creep viscosity η_{disl} by dashed line and stress limit viscosity η_y by dotted line.

model	σ_y [Pa]	η_{DL} [Pa · s]	C	boundary condition
Tsy8d19C01_v	10^8	10^{19}	1	prescribed velocity
Tsy8d19C10_v	10^8	10^{19}	10	prescribed velocity
Tsy8d19C30_v	10^8	10^{19}	30	prescribed velocity
Tsy8d19C01_fs00	10^8	10^{19}	1	free-slip
Tsy8d19C10_fs00	10^8	10^{19}	10	free-slip
Tsy8d19C30_fs00	10^8	10^{19}	30	free-slip
Tsy8d21C01_v	10^8	10^{21}	1	prescribed velocity
Tsy8d21C10_v	10^8	10^{21}	10	prescribed velocity
Tsy8d21C30_v	10^8	10^{21}	30	prescribed velocity
Tsy8d21C01_fs10	10^8	10^{21}	1	prescribed velocity ($t < 10\,\mathrm{My}$), free-slip ($t > 10\,\mathrm{My}$)
Tsy8d21C10_fs10	10^8	10^{21}	10	prescribed velocity ($t < 10\,\mathrm{My}$), free-slip ($t > 10\,\mathrm{My}$)
Tsy8d21C30_fs10	10^8	10^{21}	30	prescribed velocity ($t < 10\,\mathrm{My}$), free-slip ($t > 10\,\mathrm{My}$)
Tsy9d19C01_v	10^9	10^{19}	1	prescribed velocity
Tsy9d19C10_v	10^9	10^{19}	10	prescribed velocity
Tsy9d19C30_v	10^9	10^{19}	30	prescribed velocity
Tsy9d19C01_fs08	10^9	10^{19}	1	prescribed velocity ($t < 8\,\mathrm{My}$), free-slip ($t > 8\,\mathrm{My}$)
Tsy9d19C10_fs08	10^9	10^{19}	10	prescribed velocity ($t < 8\,\mathrm{My}$), free-slip ($t > 8\,\mathrm{My}$)
Tsy9d19C30_fs08	10^9	10^{19}	30	prescribed velocity ($t < 8\,\mathrm{My}$), free-slip ($t > 8\,\mathrm{My}$)
Tsy9d21C01_v	10^9	10^{21}	1	prescribed velocity
Tsy9d21C10_v	10^9	10^{21}	10	prescribed velocity
Tsy9d21C30_v	10^9	10^{21}	30	prescribed velocity
Tsy9d21C01_fs08	10^9	10^{21}	1	prescribed velocity ($t < 8\,\mathrm{My}$), free-slip ($t > 8\,\mathrm{My}$)
Tsy9d21C10_fs08	10^9	10^{21}	10	prescribed velocity ($t < 8\,\mathrm{My}$), free-slip ($t > 8\,\mathrm{My}$)
Tsy9d21C30_fs08	10^9	10^{21}	30	prescribed velocity ($t < 8\,\mathrm{My}$), free-slip ($t > 8\,\mathrm{My}$)

Table 7.4 Models description for thermo-chemical convection.

Models with lower stress limit and weaker decoupling layer

The models with lower stress limit $\sigma_{\mathrm{y}} = 0.1\,\mathrm{GPa}$ and weaker decoupling layer $\eta_{\mathrm{DL}} = 10^{19}\,\mathrm{Pa}\cdot\mathrm{s}$ are in Fig. 7.8 for prescribed velocity and in Fig. 7.9 for free-slip boundary condition. In these cases, the ridge push exceeds the friction on the plates contact and internal resistance against bending and hence the plate starts to subduct on its own with a free-slip condition prescribed on the top from the beginning of the calculation (contrary to the models which are discussed later). In all models, the subduction process is accelerated during passing the exothermic phase transition at $400\,\mathrm{km}$ (cf. Figs. 7.8 and Fig. 7.9, third column). Then the velocities of the subducting plates decrease due to the mechanical resistance — the plate is passing through the endothermic phase transition and in some models also the viscosity increases there. The plate velocity evolution differs between the models after the plates penetrate into the lower mantle. In the models with prescribed velocity at the top, the plate velocity is partly controlled by the boundary condition at the surface. However, velocity differentiation within the plate is observed due to the weak decoupling layer. That means that the velocity differs significantly in the individual layers of the crust. In the underlying slab, horizontal velocity does not change substantially with

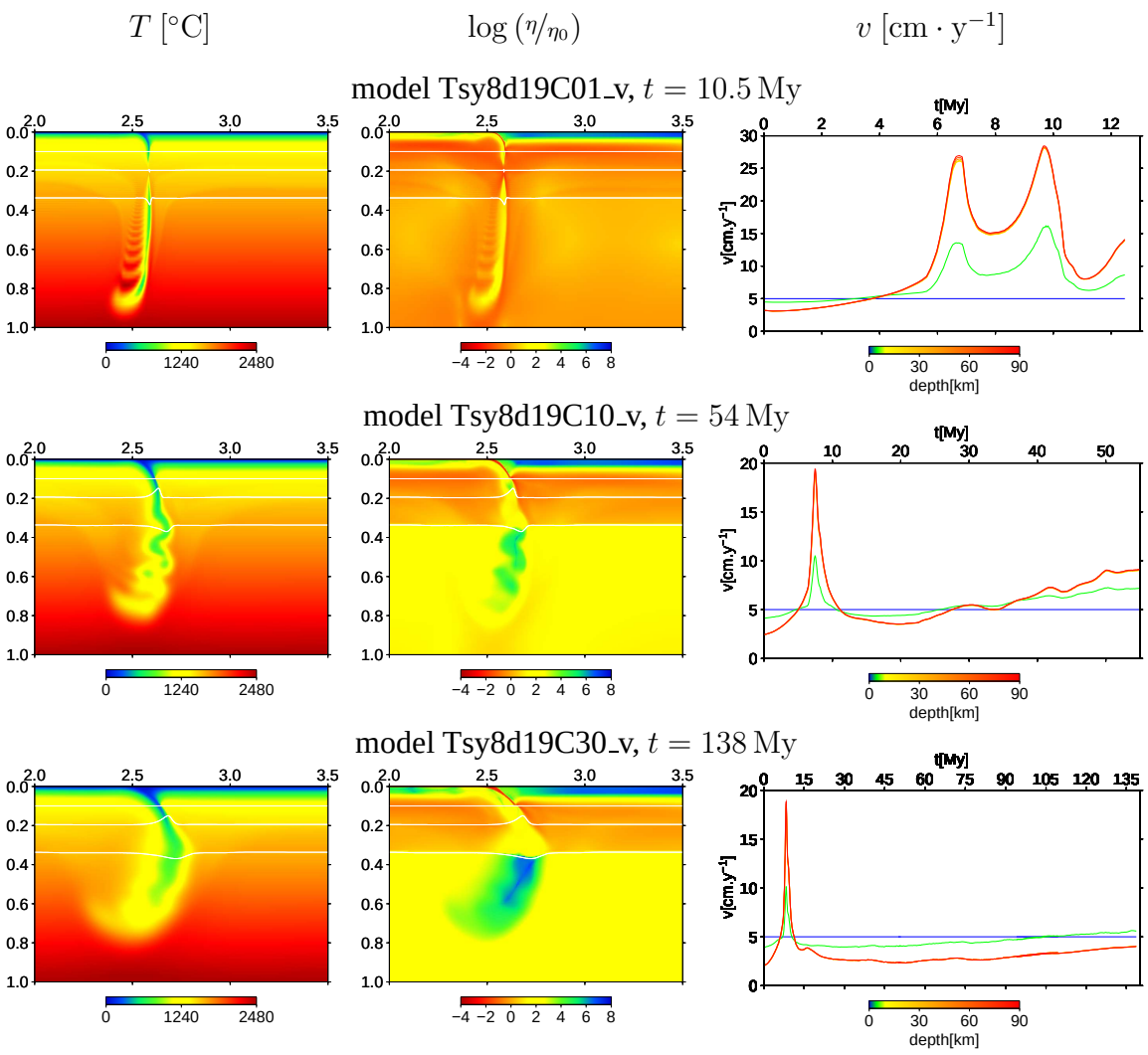

Figure 7.8 Results for models with stress limit $\sigma_y = 0.1\,\mathrm{GPa}$ and decoupling viscosity $\eta_{\mathrm{DL}} = 10^{19}\,\mathrm{Pa}\cdot\mathrm{s}$. On the top boundary, velocity is prescribed. In a $2,000\,\mathrm{km}$ deep and $3,000\,\mathrm{km}$ wide part of the model domain, the temperature (first column) and decadic logarithm of relative viscosity (second column) are shown. The time evolution of the plate velocity at the points with $x = 4,800\,\mathrm{km}$ and depth (marked by color) $z = 0$, 5, 15, 25, 45, 65 and $85\,\mathrm{km}$ is plotted in the third column.

depth up to $\sim 100\,\mathrm{km}$. In the models with free-slip boundary condition, the velocity differentiation in the crust is much weaker. The velocities in the plates in models with free-slip are considerably higher than in the model with prescribed velocity. This means that even if the decoupling layer is weak, the velocity is still partly controlled by the boundary condition.

The results for model (Tsy8d19C01_v) with prescribed velocity and no viscosity jump ($C = 1$) are in Fig. 7.8, first row. In this model, the plate penetrates into the lower mantle without significant deformation. After passing into the lower mantle, the plate velocity accelerates until the plate is detached. Then the new cycle begins. Model with prescribed free-slip condition (Tsy8d19C01_fs00) is plotted in Fig. 7.9, first row. After penetrating into the lower mantle, the plate is accelerated due to its negative buoyancy until the bottom of the studied area is reached. In this case, the velocity within the plate is unrealistically

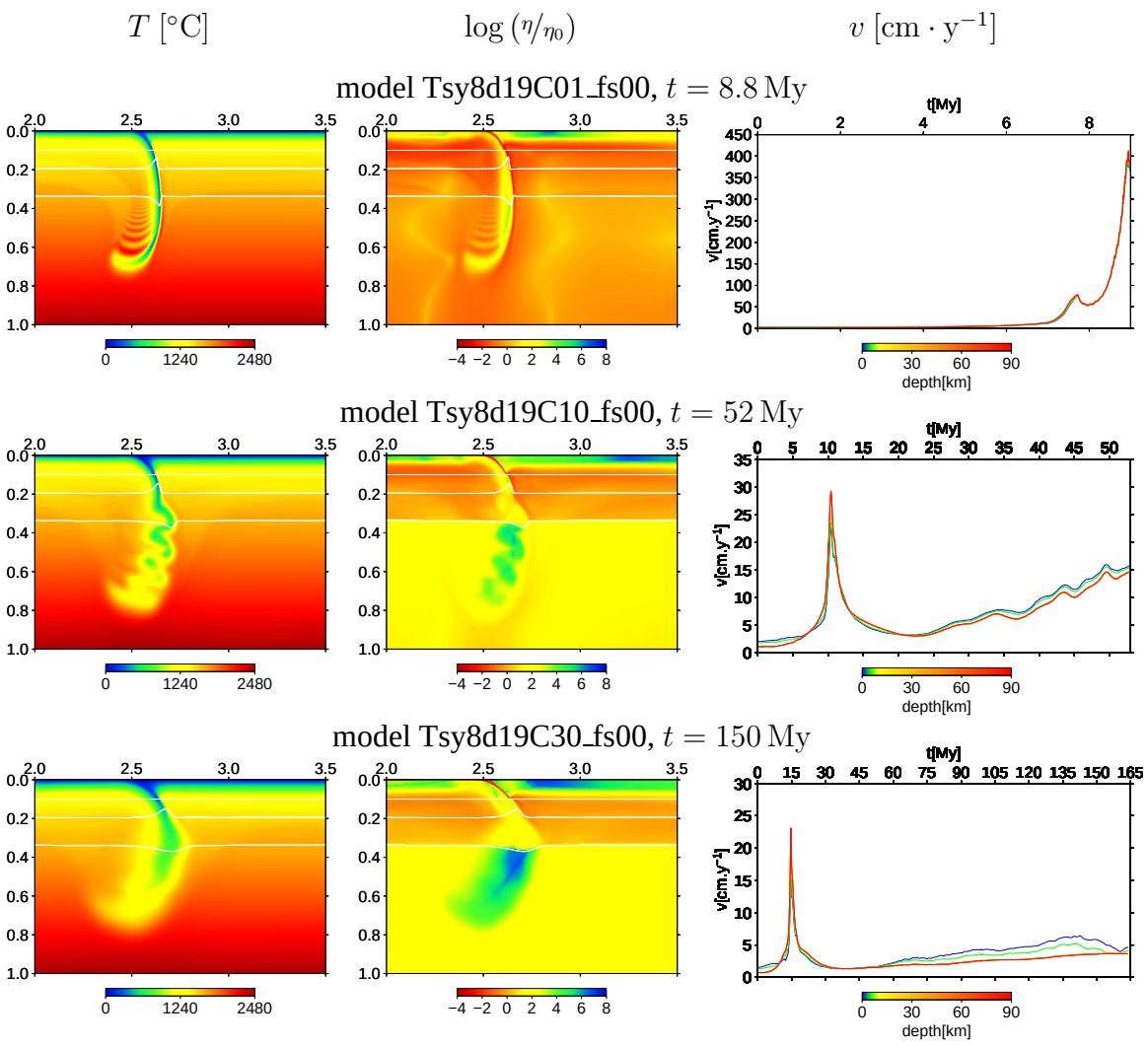

Figure 7.9 Results for models with stress limit $\sigma_y = 0.1\,\mathrm{GPa}$ and decoupling material viscosity $\eta_{\mathrm{DL}} = 10^{19}\,\mathrm{Pa}\cdot\mathrm{s}$. On the top boundary, free-slip condition is prescribed. In a $2,000\,\mathrm{km}$ deep and $3,000\,\mathrm{km}$ wide part of the model domain, the temperature (first column) and decadic logarithm of relative viscosity (second column) are shown. The time evolution of the plate velocity at the points with $x = 4,800\,\mathrm{km}$ and depth (marked by color) $z = 0$, 5, 15, 25, 45, 65 and $85\,\mathrm{km}$ is plotted in the third column.

high and the velocity in the crust is not differentiated. In both above discussed models, the plates remain thin and they are not deformed significantly in the lower mantle. Further, in these models, the numerical oscillations occur due to the high velocities within the mantle.

The models with viscosity increase $C = 10$ (Tsy8d19C10_v and Tsy8d19C10_fs00) are in Figs. 7.8 and 7.9, second row. In both models, rather large deformations (buckling) of the material are observed in the lower mantle. The buckling is slightly stronger in model Tsy8d19C10_fs00. The plate velocities (Figs. 7.8 and 7.9, third column) have similar characteristics as we described above. Further, after the tips of the plates penetrate into the lower mantle, the velocity of the subduction is increasing due to the increasing slab pull and the small oscillations occur due to the buckling.

So far, we have discussed slab morphologies in different models in one time-step. Let

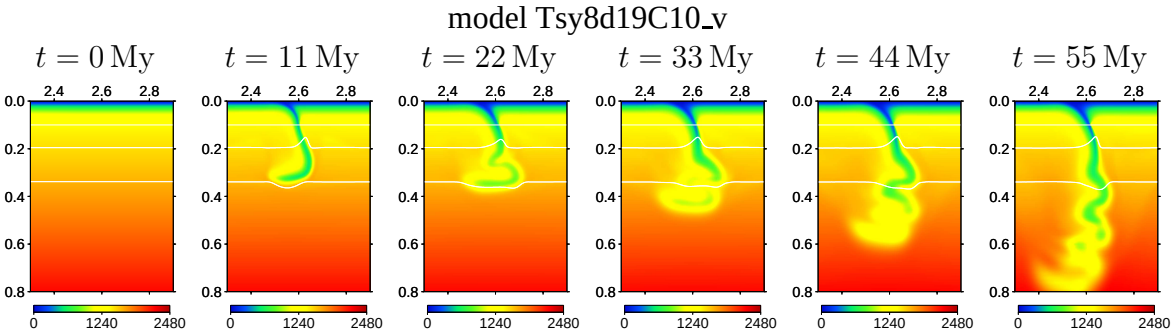

Figure 7.10 Model Tsy8d19C10_v: time evolution of temperature $[^\circ\mathrm{C}]$, $1,600\,\mathrm{km}$ deep and $1,200\,\mathrm{km}$ wide part of the model domain is shown.

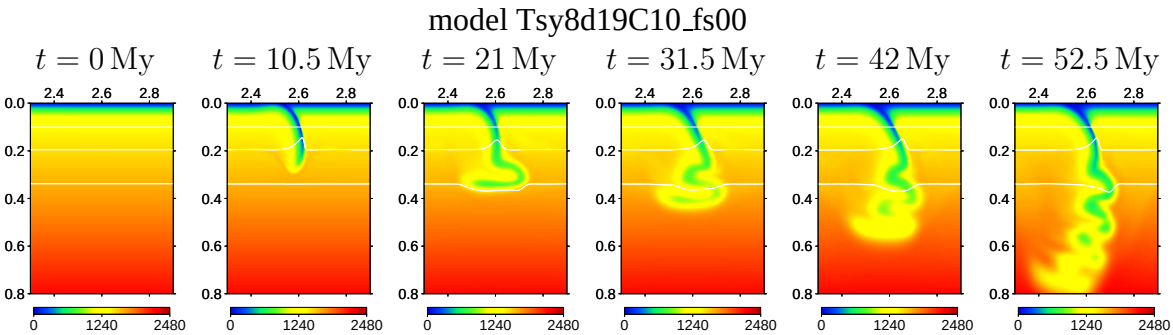

Figure 7.11 Model Tsy8d19C10_fs00: time evolution of temperature $[^\circ\mathrm{C}]$, $1,600\,\mathrm{km}$ deep and $1,200\,\mathrm{km}$ wide part of the model domain is shown.

us now illustrate the evolution of the slab in two models with different boundary conditions — prescribed velocity (Tsy8d19C10_v, Fig. 7.10) and free-slip (Tsy8d19C10_fs00, Fig. 7.11). Both models are developing rather similarly. In the model with free-slip boundary condition (Tsy8d19C10_fs00), slab is developing more slowly at the beginning before the plate passes through phase transition at $400\,\mathrm{km}$. Then the plate velocity is higher than in the model with prescribed velocity (Tsy8d19C10_v) due to the extra buoyancy introduced by the exothermic phase transition. The effect of this phase transition is somewhat suppressed in the model with prescribed velocity, where the surface boundary conditions limits the slab velocity. In both models, the subducting plates deform above the phase transition at $670\,\mathrm{km}$ due to the mechanical resistance of the lower mantle and endothermic phase transition. These deformations are enabled by rather low stress limit $\sigma_\mathrm{y} = 0.1\,\mathrm{GPa}$. Then the deformed plates slowly penetrate into the lower mantle. The velocity of the subducting plate is higher in the upper mantle than in the lower mantle (Fig. 7.12**e**).

The detail of the slab in the model Tsy8d19C10_v is in Fig. 7.12. We show here the temperature field T (panel **a**) and the temperature variation ΔT with respect to geotherm T_ref (panel **b**) to illustrate the slab morphology. The decadic logarithm of the relative viscosity and the prevailing deformation mechanisms are in panels **c** and **d**. By the prevailing deformation mechanism, we mean the mechanism which produces locally the lowest viscosity. The prevailing deformation mechanism (panel **d**) in the plate is stress limiter in the upper mantle and stress limiter together with the dislocation creep in the lower man-

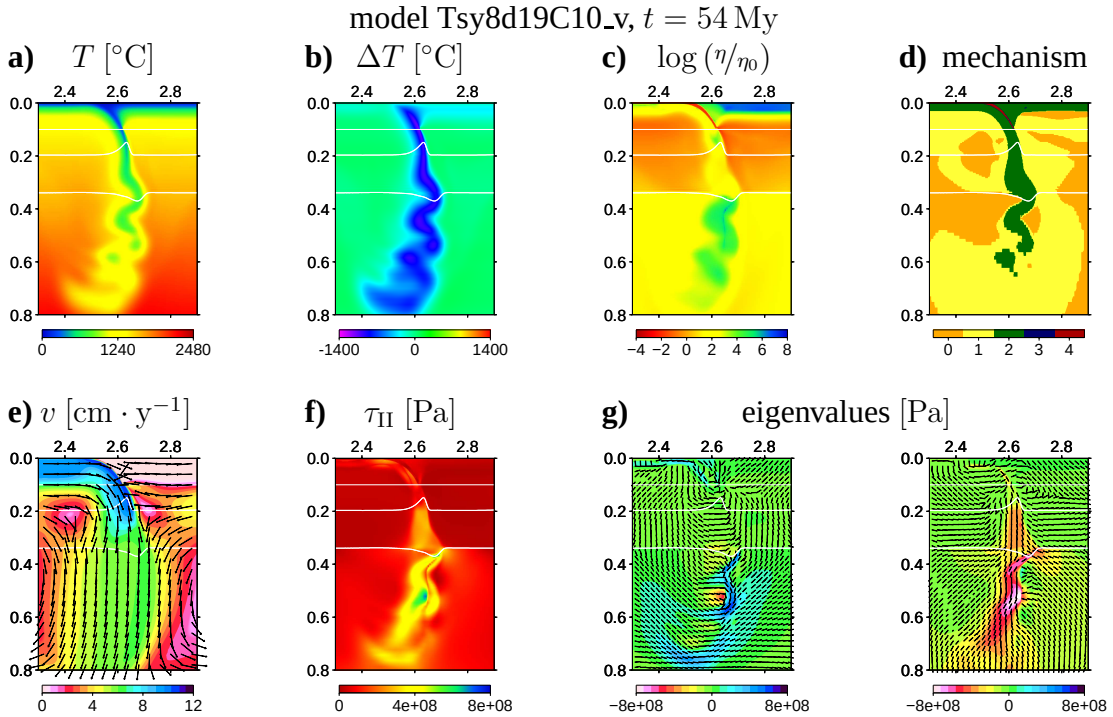

Figure 7.12 Result for model Tsy8d19C10_v after $54\,\mathrm{My}$, **a)** temperature T, **b)** temperature variation ΔT with respect to geotherm T_{ref}, **c)** relative viscosity in the log scale $\log(\eta/\eta_0)$, prevailing deformation mechanism (0 — diffusion creep, 1 — dislocation creep, 2 — stress-limiter, 3 — viscosity limit, 4 — decoupling layer for $z > 200\,\mathrm{km}$), **e)** velocity **v** (directions are marked by arrows, amplitudes by color field), **f)** second invariant of the stress tensor τ_{II} and **g)** its eigenvalues and eigenvectors are shown (axes are marked by lines, amplitudes by color field). $1,600\,\mathrm{km}$ deep and $1,200\,\mathrm{km}$ wide part of the model domain is shown.

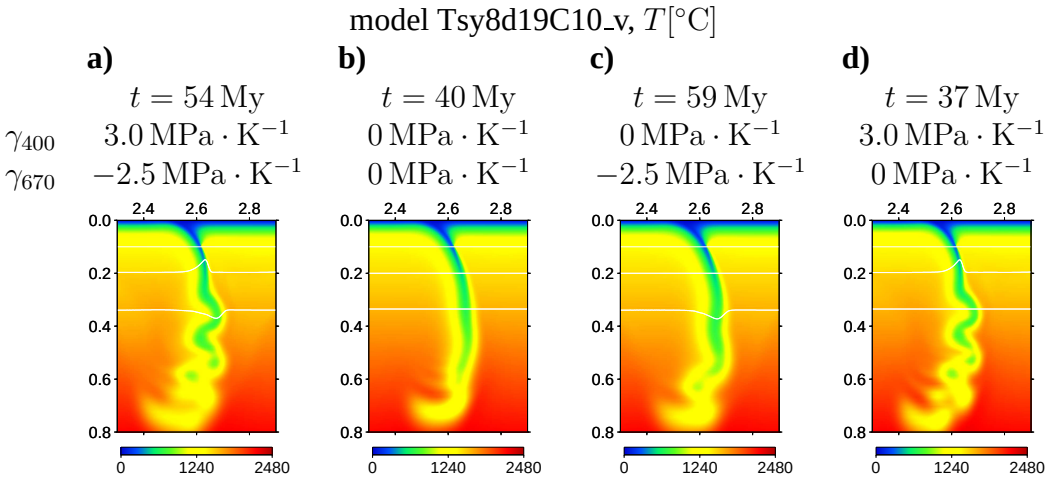

Figure 7.13 The phase transition influence, result for model Tsy8d19C10_v. $1,600\,\mathrm{km}$ deep and $1,200\,\mathrm{km}$ wide detail of the model domain is shown.

tle. The velocity field is in panel **e**, directions of the velocity are marked by arrows, the amplitudes by color field. To illustrate the stress regime within the slab, we show here the second invariant of the stress tensor (panel **f**) and its decomposition into the eigenvectors and eigenvalues (panel **g**). The axes are marked by lines and the values by color field. The dilatation (panel **g**, blue color) is observed in the plate above the $400\,\mathrm{km}$ boundary due to the buoyancy effect of the exothermic phase transition. The dilatation can be also observed in the lower mantle in the outer part of the bent plate. The plate is compressed (red color) in the vertical direction between the depths $400\,\mathrm{km}$ and $670\,\mathrm{km}$ due to the combined effect of both phase transitions and then in the lower mantle due to the viscous resistance of the lower mantle material. The prevailing rheological mechanisms and stress regime in the model Tsy8d19C10_fs00 are similar to those discussed above for model Tsy8d19C10_v.

Until now, we have discussed the effects of the viscosity and the boundary condition. Now, let us concentrate on the effect of the phase transitions on the plate morphology. To be able to study the influence of the phase transition, we subsequently enable/disable individual phase transitions in the model Tsy8d19C10_v. The results of this test are in Fig. 7.13. In panel **a**, there is an original model with both phase transitions. If the Clapeyron slopes of both transitions are set to zero, the buckling does not occur (panel **b**). Only the tip of the subducting plate is slightly deformed due to the penetration to the more viscous lower mantle. If only the Clapeyron slope of the transition at the depth $400\,\mathrm{km}$ is assumed to be zero (panel **c**), the buckling occurs only as the slab tip penetrates into the lower mantle. Later as the slab pull increases, buckling does not occur any more. If the Clapeyron slope of the phase transition at the depth $670\,\mathrm{km}$ is taken zero (panel **d**) and only the $400\,\mathrm{km}$ phase transition is considered, the buckling is observed during the penetration into the more viscous lower mantle. Hence, both the exothermic and the endothermic phase transitions support the creation of the buckling instabilities. The effect of the $400\,\mathrm{km}$ phase transition has however even more important effect on the slab thickening.

Results of the models with viscosity jump $C = 30$ are in Figs. 7.8 and 7.9, third row. For both models, the buckling occurs. At the beginning, the amplitude of the buckling instabilities is rather high. However, as the slab pull increases the buckling amplitude decreases and the plate thickening is also caused by strong vertical compression. Furthermore, the plates seem to thicken not only in the lower mantle but also between the phase transitions at $400\,\mathrm{km}$ and $670\,\mathrm{km}$. The plate velocity (Figs. 7.8 and 7.9, third column) slightly increases after the plates penetrate into the lower mantle. Further the velocity in the lower mantle is rather low (up to $\sim 2\,\mathrm{cm}\cdot\mathrm{y}^{-1}$) and the conductive warming of the slabs is clearly visible.

Models with lower stress limit and stronger decoupling layer

The results for models with lower yield stress $\sigma_\mathrm{y} = 0.1\,\mathrm{GPa}$ and stronger decoupling layer $\eta_\mathrm{DL} = 10^{21}\,\mathrm{Pa}\cdot\mathrm{s}$ are in Figs. 7.14 and 7.15. In models with prescribed velocity, the velocity within the plate is only slightly differentiated. The weak peak appears when the plates pass through the phase transition at $400\,\mathrm{km}$. For these models, the free-slip could not be prescribed from the beginning of the simulation. The ridge push is too small to overcome the friction on the contact of the plates and the bending resistance. Hence,

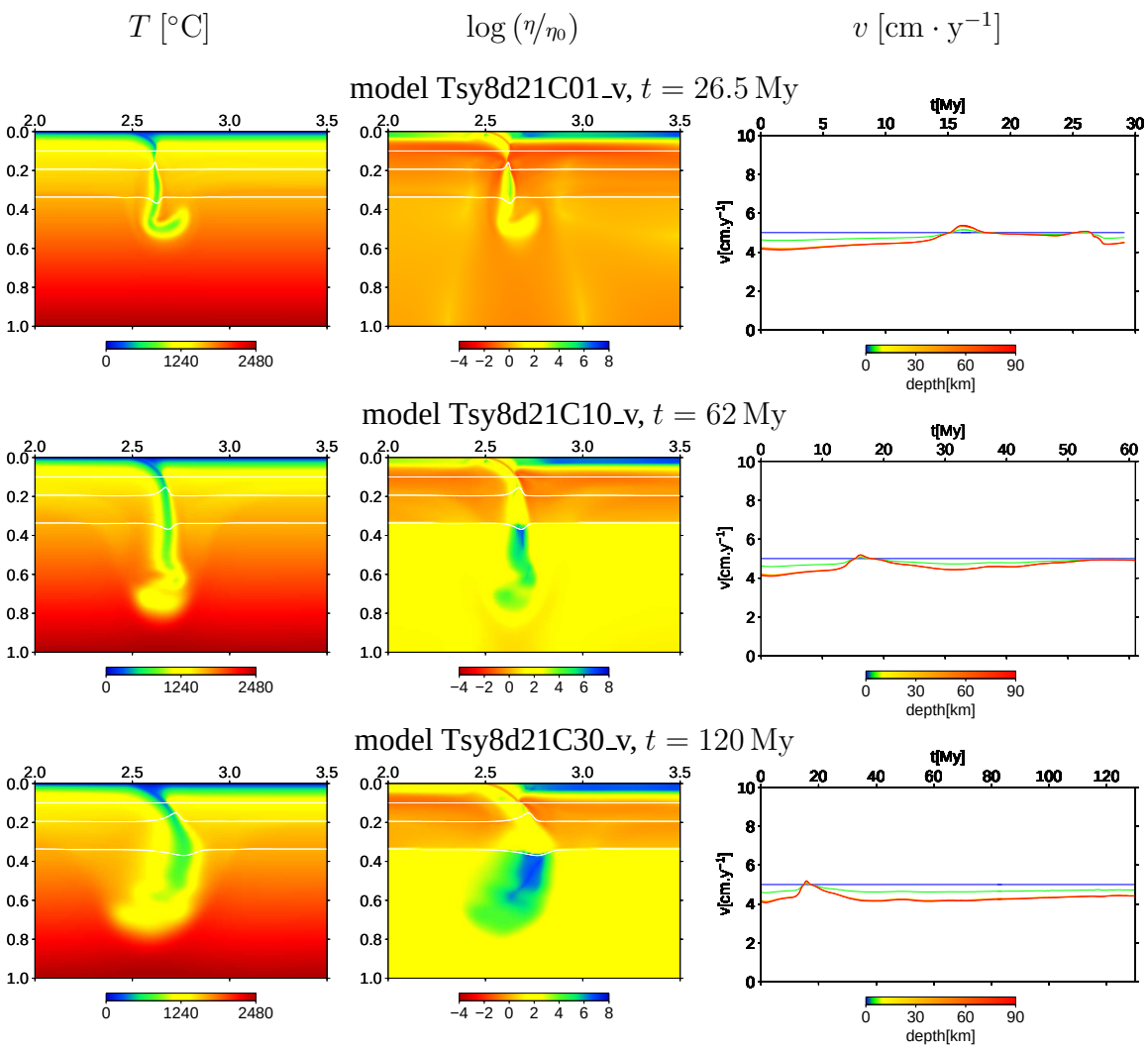

Figure 7.14 Results for models with stress limit $\sigma_y = 0.1\,\mathrm{GPa}$ and decoupling layer viscosity $\eta_{\mathrm{DL}} = 10^{21}\,\mathrm{Pa}\cdot\mathrm{s}$. On the top boundary, velocity is prescribed. In a $2,000\,\mathrm{km}$ deep and $3,000\,\mathrm{km}$ wide part of the model domain, the temperature (first column) and decadic logarithm of relative viscosity (second column) are shown. The time evolution of the plate velocity at the points with $x = 4,800\,\mathrm{km}$ and depth (marked by color) $z = 0$, 5, 15, 25, 45, 65 and $85\,\mathrm{km}$ is plotted in the third column.

we had to start the subduction process using the prescribed velocity boundary condition ($5\,\mathrm{cm}\cdot\mathrm{y}^{-1}$) for initial $10\,\mathrm{My}$. At this time, the tip of the subducting plate is approximately at the depth of $200\,\mathrm{km}$. Then the free-slip condition is prescribed — the ridge push and slab pull are already high enough to maintain the subduction process. The time evolution of the plate velocity (Figs. 7.14 and 7.15, third column) have again similar characteristics — the velocity increases when the plate passes through the phase transition at $400\,\mathrm{km}$ and decreases again when the plate reaches the phase transition at $670\,\mathrm{km}$. Then the velocity again increases due to the increasing slab pull until the plate reaches the bottom of the studied area or until it is detached. In this case, the maximum velocities are in the reasonable bounds — maximum velocity is $\sim 12\,\mathrm{cm}\cdot\mathrm{y}^{-1}$. An interesting feature of these models with free-slip boundary condition is the fact, that the trench is moving forwards probably due to the relatively strong coupling between the subducting and over-riding

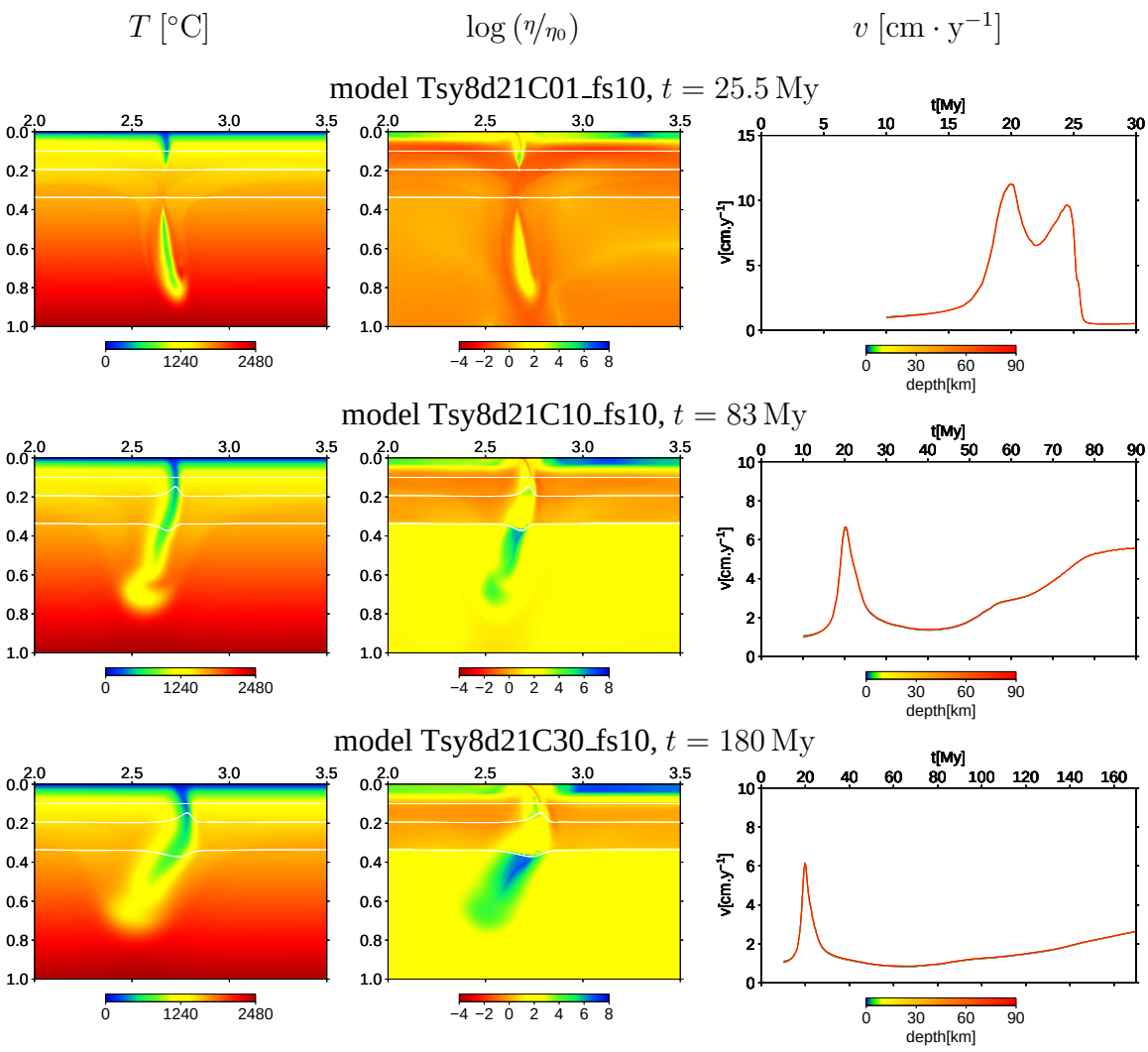

Figure 7.15 Results for models with stress limit $\sigma_y = 0.1$ GPa and decoupling layer $\eta_{\mathrm{DL}} = 10^{21}$ Pa · s. On the top boundary, free-slip is prescribed. In a $2,000$ km deep and $3,000$ km wide part of the model domain, the temperature (first column) and decadic logarithm of relative viscosity (second column) are shown. The time evolution of the plate velocity at the points with $x = 4,800$ km and depth (marked by color) $z = 0$, 5, 15, 25, 45, 65 and 85 km is plotted in the third column.

plates and relatively weak and therefore easily deformable over-riding plate.

The results for models with no viscosity jump at 670 km boundary are in Figs. 7.14 and Figs. 7.15 (first row) for models Tsy8d21C01_v and Tsy8d21C01_fs10, respectively. For both models, the plates are detached at a depth $\sim$ 400 km after they penetrate into the lower mantle. For the model with prescribed velocity Tsy8d21C01_v, the plate is deflected when it reaches the 670 km boundary. After it penetrates into the lower mantle, the detachment of the plate is observed. Then the new cycle starts and the subduction process continues. For the model with free-slip condition Tsy8d21C01_fs10, the plate is not significantly deformed after passing into the lower mantle. When the subducting plate is detached, the subduction process does not continue, since the slab pull is apparently not strong enough and contrary to the model Tsy8d21C01_v, there is no push due to the surface boundary condition.

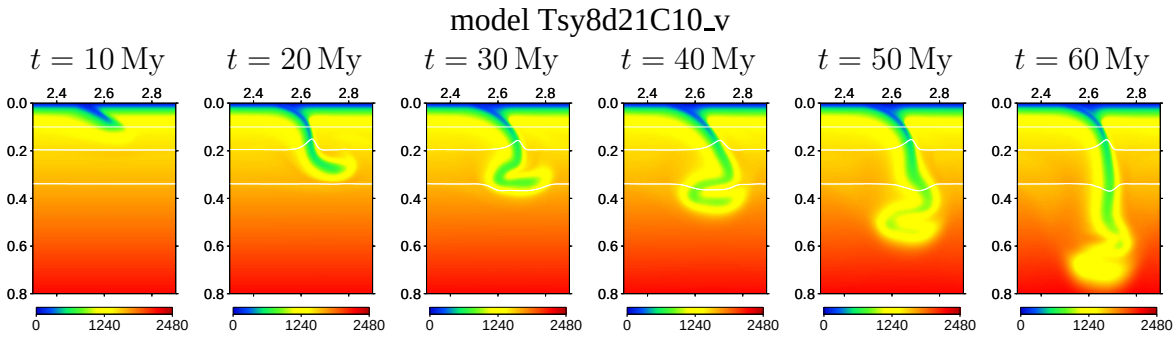

Figure 7.16 Model Tsy8d21C10_v: time evolution of temperature $[^\circ\mathrm{C}]$, $1,600\,\mathrm{km}$ deep and $1,200\,\mathrm{km}$ wide part of the model domain is shown.

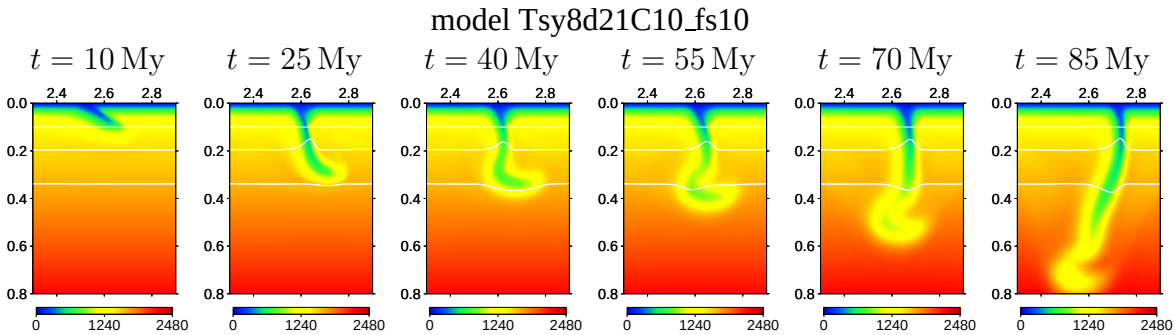

Figure 7.17 Model Tsy8d21C10_fs10: time evolution of temperature $[^\circ\mathrm{C}]$, $1,600\,\mathrm{km}$ deep and $1,200\,\mathrm{km}$ wide part of the model domain is shown.

The models with viscosity jump $C = 10$ at $670\,\mathrm{km}$ boundary are in Figs. 7.14 and 7.15, second row. For these models, there is hardly any buckling in the lower mantle — only one fold occurs before the plates penetrate into the lower mantle. Time evolution of these models are in Figs. 7.16 and 7.17. In both models, the tips of the slabs are deflected when they reach the boundary at $670\,\mathrm{km}$. After penetration into the lower mantle, the plates do not significantly deform and no thickening occurs. For model with the free-slip condition Tsy8d21C10_fs10, the forward drift of the trench is observed.

The detail of the model Tsy8d21C10_v is shown in Fig. 7.18. For this model, the prevailing deformation mechanism (panel **d**) is stress limiter in the upper mantle and dislocation creep together with the stress limiter in the lower mantle. The velocity distribution is in panel **e**. Contrary to the model with the weak decoupling layer (Fig. 7.12**e**), the velocity in the upper mantle and in the lower mantle does not differ significantly in the model Tsy8d21C10_v (Fig. 7.18**e**). Hence the buckling does not occur. The stress regime in the plate is shown in panel **g**. The dilatation (blue color) in the plate is observed above the boundary at $400\,\mathrm{km}$ due to the extra negative buoyancy caused by the exothermic phase transition. The over-riding plate is also dilating in the vicinity of the contact between the plates due to the relatively strong coupling between them (compared to the model with weaker crust). Further, the horizontal dilatation occurs in the tip of the slab at the depth $\sim 1,500\,\mathrm{km}$. The vertical compression (red color) is found between the boundaries at $400\,\mathrm{km}$ and $670\,\mathrm{km}$ and in the lower mantle similarly to the previously discussed cases.

For yet higher viscosity jump $C = 30$, the results are in Figs. 7.14 and 7.15, third

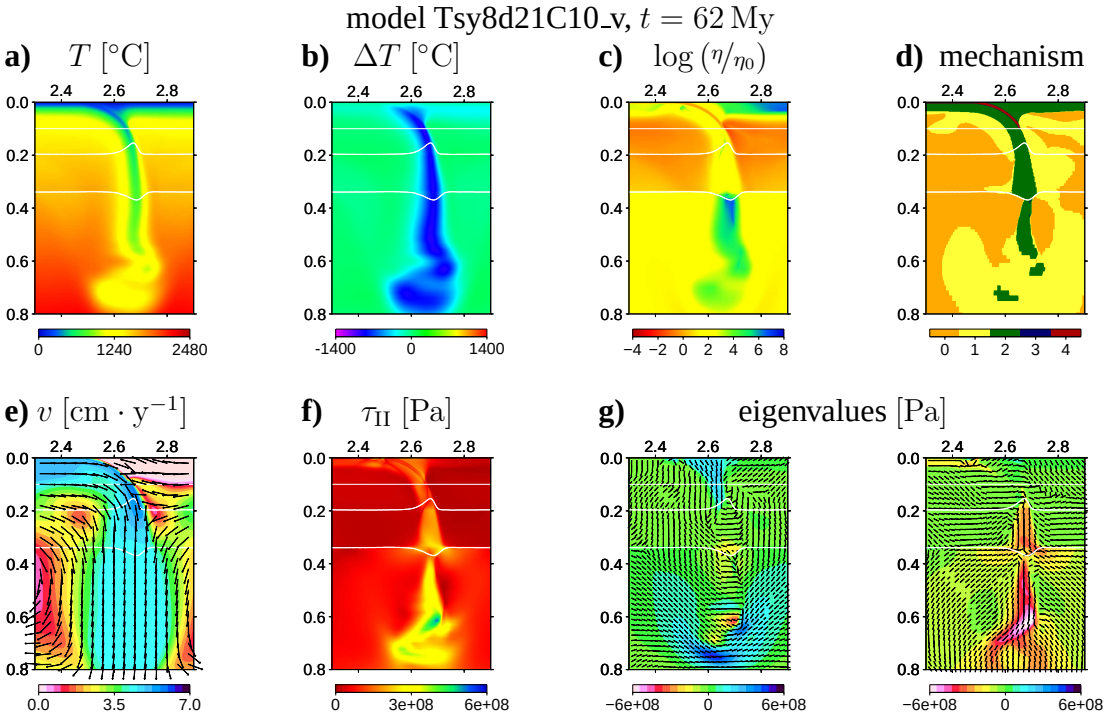

Figure 7.18 Result for model Tsy8d21C10_v after $62\,\mathrm{My}$, **a)** temperature T, **b)** temperature variation ΔT with respect to geotherm T_{ref}, **c)** relative viscosity in the log scale $\log(\eta/\eta_0)$, prevailing deformation mechanism (0 — diffusion creep, 1 — dislocation creep, 2 — stress-limiter, 3 — viscosity limit, 4 — decoupling layer for $z > 200\,\mathrm{km}$), **e)** velocity **v** (directions are marked by arrows, amplitudes by color field), **f)** second invariant of the stress tensor τ_{II} and **g)** its eigenvalues and eigenvectors are shown (axes are marked by lines, amplitudes by color field). $1,600\,\mathrm{km}$ deep and $1,200\,\mathrm{km}$ wide part of the model domain is shown.

row. For the prescribed velocity on the top boundary (model Tsy8d21C30_v, Fig. 7.14), the plate is pushed into the lower mantle. The buckled anomalies are created at the beginning — three folds occur. Then the subduction process continues without buckling. However, the plate is still thickening due to the rather large mechanical resistance of the lower mantle. This thickening is observed in the lower mantle and also between $400\,\mathrm{km}$ and $670\,\mathrm{km}$ boundary. The slab velocity in the lower mantle is rather low ($\sim 2\,\mathrm{cm} \cdot \mathrm{y}^{-1}$) and significant conductive warming of the slab is observed. For the model with a free-slip boundary condition (model Tsy8d21C30_fs10, Fig. 7.15), one fold occurs when the plate reaches the $670\,\mathrm{km}$ boundary. Then the penetration into the lower mantle slowly continues. The maximal velocity within the lower mantle is less than $2\,\mathrm{cm} \cdot \mathrm{y}^{-1}$. Again the conductive warming of the slab is significant. In the lower mantle, the plate thickens due to the compression. Further the slowly moving slab is cooling the surrounding material and hence the cold temperature anomaly looks even thicker.

Models with higher stress limit and weaker decoupling layer

The results for higher stress limit ($\sigma_{\mathrm{y}} = 1\,\mathrm{GPa}$) and weaker decoupling layer ($\eta_{\mathrm{DL}} = 10^{19}\,\mathrm{Pa} \cdot \mathrm{s}$) are in Figs. 7.19 and 7.20. For the prescribed surface velocity, the velocity within the plate is differentiated due to the weak decoupling layer. The maximum plate velocities caused by the effect of the phase transition at $400\,\mathrm{km}$ (Figs. 7.19 and 7.20, third

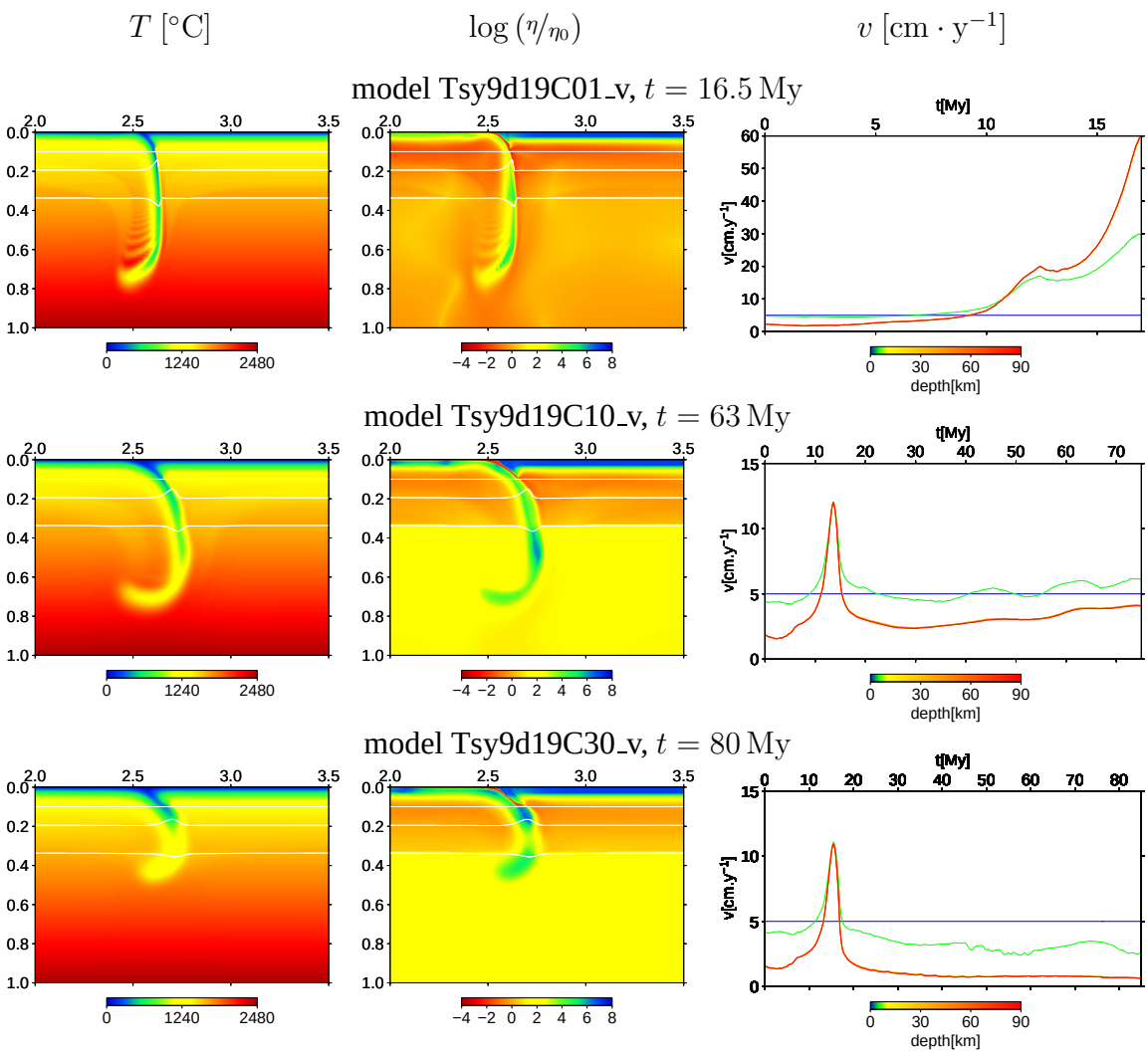

Figure 7.19 Results for models with stress limit $\sigma_y = 1\,\mathrm{GPa}$ and decoupling layer viscosity $\eta_{\mathrm{DL}} = 10^{19}\,\mathrm{Pa}\cdot\mathrm{s}$. On the top boundary, velocity is prescribed. In a $2,000\,\mathrm{km}$ deep and $3,000\,\mathrm{km}$ wide part of the model domain, the temperature (first column) and decadic logarithm of relative viscosity (second column) are shown. The time evolution of the plate velocity at the points with $x = 4,800\,\mathrm{km}$ and depth (marked by color) $z = 0$, 5, 15, 25, 45, 65 and $85\,\mathrm{km}$ is plotted in the third column.

column) are $\sim 20\,\mathrm{cm}\cdot\mathrm{y}^{-1}$ for model with no viscosity jump (model Tsy9d19C01_v) and $\sim 12\,\mathrm{cm}\cdot\mathrm{y}^{-1}$ and $\sim 11\,\mathrm{cm}\cdot\mathrm{y}^{-1}$ for models Tsy9d19C10_v and Tsy9d19C30_v, respectively.

For the model with the free-slip condition, the subduction process does not start on its own by the ridge push. For time $t < 8\,\mathrm{My}$, the prescribed velocity condition is therefore used to initiate the subduction process. Afterwards the free-slip condition is used. After $8\,\mathrm{My}$, the tip of the subducting plate is approximately $200\,\mathrm{km}$ deep. The velocity within the plate is more differentiated than for the models with the lower stress limit $\sigma_{\mathrm{y}} = 0.1\,\mathrm{GPa}$ (models Tsy8d19C01_fs08, Tsy8d19C10_fs08 and Tsy8d19C30_fs08, Fig. 7.9). The maximum plate velocities caused by the effect of the phase transition at $400\,\mathrm{km}$ are $\sim 75\,\mathrm{cm}\cdot\mathrm{y}^{-1}$ (model Tsy9d19C01_fs08, Fig. 7.20, first row), $\sim 28\,\mathrm{cm}\cdot\mathrm{y}^{-1}$ (model Tsy9d19C10_fs08, Fig. 7.20, second row) and $\sim 18\,\mathrm{cm}\cdot\mathrm{y}^{-1}$ (model Tsy9d19C30_fs08,

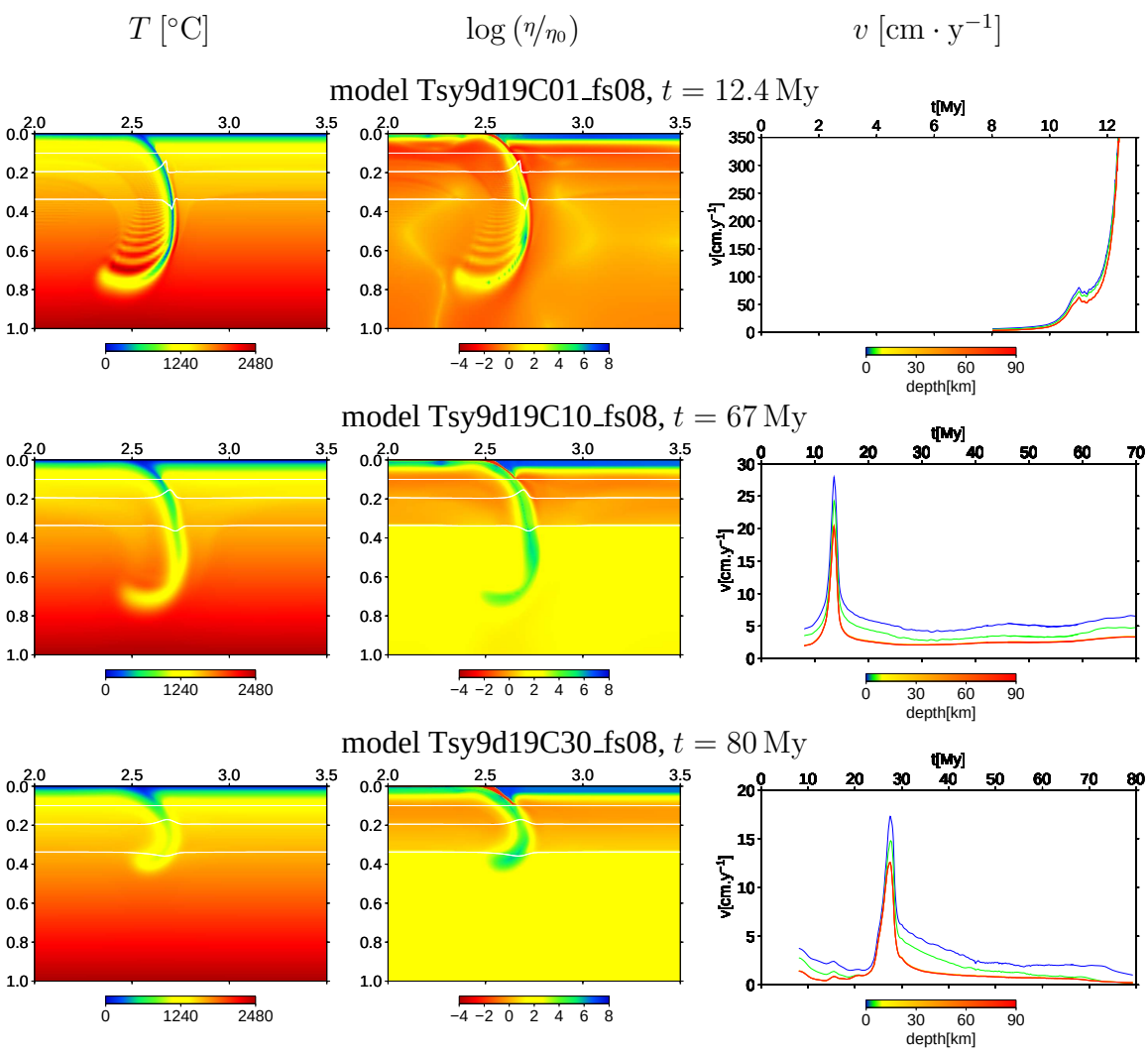

Figure 7.20 Results for models with stress limit $\sigma_y = 1\,\mathrm{GPa}$ and decoupling layer viscosity $\eta_{\mathrm{DL}} = 10^{19}\,\mathrm{Pa}\cdot\mathrm{s}$. On the top boundary, free-slip is prescribed. In a $2,000\,\mathrm{km}$ deep and $3,000\,\mathrm{km}$ wide part of the model domain, the temperature (first column) and decadic logarithm of relative viscosity (second column) are shown. The time evolution of the plate velocity at the points with $x = 4,800\,\mathrm{km}$ and depth (marked by color) $z = 0$, 5, 15, 25, 45, 65 and $85\,\mathrm{km}$ is plotted in the third column.

Fig. 7.20, third row).

Models with no viscosity jump are in Figs. 7.19 and 7.20, first row. In both models, the plates penetrate into the lower mantle without significant deformation. The plate velocities increase gradually due to the increasing slab pull with a local maximum at the time when the slab tip comes through the exothermic phase change at $400\,\mathrm{km}$ depth. For the model with a free-slip condition, the plate is more bent and the subduction is faster than for the model with prescribed velocity. Nonetheless, the velocities in both models are unrealistically high. These high velocities could be caused by the underestimation of the friction on the plates contact or by the low viscosity in the lower mantle. It can be also effect of the 2-D approach. Further, the numerical oscillations occur due to the high velocities within the mantle.

In Figs. 7.19 and 7.20 (second row), there are the models with a viscosity jump $C =$

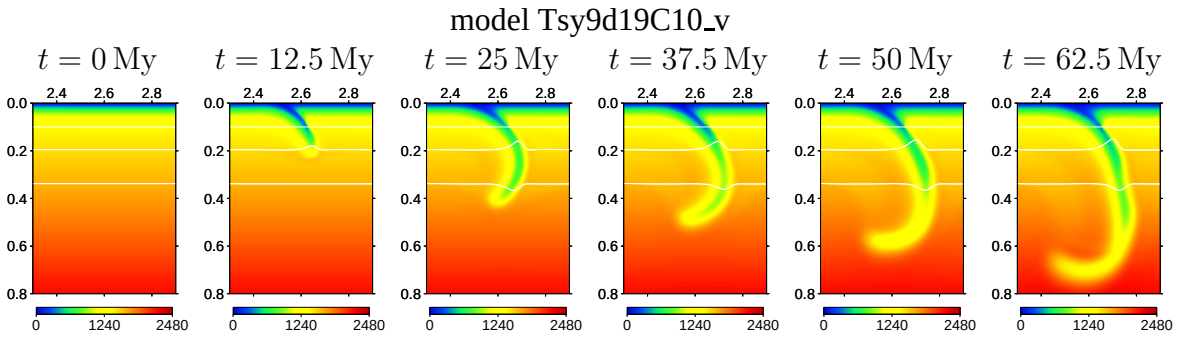

Figure 7.21 Model Tsy9d19C10_v: time evolution of temperature $[^\circ\mathrm{C}]$, $1,600\,\mathrm{km}$ deep and $1,200\,\mathrm{km}$ wide part of the model domain is shown.

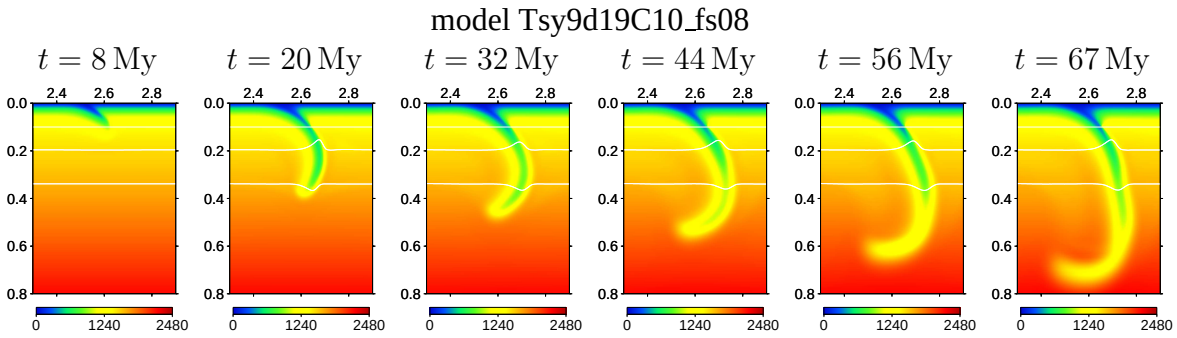

Figure 7.22 Model Tsy9d19C10_fs08: time evolution of temperature $[^\circ\mathrm{C}]$, , $1,600\,\mathrm{km}$ deep and $1,200\,\mathrm{km}$ wide part of the model domain is shown.

10. For both models, the plates do not deform significantly in the lower mantle except for the backward deflection of the slab. This deflection is developed during the slab descent through the upper mantle due to the high viscosity of the slab and low friction at the plates contact. The resulting shapes of the plates are similar in both models. The time evolutions of the temperature field in these models are in Figs. 7.21 and 7.22. Both models develop rather similarly. Contrary to the models with lower stress limit (Figs. 7.10 and Fig. 7.11), the slab is developing slightly slower in a model with the free-slip than in the model with prescribed velocity. The detail of the model Tsy9d19C10_v is in Fig. 7.23. The prevailing deformation mechanism is in panel **d**. In the subducting plate, the stress limiter controls the viscosity in the upper mantle. In the lower mantle, the dislocation creep is prevailing mechanism instead of the stress limiter. In the over-riding plate, the maximum viscosity limit is acting due to the higher stress limit and hence the low deformations. The plate velocity (panel **e**) is almost constant in both the lower and the upper mantle. The stress distribution is in panels **f–g**. The bipolar stress structure develops in the plate (panel **f**). This means that two parallel features with rather high stress are separated by relatively thin layer with low stress. This bipolarity can be observed also for the eigenvalues of the stress tensor (Fig. 7.23**g**) — the dilatation (blue color) occurs in the left-hand-side part of the subduction, the compression regime (red color) is in the right-hand-side part of the subduction in the upper mantle. In the lower mantle, the dilatation occurs in the outer parts of the slab arc, thus indicating bending.

The results for the models with a viscosity jump $C = 30$ are in Figs. 7.19 and 7.20,

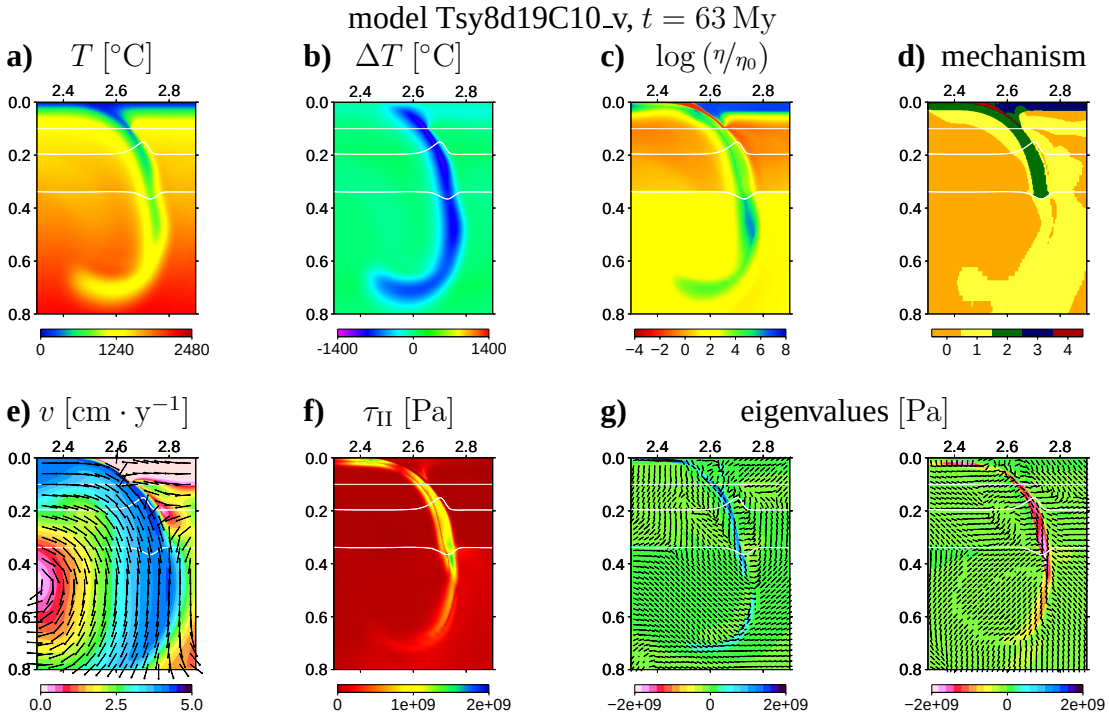

Figure 7.23 Result for model Tsy9d19C10_v after $63\,\mathrm{My}$, **a)** temperature T, **b)** temperature variation ΔT with respect to geotherm T_{ref}, **c)** relative viscosity in the log scale $\log(\eta/\eta_0)$, prevailing deformation mechanism (0 — diffusion creep, 1 — dislocation creep, 2 — stress-limiter, 3 — viscosity limit, 4 — decoupling layer for $z > 200\,\mathrm{km}$), **e)** velocity **v** (directions are marked by arrows, amplitudes by color field), **f)** second invariant of the stress tensor τ_{II} and **g)** its eigenvalues and eigenvectors are shown (axes are marked by lines, amplitudes by color field). $1,600\,\mathrm{km}$ deep and $1,200\,\mathrm{km}$ wide part of the model domain is shown.

third row. For both models, the subduction process is almost stopped due to the mechanical resistance of the high viscosity lower mantle when the plate reaches boundary at $670\,\mathrm{km}$. For model with the prescribed velocity, rather weak decoupling layer is pushed down by the boundary condition by constant velocity even if the subduction process slows down. Crust material then creates a bubble-like anomaly (Figs. 7.19, third row, between the depths $200\,\mathrm{km}$ and $400\,\mathrm{km}$).

Models with higher stress limit and stronger decoupling layer

The results for higher stress limit ($\sigma_{\mathrm{y}} = 1\,\mathrm{GPa}$) and stronger decoupling layer ($\eta_{\mathrm{DL}} = 10^{21}\,\mathrm{Pa}\cdot\mathrm{s}$) are in Figs. 7.24 and 7.25. For models with the prescribed velocity (Fig. 7.24), the plate velocity maximum associated with the phase transition at $400\,\mathrm{km}$ are not significant. The velocities within the plates are rather undifferentiated except for the model with viscosity jump $C = 30$. The free-slip condition (Fig. 7.25) is prescribed for $t > 8\,\mathrm{My}$. At this time, the tip of the subducting plate is approximately $300\,\mathrm{km}$ deep. The velocity within the plate is not differentiated and the maximum velocity caused by the phase transition at $400\,\mathrm{km}$ is less than $5\,\mathrm{cm}\cdot\mathrm{y}^{-1}$. After the penetration into the lower mantle, the plate velocities may both increase or decrease. The increase/decrease depends on the viscosity jump in the lower mantle — the velocity increases with decreasing viscosity jump.

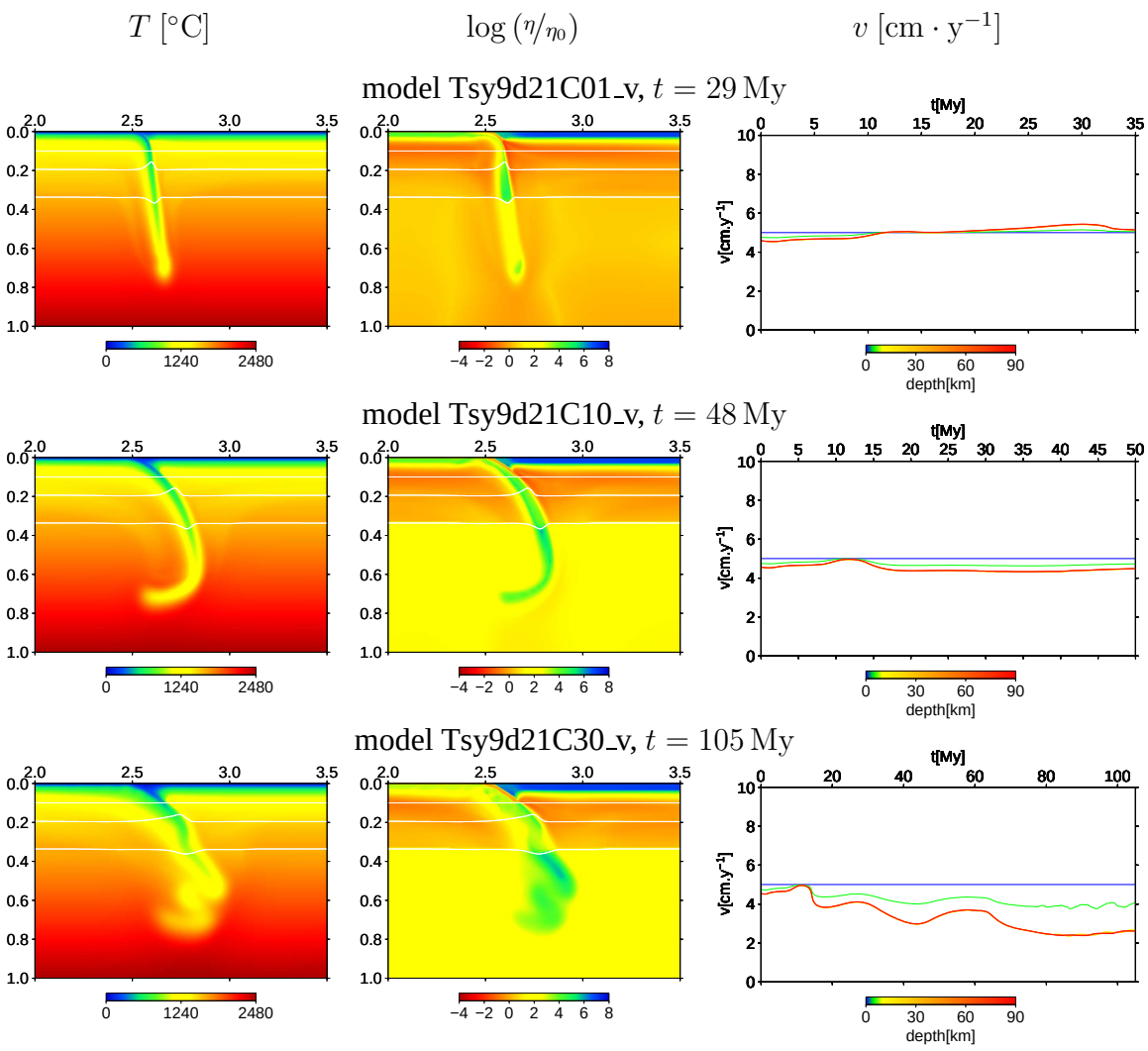

Figure 7.24 Results for models with stress limit $\sigma_y = 1\,\mathrm{GPa}$ and decoupling layer viscosity $\eta_{\mathrm{DL}} = 10^{21}\,\mathrm{Pa}\cdot\mathrm{s}$. On the top boundary, velocity is prescribed. In a $2,000\,\mathrm{km}$ deep and $3,000\,\mathrm{km}$ wide part of the model domain, the temperature (first column) and decadic logarithm of relative viscosity (second column) are shown. The time evolution of the plate velocity at the points with $x = 4,800\,\mathrm{km}$ and depth (marked by color) $z = 0$, 5, 15, 25, 45, 65 and $85\,\mathrm{km}$ is plotted in the third column.

The results for no viscosity jump at $670\,\mathrm{km}$ are in Figs. 7.24 and 7.25, first row. For these models, the plates do not deform and penetrate into the lower mantle without any deflection. For model with free-slip Tsy9d21C01_fs08 (7.25, first row), the plate is slightly steeper than for model with prescribed velocity (Tsy9d21C01_v, 7.24, first row).

The models with viscosity jump $C = 10$ are in Figs. 7.24 and 7.25, second row. In these models, significant deformations are not observed. The plate is more bent in the model with prescribed velocity (model Tsy9d21C10_v, Fig. 7.24, second row) than for the model with free-slip (model Tsy9d21C10_fs08, Fig. 7.25, second row). Generally, the plates are more bent for these models (models Tsy9d21C10_v and Tsy9d21C10_fs08) than for the models without any viscosity jump.

The results for the models with a viscosity jump $C = 30$ are in Figs. 7.24 and 7.25, third row. In the free-slip condition model (Tsy9d21C30_fs08, Fig. 7.25, third row), the

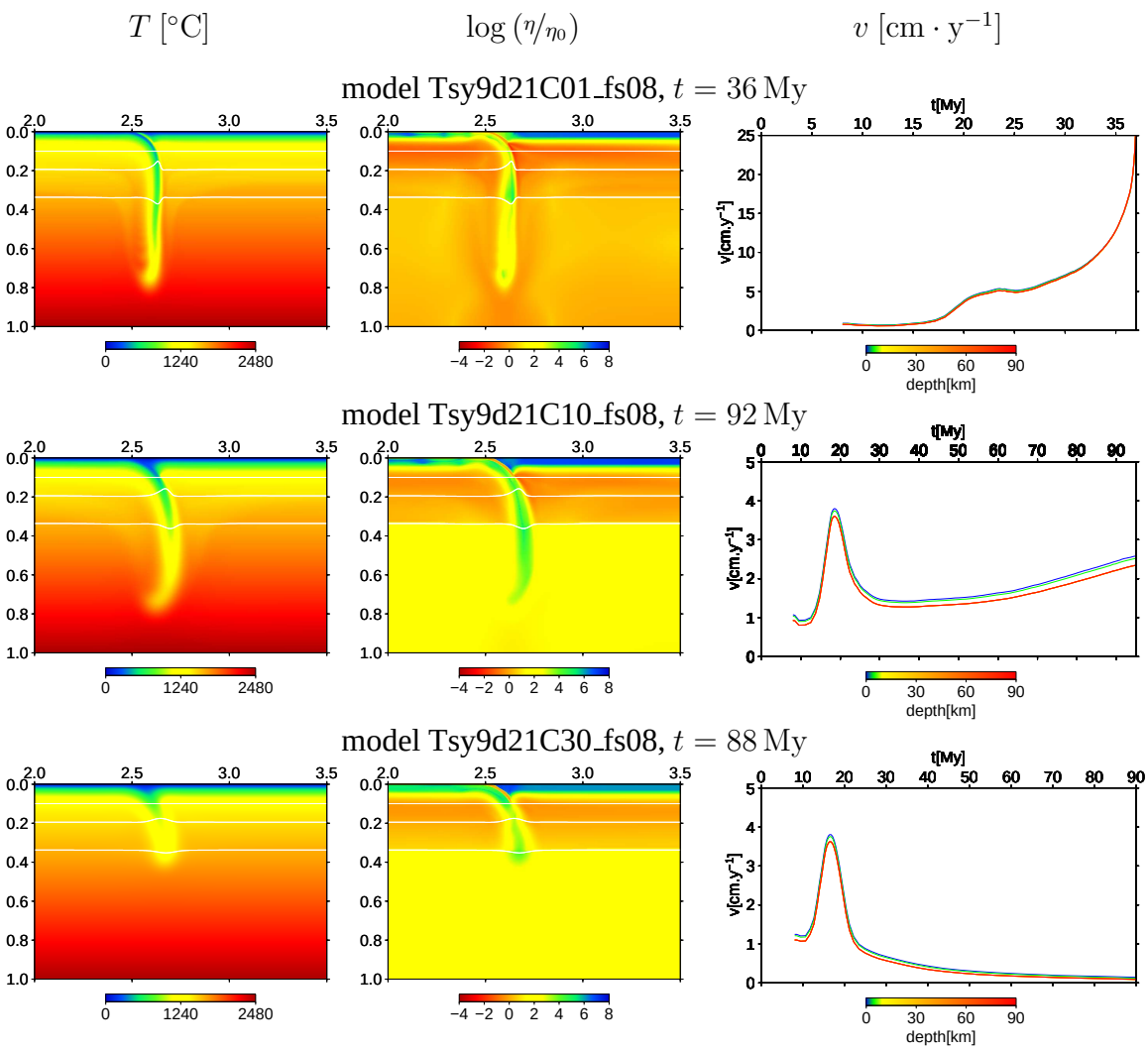

Figure 7.25 Results for models with stress limit $\sigma_y = 1\,\mathrm{GPa}$ and decoupling layer viscosity $\eta_{\mathrm{DL}} = 10^{21}\,\mathrm{Pa}\cdot\mathrm{s}$. On the top boundary, free-slip is prescribed. In a $2,000\,\mathrm{km}$ deep and $3,000\,\mathrm{km}$ wide part of the model domain, the temperature (first column) and decadic logarithm of relative viscosity (second column) are shown. The time evolution of the plate velocity at the points with $x = 4,800\,\mathrm{km}$ and depth (marked by color) $z = 0$, 5, 15, 25, 45, 65 and $85\,\mathrm{km}$ is plotted in the third column.

subduction process stops when the plate reaches the boundary at $670\,\mathrm{km}$. The slab remains there and warms up due to the heat conduction. For model with prescribed velocity (Tsy9d21C30_v), the plate is deformed in the lower mantle. The time evolution of the model Tsy9d21C30_v is in Fig. 7.26. The plate subducts under rather low angle. Despite the fact that the plate is strong ($\sigma_{\mathrm{y}} = 1\,\mathrm{GPa}$), it is deformed in the transition zone due to the rather high resistance of the lower mantle and due to the push of the boundary condition. Later, the deformed plate penetrates into the lower mantle. The detail of model Tsy9d21C30_v is in Fig. 7.27. The prevailing deformation mechanism in the subducting plate (panel **d**) is stress limiter in the upper mantle and the dislocation creep in the lower mantle. In the over-riding plate, the viscosity limit controls the viscosity except for the part close to the plates contact, where the stress limiter prevails. The subducting velocity (panel **e**) is higher in the upper mantle than in the lower mantle so the buckling is ob-

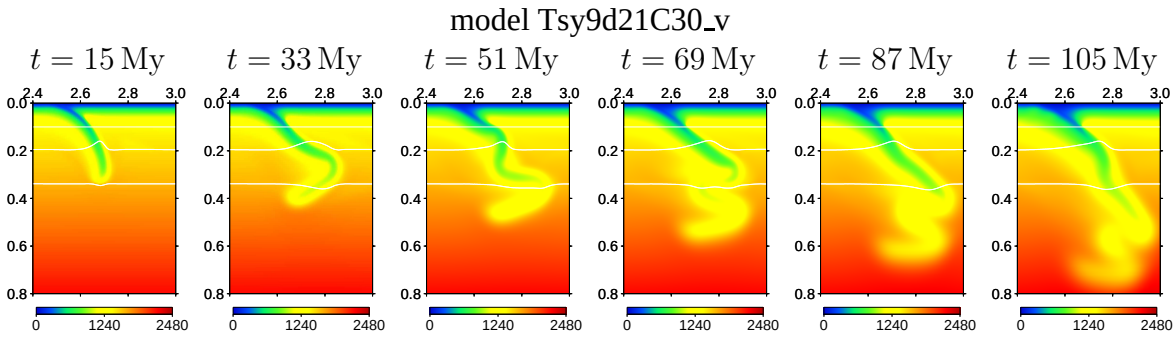

Figure 7.26 Model Tsy9d21C30_v: time evolution of temperature $[^\circ\mathrm{C}]$, $1,600\,\mathrm{km}$ deep and $1,200\,\mathrm{km}$ wide part of the model domain is shown.

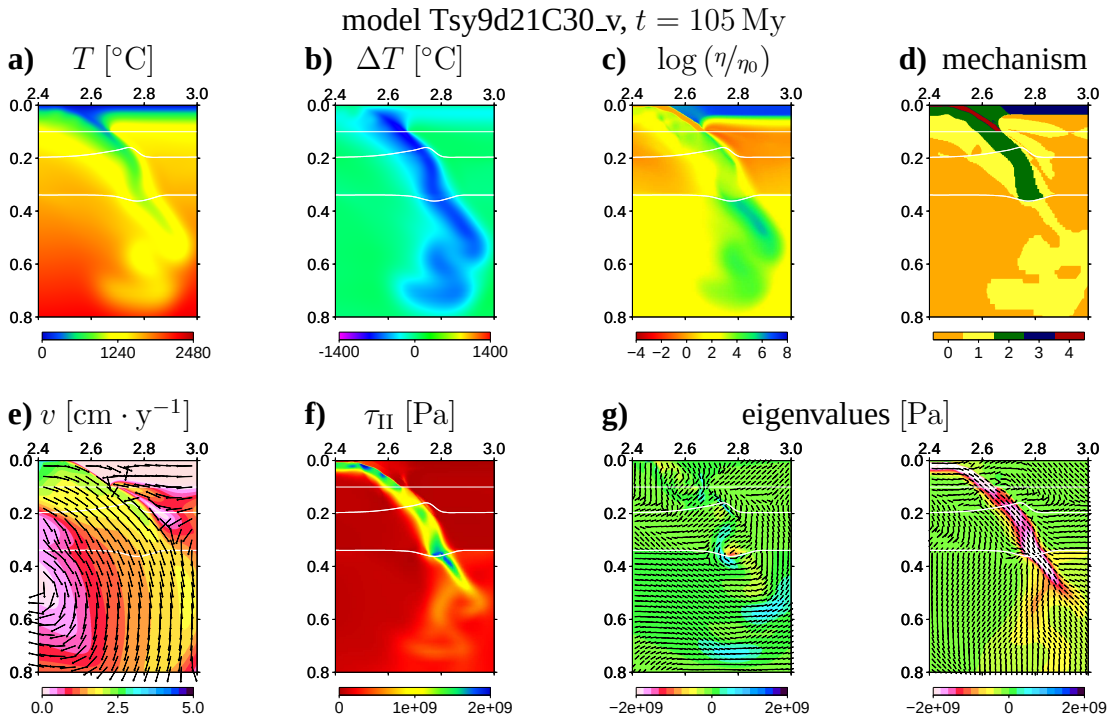

Figure 7.27 Result for model Tsy9d21C10_v after $105\,\mathrm{My}$, **a)** temperature T, **b)** temperature variation ΔT with respect to geotherm T_{ref}, **c)** relative viscosity in the log scale $\log(\eta/\eta_0)$, prevailing deformation mechanism (0 — diffusion creep, 1 — dislocation creep, 2 — stress-limiter, 3 — viscosity limit, 4 — decoupling layer for $z > 200\,\mathrm{km}$), **e)** velocity **v** (directions are marked by arrows, amplitudes by color field), **f)** second invariant of the stress tensor τ_{II} and **g)** its eigenvalues and eigenvectors are shown (axes are marked by lines, amplitudes by color field). $1,600\,\mathrm{km}$ deep and $1,200\,\mathrm{km}$ wide part of the model domain is shown.

served. The stress regime is shown in panel **f–g**. Dilatation occurs in the outer part of the folds. Strong compression is found in the plate parallel direction within the slab down to the depth $\sim 1,000\,\mathrm{km}$. In this case, the bipolar structure of the stress tensor is not observed.

7.2.3 Summary

Results of our models are summarized in Fig. 7.28. We show here the temperature variations ΔT with respect to the geotherm T_{ref} for all studied models. The results for both lower stress limit (first and second rows) and higher stress limit (third and fourth rows) are given. The characteristics of the slabs (e.g. dip angle, thickening) depend on all tested parameters (stress limiter, surface boundary condition, viscosity increase in the lower mantle and the strength of the decoupling layer).

Generally, the slabs in models with the lower stress limit can rather easily break (panels **a** and **g–h**) or buckle (panels **c–f** and **k**). For models with higher stress limit, slabs in most models do not deform significantly, hardly any thickening occurs and bipolar structure of the stress tensor similar to the one reported by Čížková et al. (2007) are observed. The backward deflection develops in most models (panels **m–r** and **u**), especially if the crustal friction is low. Some buckling is observed only for model in panel **w**.

The results for models with no viscosity increase at $670\,\mathrm{km}$ are in Fig. 7.28, first and second columns. If lower stress limit is applied, the slabs usually break-off (panels **a** and **g–h**) at the depth $\sim 400\,\mathrm{km}$ after they penetrate into the lower mantle. Only in the model with the weak coupling and the free-slip condition (panel **b**), the slab is not detached. In models with higher stress limit, the curvature of the slab arcs is higher in models with weaker decoupling layer (panel **m–n**) than in models with stronger decoupling layer (panel **s–t**). Moreover, in models with weaker decoupling layer, the unrealistically high velocities develop (panel **b** and **m–n**).

The results for the models with viscosity increase by factor 10 are shown in Fig. 7.28, third and fourth columns. For models with lower stress limit, significant deformations are observed in the lower mantle. However, they depend on the strength of the decoupling layer. The buckling occurs in the models with the weaker crust (panels **c–d**). In the models with the stronger crust (panel **i–j**), the tips of the slabs are deflected at $670\,\mathrm{km}$. Then the slabs pass into the lower mantle without significant thickening. For higher stress limit, the shapes of the slabs are rather similar for the models with the weaker decoupling layer (panels **o–p**) and for the stronger decoupling layer with prescribed velocity (panel **u**). For the model with the stronger decoupling layer and a free-slip condition (panel **v**), the slab curvature is smaller than for the models in panels **o–p** and **u**.

In Fig. 7.28, fifth and sixth columns, there are the results for the models with the viscosity increase by factor 30. The buckling occurs in most models with the lower stress limit (panels **e–f** and **k**). In the model with the stronger decoupling layer and prescribed surface velocity (panel **k**), the buckling is observed only at the beginning of the subduction process. Then the penetration into the lower mantle continues without buckling and the plate is thickened due to the compression and the conductive cooling. For model with the strong decoupling layer and free-slip (panel **l**), only one fold occurs. Then the plate slowly penetrates into the lower mantle and its width increases with increasing depth due to the compression and conductive cooling. Slabs in most models with stronger stress limit penetrate into the lower mantle with difficulties (panels **q–r** and **x**). For these models, the subduction process is almost stopped when the slabs reach $670\,\mathrm{km}$ boundary and the conductive warming is significant. In the model where an additional push induced by the boundary condition is transmitted though the relatively strong crustal layer to the

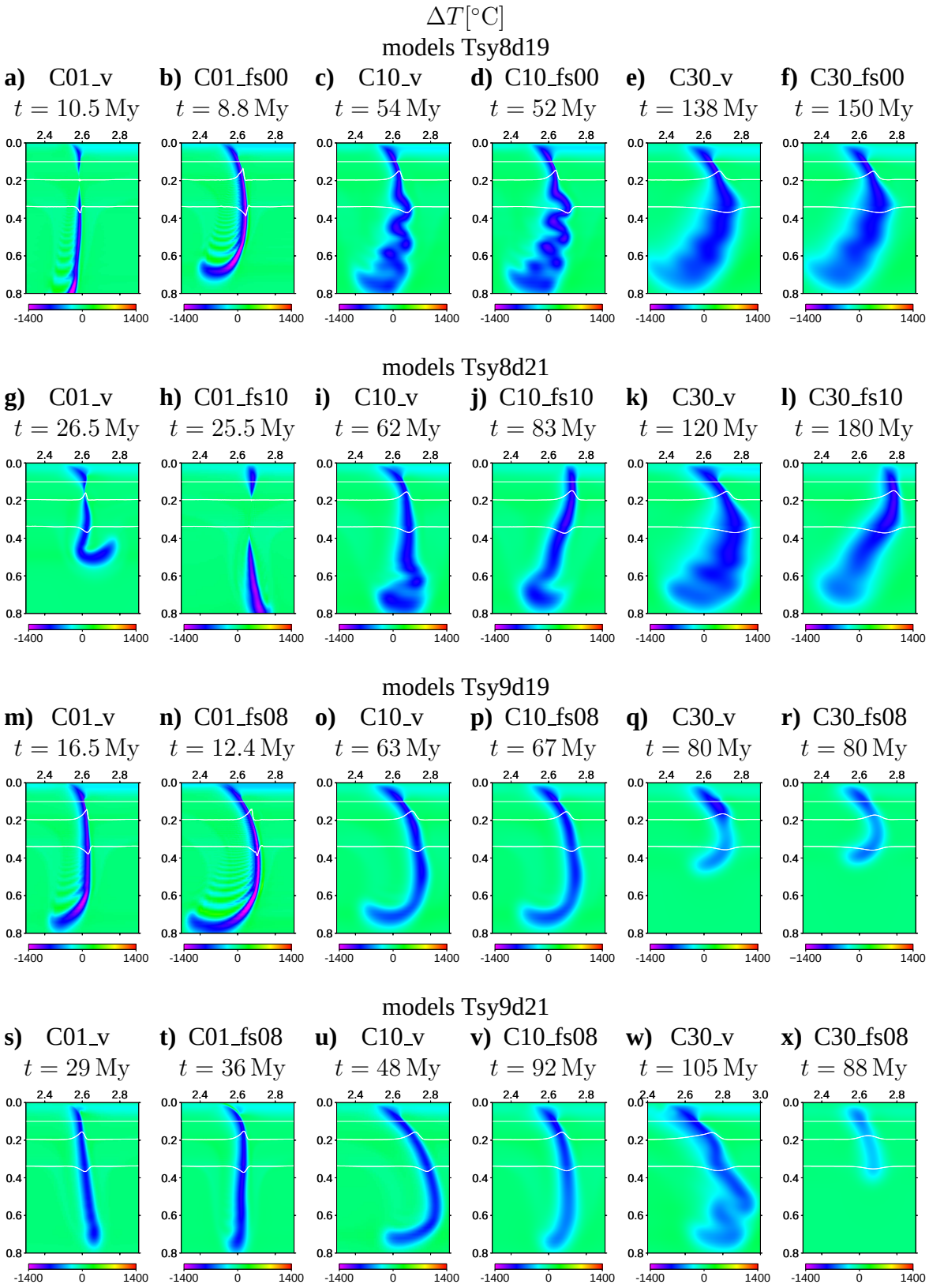

Figure 7.28 Summary of results for all models, the temperature variations $\Delta T[^\circ\mathrm{C}]$ in respect of geotherm T_{ref} are shown for $1,600\,\mathrm{km}$ deep and $1,200\,\mathrm{km}$ wide part of the model domain.

subducting plate (panel **w**), the slab penetrates into the lower mantle and the buckling is observed.

7.2.4 Seismic velocity anomalies

Finally, let us try to compare the results of our numerical modeling with seismic tomography. For this purpose, we need to convert our temperature anomalies to seismic velocity ones. The seismic velocity anomalies can be calculated from thermal and compositional structure of the mantle using the appropriate partial derivatives (sensitivities) — e.g. Deschamps and Trampert (2003). The seismic velocities and their derivatives depend on the elastic properties and the equation of state of the mantle minerals. To get the elastic parameters of the lower mantle material, we use the code kindly provided by Renata M. Wentzcovitch. It calculates polycrystalline multiphase averages of bulk and shear moduli using Hashin-Shtrinkman averages scheme (Meister and Peselnick 1966, Watt 1979). We employ the mineralogical model by Ringwood (1975) including perovskite (Pv) $(\mathrm{Mg}_{1-x}\mathrm{Fe}_x)\mathrm{SiO}_3$ and magnesiowüstite (Mw) $(\mathrm{Mg}_{1-y}\mathrm{Fe}_y)\mathrm{O}$. We take the same percentage of iron for both these minerals, i.e. $x = y = 0.12$. Further, we have to specify the ratio of magnesiowüstite to perovskite. We define it using the volume fraction of magnesiowüstite $v_f = 0.2$ at $30\,\mathrm{GPa}$ and $2,000\,\mathrm{K}$. For computing polycrystalline average of the elastic properties, we use the formulas

$$\begin{aligned} K_s(p,T) &= v_f K_s^{\mathrm{Mw}}(p,T) + (1-v_f) K_s^{\mathrm{Pv}}(p,T), \\ G(p,T) &= v_f G^{\mathrm{Mw}}(p,T) + (1-v_f) G^{\mathrm{Pv}}(p,T), \end{aligned} \tag{7.5}$$

where K_s and G are the bulk and the shear moduli, respectively. Our calculations are based on the elastic properties and equation of state of perovskite MgSiO_3 by Karki et al. (2000b) and Wentzcovitch et al. (2004). The elastic properties and equation of state of magnesiowüstite are in Karki et al. (1999) and Karki et al. (2000a). For including the iron content, we use corrections by Kiefer et al. (1999) and Karki et al. (1999) for $(\mathrm{Mg}_{1-x}\mathrm{Fe}_x)\mathrm{SiO}_3$ and $(\mathrm{Mg}_{1-y}\mathrm{Fe}_y)\mathrm{O}$, respectively. P-wave velocities are then calculated as

$$v_P(p,T) = \sqrt{\frac{K_s(p,T) + \frac{4}{3}G(p,T)}{\rho(p,T)}} \tag{7.6}$$

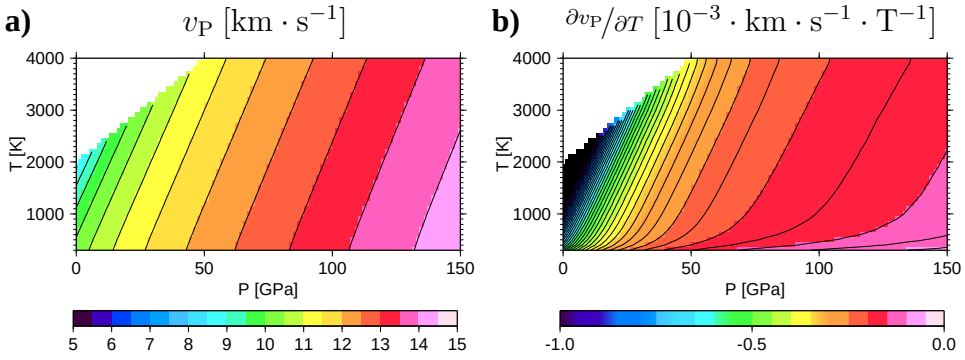

Figure 7.29 The **a)** P-wave velocity for the lower mantle material and **b)** its derivative with respect to the temperature depending on temperature and pressure.

and we calculate its derivative $\frac{\partial v_P}{\partial T}$ numerically. Both v_P and $\frac{\partial v_P}{\partial T}$ are in Fig. 7.29.

Once we have the derivative, we compute the seismic velocity anomalies for our subduction models as follows:

$$\frac{\delta v_{\mathrm{P}}}{v_{\mathrm{P}}}(p(z), T(x,z)) = \frac{\partial v_{\mathrm{P}}}{\partial T}(p(z), T(x,z)) \cdot \Delta T(x,z) \frac{1}{v_{\mathrm{P}}(p(z), T_{\mathrm{ref}}(z))}. \tag{7.7}$$

For several models where the slab thickening occurs (Fig. 7.28, panels **c–f**, **k**, **l** and **w**), the P-wave velocity anomalies are given in Fig. 7.30. Following Ribe et al. (2007), we show here the isolines of seismic velocity anomaly for $0.2\,\%$ and $0.3\,\%$. The estimated slabs widths are given in Tab. 7.5. Let us compare them to the slabs widths by Ribe

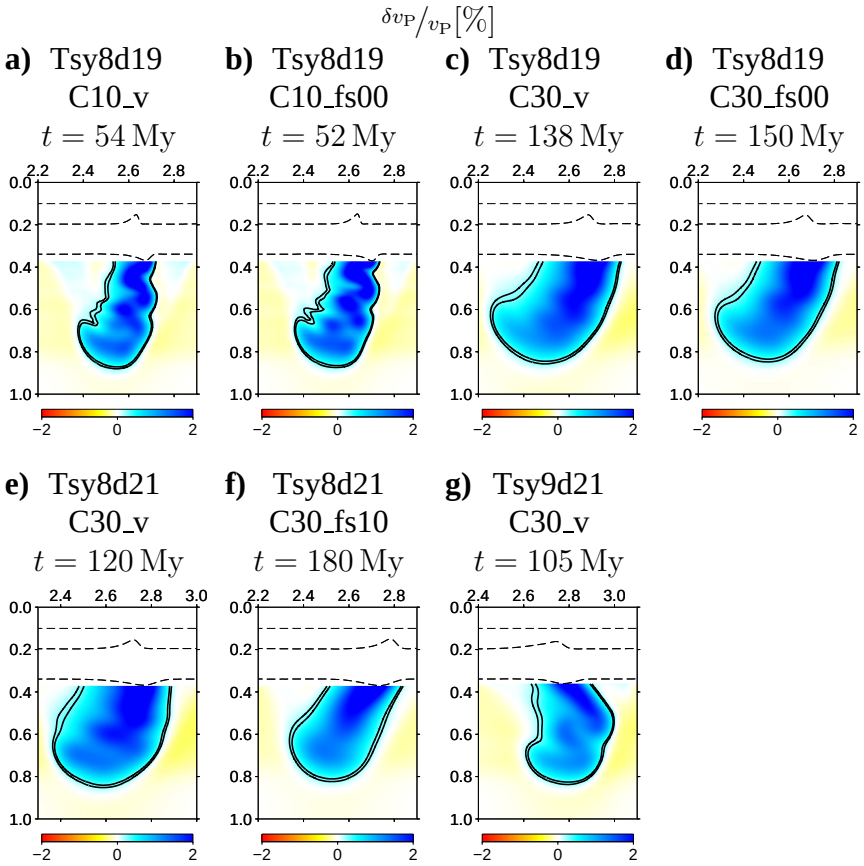

Figure 7.30 The estimation of the width of the slabs in the lower mantle using $^{\delta v_{\mathrm{P}}}/_{v_{\mathrm{P}}} = 0.2$ and $0.3\,\%$ isoline (solid line) for chosen models. Broken lines denote the depth $200\,\mathrm{km}$ and phase transitions. $2,000\,\mathrm{km}$ deep and $1,600\,\mathrm{km}$ wide part of the model domain is shown.

a) Tsy8d19 C10_v	**b)** Tsy8d19 C10_fs00	**c)** Tsy8d19 C30_v	**d)** Tsy8d19 C30_fs00	**e)** Tsy8d21 C30_v	**f)** Tsy8d21 C30_fs10	**g)** Tsy9d21 C30_v
estimated minimal slab width below boundary at $670\,\mathrm{km}$						
$360\,\mathrm{km}$	$360\,\mathrm{km}$	$690\,\mathrm{km}$	$690\,\mathrm{km}$	$800\,\mathrm{km}$	$580\,\mathrm{km}$	$490\,\mathrm{km}$
estimated maximal slab width in the lower mantle						
$580\,\mathrm{km}$	$620\,\mathrm{km}$	$790\,\mathrm{km}$	$760\,\mathrm{km}$	$890\,\mathrm{km}$	$690\,\mathrm{km}$	$650\,\mathrm{km}$

Table 7.5 The estimated width of the slabs for models shown in Fig. 7.30 and isolines $0.2 - 0.3\,\%$.

et al. (2007), who estimate the slab width to be up to $460\,\mathrm{km}$ below the boundary at $670\,\mathrm{km}$. We obtain comparable slabs widths for models with lower stress limit, weaker decoupling layer and viscosity jump 10 (Fig. 7.30**a–b**). In these cases, the slabs widths are approximately $360\,\mathrm{km}$ below the $670\,\mathrm{km}$ boundary. For models with the viscosity increase 30 at $670\,\mathrm{km}$ and lower stress limit (Fig. 7.30**c–f**), the slab velocity in the lower mantle is low (up to $\sim 2\,\mathrm{cm}\cdot\mathrm{y}^{-1}$) and conductive cooling of the ambient mantle is rather efficient therefore the plates become considerably wider than in Ribe et al. (2007). For these models, the slabs widths are in the range $(580, 800)\,\mathrm{km}$ below the $670\,\mathrm{km}$ boundary (Fig. 7.30**c–f**). For the only model with higher stress limit which shows lower mantle thickening, the estimated width below $670\,\mathrm{km}$ boundary ($490\,\mathrm{km}$) is in agreement with Ribe et al. (2007).

7.2.5 Discussion

In our models, we study the influence of the stress limit, the boundary conditions, the viscosity increase at $670\,\mathrm{km}$ boundary and the viscosity of the decoupling layer. We concentrate on relatively old slabs ($t = 100\,\mathrm{My}$). We use the activation parameters based on experimentally derived values (Frost and Ashby 1982, Karato and Wu 1993, Yamazaki and Karato 2001). The yield stress of the power-law stress-limiting mechanism is less constrained, however, the values in the range between $0.1\,\mathrm{GPa}$ and $1\,\mathrm{GPa}$ are generally assumed (Kameyama et al. 1999, van Hunen et al. 2004, Čížková et al. 2007). Further, the viscosity increase by factor 1, 10 and 30 at $670\,\mathrm{km}$ boundary is investigated. We limit ourselves to the maximum viscosity increase $C = 30$, even though sometimes much higher increase (up to $100 - 1,000$) is predicted (Forte and Mitrovica 1996, Kido and Čadek 1997). For the viscosity increase by a factor 30, the subduction process is nearly stopped if no extra push is applied by the boundary conditions. Hence, we expect that the slabs would not be able to penetrate into the lower mantle if the viscosity jump is even higher. Finally, we investigate the influence of the top boundary condition and coupling between the subducting and over-riding plates.

The resulting shape and the wavelength of the subducting plate in the lower mantle depends also on the decoupling between the plates, i.e. on the strength of the crust. In the oceanic plates, the crust consists of less-dense basalt. As it subducts, it transforms into stronger and denser eclogite by series of phase transitions. The properties of the basalt-to-eclogite metamorphism and rheological properties of basalt and eclogite are not well known and they strongly depend on the content of water and fugacity (Kohlstedt et al. 1995). Vlaar et al. (1994) use dislocation creep of diabase to describe rheological properties of both basalt and eclogite. For temperature interval $600\,^{\circ}\mathrm{C}$ and $1,750\,^{\circ}\mathrm{C}$, they get viscosities between $\sim 10^{19} - 7\cdot 10^{21}\,\mathrm{Pa}\cdot\mathrm{s}$ for $\dot{\varepsilon}_{\mathrm{II}} = 10^{-15}\,\mathrm{s}^{-1}$. Here we use a simple approximation of the crustal properties — crust material has no density contrast with respect to the mantle one and we assume two constant values of its viscosity ($10^{19}\,\mathrm{Pa}\cdot\mathrm{s}$ and $10^{21}\,\mathrm{Pa}\cdot\mathrm{s}$) in agreement with the above mentioned results by Vlaar et al. (1994).

In our models, the thickening of the slabs in the lower mantle is caused by two mechanisms — buckling and/or thickening due to the compression. The buckling is observed in the models with the lower stress limit and viscosity increase in the lower mantle (Fig. 7.28, panels **c–f**, **k**). For models with higher stress limit, the significant slab deformation occurs

only in the model with a strong decoupling layer, viscosity increase by factor 30 and a prescribed velocity on the top boundary (Fig. 7.28, panel **w**). The thickening in the lower mantle due to compression and conductive cooling is also observed (Fig. 7.28, panel **l**). For models with viscosity increase 30, the widths of the plates are too high compare to the seismic tomography models. The velocities within the lower mantle are rather low and the slab thickening due to the conductive cooling is significant.

Further, we observe the forward shift of the trench for the models with the free-slip, lower stress limiter and stronger decoupling layer (models in Fig. 7.28 panel **h**, **j** and **l**). The trenches migrate to the right, i.e. in the direction of the subducting plate. Here the coupling between the crustal layer and the subducting and the over-riding plates is rather strong and thanks to the rather low stress limit, the over-riding plates deform and part of them may subduct together with the subducting plate.

In some of our models with the weaker decoupling layer (model in Fig. 7.28 panels **b**, **m** and **n**), the plate velocities are unrealistically high. This can be caused by several factors, e.g. underestimation of the friction on the contact between the subducting and the over-riding plates, too low viscosity in the lower mantle or by neglecting 3-D effects.

Further, the plate-velocity peak caused by an exothermic phase transition at $400\,\mathrm{km}$ can be also rather high in the models with weaker decoupling layer. The velocity can even reach $\sim 75\,\mathrm{cm}\cdot\mathrm{y}^{-1}$ depending on the viscosity increase at $670\,\mathrm{km}$. These high velocities can be again caused by the underestimation of the friction on the plates contact or by two-dimensional approximation. In three-dimensional reality, the plate would reach the phase transition at $400\,\mathrm{km}$ gradually and hence the speeding effect of an exothermic phase transition would not be instantaneous and could therefore be lower.

Our results agree quite well with previous works. Christensen (1996) uses a 2-D Cartesian model of subduction with depth- and temperature dependent viscosity and he obtains buckling features for models with viscosity jump at $660\,\mathrm{km}$ or with strong phase transition at $660\,\mathrm{km}$. For a cylindrical 2-D model and composite rheology, McNamara et al. (2001) get the buckling instabilities and its degree increases with decreasing plate strength. In a 2-D Cartesian model with visco-plastic rheology, viscosity increase at $660\,\mathrm{km}$ but without phase transitions, Enns et al. (2005) also predict buckling — a higher degree of buckling is observed for weak and thin plates.

We conclude that the presence of the major phase transitions in the mantle and a viscosity increase enable the buckling of the relatively weak slab in the mantle. Further, we show that the effect of the crustal layer (especially its strength) may have important implications. Hence, in the future, we plan to concentrate on the effect of crust layer parameters in more details. Especially, the effect of the water presence within the oceanic crust may play an important role. The water content depends on the plate velocity — the amount of water content within the crust increases with decreasing plate velocity (Gorczyk et al. 2007). Consequently, the viscosity of the crust increases with increasing plate velocity. This is opposite to the effect of dislocation creep. The unrealistically high plate velocities in some of our models can be suppressed by this effect.

Chapter 8

Conclusions

We numerically solve the equations describing the thermo-chemical convection using method introduced by Gerya and Yuen (2003). This method combines the Eulerian and Lagrangian approaches. The momentum equation, continuity equation and the heat equation without advection and latent heating are solved using finite difference method. The heat and material advection and latent heating part of the heat equation are solved using marker technique. It turns out that the interpolation of the temperature and scalar properties of the fluid are essential for numerical stability. For interpolation of the temperatures from markers to Eulerian grid, we suggest and use here a different scheme than Gerya and Yuen (2003).

We wrote the code to solve the equations in a two dimensional Cartesian domain using Fortran 90. For solving the momentum and continuity equations and the heat equation, we use LU decomposition from LAPACK subroutines. The code is parallelized using shared memory model and OpenMP instruction. For testing our code, we employ several fluid mechanical problems with analytical solution. Our results were also compared with the benchmark of Blankenbach et al. (1989). Our code includes shear heating, adiabatic heating and latent heating. It can handle chemically different materials, non-linear viscosity depending on chemical composition, phase transitions, strain rate invariant and temperature and pressure. It allows to employ spatially dependent thermal expansivity, thermal conductivity and internal heating.

For high resolution model runs needed in detailed subduction modeling, the computer demands are essential. Therefore, further parallelization of the code using distributed memory is planned to get higher resolution of the Eulerian grid and speed-up the computations. In the future, the elasticity which plays an important role in the process of subduction should also be included.

We apply our code to the problem of subduction and we study the fate of the slabs in the mantle. Especially, we concentrate on the effect of the slab thickening in the lower mantle. We employ two models. In the first simple mechanical model, the mantle convection is driven by a compositional buoyancy. We study the effect of the viscosity contrast between the subducting plate and the mantle material in the upper and the lower mantle and the effect of the viscosity increase at the $670\,\mathrm{km}$ boundary. We suppose constant viscosities for each material and each phase. In these models, no buckling is observed. Some thickening (by approximately factor 2) due to the compression is observed only for

model with rather low viscosity contrast of 10 between the subducting plate and the ambient mantle and with viscosity increase by factor 10 in both plate and mantle materials in the lower mantle. For most models, no significant deformation at the viscosity barrier at the $670\,\mathrm{km}$ depth is observed. Only if the relatively high viscosity increase ($1,000$) at $670\,\mathrm{km}$ boundary is employed, the plate is bent when it penetrates into the lower mantle.

In the second model, the subduction process is driven by thermal buoyancy. We employ composite rheology including diffusion creep, dislocation creep and stress limiter. We find that the buckling occurs for relatively weak slabs in the lower mantle. In the models with viscosity jump equal to 10, this effect is observed if the weaker decoupling layer is used and for both prescribed velocity and free-slip boundary conditions. We show that the presence of the phase transitions (especially exothermic transition at $400\,\mathrm{km}$) supports the creation of the buckling instabilities. For higher viscosity jump (30), the buckling is observed in all models except for the model with stronger decoupling layer and free-slip condition. In this model, the thickening due to the compression and conductive cooling is observed. If stronger slabs are assumed, the buckling does not occur in most models. In these models, the plates subduct without any significant deformation. The resulting plate shapes depend on the boundary conditions, the viscosity increase at $670\,\mathrm{km}$ and strength of the decoupling layer. Therefore, we can conclude that the long-wavelength character of the lower mantle fast seismic velocity anomalies traditionally associated with slabs could be explained either by the buckling of relatively weak slabs or by thickening due to the compression and conductive cooling in the higher viscosity lower mantle.

Epilogue

The structure of the Earth's interior reflected in the seismic tomography images is quite complex. Since the onset of both the numerical modeling of convection and the global seismic tomography, great effort has been dedicated to reconcile results of both approaches. Convection modelers tried to vary the parameters of their thermal/thermo-chemical models to get the mantle structure and its characteristics as close as possible to the tomographic ones. On the other hand, the real resolution power of the tomographic inversion was questioned and investigated, which is necessary before one can draw the reliable conclusions about the dynamic processes in the mantle.

In this work, we deal with the problem of the correspondence of the tomographic images and convection models employing both these approaches. First, we assume that the seismic velocity anomalies in the Earth's mantle arise from the thermal structure driven by convection and, using a snapshot of thermal convection model to construct synthetic data, we study the ability of the tomographic inversion to retrieve the geodynamic models. In the second, more traditional approach, we rely on the results of the real data tomographic inversion, where the thickening of the slabs is observed in the lower mantle and we try to get such behavior of the slabs in our regional scale convection model.

Apparently none of these two approaches is better than the other one. A synthesis of both of them may however ultimately bring us further on the way of revealing the structure of the Earth's mantle and understanding the dynamic processes in it.

References

Abers, G., Roecker, S., 1991. Deep structure of an arc-continent collision: earthquake relocations and inversion for upper mantle P- and S- velocities beneath Papua New Guinea. *J. Geophys. Res. 96*, 6379–6401.

Aki, K., Christoffersson, A., Husebye, E., 1977. Determination of the three-dimensional seismic structure of the lithosphere. *J. Geophys. Res. 82*, 277–296.

Aki, K., Richards, P., 1980. *Quantitative Seismology*. W.H. Freeman and Company, San Francisco.

Ashby, M., Verrall, R., 1977. Micromechanism of flow and fracture, and their relevance to the rheology of the upper mantle. *Phil. Trans. R. Soc. Lond. A. 288*, 59–95.

Badro, J., Rueff, J., Vanko, G., Monaco, G., Fiquet, G., Guyot, F., 2004. Electronic transitions in perovskite: Possible nonconvecting layers in the lower mantle *305*, 383–386.

Becker, T., Boschi, L., 2002. A comparison of tomographic and geodynamic mantle models. *Geochem. Geophys. Geosyst. 3*, doi:10.129/2001GC000168.

Běhounková, M., Čížková, H., Matyska, C., 2005. Resolution tests of global geodynamic models by travel-time tomography. *Stud. Geophys. Geod. 49*, 343–363.

Běhounková, M., Čížková, H., Matyska, C., Yuen, D., Wang, M., 2007. Resolution tests of 3-D convection models by travel-time tomography: Effects of Rayleigh number and regular vs. irregular parameterization. *Geophys. J. Int. 170*, 401–416.

Bijwaard, H., Spakman, W., Engdahl, E., 1998. Closing the gap between regional and global travel time tomography. *J. Geophys. Res. 103*, 30055–30075.

Bina, C., Helffrich, G., 1994. Phase transition clapeyron slopes and transition zone seismic discontinuity topography. *J. Geophys. Res. 103*, 15853–15860.

Birdsall, C., Langdon, A., 1991. *Plasma physics via computer simulation*. McGraw-Hill, Inc.

Blankenbach, B., Busse, F., Christensen, U., Cserepes, L., Gunkel, D., Hansen, U., Harder, H., Jarvis, G., Koch, M., M. G., Moore, D., Olson, P., Schmeling, H., Schnaubelt, T., 1989. A benchmark comparison for mantle convection. *Geophys. J. Int. 91*, 23–38.

Boschi, L., 2001. Application of linear inverse theory in modern global seismology, Ph.D. thesis, Harward University.

Boschi, L., 2006. Global multiresolution models of surface wave propagation: comparing equivalently regularized born and ray theoretical solutions. *Geophys. J. Int. 167*, 238–252.

Boschi, L., Ampuero, J.-P., Peter, D., Mai, P., Soldati, G., Giardini, D., 2007. Petascale computing for future breakthroughs in global seismology. *Phys. Earth Planet. Inter. 163*, 245–250.

Boschi, L., Dziewonski, A., 1999. "High" and "Low" resolution images of the Earth's mantle: Implications of different approaches to tomographic modeling. *J. Geophys. Res. 104*, 25567–25594.

Bunge, H., P., Davies, J., 2001. Tomographic images of a mantle circulation models. *Geophys. Res. Let. 28*, 78–80.

Bunge, H., P., Richards, M., Baumgardner, J., 1996. Effect of depth-dependent viscosity on the planform of mantle convection. *Nature 379*, 436–438.

Čadek, O., Fleitout, L., 2003. Effect of lateral viscosity variations in the top 300 km on the geoid and dynamic topography. *Geophys. J. Int. 152*, 566–580.

Červený, V., Klimeš, L., Pšenčík, I., 1988. Complete seismic ray-tracing in three-dimensional structures. In: Doornbos, D. (Ed.), Seismological algorithms. Academic Press, New York, pp. 89–168.

Chen, P., Jordan, T., Zhao, L., 2007. Full 3D tomography: A comparison between the scattering-integral and adjoint-wavefield methods. *Geophys. J. Int.*, in press.

Chiao, L.-Y., Liang, W.-T., 2003. Multiresolution parameterization. *Geophysics 68*, 199–209, doi

10.1190/1.1543207.

Christensen, U., 1996. The influence of trench migration on slab penetration into the lower mantle. *Earth Plan. Sci. Let. 140*, 27–39.

Christensen, U., 1998. Dynamic phase boundary topography by latent heat effects. *Earth Plan. Sci. Let. 154*, 295–306.

Christensen, U., Yuen, D., 1984. The interaction of a subducting lithospheric slab with a chemical or phase boundary. *J. Geophys. Res. 89*, 4389–4402.

Christensen, U., Yuen, D., 1985. Layered convection induced by phase transitions. *J. Geophys. Res. 99*, 10291–10300.

Čížková, H., van Hunen, J., van den Berg, A., 2007. Stress distribution within subducting slabs and their deformation in the transition zone. *Phys. Earth Planet. Inter. 161*, 202–214.

Čížková, H., van Hunen, J., van den Berg, A., Vlaar, N., 2002. The influence of rheological weakening and yield stress on the interaction of slabs with 670 km discontinuity. *Phys. Earth Planet. Inter. 199*, 447–457.

Čížková, H., Čadek, O., 1997. Effect of a viscosity interface at 1000 km depth on mantle convection. *Stud. Geophys. Geod. 41*, 297–306.

Čížková, H., Yuen, D., Zhou, H.-W., 1997. Slope of the geoid spectrum and constraints on mantle viscosity stratification. *Geophys. Res. Let. 23*, 3,063–3,066.

Coates, R., Chapman, C., 1990. Ray perturbation-theory and the Born approximation. *Geophys. J. Int. 100*, 379–392.

Dahlen, F., Hung, S., Nolet, G., 2000. Frechet kernels for finite-frequency traveltimes - I. Theory. *Geophys. J. Int. 141*, 157–174.

Deschamps, F., Trampert, J., 2003. Mantle tomography and its relation to temperature and composition. *Phys. Earth Planet. Inter. 140*, 277–291.

Dziewonski, A., 1984. Mapping the lower mantle: determination of lateral heterogeneity up to degree and order 6. *J. Geophys. Res. 89*, 5929–5953.

Dziewonski, A., 2000. Global seismic tomography: Past, present and future. In: E. Boschi, G. E., Morelli, A. (Eds.), Problems in geophysics for the new millennium. Editrice Compositori, Bologna, Italy, pp. 289–349.

Dziewonski, A., Anderson, D., 1981. Preliminary reference Earth model. *Phys. Earth Planet. Inter. 24*, 297–356.

Enns, A., Becker, T., Schmeling, H., 2005. The dynamics of subduction and trench migration for viscosity stratification. *Geophys. J. Int. 160*, 761–775.

Fornberg, B., 1995. *A practical guide to pseudospectral methods*. Cambridge University Press, Cambridge.

Forte, A., Mitrovica, J., 1996. New inferences of mantle viscosity from joint inversion of long-wavelength mantle convection and post-glacial rebound data. *Geophys. Res. Let. 23*, 1147–1150.

Frost, H., Ashby, M., 1982. *Deformation Mechanism Maps*. Pergamon Press, Oxford.

Fukao, Y., To, A., Obayashi, M., 2003. Whole mantle P wave tomography using P and PP-P data. *J. Geophys. Res. 108*, No. 2021.

Gaherty, J., Hager, B., 1994. Compositional vs. thermal buoyancy and the evolution of subducted litosphere. *Geophys. Res. Let. 21*, 141–144.

Gerya, T., Perchuk, L., van Reenen, D., Smit, C., 2000. Two-dimensional numerical modeling of pressure-temperature-time paths for the exhumation of some granulite facies terrains in the precambian. *J. Geodynam. 30*, 17–35.

Gerya, T., Yuen, D., 2003. Characteristics-based marker-in-cell method with conservative finite-differences schemes for modeling geological flows with strongly variable transport properties.

Phys. Earth Planet. Inter. 140, 293–318.

Gorczyk, W., Willner, A., Gerya, T., Connolly, A., Burg, J.-P., 2007. Physical controls of magmatic productivity at Pacific-type convergent margins: numerical modelling. *Phys. Earth Planet. Inter. 163*, 209–232.

Grand, S., van der Hilst, R., Widiyantoro, S., 1997. Global seismic tomography: A snapshot of convection in the earth. *GSA Today 7*, 1–7.

Gurnis, M., Hager, B., 1988. Controls of the structure of subducted slabs. *Nature 335*, 317–321.

Hager, B., Richards, M., 1989. Long wavelength variation in Earth's geoid: physical models and dynamical implications. *Philos. Trans. R. Soc. Lond. 328*, 309–327.

Hansen, P., 1992. Analysis of discrete ill-posed problems by means of the l-curve. *SIAM Rev. 34*, 561–508.

Hansen, P., 2000. The L-curve and its use in the numerical treatment of inverse problems. In: Johnston, P. (Ed.), Advances in Computational Bioengineering. WIT Press, Southampton, pp. 119–142.

Hockney, R., Eastwood, J., 1988. *Computer simulations using particles*. IOP Publishing Ltd, Bristol.

Hofmeister, A., 2005. Dependence of diffusive radiative transfer on grain-size, temperature, and Fe-content: Implications for mantle processes. *J. Geodynamics. 40*, 51–72.

Honda, S., 1996. Applicability of adaptive grid inversion to imaging thermal anomalies caused by convection. *Geophys. Res. Let. 23*, 2733–2736.

Iitaka, T., Hirose, K., Kawamura, K., Murakami, M., 2004. The elasticity of the $MgSiO_3$ post-perovskite phase in the Earth's lowermost mantle. *Nature 430*, 442–445.

Inoue, H., Fukao, Y., Tanabe, T., Ogata, Y., 1990. Whole mantle P-wave travel time tomography. *Phys. Earth Planet. Inter. 59*, 294–328.

ISC, 1964-2001. International Seismological Centre, On-line Bulletin.
URL `http://www.isc.ac.uk/Bull`

Ita, J., King, S., 1994. Sensitivity of convection with an endothermic phase change to the form of governing equations, initial conditions, boundary conditions, and equation of state. *J. Geophys. Res. 99*, 15919–15938.

Johnson, S., Masters, T., Tackley, P., Glatzmaier, G., 1993. How well can we resolve a convecting Earth with seismic data? *Eos. Trans. AGU 80*, fall Meeting suppl.

Kameyama, M., Yuen, D., Karato, S.-I., 1999. Thermal-mechanical effects of low-temperature plasticity (the peierls mechanism) on the deformation of viscoelastic shear zone. *Earth Plan. Sci. Let. 168*, 159–172.

Kárason, H., van der Hilst, R., 2001. Tomographic imaging of the lowermost mantle with differential times of refracted and diffracted core phases (PKP, PKP_{diff}). *J. Geophys. Res. 106*, 6569–6587.

Karato, S.-I., 1993. Importance of anelasticity in the interpretation of seismic tomography. *Geophys. Res. Let. 20*, 1623–1626.

Karato, S.-I., Wu, P., 1993. Rheology of the upper mantle: A synthesis. *Science 260*, 83–108.

Karki, B., Wentzcovitch, R., de Gironcoli, S., Baroni, S., 1999. First-principles determination of elastic anisotropy and wave velocities of MgO at lower mantle conditions. *Science 286*, 1705–1707.

Karki, B., Wentzcovitch, R., de Gironcoli, S., Baroni, S., 2000a. High-pressure lattice dynamics and thermoelasticity of MgO. *Phys. Rev. B. 61*, 8793–8800.

Karki, B., Wentzcovitch, R., de Gironcoli, S., Baroni, S., 2000b. Ab initio lattice dynamics of $MgSiO_3$ perovskite at high pressure. *Phys. Rev. B. 62*, 14,750–14,756.

Katsura, T., Yokoshi, S., Shastkiy, A., Okube, M., Fukui, H., Ito, E., Tomioka, N., Sugita, M.,

Hagiya, K., Kuwata, O., Ohtsuka, K., Nozawa, A., K, F., 2005. Precise determination of thermal expansion coefficient of MgSiO3 perovskite at the top of the lower mantle conditions. In: van der Hilst, R. (Ed.), rd workshop on Earth's Mantle Composition, Structure and Phase Transitions. Saint Malo, France.

Kido, M., Čadek, O., 1997. Inferences of viscosity from the oceanic geoid: Indication of a low viscosity zone below the 660-km discontinuity. *Earth Plan. Sci. Let. 151*, 125–137.

Kiefer, B., Stixrude, L., Wentzcovitch, R., 1999. Elasticity of (Mg,Fe)SiO_3-perovskite at high pressures. *Geophys. Res. Let. 29*, No. 11, 1539.

Klimeš, L., 2002. Application of medium covariance functions to travel-time tomography. *Pure Appl. Geophys. 159*, 1791–1810.

Kohlstedt, D., Evans, B., Mackwell, S., 1995. Strength of the lithosphere: constraints imposed by laboratory experiments. *J. Geophys. Res. 100*, 17,587–17,602.

Lambeck, K., Johnston, P., 1998. The viscosity of the mantle: evidence from analysis of glacial-rebound phenomena. In: Jackson, I. (Ed.), The Earth's mantle: composition, structure and evolution. Cambridge University Press, pp. 461–502.

LAPACK, 3.1.1.
URL `http://www.netlib.org/lapack/`

Lei, J., Zhao, D., 2006. Global P-wave tomography: On the effect of various mantle and core phases. *Phys. Earth Planet. Inter. 154*, 44–69.

Lévêque, J.-J., Rivera, L., Wittlinger, G., 1993. On the use of the checker-board test to assess the resolution of tomographic inversion. *Geophys. J. Int. 115*, 313–318.

Li, X., Romanowicz, B., 1995. Comparison of global wave-form inversions with and without considering cross-branch modal coupling. *Geophys. J. Int. 121*, 695–709.

Li, X.-D., Romanowicz, B., 1996. Global mantle shear-velocity model developed using nonlinear asymptotic coupling theory. *J. Geophys. Res. 101*, 22245–22272.

Marquering, H., Nolet, G., Dahlen, F., 1998. Three-dimensional waveform sensitivity kernels. *Geophys. J. Int. 132*, 521+.

Masters, G., Johnson, S., Laske, G., Bolton, H., 1996. A shear-velocity model of the mantle. *Phil. Trans. R. Soc. Lond. A 354*, 1385–1411.

McNamara, A. K., Karato, S.-I., van Keken, P. E., 2001. Localization of dislocation creep in the lower mantle: implications for the origin of seismic anisotropy. *Earth Plan. Sci. Let. 191*, 85–99.

Mégnin, C., Bunge, H., Romanowicz, B., Richards, M., 1997. Imaging 3-D spherical convection models: What can seismic tomography tell us about mantle dynamics? *Geophys. Res. Let. 24*, 1299–1302.

Mégnin, C., Romanowicz, B., 2000. A comparison between tomographic and geodynamic models of the Earth's mantle. In: van der Hilst, R. (Ed.), Dynamics of Plate Motions. AGU, Washington DC.

Meister, R., Peselnick, L., 1966. Variational method of determining effective moduli of polycrystals with tetragonal symmetry. *J. Appl. Phys. 37*, 4121–4125.

Menke, W., 1989. *Geophysical data analysis: Discrete inverse theory*, rev Edition. Academic, San Diego.

Mitrovica, J., Forte, A., 2004. A new inference of mantle viscosity based upon joint inversion of convection and glacial isostatic adjustment data. *Earth Plan. Sci. Let. 225*, 177–189.

Montelli, R., Nolet, G., Dahlen, F., Masters, G., Engdahl, E., Hung, S.-H., 2004a. Finite-frequency tomography reveals a variety of plumes in the mantle. *Science 303*, 338–343.

Montelli, R., Nolet, G., Masters, G., Dahlen, F.A., H. S.-H., 2004b. Global P and PP travel-time tomography: rays versus waves. *Geophys. J. Int. 158*, 637–654, doi: 10.1111/j.1365-

246X.2004.02346.x.

Murakami, M., Hirose, K., Kawamura, K., N., S., Ohishi, Y., 2004. Post-perovskite phase transition in $MgSiO_3$. *Science 304*, 855–858.

Nolet, G., Montelli, R., 2005. Optimal parametrization of tomographic models. *Geophys. J. Int. 161*, 365–372.

Oganov, A., Ono, S., 2004. Theoretical and experimental evidence for a post-perovskite phase of $MgSiO_3$ in Earth's D" layer. *Nature 430*, 445–448.

Paige, C., Saunders, M., 1982a. LSQR: An algorithm for sparse linear equation and sparse least squares. *ACTM Trans. Math. Softw. 8*, 43–71.

Paige, C., Saunders, M., 1982b. LSQR: Sparse linear equations and least squares problems. *ACTM Trans. Math. Softw. 8*, 195–209.

Peltier, W., 1996. Mantle viscosity and ice-age ice sheet tomography. *Science 273*, 1359–1364, No. 5280.

Peter, D., Tape, C., Boschi, L., 2007. Surface wave tomography: global membrane waves and adjoint methods. *Geophys. J. Int.*, submitted.

Press, W., Teukolsky, S., Vetterling, W., Flannery, B., 1992. *Numerical recipes in FORTRAN: the art of scientific computing*, 2nd Edition. Cambridge University Press.

Ribe, N., 2003. Periodic buckling of viscous sheets. *Phys. Rev. E Stat. Phys. Plasmas Fluids Relat. Interdiscip. Topiccs 68*, 036305.

Ribe, N., Stutzmann, E., Ren, Y., van der Hilst, R., 2007. Buckling instabilities of subducted lithosphere beneath the transition zone. *Earth Plan. Sci. Let. 254*, 173–179.

Ricard, Y., Richards, M., Lithgow-Bertelloni, C., le Stunff, Y., 1993. A geodynamic model of mantle density heterogeneity. *J. Geophys. Res. 98*, 21,895–21,909.

Richards, M., Ricard, Y., Lithgow-Bertelloni, C., Spada, G., Sabadini, R., 1997. An explanation for Earth's long term rotational stability. *Science 275*, 372–375.

Ringwood, A., 1975. *Composition and petrology of the Earth's mantle*. McGraw-Hill, New York.

Saad, Y., SPARSKIT.
URL `http://www-users.cs.umn.edu/~saad/software/SPARSKIT/sparskit.html`

Shepard, D., 1968. A two-dimensional interpolation function for irregularly-spaced data. *Proceedings of the 23rd National Conference, ACM, New York*, 517–524.

Soldati, G., Boschi, L., 2005. The resolution of whole Earth seismic tomographic models. *Geophys. J. Int. 161*, 143–153.

Spakman, W., Bijwaard, H., 2001. Optimization of cell parameterization for tomographic inverse problems. *Pure Appl. Geophys. 158*, 1401–1423.

Steinbach, V., Yuen, D., 1995. The effects of temperature dependent viscosity on mantle convection with two mantle major phase transitions. *Phys. Earth Planet. Inter. 90*, 13–36.

Su, W.-J., Woodward, R., Dziewonski, A., 1994. Degree-12 model of shear velocity heterogeneity in the mantle. *J. Geophys. Res. 99*, 4945–4980.

Tackley, P., 2002. Strong heterogeneity caused by deep mantle layering. *Geochem. Geophys. Geosyst. 13*, doi:10.1029/2001GC000167.

Tackley, P., Stevenson, D., 1993. A mechanism for spontaneous self-perpetuating volcanism on terrestrial planets. In: Stone, D., S., R. (Eds.), Flow and creep in the Solar system: observations, modeling and theory. Kluwer Academic, pp. 307–321.

Tarantola, A., 1987. *Inverse problem theory*. Elsevier, Amsterdam.

Trampert, J., Snieder, R., 1996. Model estimation biased by truncated expansion: Possible artifacts in seismic tomography. *Science 271*, 1257–1260.

Tromp, J., Tape, C., Liu, Q., 2005. Seismic tomography, adjoint methods, time reversal and

banana-doughnut kernels. *Geophys. J. Int. 160*, 195–216.

Tsuchiya, T., Tsuchiya, J., Umemoto, K., Wentzovitch, R., 2004. Phase transition in $MgSiO_3$ perovskite in the Earth's lower mantle. *Earth Plan. Sci. Let. 224*, 241–248.

Turcotte, D., Oxburgh, E., 1967. Finite amplitude convective cells and continental drift. *J. Fluid Mech. 28*, 29–42.

Turcotte, D., Schubert, G., 2002. *Geodynamics*, 2nd Edition. Cambridge Univ., New York, NY.

van den Berg, A., van Keken, P., Yuen, D., 1993. The effects of a composite non-newtonian and newtonian rheology on mantle convection. *Geophys. J. Int. 115*, 62–78.

van der Hilst, R.D., Li, C., Kárason, H., 2004. A new global model for 3D variations in P wavespeed in Earth's mantle, AGU, Fall meeting.

van der Hilst, R., Widiyantoro, S., Engdahl, E., 1997. Evidence for deep mantle circulation from global tomography. *Nature 386*, 578–584.

van Hunen, J., 2001. Shallow and buoyant lithospheric subduction: causes and implications from thermo-chemical numerical modeling, Ph.D. thesis, Utrecht University.

van Hunen, J., van den Berg, A., Vlaar, N., 2004. Various mechanisms to induce present-day shallow flat subduction and implications for the younger Earth: a numerical parameter study. *Phys. Earth Planet. Inter. 146*, 179–194.

Varshalovich, D., Moskalev, A., Khersonskii, V., 1989. *Quantum Theory of Angular Momentum*. World Scientific, Singapore.

Vasco, D., Johnson, L., Marques, O., 2003. Resolution, uncertainty, and whole Earth tomography. *J. Geophys. Res. 108*, No. 2022.

Vasco, D., Johnson, L., Pulliam, R., 1995. Lateral variation in mantle velocity structure and discontinuities determined from P, PP, S, SS and SS-SdS travel time residuals. *J. Geophys. Res. 100*, 24037–24059.

Vlaar, N., van Keken, P., van den Berg, A., 1994. Cooling of the Earth in the Archaean: consequences of pressure-release melting in a hotter mantle. *Earth Plan. Sci. Let. 121*, 1–18.

Watt, J. P., 1979. Hashin-Shtrikman bounds on the effective elastic moduli of polycrystals with orthorhombic symmetry. *J. Appl. Phys 50*, 6290–6295.

Weinberg, R., Schmeling, H., 1992. Polydiapirs: multiwavelength gravity structures. *J. Struct. Geol. 14*, 425–436.

Wentzcovitch, R., Karki, B., Cococcioni, M., de Gironcoli, S., 2004. Thermoelastic properties of $MgSiO_3$-perovskite: insights on the nature of the Earth's lower mantle. *Phys. Rev. Let. 92*, No. 018501.

Woodhouse, J., Dziewonski, A., 1984. Mapping the upper mantle: Three dimensional modelling of Earth structure by inversion of seismic waveforms. *J. Geophys. Res. 89*, 5953–5986.

Woodward, M., 1992. Wave-equation tomography. *Geophysics 57*, 15–26.

Yamazaki, D., Karato, S.-I., 2001. Some mineral physics constraints on the rheology and geothermal structure of Earth's lower mantle. *American Mineralogist 86*, 385–391.

Yanagisawa, T., Yamagishi, Y., 2005. Rayleigh-Benard convection in spherical shell with infinite Prandtl number at high Rayleigh number. *Journal of the Earth Simulator 4*, 11–17.

Zhang, S., Yuen, D., 1996. Various influences on the dynamic of mantle plumes in the time-dependent 3-D compressible spherical-shell convection. *Phys. Earth Planet. Inter. 94*, 241–267.